THÈSE

présentée pour l'obtention du grade de

Docteur

de

L'Université Paris 13

Spécialité: Mécanique et Matériaux

et de

L'Université de Science et Technologie AGH de Cracovie

par

Mariusz JĘDRYCHOWSKI

Etude expérimentale et modélisation des mécanismes de recristallisation et de la croissance de gains dans des métaux de structure hexagonale.

soutenue publiquement **le 15 décembre 2014 à Cracovie**

devant le jury composé de

Mme Nathalie BOZZOLO, Professeur, MinesParistech (France), rapporteur

M. Krzysztof SZTWIERTNIA, Professeur, Académie des Sciences de Pologne (rapporteur)

Mme Danièle CHAUBET, Maître de Conférences, Université Paris 13 (France), examinatrice

M. Krzysztof WIERZBANOWSKI, Professeur, Université AGH (Pologne), rapporteur

Mme Brigitte BACROIX, Directrice de recherche CNRS, Université Paris 13 (France), directrice de thèse

M. Jacek TARASIUK Professeur, Université AGH (Pologne), co-directeur de thèse

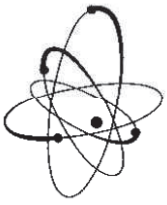

Faculty of Physics and Applied Computer Science
AGH University of Science and Technology,
Kraków, Poland

LSPM – CNRS,
Université Paris 13, PRES Sorbonne Paris Cité
99. av. J.B. Clément, 93430 Villetaneuse, France

DISSERTATION

submitted for the degree of

Doctor

of

Paris 13 University

Specialty: Mechanics and Materials

and of

AGH University of Science and Technology,

by

Mariusz JĘDRYCHOWSKI

Investigation of recrystallization and grain growth in hexagonal metals and computer modeling of these phenomena

Defended publicly on December 15th, 2014 in Kraków
In the presence of the committee composed of

Nathalie BOZZOLO, Professor, MinesParistech (France), referee
Krzysztof SZTWIERTNIA, Professor, Polish Academy of Sciences (Poland), referee
Danièle CHAUBET, Associate Professor, Paris 13 University (France), examiner
Krzysztof WIERZBANOWSKI, Professor, AGH University (Poland), examiner
Brigitte BACROIX, CNRS Research Scientist, Paris 13 University (France), PhD supervisor
Jacek TARASIUK Professeur, Université AGH (Poland), PhD supervisor

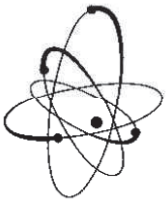

Faculty of Physics and Applied Computer Science
AGH University of Science and Technology,
Kraków, Poland

LSPM – CNRS,
Université Paris 13, PRES Sorbonne Paris Cité
99. av. J.B. Clément, 93430 Villetaneuse, France

This PhD thesis has been completed within the framework of the Human Capital Operational Program POKL.04.01.01-00-434/08-02 co-financed by the European Union.

This PhD thesis has been also partly supported by the scholarship granted by French Government.

Declaration of the author of this dissertation:

Aware of legal responsibility for making untrue statements I hereby declare that I have written this dissertation myself and all the contents of the dissertation have been obtained by legal means.

data, podpis autora

Declaration of the thesis Supervisor:

This dissertation is ready to be reviewed.

data, podpis promotora rozprawy

Acknowledgements

Foremost, I would like to thank my supervisors
prof. Jacek Tarasiuk and prof. Brigitte Bacroix
for providing me with the opportunity to undertake research in an interesting scientific field of physics and materials science.

I am deeply grateful for all their support, valuable guidance and encouragement, which I received throughout the research work. It has been greatly fortunate for me to be under their supervision.

I am sincerely indebted to Jacek Tarasiuk for being not only the supervisor, but most of all the person who I could trust and rely on over past years. It has been a great honor and privilege for me to share with him all these important moments full of inspiration as well as valuable discussions.

My special thanks are expressed to dr Marianna Marciszko, dr Krzysztof Janc and dr Sebastian Wroński for their kindness and support during my PhD studies. Also, I want to thank all colleagues from Faculty of Physics and Applied Computer Sciences and from Laboratoire des Sciences des Procédés et des Matériaux for positive atmosphere during research work.

Last but not the least I would like to thank my family for help, support and patience.

Streszczenie:

Zjawiska rekrystalizacji i rozrostu ziaren zajmują ważne miejsce w nauce o materiałach. Są one również szczególnie istotne z punktu widzenia współczesnych procesów technologicznych, bazujących na odpowiedniej obróbce termomechanicznej.

To właśnie w ten sposób aktywowane są wspomniane zjawiska, co w konsekwencji prowadzi do przebudowy mikrostruktury oraz tekstury materiału polikrystalicznego, a zatem zmiany parametrów wpływających w wyraźny sposób na własności fizyczne i mechaniczne końcowego produktu metalurgicznego.

Głównym celem przedstawionej tezy jest zbadanie rekrystalizacji i rozrostu ziaren w kontekście metali heksagonalnych. W szczególności rozważane są tytan oraz cyrkon, które ze względu na unikalne własności cieszą się rosnącym zainteresowaniem ze strony nauki, jak również nowoczesnej techniki. Ponadto gruntowne zrozumienie omawianych zjawisk występujących w tych metalach to stosunkowo nowy problem podejmowany w nielicznych pracach.

W przedstawionej tezie zastosowano dwa podejścia badawcze ściśle ze sobą powiązane, odpowiednio eksperyment i symulacje komputerowe.

W części eksperymentalnej przygotowano zestaw próbek dla tytanu i cyrkonu, które następnie poddano pomiarom opartym na technice dyfrakcji elektronów wstecznie rozproszonych (EBSD) oraz dyfrakcji rentgenowskiej. W tym miejscu należy zwrócić uwagę na autorską metodą opisu i analizy obszarów przynależących do granic międzyziarnowych, która została wykorzystana do opracowania otrzymanych danych doświadczalnych.

Z kolei w części modelowej przygotowano od podstaw oprogramowanie służące do symulacji zjawisk rekrystalizacji i rozrostu ziaren. W głównej mierze składa się ono z odpowiednio zaimplementowanego modelu Pottsa bazującego na podejściu Monte Carlo. Natomiast elementami dodatkowymi są narzędzia do wizualizacji danych, a także konfiguracji parametrów modelu.

Analiza danych eksperymentalnych wykazała, że odkształcenie plastyczne tytanu zadane poprzez walcowanie na zimno prowadzi do silnie zróżnicowanej mikrostruktury. Wynika ona ze sposobu, w jaki materiał ten reaguje na przyłożone naprężenia. W szczególności podkreślono wpływ bliźniakowania, który wyraźnie uwidacznia się na początku procesu odkształcenia (w tym przypadku jest to 20% zgniotu). W rezultacie, większość ziaren ulega kilkukrotnemu podzieleniu poprzez uformowanie się granic bliźniaczych. Z drugiej strony, w mikrostrukturze tytanu wciąż wystę-

pują ziarna, które są niekorzystnie zorientowane, jeśli chodzi o bliźniakowanie. Ich kształt pozostaje w zasadzie niezmieniony, natomiast wewnętrzna struktura krystalograficzna ulega stopniowym zniekształceniom, w wyniku zwiększającej się liczby dyslokacji. Te z kolei objawiają się w danych eksperymentalnych pod postacią dezorientacji lokalnych.

Dalsze odkształcenie (odpowiednio 40% i 60% zgniotu) wzmacnia opisane odmienne zachowanie pomiędzy ziarnami. Oznacza to, że podzielone ziarna ulegają dalszemu rozdrobnieniu, natomiast nieliczne, pozostałe łączą się w stosunkowo duże obszary cechujące się występowaniem wyraźnych, wewnątrz-ziarnowych gradientów orientacji.

Zaobserwowane różnice pomiędzy badanymi trzema stopniami odkształcenia mają znaczący wpływ na zjawiska rekrystalizacji i rozrostu ziaren. Obszary pofragmentowane i silnie rozdrobnione są preferowanym miejscem do zarodkowania i rozrostu nowych, zrekrystalizowanych ziaren.

Wynika stąd fakt, iż najbardziej zaawansowana ewolucja mikrostruktury występuje w próbkach uprzednio zwalcowanych do 60%. W tym przypadku ziarna po rekrystalizacji są najmniejsze, co implikuje możliwość ich dalszego rozrostu w trakcie wygrzewania. Dodatkowo pokazano, że rozrost ten wiąże się z różnicą pomiędzy globalnym a lokalnym rozkładem dezorientacji.

Dla porównania, ta sama obróbka cieplna próbki zwalcowanej do 20% skutkuje znacznie mniejszą liczbą zarodków, wyraźnie większym rozmiarem ziaren po rekrystalizacji i ograniczoną fazą dalszego rozrostu.

Przedstawione mechanizmy rozrostu ziaren skorelowano ze zmianami w teksturze tytanu. Analiza stanów częściowej rekrystalizacji oraz stanów w pełni zrekrystalizowanych wskazuje na nieznaczną ewolucję tekstury we wszystkich rozważanych próbkach. Dopiero zaawansowany rozrost ziaren, dyskutowany dla próbki o 60% zgniocie, implikuje stopniowy obrót głównej składowej tekstury o kąt 30° wokół osi **c**. Przejście to odnotowane jest w literaturze jako zamiana składowej $\{hkil\}<10\bar{1}0>$ na składową $\{hkil\}<11\bar{2}0>$.

Wnioski wyciągnięte na bazie wyników doświadczalnych zostały sformułowane w postaci modelu fizycznego, który następnie zastosowano w symulacjach zjawisk rekrystalizacji i rozrostu ziaren. Pokazano, że wykonane modelowanie komputerowe prowadzi do satysfakcjonujących i zgodnych z eksperymentem rezultatów.

W przypadku cyrkonu celem badania była analiza początkowych etapów odkształcenia (17%) - wymuszonego poprzez ściskanie w kanale w dwóch prostopadłych kierunkach (ND i TD) - i jego wpływu na stan częściowo zrekrystalizowany.

Odnotowano, że w obu rozważanych przypadkach ziarna mają tendencje do łączenia się w większe obszary, w wyniku akumulacji dezorientacji lokalnych, co w konsekwencji prowadzi do przerwania granicy wysokokątowej, a nawet jej zamiany na granicę niskokątową – podobny mechanizm wskazano dla tytanu.

Jednocześnie pokazano, że próbki ściskane w kierunku TD są łatwiejsze w odkształceniu, prawdopodobnie w związku z większą aktywnością bliźniakowania tuż po rozpoczęciu zakresu plastycznego. Ta różnica objawia się na krzywych ściskania, a także wpływa na większą liczbę granic wysokokątowych w próbkach ściskanych w kierunku TD, zwłaszcza w przypadku końcowego odkształcenia.

To odmienne zachowanie mikrostruktur cyrkonu po odkształceniu zostało powiązane z ewolucją mikrostruktury po częściowej rekrystalizacji poprzez mechanizm SIBM (Strain Induced Boundary Migration). Zakłada się zatem, że fragment ziarna odkształconego przylegający do granicy wysokokątowej ulega rozrostowi, który generowany jest poprzez gradient energii zgromadzonej.

Przeprowadzone symulacje komputerowe są w zgodzie z wysuniętą hipotezę. Otrzymane wyniki są bardzo zbliżone do eksperymentalnych danych EBSD zarówno pod względem tekstury, jak i mikrostruktury.

Kolejnym interesującym rezultatem związanym z cyrkonem jest ewolucja tekstury, która występuje zanim rekrystalizacja jest zakończona. Jest to przede wszystkim widoczne w próbce ściskanej w kierunku ND. Co więcej, należy zauważyć, że taka geometria w dobrym przybliżeniu odpowiada walcowaniu. Zatem ponownie analizowane jest wspomniane przejście pomiędzy składowymi tekstury $\{hkil\}<10\bar{1}0>$ i $\{hkil\}<11\bar{2}0>$, które zazwyczaj obserwowane jest dopiero po odpowiednio długim rozroście ziaren – fakt ten wykazano także dla rozpatrywanego wyżej tytanu. Natomiast w badanym cyrkonie jest ono możliwe już w fazie częściowej rekrystalizacji. Wynik ten zestawiono z dodatkową analizą tekstur obszarów przygranicznych, co także dało przesłanki ku przedstawionemu modelowi SIBM.

Podsumowując, w oparciu o przedstawione wyniki i dyskutowane wnioski można zauważyć, że zaproponowane modele fizyczne i hipotezy dotyczące rekrystalizacji i rozrostu ziaren w badanych metalach heksagonalnych zostały pozytywnie zweryfikowane.

W tym kontekście, należy pokreślić fakt, że znaczna część rezultatów otrzymanych w tej pracy została opublikowana w czasopismach naukowych, a także przedstawiona na międzynarodowych konferencjach naukowych.

Résumé

La compréhension et la modélisation des mécanismes de recristallisation et de croissance des grains occupent une place importante dans la science des matériaux. Mais, ils sont aussi essentiels pour de nombreux processus industriels de transformation des matériaux qui s'appuient sur des traitements thermomécaniques qui doivent être optimisés. En effet, au cours de ces traitements, qui comprennent généralement des phases de déformation et de recuit, la microstructure et la texture des matériaux polycristallins évoluent considérablement, induisant une modification des propriétés physiques et mécaniques du produit final.

L'objectif principal de cette thèse est d'étudier les mécanismes de recristallisation et de croissance des grains dans les métaux de structure cristallographique hexagonale. Nous avions étudié dans ce travail le titane et le zirconium qui, en raison d'une combinaison unique de propriétés mécaniques et physiques suscitent un intérêt croissant tant d'un point de vue scientifique que technique. En outre, une compréhension fine des phénomènes que l'on rencontre dans ces métaux lors de recuits, constitue un problème relativement nouveau, traité dans peu de publications à ce jour.

Dans la thèse présentée, deux approches de recherche étroitement liées, à savoir l'observation expérimentale et la simulation numérique, ont été menées de front.

La partie expérimentale comprend la préparation d'un ensemble d'échantillons de titane et de zirconium déformés à des degrés divers (par laminage à froid principalement) puis soumis à différents recuits, dont les microstructures ont ensuite été caractérisées à l'aide des techniques de diffraction des électrons rétrodiffusés (EBSD) et des rayons X (DRX). Afin d'extraire le plus de données quantitatives possible de ces mesures, nous avons proposé une méthode d'analyse originale, permettant de caractériser de façon précise les zones proches des joints de grains. Cette méthode a permis une analyse plus approfondie des évolutions microstructurales rencontrées.

La partie numérique comprend le développement d'un logiciel de simulation des mécanismes de recristallisation et de croissance des grains. Ce logiciel est basé sur le modèle de Potts implémenté selon l'approche de Monte Carlo. Des outils de visualisation de données ainsi que de configuration des paramètres du modèle ont également été développés.

L'analyse des données expérimentales a démontré que la déformation plastique du titane imposée par le laminage à froid conduisait à une microstructure hétérogène. L'influence du maclage qui apparaît au début du processus de déformation (aux alentours de 20%) a tout d'abord été mise en évidence : la plupart des grains sont

fragmentés à plusieurs reprises par la formation successive de plusieurs joints de macles. Par ailleurs, les grains orientés défavorablement vis-à-vis du maclage se fragmentent également mais de façon continue : leur forme évolue peu mais une microstructure de dislocations apparaît que l'on peut caractériser grâce aux mesures de désorientations locales. Entre 40% et 60% de déformation, les hétérogénéités intra et inter granulaires augmentent, et l'on distingue de mieux en mieux deux populations de grains : ceux fragmentés ou divisés en plusieurs « sous-grains » par maclage et ceux fragmentés par déformation par glissement, qui forment de larges zones présentant des gradients continus d'orientations.

Ces différences observées à différents degrés de déformation influencent significativement les phénomènes de recristallisation et de croissance des grains. Les zones très fragmentées constituent en effet un environnement privilégié pour la germination et la croissance de nouveaux grains recristallisés.

En conséquence, l'évolution la plus marquée de la microstructure lors d'un recuit survient dans les échantillons laminés au préalable à 60%. Dans ce cas, les grains sont les plus petits après recristallisation, ce qui leur donne de plus la possibilité de croitre ultérieurement au cours d'un second traitement thermique. En plus, il a été montré que cette croissance était liée à la différence entre la distribution globale et locale de désorientation.

Aux fins de comparaison, le même traitement thermique que celui imposé à l'échantillon déformé de 60% pour assurer la recristallisation primaire complète a été imposé à l'échantillon laminé à 20%. On observe un nombre de germes bien inférieur et par conséquent, une taille de grain nettement plus grande après recristallisation puis une phase de croissance limitée.

Les mécanismes de la croissance des grains présentés sont corrélés aux changements de texture. L'analyse des états partiellement et entièrement recristallisés indique une évolution limitée de la texture dans tous les échantillons considérés. Ce n'est que la croissance avancée des grains discutée pour l'échantillon préalablement déformé de 60% qui conduit à une rotation graduelle et visible de la composante principale de la texture de 30° autour de l'axe **c**. Ce passage est noté dans la littérature comme un changement de la composante $\{hkil\}<10\bar{1}0>$ pour la composante $\{hkil\}<11\bar{2}0>$.

Les conclusions tirées sur la base de ces résultats expérimentaux ont été formulées sous forme d'un modèle physique qui a été ensuite appliqué dans des simulations de recristallisation et de croissance de grains. La mise en œuvre numérique réalisée pour le titane mène à des résultats satisfaisants et conformes à l'expérience.

Dans le cas du zirconium, l'objectif de l'étude était d'analyser les étapes initiales de la déformation (17%) imposée en compression plane dans deux directions différentes (ND et TD) et l'influence de celle-là sur l'état partiellement recristallisé.

Dans ces deux cas considérés, il a été noté que la déformation progressive dans des grains d'orientations proches entraînait la formation de grosses zones largement désorientées, comprenant de nombreux joints à faible désorientation et des fragments de joints à forte désorientation. Le même phénomène avait été observé dans du titane déformé en traction.

Il a également été montré que les échantillons compressés dans la direction TD se déformaient plus facilement que ceux comprimés dans la direction ND, probablement en raison d'une légère activité de maclage plus élevée au tout début de la déformation plastique. Cette différence se manifeste sur l'allure des courbes de compression, mais surtout, elle entraine la formation d'un nombre plus grand de joints à forte désorientation dans les échantillons comprimés dans la direction TD.

Compte tenu de la répartition particulière des joints de grains et des faibles taux de déformation, ces microstructures apparaissent comme très favorables à l'activation du mécanisme de migration de joints induite par la déformation (SIBM – Strain Induced Boundary Migration) ; de fait, c'est le mécanisme principalement observé lors de la recristallisation du zirconium après déformation modérée.

Les simulations effectuées sont en accord avec l'activation de ce mécanisme. Là encore, les résultats obtenus s'approchent beaucoup des données expérimentales, à la fois pour la texture et la microstructure.

Nous avons également observé une évolution particulière de la texture, en toute fin de recuit, et tout particulièrement dans l'échantillon comprimé le long de la direction ND dans lequel le transfert mentionné ci-dessus entre les composantes $\{hkil\}<10\bar{1}0>$ et $\{hkil\}<11\bar{2}0>$ se produit sans croissance des grains (dans la littérature, la croissance de grains est souvent évoquée pour interpréter cette évolution de texture). Dans le cas présent, et grâce à l'analyse supplémentaire de texture des zones proches des différents joints de grains (intra et intergranulaires), nous avons pu montrer que cette évolution de texture était le résultat du mécanisme de SIBM.

Pour conclure, on peut souligner, sur la base des résultats présentés et des conclusions discutées, que les modèles physiques proposés et les hypothèses émises relatives à la recristallisation et à la croissance des grains dans les métaux hexagonaux étudiés se sont avérés conformes à la réalité expérimentale. Une part importante des résultats obtenus dans cette étude a déjà été publiée dans des revues scientifiques et présentée dans des conférences scientifiques internationales.

Contents

CHAPTER 1

Introduction

Recrystallization of plastically deformed polycrystalline material and subsequent grain growth process are recognized as physical phenomena that cover a vast scientific space in the field of materials science. Moreover, both are very alive and still evolving subjects containing puzzling problems as well as complex aspects to be understood better. In consequence, much curiosity as well as increased interest of researchers is directed towards this domain.

Simultaneously, recrystallization and grain growth, as a processes driven by combination of deformation and high-temperature annealing, are of the key importance from the viewpoint of industrial processing route which, in general, is based on such thermo-mechanical treatment. Consequently, it is often emphasized that both of them play tremendous role in the development of specially tailored behavior of metallurgical products which is required for cutting edge applications of modern technique and daily-life necessities as well.

Therefore, much attention has been paid to the way how evolution of texture and microstructure, induced by appropriate heat-treatment, can by employed in order to predict, improve and control the macroscopic properties of the polycrystalline materials. These properties are, in particular: mechanical strength, electrical conductivity, corrosion resistance, ductility, hardness and fatigue resistance. In this regard, aluminium beverage can and ferritic steel used in electricity transformers are usually mentioned as the most famous examples of such successful enhancements.

Hence, the industrially motivated need to design the desired properties has been found as important driving force for metallurgical investigations associated with

recrystallization and grain growth. Advances in knowledge about the underlying mechanisms governing these phenomena during different metal working processes and their impact on material texture and microstructure are thus regarded as essential to achieve goals set by modern engineering and technique.

As a consequence of the presented views, recrystallization and grain growth have been subjected to extensive research over the last decades. Those scientific efforts have contributed towards better understanding and more comprehensive coverage of these phenomena in the literature.

An important issue that deserves special attention, in respect to this topic, is the way how term 'recrystallization' is understood since more detailed expressions, such as primary and secondary recrystallization, can be found. The primary recrystallization is a process of transformation of deformed matrix into almost strain-free microstructure. It is usually explained in terms of formation and migration of high angle grain boundaries driven by stored energy of deformation. In contrary, secondary recrystallization is regarded as the further grain growth process of already recrystallized grains which is driven by boundary curvature. In accordance with the most popular convention, the term 'recrystallization' used in this thesis is related only to primary recrystallization.

Nevertheless, there are still important and pending issues which need to be undertaken in order to refine satisfactory theory of recrystallization and grain growth. In this context, it has to be emphasized that in the past the conducted research was concentrated around cubic metals and its alloys, whereas today a much wider range of investigation directions is covered.

One of them focuses on hexagonal metals, especially magnesium, titanium and zirconium, which due to exceptional properties have gained much scientific attention. Also, the detailed studies and final conclusions about the nature of the physical mechanisms occurring during annealing treatment of these metals are still far from being achieved, as it has been less investigated problem so far.

Therefore, the main purpose of this thesis is to contribute in the mentioned subject, and thus to characterize and analyze recrystallization and grain growth phenomena taking place in hexagonal titanium and zirconium. Two alternative investigation approaches are used for that reason, namely experiment and computer modeling. In this place, it should be emphasized that most of the experimental work was carried out in LSPM laboratory in Paris–Villetaneuse thanks to a long time collaboration between AGH–UST and LSPM, which also gave an opportunity for co-supervised character of this thesis.

A substantial development observed during the last years in experimental techniques as well as modeling methods should be mentioned since it has resulted in amazing insights into the problem considered in this thesis. A clear example that demonstrate this progress in available analysis tools concerns the explanation of mystery of damask steel production in which the important role of appropriate heat-treatment has been revealed.

New perspectives are thus provided now for micro-scale observation of processes induced by the combination of deformation, recrystallization and related annealing phenomena. This is especially important in the case of the mentioned hexagonal metals which were difficult to examine experimentally couple years ago, mainly due to technological limitations.

Regarding the results obtained in this thesis, in the experimental part, titanium and zirconium samples have been thermo-mechanically treated and prepared for measurements. Electron Backscatter Diffraction (EBSD) is chosen on the first place among all available experimental techniques to be used, as it allows to measure crystallographic orientations from predefined discrete coordinates through an automated orientation mapping procedure. Consequently, it gives an access into material characterization, which is necessary in terms of recrystallization investigation. This is the reason why it is so hard to imagine that kind of study to be performed without such a technique. Hence, different EBSD based analyzes are employed in order to describe and understood microstructure and texture evolution observed in the considered titanium and zirconium samples.

In the modeling part, a wide range of various methods can be considered. Nevertheless, Monte Carlo Potts model is selected as the most appropriate in the case of this thesis. Therefore, it is developed, implemented and then applied to simulate and validate hypotheses concerning several examples of recrystallization and grain growth.

In conclusion, the sequence of the next chapters included in this thesis is as follows: Chapter 2 is intended as a brief theoretical background about recrystallization and related annealing phenomena. However, it is emphasized that only the most important and relevant aspects are presented since recrystallization itself is a very broad topic in materials science. In addition, fundamentals of this subject have been comprehensively covered in the literature.

Chapter 3 deals with crystallographic structure, thermo-mechanical properties and industrial significance of hexagonal metals. Although, the main objective of

this section is to overview the mechanisms of deformation and recrystallization which have been already reported for titanium and zirconium.

Chapter 4 provides a description of experimental methods which are available for description of material microstructure and texture. EBSD technique is of key importance in this case. Hence, it is analyzed in terms of fundamental concepts, obtained benefits, practical issues and applications.

Chapter 5, in turn, gives a general report on simulation approach with a strong emphasis on the Monte Carlo Potts model which is described and analyzed in more details. In this context, various issues are discussed including a short view on the origin of the model, its features, main advantages and disadvantages, further improvements and modifications as well as brief summary of possible applications.

Chapter 6 is inclined toward more practical side of topics discussed in the Chapter 5. Therefore, a major accent is placed on implementation aspects. In particular, structure of simulation framework developed in this thesis is explained. Also, testing procedures are presented in order to confirm validity of the obtained Monte Carlo model.

Chapter 7 introduces a new analysis approach that can be used to characterize grain boundary area on the basis of topological information provided by orientation mapping. Therefore, it might be considered as additional content that is slightly off from the main topic of this thesis. Nevertheless, the proposed method can provide interesting insight into evolution of grain boundary structure which is important from the viewpoint of the performed investigation as confirmed on attached examples and presented results.

Chapters 8 and 9 constitute the crucial part of the thesis. The first one is devoted to investigation of primary recrystallization and grain growth in cold-rolled titanium, whereas the second deals with the characterization of primary recrystallization in the case of compressed zirconium. In both cases the presented results are obtained from experimental measurements and modeling.

Chapter 10 contains general conclusions and final comments on the results obtained in this thesis as well as formulation of further perspectives.

CHAPTER 2

Theoretical background on some of the fundamentals of recrystallization and grain growth phenomena

THERMO-MECHANICAL treatment of plastically deformed polycrystalline materials is a common method which is applied in order to produce final metallurgical product of a desired shape change. From industrial point of view, it is relatively simple process to characterize. First, dimensions of the material are significantly changed as a result of the applied plastic deformation. Then, annealing in high temperature is performed. However, the shape remains almost unchanged in this case thus, at first glance, "nothing happens", colloquially speaking, from the perspective of an external observer.

Nevertheless, a far more complex behavior is discovered when a closer look is taken on the thermo-mechanically processed material, especially at micro and nano-scale where plenty of various physical phenomena, coupled with each other, take place. These are described in the following paragraphs on the basis of available literature, namely [1–4].

2.1 Deformation

From microscopic point of view, microstructure has to be dramatically changed in order to accommodate externally imposed strain. In this context, grains can evolve

in various ways. For instance, some of them become wide areas of crystallographic orientation spread, whereas others can be highly fragmented in terms of shape. Obtained microstructure is thus significantly modified in terms of grain size and grain shape, including additional grain boundaries to be created. There are two alternative mechanisms which are responsible for the abovementioned evolution of crystal lattices, namely slip and twinning.

In the first case atoms are irreversibly moved in such a way that particular crystal planes slide past each other, which is possible due to creation and propagation of crystal lattice defects. Mostly, dislocations are involved during this process. However, such a situation can take place only if several conditions are fulfilled, particularly an appropriate state of stress has to be applied.

The crystallographic slip is activated on the most densely packed crystallographic planes and toward crystallographic direction in which atoms are most closely spaced. Hence, this deformation mode is described using slip systems $(hkl)[uvw]$ – a combination of slip direction $[uvw]$ and slip plane (hkl). Slip systems are further extended into slip system families $\{hkl\}<uvw>$ according to particular crystal symmetry which provides additional equivalent directions and planes.

In contrary, the twinning deformation mode relies on co-operative shear movement of atoms. In this case, twin structure is created as a mirror reflection of parent crystal lattice. Special crystallographic plane is necessary for the reflection thus twin systems $\{hkl\}<uvw>$ are also described using crystallographic plane and crystallographic direction.

Deformation twins are very distinctive in terms of their shape, which makes them easy to find in the microstructure. They are formed as lenticular or long and narrow grains. In addition, they usually tend to cross the whole parent grain.

Besides topological changes, activation of deformation modes leads to an important evolution of texture. Orientation of the deformed grains is not changed randomly thus strong deformation texture can be formed. The reason of such behavior lies in the fact that either slip or twinning are activated on particular systems, that means preferred orientations. As a result, deformed texture often consists of several main components that are responsible for anisotropy of mechanical properties. In this regard, problems with formability may occur, which is unfavorable from industrial point of view. Therefore, it is necessary in some cases to make the deformation texture balanced or randomized.

Another effect connected with plastic deformation is the increase of dislocation density by several orders of magnitude. Regular distance between atoms is highly

perturbed by these defects, which means that additional energy is accumulated in the material as so-called stored energy of deformation. However, it should be noted that during deformation most of the applied external work is dissipated in the form of heat, and only a small part of the used energy is transferred into the stored energy. Nevertheless, this small part, just a few of $\frac{\mathrm{J}}{\mathrm{g \cdot mol}}$ [2], can play crucial role when further heat treatment is performed.

2.2 Recovery and static recrystallization

Heat treatment of plastically deformed microstructure can lead to various phenomena; among them there are: recovery, static recrystallization, normal grain growth and abnormal grain growth. In addition, they may be governed by various mechanisms depending on applied annealing conditions and properties of the heat-treated material.

Recovery is a process in which dislocation cell walls or even sub-grains can be formed within the deformed grains due to annihilation and rearrangement of dislocations. As a result, part of the stored energy is released. Also, mechanical properties can be slightly modified. Therefore, recovery is often analyzed in experiments based on calorimetric or hardness measurements.

Nevertheless, it has to be kept in mind that changes introduced by recovery are very local and subtle, whereas overall microstructure still consists of deformed grains. In other words, most of high angle grain boundaries, which are understood as those with misorientation greater than $10^\circ - 15^\circ$, remain unchanged.

In contrary to recovery, static (primary) recrystallization requires much higher temperature to be activated, but if it happens, then whole deformed microstructure is completely replaced with a new microstructure consisting of new strain free grains. Such a transformation, according to the definition, is expressed in terms of formation and migration of high angle grain boundaries driven, at the first place, by the stored energy of deformation [3]. Hence, high angle grain boundary is considered as a 'recrystallization front' that is a sharp interface separating deformed and new emerging grains. At the end of the transformation, the stored energy is almost completely released, which implies that substantial fraction of dislocations is annihilated.

In more details, recrystallization consists of two central stages: nucleation (in which new strain free grains are formed) and further growth of the created grains (which is continued until none of the deformed grains remains in the microstructure).

The latter process is considered first in the following paragraph, then important role of nucleation is discussed.

Migration rate of high angle grain boundaries during growth stage is governed by the following general rule [1]:

$$V = M \cdot P, \tag{2.1}$$

where M is mobility, i.e., the ability of boundary to be moved under a driving pressure P. In this case, P is proportional to the stored energy of deformation.

Based on the above Equation 2.1, it is clear that even if driving pressure is high enough, the final velocity of migration (growth rate) V can be significantly reduced in the case of less mobile boundaries.

According to "Cahn-Cottrell" mechanism [2], under the same driving pressure, high angle grain boundaries can rapidly migrate due to high mobility, whereas low angle grain boundaries are much more difficult to move. Hence, mobility is often approximated by a special type of function of misorientation angle (ω), as exposed by Humphreys (1997) [5], the following relation has been derived:

$$M(\omega) = M_m \left[1 - e^{-B\left(\frac{\omega}{\theta_m}\right)^n} \right], \tag{2.2}$$

where M_m and θ_m are mobility and minimal misorientation of high angle grain boundary, respectively, while B, n are constants. From that point of view, it is also clear why recrystallization is explained in terms of rapid movement of only high angle grain boundaries.

The significant role of misorientation in controlling grain boundary mobility has been confirmed without doubt by many investigations (see chapter 5 in [4] for more details). However, it has to be kept in mind that the presented Equation 2.2 is still an approximation of the real scenario since there are factors like solutes or temperature which can strongly affect the final mobility. Moreover, it should be recalled that real grain boundary is defined as three-dimensional interface between regions of different crystallographic orientation. Therefore, the geometry of such is mathematically described by at least five independent parameters, which include the abovementioned crystallographic misorientation angle between the separated crystal lattices and the spatial orientation of the boundary plane. The impact of misorientation has been already shown, whereas boundary plane is often neglected due to the problems with experimental measurements. Nevertheless, its inclination

may significantly affect the mobility, which is expressed in the following Herring relation [6, 7]:

$$v = M(\gamma + \gamma")P = M^*P, \tag{2.3}$$

where $M^* = M(\gamma + \gamma")$ is a reduced mobility, $(\gamma + \gamma")$ is an interface stiffness and $\gamma"$ is second derivative of boundary free energy with respect to interface inclination.

Regarding the first process, crucial to initiate the whole recrystallization phenomenon, - that is nucleation - it is noted that few mechanisms may be employed in order to provide population of growing sub-grains.

In the most common view, nucleation appears as a rapid activation of small nuclei to form new grains. Unfortunately, it is difficult to analyze this stage with desired level of details due to the scale and kinetics of this process. Moreover, nucleus itself is not precisely defined. In compliance with the developed convention, recrystallization nucleus is considered as small volume, which in practice means less than few µm of almost dislocation free crystal lattice. In addition, the volume should be separated from deformed microstructure by high angle grain boundary. It is a real problem to perceive them experimentally and analyze quantitatively at such a scale, especially in 3D. Therefore, what is mostly observed is the stage when small recrystallization grains appear as a result of nuclei growth.

Nevertheless, there is one important conclusion about the nature of nucleation process. It is widely acknowledged, after first suggestion of Robert Cahn [8, 9], that potential nuclei sites already pre-exist in the deformed microstructure in the form of recovered sub-grains or cells before recrystallization is actually started, instead of being a completely new crystals with a new orientation created due to thermal fluctuations of annealing. As a consequence of such mechanism, a new recrystallization grain is expected to inherit its orientation from local region of deformed structure from which it grew.

It also implies that number of possible nuclei sites is strongly connected with the accommodated strain. Higher strain leads to higher density of deformation structures which, in turn, can provide more nuclei. This usually results in decreased grain size after recrystallization since many small grains are formed instead of less numerous but much larger grains.

Another well known observation is that only a small part, less than few percents [2], of all possible nucleation sites (sub-grains) is capable to grow and increase their volume over annealing. The main obstacle comes from the fact that difference

of stored energy between an interior of a nucleus and surrounding matrix, which enhances the growth, is too low to compete with tendency to minimize much higher interfacial energy of the nucleus boundary, which - in contrary - enhances shrinkage.

There are two main conditions which, if fulfilled, imply high possibility of successful transition from a nucleus to a growing grain. The first one is the already mentioned high misorientation (usually more than 15°) of interface between nucleus and surrounding deformed matrix. The second one is an appropriate size of the nuclei, or in other words sufficiently large radius of curvature; large nuclei have higher opportunity to survive and grow, while too small are predestined to disappear. Both conditions have reasonable justification. Higher misorientation gives rapid migration of a nucleus boundary, as already explained above (Equation 2.2). Therefore, appropriately misoriented deformation zones, such as high angle grain boundaries, intersections of twins, transition bands, shear bands and zones around large particles, are usually considered as preferred places, where successful sub-grain growth is observed. Larger initial radius, in turn, gives energy advantage for growing, in analogy to formation of gas bubbles in the water.

Apart of the abovementioned general nucleation mechanism, there is another important process of sub-grain formation which can be regarded in some sense as nucleation phenomena. This is strain-induced boundary migration (SIBM) described by Beck and Sperry (1950) [10]. SIBM concerns a situation when the grain boundary separates grains which are highly different in terms of dislocation density; one has low stored energy, whereas the second has high stored energy. This significant difference in accumulated strain can lead such a boundary to bow out toward the grain of higher energy. As a result, a strain-free sub-grain is formed nearby bulged boundary part. Obviously, the orientation of new emerging grain is almost identical to the place of origin, which is the grain of lower dislocation content.

It should be emphasized that SIBM is often observed at lower accommodated strains, for instance 20% in the case of reduction in rolled aluminum [4].

In accordance to the both described processes: nucleation and growth, a recovery influence should be discussed, since recovery and primary recrystallization are strongly connected. Both are generally regarded as competing processes. Extensive recovery can be observed if recrystallization is inhibited in some way, but also recrystallization can be retarded by recovery, as the latter is responsible for the decrease of the stored energy – the main driving force for recrystallization. However, there is also the other side since recovery of dislocation structure can provide strain free cells or sub-grains which are necessary for nucleation of recrystallization grains.

2.3 The phenomenological rules of primary recrystallization

Recrystallization, with all the affecting factors that have to be considered, seems to be too complex phenomenon to be described by strict laws delivered from the fundamental principles of physics. Despite that, some phenomenological rules have been noticed and confirmed by many studies. The most important ones are listed below.

1. Since recrystallization is thermally activated process, it is expected that recrystallization rate will follow Arrhenius type formula:

$$\frac{1}{\tau_R} = A \cdot e^{\left(\frac{Q_R}{R_G T}\right)}, \tag{2.4}$$

   where τ_R is a time constant that characterize recrystallization rate, Q_R is an activation energy, T is an annealing temperature (in Kelvin), A is a pre-exponential factor and R_G is an universal gas constant.

2. Based on the above equation, it is noted that stored energy of deformation has to be high enough to start recrystallization. It is a condition of minimal level of introduced deformation. In this context, increasing deformation provides better nucleation and higher driving force. In such a case, recrystallization can occur at lower temperature.

3. Similarly, a sufficiently high temperature is demanded to finish recrystallization at a finite time. Lower temperature results in longer annealing time that is needed to complete the recrystallization process.

4. The recrystallized grain size can be controlled by the amount of prior deformation. Higher deformation produces higher density of potential nuclei sites which, in turn, leads to smaller grain size after recrystallization.

5. Among factors that affect recrystallization rate, there are: the mode of deformation, strain path changes, boundary character, solutes, strain rate, deformation temperature and heating rate.

2.4 Grain growth of recrystallized microstructure

Further annealing of recrystallized grains leads to pure grain growth process, sometimes referred as 'secondary recrystallization'. Despite the fact that stored energy of deformation is already released, grains can still increase their volume in order to reduce area occupied by grain boundary and thus to decrease Gibbs free energy. In this case, the boundary curvature κ and the boundary energy γ are regarded as the main driving forces under which elements of grain boundaries are moved with velocity V toward their local center of curvature, what is expressed in the following equation [1]:

$$V = M\gamma\kappa. \tag{2.5}$$

In spite of this tendency, grain with convex boundary shrinks, whereas migration of concave boundaries increases volume of the grain. Both situations are schematically presented in the Figure 2.1. As a consequence of grain growth, bigger grains become larger at an expense of disappearance of the smallest one.

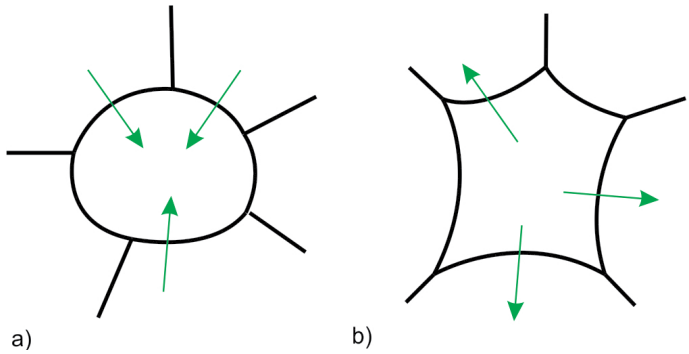

Figure 2.1: Shrinkage of the grain with convex boundary (a) and growth of the grain with concave boundaries (b).

Evolution of grain boundary structure during grain growth is a geometrically complex process. For instance, special configurations of grain boundary segments can be formed such as triple junctions (where boundaries join each other at 120°) or quadruple points. Those are much more difficult to move, especially when equilibrium state is formed due to the same energies of connected boundary segments.

However, some general remarks about statistical behavior of growing grains have been noted. It is frequently assumed that in nature of not impeded normal growth is to increase average grain radius as a power law of time. Moreover, grain growth is of-

ten characterized as quasi-stationary process that exhibits statistical self-similarity. It means, for instance, that the normalized grain size distribution remains unchanged over time.

Finally, it should be mentioned that apart from normal grain growth, there is also a possibility of 'abnormal grain growth', when only particular grains become extremely larger than the rest, but it is out of the scope of this chapter.

2.5 Physical models of recrystallization and grain growth

In the light of the presented theoretical background, it is clear that recrystallization is strongly connected with deformation state, especially in terms of distribution of the stored energy. Therefore, it is necessary to understand how deformed microstructure is formed in order to investigate such phenomenon as recrystallization.

On the other hand, even if deformed microstructure is well characterized, it is still a challenging problem to analyze and fully comprehend mechanisms of recrystallization, especially on the basis of theoretical approach. The main difficulty that makes it so complex to study is a wide range of various interactions between emerging and growing grains as well as inhomogeneity of driving pressure. In spite of this, only simple analytical models have been proposed so far. Moreover, they usually deal with only one aspect of recrystallization, and grain growth as well, which is the kinetics of the process. The best known examples of such models are briefly presented in the following paragraphs.

JMAK model

The main idea behind an analytical description of the kinetics of recrystallization is to consider this process as a phase transformation performed at constant temperature, where strain free grains constitute a new phase which grows into an old phase represented by the deformed microstructure. Then, the kinetics of recrystallization can be analyzed in terms of evolution of recrystallized volume fraction X_v over time. Such an approach allows to make use of Johnson-Mehl-Avrami-Kolmogorov model [11,12] which has been originally developed in order to study kinetics of phase transformations. It is also assumed in this model that nucleation sites are randomly distributed in the microstructure and the growth process of nuclei is isotropic. In ad-

dition, growth rate must be constant. If it is so, then recrystallized volume fraction X_v obtained after time t can be expressed by the JMAK equation:

$$X_v(t) = 1 - e^{(Kt^n)}, \tag{2.6}$$

where K and n are constants. Example kinetics obtained based on that relation is presented in the figure below.

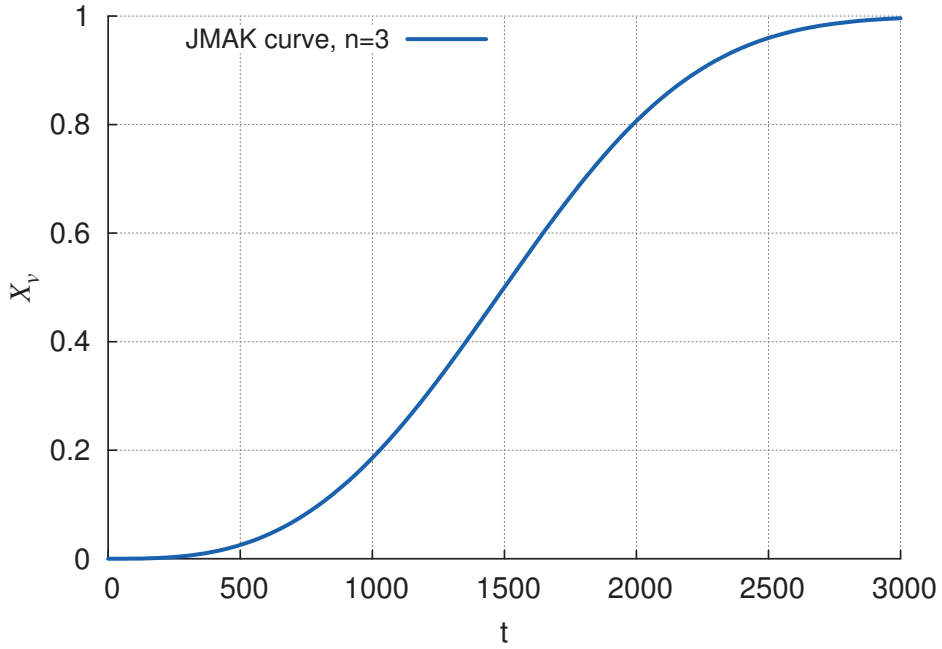

Figure 2.2: Sigmoidal kinetics of primary recrystallization derived from JMAK equation.

It can be seen that overall recrystallization kinetics is divided into three stages: incubation time before actual recrystallization is started and increasing rate of recrystallization due to appearance of first grain, then a linear region, and finally, a saturation region when rate of recrystallization is decreasing because almost all of the deformed grains are already consumed by recrystallization grains.

Regarding JMAK constants, K and n, both do not have clear physical interpretation. However, they are often analyzed using a rewritten form of the JMAK equation:

$$ln\left(-ln\left(1 - X_v\left(t\right)\right)\right) = ln\left(K\right) + nln\left(t\right). \tag{2.7}$$

This shows that value of n can be determined as a gradient of straight line given by

the above relation. Consequently, based on that value, conclusions can be withdrawn on the type of nucleation (whether nuclei are already in the deformed microstructure – site saturated nucleation or are created during recrystallization – constant rate nucleation) and the dimensionality of the space. For instance, recrystallization with site saturated nucleation leads to n equal to 3 in 3D, whereas n is equal to 2 in 2D. More details about n value can be found in [4].

It should be noted that the presented approach is a very simple approximation of real recrystallization process since only one parameter is used in JMAK analysis as well as many effects, recovery for instance, are not incorporated. Also, in most cases nucleation occurs in a non-random manner as well as growth rate is not constant due to microstructure inhomogeneity. This implies very limited application of the JMAK model. Therefore, it is rarely observed that experimental data are in agreement with this theory. Nevertheless, JMAK plots are frequently used as a reference, especially in computer simulations.

It should be also mentioned that JMAK model has been extended by Vandermeer and Rath (1989) [13]. In the proposed approach, called Microstructural Path Methodology, additional parameters are incorporated in the model in order to characterize better the recrystallized volume fraction. As a result, it is possible to analyze more precisely nucleation and growth rates using experimental measurements. Despite that, as in the case of JMAK model, the constraints of randomly distributed nuclei sites as well as globally determined grain growth rate constitute a deviation from reality where lower values of the Avrami exponent is usually found.

Models of normal grain growth kinetics

Two alternative approaches in modeling of normal isotropic grain growth kinetics have been proposed, almost at the same time, in 1952 [14, 15].

First approach has been presented in the work of Burke and Turnbull (1952) [14]. They considered a particular grain of radius R separated by spherical boundary, and assumed that the curvature κ of this boundary, the only driving pressure, is inversely proportional to R, as denoted below:

$$\frac{1}{K} \propto R \tag{2.8}$$

Velocity V can be thus defined as $\frac{dR}{dt}$. Hence, Equation 2.5 can be rewritten in the following way:

$$\frac{dR}{dt} = \frac{C \cdot M \cdot \gamma}{R}. \tag{2.9}$$

This brings us to the second assumption of structure self-similarity which means that evolution of average grain radius $\langle R \rangle$ of the microstructure should be the same as in the case of arbitrary grain. In consequence, substitution of R with $\langle R \rangle$ is allowed. After integration over time, the following equation is obtained:

$$\langle R \rangle^2 - \langle R_0 \rangle^2 = D \cdot t, \tag{2.10}$$

where $\langle R_0 \rangle$ is initial average grain radius, $\langle R \rangle$ is average grain radius at given time and D is integration constant.

Based on that, it is clear that if $\langle R \rangle$ is much higher than the initial$\langle R_0 \rangle$, then parabolic grain growth law is obtained:

$$\langle R \rangle^2 = D \cdot t, \tag{2.11}$$

which is usually rewritten in more general form:

$$\langle R \rangle = D \cdot t^{\frac{1}{n}}. \tag{2.12}$$

The constant $\frac{1}{n}$ in the above equation is termed as the grain growth exponent. In the idealized case of isotropic normal grain growth it is equal to 0.5.

According to the second model, introduced by von Neumann (1952) and extended by Mullins (1956) [15, 16], the growth rate $\frac{dA}{dt}$ of a given 2D grain can be expressed based on topological considerations, as follows:

$$\frac{dA}{dt} = \frac{1}{3}\pi m \gamma \left(n - 6\right), \tag{2.13}$$

where A is an area size occupied by grain and n is a number of sides of a grain, or in other words, number of neighboring grains. M and γ are mobility and energy of grain boundary, respectively, as previously depicted.

Consequently, 6 sides is the critical number for 2D grain growth; $n < 6$ results in shrinking of the grain, while $n > 6$ results in the growth.

Based on that, the von Neumann-Mullins relation indicates that growth of a 2D grain is independent of its size or detailed shape.

This model has been generalized further, mainly by Gottstein and Shvindlerman, to incorporate more effects such as limited triple junction mobility [17–20].

To sum up, the described theories provide interesting hypotheses which can be compared with experiments or investigated by simulation approach.

However, a special care should be preserved since assumptions adopted in the both presented models are often far from the reality.

2.6 Influence of recrystallization and grain growth on texture evolution

Similarly to deformation, recrystallization and related annealing phenomena can have a significant impact on final physical and mechanical properties of the material. This is basically due to formation of recrystallization texture during heat-treatment.

There are several reasons why recrystallization texture can be developed. Non-random spatial distribution of nucleating sub-grains should be mentioned at the first place. Another possibility is related with differences in growth rate between orientations. Also, 'orientation pinning' [21] can appear when microstructure contains many grains of similar orientation after recrystallization which cannot grow during grain growth stage due to low misorientation interface between them thus other orientations start to develop.

Therefore, various scenarios of recrystallization induced texture should be considered such as weakening of deformation texture, strongly randomized texture or entirely new texture. A special case is a scenario when strong texture is developed.

A good example of such situation is a domination of one orientation – cube component – in the recrystallization texture of heavily rolled aluminum or other FCC metals. The mechanism behind origin of such texture evolution has been discussed over the years, also due to the industrial importance of this effect. For instance, cube texture component is needed in order to reduce plastic anisotropy in production of aluminum beverage can.

Two alternative models have been proposed: oriented nucleation and oriented growth. First assumes much higher frequency of sub-grains with particular orientations, whereas the second concerns much faster growth of particular orientations. Both mechanisms have been investigated experimentally. Also, simulation approach has been used to compare them [22]. However, the final conclusions about the described origin of strong cube texture are still argued.

CHAPTER 3

Hexagonal metals

A wide range of various materials has been thermo-mechanically tested in order to investigate the mechanisms of deformation, recrystallization and grain growth. The motivation behind these studies has arisen from a desire to develop improved properties of materials being used in industrial applications. At the same time, the scientific efforts carried out to meet the needs of growing industry have given an opportunity to discover, understand better and explore further the details of physical processes driven by an annealing treatment.

Cubic metals and alloys, such as steel, aluminum or copper, have been the main group of materials being subjected to thermo-mechanical investigations, performed over the years, also due to important role played by them in the industry. This fact can be confirmed on the basis of fundamental work of Hatherly and Humphreys (2004) [4], which covers the most important aspects of recrystallization and related annealing phenomena that have been collected until the 2004. Almost all the results presented, discussed and summarized by them concern cubic metals.

However, it has been shown quite recently by Randle (2009) [23] that the above-mentioned domination is less significant now than in the past. Among others, this is due to the fact that in the field of metallic materials, a new group of hexagonal metals is emerging from the shadow of the cubic metals. Moreover, based on the report provided by Randle, it is clear that there are three particular metals in this hexagonal group that have gained the most of the scientific attention. Therefore, it is represented, in the following order of popularity, by: magnesium, titanium and zirconium.

As it is noted at the beginning, the technological development is one of the main driving forces to explore new materials. Things are no different in the case of hexagonal metals, especially now, when they are slightly more accessible in terms of industrial fabrication as well as scientific research. In addition, industrial interest in these metals is greatly enhanced by the fact that progressing technological development encounters more and more sophisticated problems, which need extraordinary solutions. The application of hexagonal metals is considered as one of them.

This is one of the main reasons why application range of hexagonal metals has been greatly increased. Modern technologies more often take advantage of the exceptional properties provided by magnesium, titanium and zirconium. Today, mentioned metals are applied in various technological branches such as aerospace, aviation, nuclear industry or biomedicine.

Magnesium and its alloys are famous for relatively good strength and stiffness in relation to very low density. As a result, they are used as a replacement of heavier materials in production of lightweight structural parts for transportation (vehicles and aerospace applications [24]) as well as for electronic devices.

Titanium and its alloys are well known for very high resistance to fatigue, high ductility, high strength combined with relatively low weight and high temperature capability. Therefore, they can be mostly found in aircrafts [25] and aerospace shuttles (jet turbine engine, fan, landing gears, airframe in fighter aircraft) [24], but also in construction industry, architecture and other customer goods [26].

Perhaps the most important application of titanium is the one related to bioengineering and biomedical implants [25]. Till now, apart from titanium, there is no other metal that could face up so well to medical expectations of high biocompatibility and excellent corrosion resistance. Titanium stiffness is another significant factor from the viewpoint of the orthopedic implants. It is due to the fact that bone needs appropriate stress state for development and strengthening along the implant; otherwise it is highly susceptible to fracture. In the case of titanium, stiffness is good enough to ensure implant stability in the body, but at the same time it is not too high thus part of the stresses can be transferred to the bone [27].

Zirconium alloys, in turn, have low capture cross-section for thermal neutrons followed by good resistance to corrosion as well as good high-temperature strength. Such properties predestine them to be used in the nuclear reactor systems [28, 29] where, for instance, they are employed as structural material in construction of thin-walled cladding tubes for radioactive fuel, channel sheets for boiling water reactors, spacer grids for light water reactors as well as Calandria tubes for heavy water

reactors [30].

In connection with the application driven purpose to investigate hexagonal metals, it is necessary to find a way how those favorable properties of hexagonal metals can be controlled or even optimized further.

For instance, one of the active research topics that concerns hexagonal metals is linked with tendency to develop microstructure with ultra-fined grains, as they improve the material strength and other properties [31–35].

The key point of interest is thus to understand evolution of texture and microstructure during thermo-mechanical treatment.

Regarding that fact, it should be emphasized that the behavior observed during deformation and recrystallization of hexagonal metals is much different from the one observed in cubic metals.

Moreover, a satisfactory theory of the physical mechanisms taking place during annealing treatment of magnesium, titanium or zirconium is still far from being achieved, as it has been less investigated problem so far.

Therefore, despite the role played by industrial applications, the increased interest in hexagonal metals is, most of all, associated with a desire of scientists who take advantage of recent developments in experimental techniques, like EBSD (Electron Backscatter Diffraction), to explore and understand hexagonal metals better. This is also the most important motivation which accompanies this thesis.

3.1 Hexagonal structure

The three-dimensional hexagonal close-packed (HCP) structure can be described using two types of 2D atomic layers (in $x-y$ plane), A and B, which are specially arranged along z-axis. Both of them are hexagonal lattices, where each atom is equally spaced from all the six nearest neighbors. The distance between them is given by a. However, positions of atoms in layer B are appropriately shifted in reference to layer A. Hence, HCP structure can be built by sequential stacking of A and B layers one over the other, which is labeled as ABABAB(...) – Figure 3.1.

As a consequence of the AB ordering, the primitive cell contains two atoms, first one at coordinates $(0, 0, 0)$ belonging to A layer and second one at coordinates $\left(\frac{2}{3}, \frac{1}{3}, \frac{1}{2}\right)$ belonging to B layer.

Therefore, the primitive hexagonal unit cell can be defined using three basis vectors $(\mathbf{a_1}, \mathbf{a_2}, \mathbf{c})$. The first two lie in A layer and have the same length, given by a, while the third one, perpendicular to A layer, has a length c, which is defined by

cell height, namely the distance between two the nearest A layers.

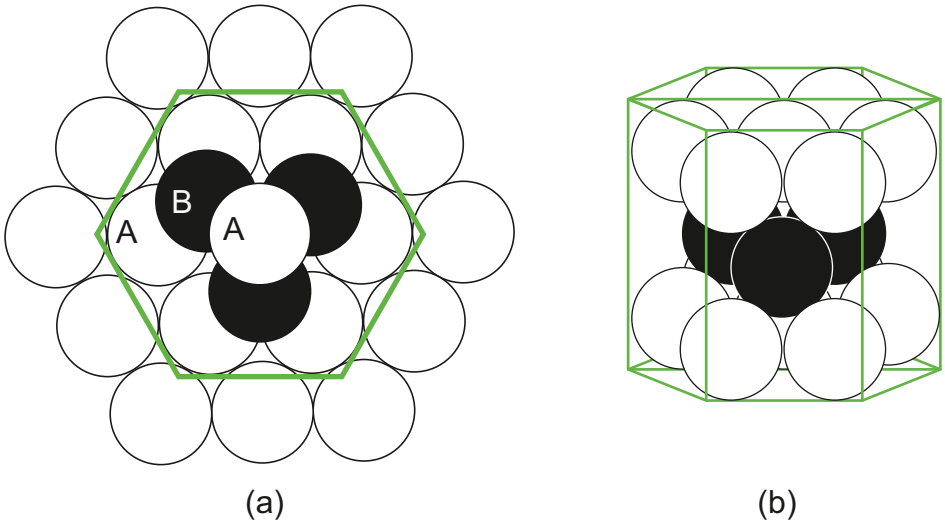

Figure 3.1: Stacking of A and B layers in HCP structure: top view (a) and side view (b).

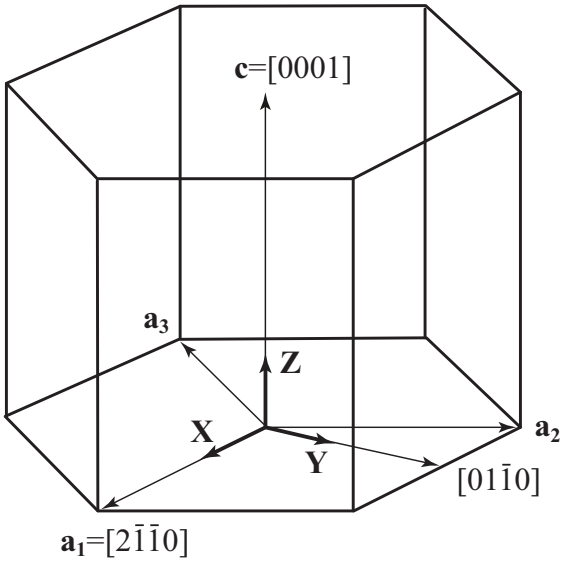

Figure 3.2: The HCP unit cell with an example of crystal reference system.

Since A layer is a hexagonal lattice, an angle between $\mathbf{a_1}$ and $\mathbf{a_2}$ is equal to 120° which implies the application of four Miller-Bravais indices in order to describe orientations in HCP structure without ambiguity connected with different available conventions used in the case of only three indices. In the conventional four-index Miller-Bravais system a crystal direction has the following form [36]:

$$[uvtw] = u\mathbf{a_1} + v\mathbf{a_2} + t\mathbf{a_3} + w\mathbf{c}, \tag{3.1}$$

where $t = -(u + v)$.

Also, an orthogonal basis is shown by the axes $(\mathbf{X}, \mathbf{Y}, \mathbf{Z})$ in the Figure 3.2. The chosen basis axes are parallel to the $[2\bar{1}\bar{1}0], [01\bar{1}0], [0001]$ directions, respectively, which is consistent with the convention of the particular texture software (TSL^{TM}OIM Analysis 5.3) used in this work.

The most important crystallographic planes and directions in HCP metal, defined using four indices convention, have been given by Partridge (1967) [37]. Examples are presented in the Figure 3.3.

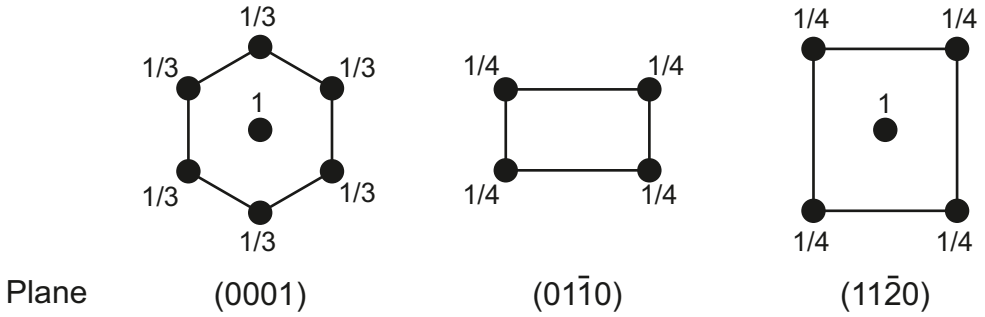

Figure 3.3: Important planes and directions in HCP metals.

Regarding cell axes, the very important factor used to describe HCP structure is c/a axial ratio, given by the height of the unit cell (c) divided by the side length of the hexagonal base (a). The c/a of a particular hexagonal metal is often compared with the ideal ratio obtained from hard-sphere model of atoms. This information is especially useful when the most densely packed planes are analyzed. Based on the c/a, the following conclusion has been drawn for two the most typical hexagonal planes: the basal (0001) and the prism $(10\bar{1}0)$; if the c/a is higher or close to ratio of ideal sphere packing, given by $\frac{\sqrt{8}}{3} = 1.633$, then basal plane is the most densely packed; otherwise, prism plane is taking the lead in terms of density of packed atoms [37].

Such observation could give an insight into possible deformation modes since they should be activated on the most densely packed planes. Unfortunately, in the case of HCP structure, the situation is more complicated. This is due to the fact that there are planes which contain non-uniformly spaced atoms. To overcome this problem, it is assumed that basal plane is not perfectly flat thus it can contain atoms from A and B layers. At the same time, number of atoms belonging to prism plane is

doubled. In this model the new ideal c/a ratio is given by $\sqrt{3}$. Such an approach predicts well possible slips systems for some of the hexagonal metals. Despite that, it is wrong in some other cases [28].

Hexagonal metals are expected to present strong anisotropy of physical, mechanical and chemical properties, which is inherently connected with the fact that c is not equal to a. Therefore, various properties can appear as different in respect to the orientation of c-axis or the basal plane. In particular, as discussed below, the c/a factor is of key importance for the evolution of texture microstructure and microstructure during thermo-mechanical treatment.

3.2 Deformation of hexagonal metals

A strong influence of crystallographic structure on material properties is evident when cubic and hexagonal metals are compared in terms of deformation process and related texture evolution.

In the first case, cubic symmetry implies domination of slip deformation mode, while twinning plays less important role. Moreover, in many cases, one slip system family contains a large number of independent slip systems. This allows things to be much simpler since activation of only one slip system family may be enough to maintain plastic deformation, especially at lower strains.

In the second case, deformation is more heterogeneous and much more complex. The activation of slip is highly limited since there are only two possible slip family directions: $\mathbf{a} = <11\bar{2}0>$ which is the easiest to activate thus most frequent one, and $\mathbf{c} + \mathbf{a} = <11\bar{2}3>$ which is much less observed. Moreover, the deficiency of slip directions is worsen further by small number of possible slip planes as $\{0001\}$, $\{10\bar{1}0\}$ and $\{10\bar{1}1\}$ are the only slip planes that contain direction $\mathbf{a}$. As a result, just few slip system families can be operative in hexagonal metals, as listed in the Table 3.1. Also, Figure 3.4 presents schematic view on all of them.

According to the von Mises condition, a homogeneous deformation takes place only if at least five independent slip systems are activated in order to accommodate the externally imposed strain [38]. From that point of view, it should be emphasized that most of hexagonal slip families provide less than the required number of independent slip systems. Moreover, even cross-slip from one plane to another may be insufficient since some of the slip systems are equivalent between families in such process. In addition to this, only part of the described systems can be usually activated at room temperature. Also, easy slip directions $<\mathbf{a}>$ are perpendicular to the c-axis thus

Table 3.1: The most common slip systems in hexagonal metals [37].

			Number of slip systems	
Slip system family	Slip direction	Slip plane	Toal	Independent
Basal <**a**>	$<11\bar{2}0>$	(0001)	3	2
Prismatic <**a**>	$<11\bar{2}0>$	$\{10\bar{1}0\}$	3	2
Pyramidal <**a**>	$<11\bar{2}0>$	$\{10\bar{1}1\}$, $\{10\bar{1}2\}$	6	4
Pyramidal <**c** + **a**>	$<11\bar{2}3>$	$\{11\bar{2}2\}$	6	5

Prismatic slip is often termed as easy glide system.

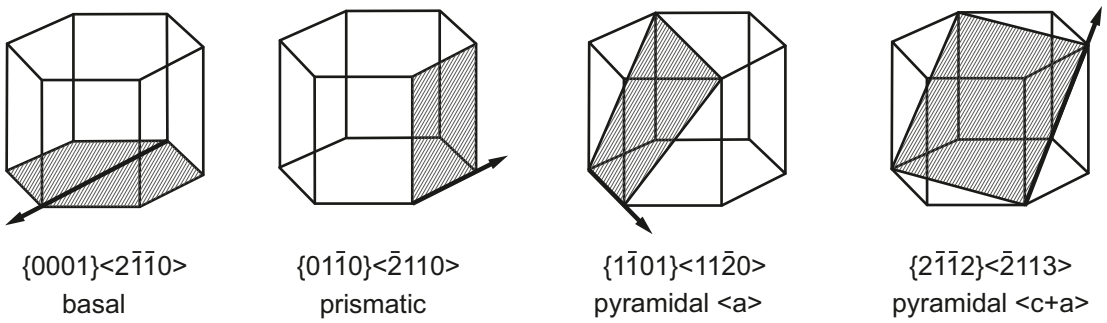

Figure 3.4: Slip systems in hexagonal metals.

elongation or compression along the *c*-axis cannot be handled by such a slip.

Therefore, apart from insufficient slip mode, deformation twinning has to contribute in accommodation of the imposed strain, mainly in directions out of the basal plane, especially at low temperatures and low strains. This is the reason why much research attention is often paid to characterize deformation twinning in hexagonal metals [39–55].

There are two main types of deformation twins which are usually distinguished based on the imposed strain conditions. Tensile twins are formed when extension strain component is parallel to *c*-axis, whereas compression twins are formed when contraction strain component is parallel to *c*-axis [56] – Figure 3.5.

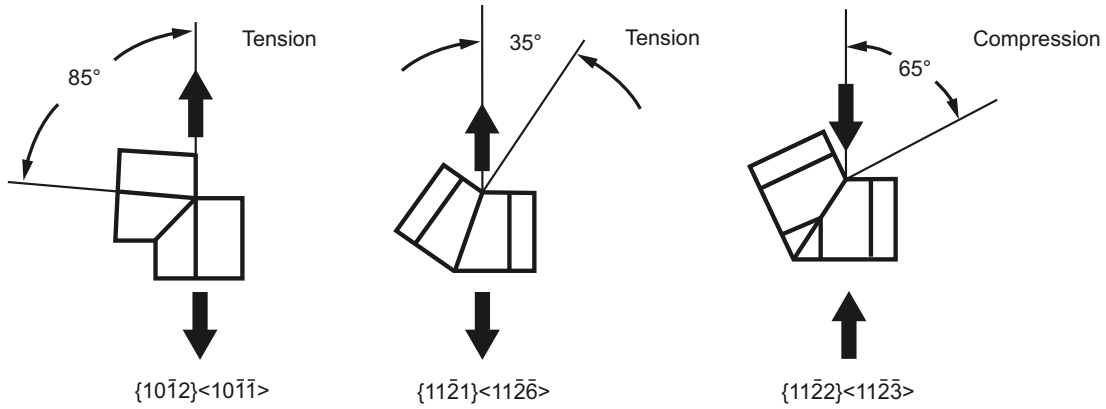

Figure 3.5: Geometry of twinning in the case of tensile and compression twins.

As a result, c-axis of the created twin is rotated around particular direction at strictly defined angle, as indicated in the following Table 3.2.

Table 3.2: The different twinning modes in titanium and the corresponding rotation angles of the c-axes.

Twin plane		Rotation axes	Rotation angle
Tensile	{10$\bar{1}$2}	<12$\bar{1}$0>	85°
Tensile	{11$\bar{2}$1}	<1100>	35°
Compression	{11$\bar{2}$2}	<1100>	65°

Two successive stages are necessary to create a twin: nucleation and further growth [39]. In addition, various families of crystallographic planes can be subjected to twinning, for example: {10$\bar{1}$2}, {10$\bar{1}$1}, {11$\bar{2}$1}, {11$\bar{2}$2}, {11$\bar{2}$3} and {11$\bar{2}$4} are frequently reported.

Again, c/a is one of the main factors to decide whether compression or tensile twin is activated on a particular plane. It is generally acknowledged that if c/a is less than value provided by ideal sphere packing, then {10$\bar{1}$2} and {11$\bar{2}$1} are tension twins, while {11$\bar{2}$2} is compression twin. In the opposite case, {10$\bar{1}$2} is a compression twin.

The shape of the twin is strongly connected with twinning shear. For instance, in titanium {10$\bar{1}$2} twin tends to have wide lenticular shape observed on the cross-section because of small shear, while {11$\bar{2}$1} twin is a narrow lamellae [37].

In connection with the abovementioned, various slip systems and twinning systems have to be involved during deformation of hexagonal metals which, in addition,

may interact with each other. Overall deformation can be thus described as interplay between them. It is frequently observed in hexagonal metals that reorientation caused by activation of one mode promotes another mode to operate. Such mechanism is mostly realized by the twinning. For example, double twinning frequently occurs, where secondary twins of one type are created inside the primary twin of another type. Similarly, specific crystallographic planes can be reoriented by twinning to a more favorable orientation from the viewpoint of slip activation. As a result, development of plastic strain in HCP grains can be highly heterogeneous, which is difficult to analyze since significantly different deformation modes can operate on them.

Another difficulty connected with analysis of deformation comes from the fact that even between metals belonging to hexagonal group the situation is not clear. This is mainly due to the role played by strong texture and influence of c/a on active slip and twinning systems. However, there are also other factors that have to be taken into account, such as: strain rate, stacking fault energy, temperature, texture, presence of impurities. Therefore, each hexagonal metal has own specific operating modes. Examples are presented below for magnesium, titanium and zirconium based on [28, 37, 51, 54, 56, 57].

Table 3.3: Main deformation modes observed experimentally in Mg, Ti and Zr.

Metal	c/a	Primary slip	Secondary slip	Twinning planes
Mg	1.624	(0001) <11$\bar{2}$0>	{1$\bar{1}$00} <11$\bar{2}$0>	Tensile {10$\bar{1}$2}
			{11$\bar{2}$2} <11$\bar{2}$3>	Compression {10$\bar{1}$1}
Ti	1.587	{1$\bar{1}$00} <11$\bar{2}$0>	(0001) <11$\bar{2}$0>	Tensile {10$\bar{1}$2}
			{11$\bar{2}$2} <11$\bar{2}\bar{3}$>	Tensile {11$\bar{2}$1}
				Compression {10$\bar{1}$1}
Zr	1.593	{10$\bar{1}$0} <11$\bar{2}$0>	(0001) <11$\bar{2}$0>	Tensile {10$\bar{1}$2}
			{11$\bar{2}$2} <11$\bar{2}\bar{3}$>	Tensile {11$\bar{2}$1}
				Compression {10$\bar{1}$1}

Primary slip – mostly observed at room temperature

Secondary slip – mostly at observed elevated temperatures

3.3 Plasticity of hexagonal metals – the influence of twinning

Regarding various combinations of reduced operation of slip systems and role played by extensive activation of deformation twinning, it has been investigated how they affect crystal plasticity of hexagonal metals, particularly in terms of ductility.

It has been shown that despite inadequate number of active and independent slip systems, some of the HCP metals remain surprisingly ductile like titanium or zirconium, especially at low temperatures. This property is related to a large number of twinning systems operating in those metals [56, 58].

However, the increased ductility is not achieved directly because of twinning mode since it has been reported that twins contribution in accommodation of total strain is relatively small, less than 15% in zirconium [37]. The main role played by twins is rather to facilitate slip activation by slip plane favorable reorientation of hard to deform *c*-axis thus higher deformation magnitude can be obtained in zirconium or titanium without cracking. Hence, strong twinning influence has to be taken into account when mechanical response, namely stress-strain curve, of these metals is investigated. Examples can be seen in the following publications which concern titanium [59–61] and zirconium [62].

Magnesium is another interesting example of twin influenced ductility. It is one of the hexagonal metals that possesses the lowest ductility and formability at room temperature. This is mainly due to dislocation activity which is often restricted to the basal plane, the most densely packed one in this case. However, it has been reported that activation of twins may increase magnesium ductility in some cases due to reorientation mechanism mentioned above, which results in relatively small work hardening [46, 63, 64].

One the other hand, massive twinning may be disadvantageous since twin boundaries can act as barriers to propagation of dislocations, which implies strain hardening in effect [64]. Also, grains can be reoriented by twinning in a way that leads to a texture which is unfavorable for slip [63]. This is especially important for magnesium with formed strong basal texture. In this case, further deformation induced by rolling or compression, where compression axis is perpendicular to basal plane, cannot be accommodated by basal slip system. Moreover, activation of compression twins, promoted by this basal texture [51, 54], facilitates fast shear band formation and crack propagation [47, 65].

3.4 Recrystallization and grain growth characterization in hexagonal metals

The fundamental mechanisms of plastic deformation have been relatively well studied in hexagonal metals, whereas the processes of recovery, primary recrystallization and grain growth occurring during heat treatment have been much less investigated. One of the reasons of this situation is connected with limited insight provided by experimental techniques dozens years ago. Only quite recent improvements of EBSD allowed to measure metal with HCP structure using this technique, and so new possibilities are now available in the analysis of annealing phenomena. More details about the abovementioned progress in experimental techniques, particularly EBSD, can be found in the next chapter.

Therefore, before EBSD dissemination micro-hardness test have been usually employed to examine softening introduced by recrystallization, whereas annealed microstructures have been characterized only in terms of roughly estimated grain size distributions and quantitative observations, both obtained from optical microscopy. In addition, transmission electron microscopy have been used in order to analyze changes taking place locally inside the grains, especially dislocations rearrangement.

On this basis, it has been shown, for instance, that recrystallization in titanium leads to equiaxed grains without annealing twins, while during grain growth average grain size is increasing according to power law of time [66]. Also, self-similarity and log-normal character of grain size distribution have been reported in this case. Other conclusions concern early stages of deformation, associated annihilation of dislocations and observed mechanisms of nucleation, particularly formation of high angle grain boundary due to coalescence of sub-grains. In another study of titanium, interesting influence of rolling temperature and created deformation twins on competition between recovery and recrystallization has been revealed [67]. Briefly, intersecting lamellar $\{10\bar{1}1\}$ twins seem to be more suitable for successive nucleation than lenticular $\{11\bar{2}2\}$ twins thus static recrystallization has been observed in the first case, whereas recovery becomes predominate, especially at lower reductions, in the second.

Regarding grain growth kinetics, it has been suggested several times that grain growth exponent is equal to 0.33 for titanium [68] and zirconium as well [69]. On the other hand, Contieri et al. (2010) have found that the exponent value should be in the range from 0.5 to 0.58 [70].

Nevertheless, all these early results have to be carefully treated and interpreted. In contrary, modern experimental investigations allow to relate reconstruction of annealed microstructure with accompanied texture evolution. Also, they provide much more reliable data. Examples of such as well as conclusions reported in the literature concerning recrystallization and grain growth occurring in particular hexagonal metals are discussed in the section 3.6.

Going back to heat treatment procedure, it has to be kept in mind that hexagonal metals like titanium or zirconium are subjected to phase transformation from HCP alpha structure to cubic beta structure, which takes place in very high temperature, thus it is another important topic in the field of characterization of hexagonal metals [71–73].

3.5 Texture evolution in hexagonal metals during cold-rolling and further annealing

In many experimental investigations texture analysis is the most important point of interest, especially when deformation is introduced by cold-rolling or compression since such mechanical treatment is often applied in the industry to produce large and thin sheets of material.

As far as HCP metals are concerned, texture evolution during cold-rolling or compression can be roughly approximated by movement of main maxima observed on {0001} pole figure (Figure 3.6), where RD is rolling (or elongation direction) and TD is transverse direction.

For instance, magnesium has characteristic strong basal texture which consists of main component located in the center of {0001} pole figure, whereas the rest of orientations is concentrated in the vicinity of normal direction. Such texture may be further evolved by additional deformation which results in spread of orientations toward rolling direction.

In contrary, the deformation textures in titanium and zirconium are much different since basal poles are shifted toward transverse direction at an angle of $30° - 45°$. Also, orientations defined by $<10\bar{1}0>$ direction tend to dominate in the texture. It means that the main component of deformation texture can be described by tilted $\{0001\}<10\bar{1}0>$ orientation. After that texture is practically stable as further deformation leads to only slight changes in the texture.

Texture evolution caused by plastic deformation has been very well documented.

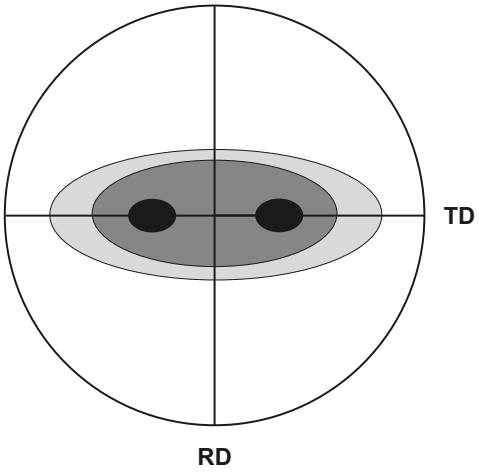

Figure 3.6: Sketch of classical {0001} pole figure usually obtained after rolling.

A detailed report can be found in [74]. Nevertheless, the connection between active deformation modes and texture formation seems to be still a challenging puzzle in HCP metals.

For instance, the texture observed in magnesium can be easily explained by activation of basal slip system combined with tensile twining, whereas additional pyramidal glide $\{11\bar{2}\bar{2}\}<11\bar{2}3>$ is responsible for the movement of orientations toward rolling direction.

On the other hand, the role played by deformation mechanisms being involved in the evolution of deformation texture in titanium or zirconium is much more difficult to understand. The main problem in this case arises from the fact that the observed texture development cannot be obtained only by activation of deformation modes, mainly prismatic slip system, which are confirmed experimentally in those metals at room temperature. Therefore, additional systems have to be taken into account. In particular, it has been shown that deformation texture of titanium and zirconium can be reproduced using combination of prismatic and basal systems [74].

Another solution is to assume that pyramidal slips $<11\bar{2}3>$ are activated, even if it is not usually observed at ambient temperature, in order to move basal poles from normal direction toward transverse direction. In this scenario, texture stability at higher deformation can be also understood. This is due to the fact that only slight changes of basal poles, located between the normal and transverse directions, are necessary since they are already well oriented for activation of pyramidal slip [39].

The mechanism involving presence of pyramidal slip is thus incorporated in crystal plasticity models of titanium or zirconium as it gives better results in prediction of

deformation textures in some cases [75–77].

An alternative explanation of deformation textures developed in zirconium and titanium employs sequence of complex operations performed with $\{10\bar{1}2\}$, $\{11\bar{2}2\}$ twins. A good example of such operation is the effect caused by compression twins, which when active, move orientations initially parallel to normal direction outside of the center of the {0001} pole figure.

After annealing, it has been reported that texture evolution resulted from recrystallization of hexagonal metals is rather limited. It means that the obtained ODF (Orientation Distribution Function) is weakened, although it resembles the one from deformed state. Such behavior is much different in comparison to some of the cubic metals, where particular texture components can disappear completely, whereas other emerge, as it is in the case of cube orientation dominating in the texture of recrystallized copper [78, 79]. Therefore, grain growth stage is often necessary to observe more notable evolution, at least in titanium [66] and zirconium, where it has been reported that main maxima of deformation and grain growth textures are related with rotation by 30° around <0001> axis [80]. Hence, main deformation texture component - tilted $\{0001\}<10\bar{1}0>$ - is replaced by grain growth component which is defined by the same tilted {0001} plane and $<11\bar{2}0>$ direction. Nevertheless, it still does not imply significant changes.

The described slight texture evolution during recrystallization is an important problem in the case of magnesium as it usually possesses strong basal texture after deformation which, in turn, is rather unfavorable from the formability point of view. Therefore, an appropriate way of modification of magnesium texture is being looked for to improve ductility, for instance [81]. However, as already mentioned above, this cannot be achieved by simple annealing.

3.6 Literature overview on EBSD investigations concerning recrystallization and grain growth in titanium and zirconium

Magnesium, titanium and zirconium are the most important hexagonal metals to be investigated as far as fundamental understanding of physical processes taking place during thermo-mechanical treatment is concerned. In addition, all of them can boast of special properties used in particular industrial applications.

Of those three, titanium and zirconium are very alike in terms of physical prop-

erties. Both exhibit almost the same c/a ratio thus similar deformation modes are expected to occur in those metals. Magnesium, in turn, is much different. The c/a ratio in this case favors other deformation mechanisms, which results in another evolution of deformation texture accompanied with highly reduced ductility.

Starting from this point of view, it would be very interesting to compare magnesium, titanium and zirconium in terms of recrystallization and grain growth phenomena using one appropriately designed experiment. Unfortunately, such juxtaposition is extremely difficult to arrange. The main reason lies on magnesium side. First of all, it is hard to deform magnesium at room temperature by compression or rolling without problematic fracture. Such behavior has been also observed during preliminary tests performed in this thesis. Therefore, deformation at elevated temperature has to be introduced to avoid cracks, which is rather unwanted in the scope of whole experiment. The second main problem is caused by high chemical reactivity of magnesium which implies more complex surface preparation method for EBSD measurements than in the case of titanium or zirconium. After many attempts performed in LSPM laboratory, none of the used preparation scenarios was good enough to ensure satisfactory results.

In this connection, the analysis has been focused on the investigation of titanium and zirconium, which is still a big challenge since both metals are difficult to deform by compression. Also, much attention is required to measure them experimentally, whether using EBSD technique or X-ray diffraction.

It should be mentioned that scientific efforts, mainly modern EBSD studies, have been already devoted to relate mechanisms being operative during recrystallization and grain growth in titanium and zirconium. Those experimental insights into the investigated phenomena and obtained conclusions are shortly reviewed below.

The most methodical approach has been presented by two research groups supervised by Brigitte Bacroix [82–87] and Nathalie Bozzolo [88–98], respectively.

The first one has mainly dealt with deformation, recrystallization and related annealing phenomena of Zr-2Hf alloy, which was strained up to 55% by channel-die compression. It has been shown that imposed compression of initially equiaxed grains results in high heterogeneity of the obtained microstructure. It contains highly deformed and less deformed zones. During annealing the highly deformed areas are subjected to nucleation, especially at twin intersections, and growth of new recrystallization grains, whereas the low deformed areas are subjected to recovery. As a result, the recrystallized microstructure consists of large, but less numerous, grains surrounded by many clusters of smaller grains.

Moreover, it has been shown, based on in-situ high voltage electron microscopy, that two types of nucleation are operative, i.e. classical one originated from recrystallization nuclei and another one associated with recovery process which, due to annihilation and rearrangements of dislocations and SIBM, leads to formation of sub-grain structure. It is also considered in this second case that growth of emerging grain is initiated and supported by coalescence of smaller sub-grains.

Deformation texture contains two main maxima: major tilted $\{0001\}<10\bar{1}0>$ component and minor tilted $\{0001\}<11\bar{2}0>$ component. In both cases, tilted refers to the fact that c-axis perpendicular to $\{0001\}$ plane is inclined at $20^\circ - 30^\circ$ from ND toward TD. Also, it has to be mentioned that tilted $\{0001\}<10\bar{1}0>$ component is created during compression by rotation of the initially dominating tilted $\{0001\}<11\bar{2}0>$ component.

Recrystallization does not change the texture in a significant manner. At early stages of recrystallization, texture of the new emerging grains reassembles general outline of deformation texture, but at the same time it is much more random thus oriented nucleation is not confirmed in this case. However, after slightly longer annealing, two major components: tilted $\{0001\}<10\bar{1}0>$ and tilted $\{0001\}<11\bar{2}0>$ are restored and kept until the end of recrystallization. It is emphasized that both components are equally pronounced, i.e. tilted $\{0001\}<10\bar{1}0>$ does not dominate, as before annealing.

Similar results have been reported by this group for the recrystallization of a cold-rolled Zircaloy-4 [82]. Also, they are in good agreement with observations from Jiang et al. (2008) [99].

Such evolution could be related with the fact that tilted $\{0001\}<10\bar{1}0>$ has the highest stored energy values thus it is decreasing first during recrystallization.

Only further grain growth leads to texture evolution, which is manifested by domination of tilted $\{0001\}<11\bar{2}0>$ component. This is due to the largest grains which preferentially posses this orientation [83]. It is explained based on a hypothesis that tilted $\{0001\}<10\bar{1}0>$ component contains remaining of residual plastic strain therefore it is consumed by growing strain-free tilted $\{0001\}<11\bar{2}0>$ component due to SIBM mechanism.

Finally, in the recent work of this group [86] a much more detailed investigation of texture evolution combined with a thorough examination of orientation dependent stored energy is performed in order to characterize mechanisms of nucleation and grain growth in compressed as well as highly cold-rolled zirconium.

It is also concluded that the maximum which usually is observed in the misori-

entation profile at 30° after annealing is not related with the simultaneous presence of the two considered components. It is rather resulted from misorientations between orientations belonging to one of the fibers: $\{hkil\}<11\bar{2}0>$ or $\{hkil\}<10\bar{1}0>$, respectively [87].

The second group considered recrystallization as well as grain growth in cold-rolled zirconium [91, 94, 96–98] and cold-rolled titanium [89, 92, 95]. Therefore, they have taken an opportunity to compare directly both materials using similar deformation and heat-treatment, and relate observed mechanisms of annealing phenomena [88, 90, 93].

It appears that texture and microstructure evolution observed in this case during thermo-mechanical treatment of zirconium (Zr702α) has much in common with the already described Zr-2Hf alloy. Again, deformation introduced by cold-rolling along original rolling direction to achieve 80% of thickness reduction leads to formation of main $\{hkil\}<10\bar{1}0>$ component in the texture, where $\{hkil\}$ is $\{0001\}$ plane tilted 30° from ND in the ND-TD plane, whereas after primary recrystallization the obtained texture is a weakened version of the deformation texture. More detailed analysis of orientation of emerging grains excludes the possibility of oriented nucleation. Also, a slight tendency to develop orientations around tilted $\{0001\}<11\bar{2}0>$ component is revealed during further stages of recrystallization. This is explained in terms of growth competition between facing recrystallization grains associated with lower probability of orientation pinning in this component. Additional annealing allows grain growth process to modify the texture, as previously, by domination of the tilted $\{0001\}<11\bar{2}0>$ component. This evolution is clarified using partial textures of the largest and the smallest recrystallization grains. In general, grains with the tilted $\{0001\}<11\bar{2}0>$ orientation have size advantage thus they are developed during further growth.

Regarding microstructure evolution, high heterogeneity is confirmed after deformation. Moreover, it has significant influence on recrystallization and kinetics of this process. After partial recrystallization, the most deformed zones, which probably contain the combination of lamellar and heavily deformed structures, are replaced very fast by new equiaxed grains gathered in the form of wavy lines, whereas large, elongated and less deformed areas with orientation close to $\{0001\}<10\bar{1}0>$ are not subjected to recovery nor recrystallization. Consequently, they are slowly consumed at the very end of primary recrystallization process.

Three mechanisms are involved: SIBM, sub-grain formation and growth due to recovery and growth of adjacent grains toward a still deformed grain. Further grain

growth phenomenon results in moderate increase of average grain size due to slow and impeded boundary migration, which is caused by precipitates. The latter are also responsible for abnormal grain growth in the case of longer annealing time at 800°C.

In this regard, based on misorientation angle distribution, it can be concluded that there is no special grain boundary which could significantly affect microstructure and texture evolution [94]. However, more detailed analysis suggests that boundaries with $<11\bar{2}0>$ misorientation axis can have special properties. Moreover, interfaces with following misorientations: $30°<10\bar{1}0>$ and $60°-65°<11\bar{2}0>$ may be considered as candidates for low energy boundaries [96].

In spite of the discussed texture stability after primary recrystallization, various thickness reductions (40%, 50%, 60%, 80%) and different rolling directions (standard RD, TD, CR – cross rolling) have been investigated to understand this effect. It has been found that deformation texture can be changed during recrystallization only in the case of moderate thickness reduction – 40%, no matter which rolling direction was used or, in the case of TD rolling, no matter which strains was accommodated. These observations have been related with different mechanisms of microstructure evolution between considered cases which, in turn, have been linked with the influence of local deformation structures and deformation textures. In particular, the interplay between oriented nucleation and preferred growth has been discussed. In this regard, it has been recalled that recrystallization of highly RD rolled microstructure does not employ oriented nucleation, whereas oriented growth is rarely observed. More details about this particular study can be found in [98].

As far as titanium is concerned, it has been already underlined above that this metal has been investigated using the same methodology as the one applied to zirconium, i.e., the same deformation mode – cold rolling, thickness reductions, annealing conditions and experimental techniques. Also, most of the results concern titanium rolled by 80% along prior rolling direction. In this case, it is clear that mechanisms controlling deformation, subsequent recrystallization and further grain growth are very alike to those already described for zirconium. Both materials exhibit important role of heterogeneity of deformed microstructure, strong recovery impact, similar texture components and related slight texture evolution during recrystallization as well as mechanism of main components exchange during grain growth which involves two main processes: correlation between particular orientation and grain size and orientation pinning.

Nevertheless, there is an important difference between titanium and zirconium

which is reflected in the way heterogeneity of deformation microstructure is formed [93]. This is the subject where primary role of twinning is revealed. Cold-rolling in zirconium is dominated by slip. Twinning also occurs, but it is in the background of the deformation process. Consequently, three types of zones are generated in the zirconium microstructure: large, elongated and only slightly deformed grains, moderately deformed zones comprising of large lamellar cell blocks and zones which undergo the highest deformation. The important point to be emphasized is the fact that more deformed substructures have surprisingly high fraction of low angle misorientations.

In contrary, deformation of titanium starts from significant occurrence of tensile and compressive twins which leads to severe fragmentation of most of the grains. At higher strains, the highly divided grains are further refined into extremely small substructures due to slip activity and shear bands formation. Consequently, after 80% of thickness reduction almost 85% of titanium microstructure is covered by nano-scale dislocation cells separated by high angle misorientations (more than 30°), whereas the rest consists of large, lamellar and much less deformed grains, which at the beginning of deformation were unfavorably oriented to twinning. In addition, twinning has also small impact on texture evolution [95].

Based on the discussed comparison, it can be concluded that the deformation heterogeneity of titanium microstructure is even more extreme than in zirconium. This, in turn, has a consequence in recrystallization behavior, particularly the kinetics of this process.

Nearly 85% of highly fragmented areas is rapidly recrystallized, whereas the rest is slowly consumed by growing grains. This substantial influence of twin related heterogeneity has been also confirmed by other authors.

For instance, Shi et. al. (2008) have presented beautiful example of heterogeneity gradient that results in highly localized formation of the grains at the beginning of recrystallization, i.e., surface layer of the sample [100] – see Figure 3.7, while Chun and Hwang (2008) have shown that temperature increased heterogeneity leads to increased fraction of grain clusters and finer microstructure after recrystallization as a consequence [101].

Another difference between these two metals is kinetics of grain growth process. In titanium precipitation does not influence boundary motion in such a significant manner as in the case of zirconium. Therefore, the increase of grain size during extensive annealing is more pronounced in this material. This is also the reason why abnormal grain growth has been not observed in the investigated titanium

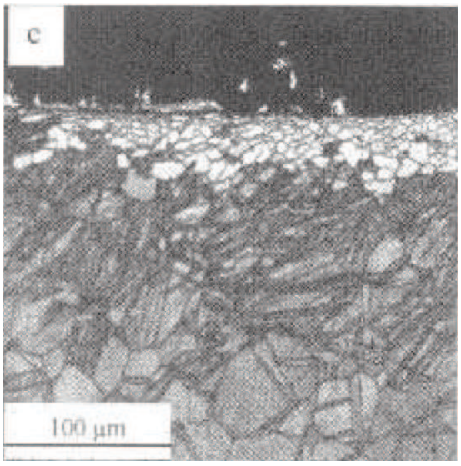

Figure 3.7: Topological map presenting microstructures of partially recrystallized titanium reported by Shi et al. (2008) [100].

samples.

3.7 Summary. Aim of the experimental work

In the light of the abovementioned views, it can be concluded that there are interesting observations and important conclusions concerning recrystallization and grain growth in Zr and Ti which should be further investigated. Therefore, the aim of this thesis is to contribute to the already performed efforts.

For that reason, two experiments have been performed. Both focus on much lower strains than the one discussed above. First is about recrystallization and grain growth in titanium cold-rolled up to 60% of thickness reduction. The second deals with partial primary recrystallization of zirconium channel die compressed along directions ND and TD. In this case maximum strain is less than 17%.

Moreover, obtained experimental results will be used in order to develop physical model of recrystallization and grain growth in titanium and zirconium which could be applied and tested in the way of computer simulations.

CHAPTER 4

Experimental methods

A wide range of experimental techniques is available to be used for polycrystalline material characterization. Most of them are based on the fact that appropriate incident beam of the radiation is diffracted on crystallographic lattice planes of the material, as it is depicted by the famous Wulff-Bragg's Law [102]. Different types of radiation, namely X-rays, neutrons, electrons, can be employed for that reason depending on the needs and nature of provided information.

However, in order to conduct a broad and advanced investigation of complex phenomena, such as deformation, recrystallization and grain growth, taking place in a textured polycrystalline material, many different factors have to be taken into account as it is desirable to find a link between microstructural features introduced by deformation and final material properties achieved in the annealed state. Therefore, an experiment has to provide as complete data as it is possible, and thus not only information about the evolution of bulk texture (X-ray or neutron diffraction), nor grains topology (electron microscopy, optical microscopy) is required, but both of them at the same time: microstructure and crystallographic texture, which is referred as microtexture [103]. This is a modern investigation approach that results in statistically rich datasets consisting of many orientations of the crystals and their spatial location in a chosen area of the specimen surface layer. The measurement is carried on by orientation mapping procedure, in which focused radiation beam probes given area in a point by point way to find orientation related to each point. Hence, beam spot size has to be much smaller than the grain size. This implies condition of sufficient spatial resolution which generally selects electrons as a radiation

source in this case.

Electron Backscatter Diffraction (EBSD) technique is capable to measure microtexture with appropriate statistics and spatial resolution of the obtained data, and thus it is the most common experimental technique applied for that reason among all other electron diffraction methods. For example, EBSD can assess information about microtexture in the case of highly deformed structures, or fine-grained microstructures, with grain size in the range of micrometers as well as from microstructures after extensive grain growth (range of millimeters). EBSD is, therefore, an universal and very popular technique in the materials science where it is applied to investigate various types of materials: metals, ceramics, composites, geological materials and so on. Nowadays, it is hard to imagine that material study can be performed without this tool. This is also the main reason why EBSD is used so extensively in this thesis.

Therefore, brief technical view on mechanisms being used in EBSD technique is presented further as a quick introduction to this method. However, it has to be kept in mind that complete theoretical description of physical phenomena underlying EBSD concept is much more complex. Next paragraphs concern EBSD features, applications and possible analyzes resulting from them. Some disadvantages are also discussed with a focus on demanding sample surface preparation method. In addition, selected practical aspects of EBSD measurements are discussed.

More details about different topics connected with EBSD technique can be found in the comprehensive literature review [80, 104–106].

Regarding crystallographic texture measurements, there are several techniques which can be applied for that reason. Thorough description of each of them has been concluded in [80, 107]. As far as only bulk textures measurement is concerned, classical X-ray pole figure goniometer method followed by neutron diffraction and synchrotron X-ray diffraction remain one of the most common experimental techniques. Nevertheless, the final choice of the right technique is governed by many factors; one of the most important is the equipment availability. From this point of view, techniques which use neutron or synchrotron radiation are not further discussed as the access to them is rather limited. Therefore, in the thesis special attention is paid on the X-ray texture goniometer. The disadvantages of this technique are also emphasized, especially in the case of hexagonal textures.

Moreover, X-ray pole figure goniometer is compared with EBSD, which has become a serious alternative and strong candidate in this competition of texture measurement techniques. The comparison of EBSD and X-ray diffraction is continued

in the last paragraph which concerns methods used for stored energy measurements.

4.1 Electron Backscatter Diffraction (EBSD)

Basic technical equipment necessary to set up EBSD consists of scanning electron microscope – SEM (Figure 4.2) connected with EBSD detector (phosphorus-screen and CCD camera), hardware module used to control the microscope, and computer module responsible for acquisition and analysis of the data. All these elements are presented on the example EBSD system which was used in this thesis (Figure 4.1).

Figure 4.1: Elements of the EBSD equipment.

EBSD technique, as the name suggests, makes use of backscattered electrons – BSE which occur in sample as a consequence of inelastic scattering of incident electron beam on sample atoms. Despite the fact that the incident electrons are highly energetic, the penetration depth is rather low (tens of micrometers) due to De Broglie relation (see Equation 4.1) and strong absorption effects thus, to be precise, it has to be noted that described phenomenon is generally related with sample surface layer.

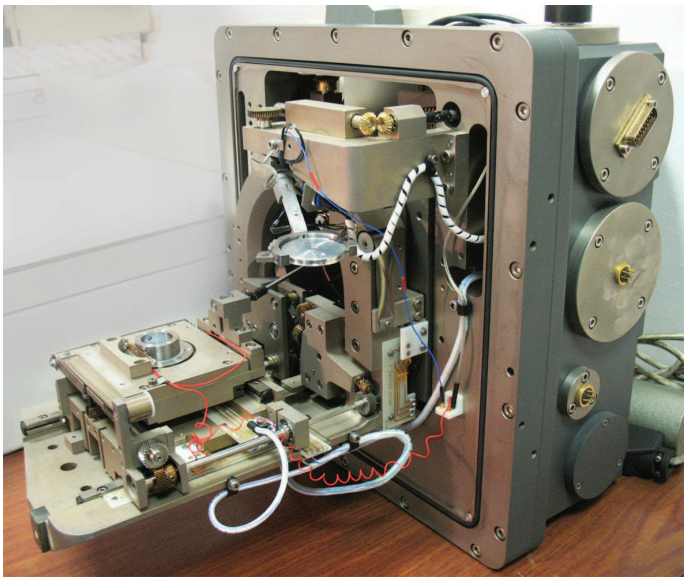

Figure 4.2: Construction of SEM on the example of Cambridge S306 microscope.

The well known De Broglie relation is expressed as:

$$\lambda_e = \frac{h}{m_e V_e}, \tag{4.1}$$

where: h - Planck's constant, and λ_e, m_e,V_e - wavelength, mass and velocity of the electrons, respectively.

Part of BSE can be subjected to classical Bragg's diffraction on crystallographic planes. However, in this case incident BSE beam is differentiated in terms of energy thus instead of typical parallel diffracted beam, Kossel cones are emitted toward the detector, where are registered in a final form of Kikuchi patterns (EBSPs – Electron backscatter patterns) which are a 3D projection of the cones on a 2D detector surface. Also, the background (noise) signal occurs due to the rest of detected BSE.

An important geometrical condition has to be fulfilled in order to observe the satisfactory Kikuchi patterns. The sample has to be tilted toward the detector, usually by an angle of 70°, in order to increase fraction of BSE escaping from sample surface (Figure 4.3). As a result, the incoming signal is strengthen as well as contrast of the EBSPs is increased [108, 109].

Measurement procedure is a little bit more difficult and risky because of this condition, especially in the case of big samples since the space between EBSD detector as well as electron column is highly limited (see example in the Figure 4.4), but on the other hand it is not such a big problem in the modern EBSD systems.

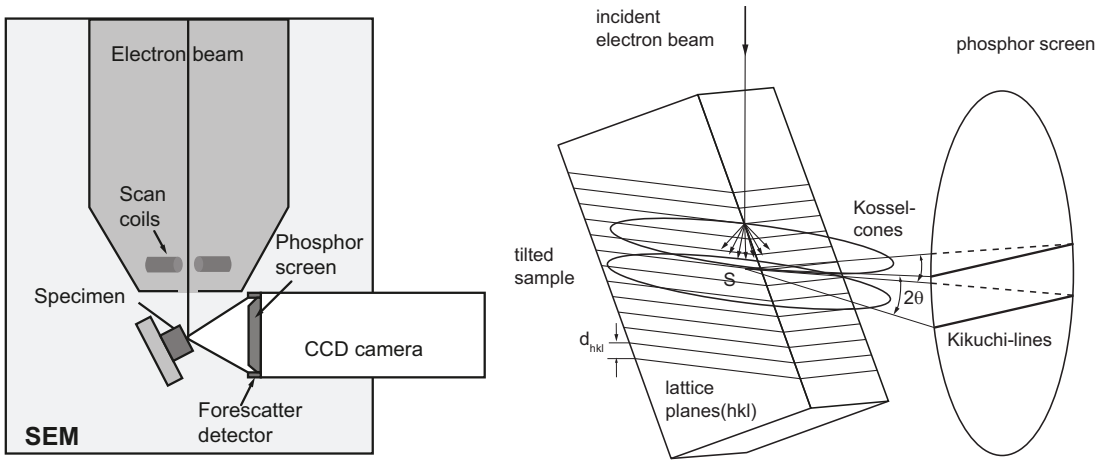

Figure 4.3: Schematic view on origin of Kikuchi patterns.

The fundamental basis of EBSD approach lies in the fact that each crystallographic orientation has its own Kikuchi pattern. Hence, it is possible to scan area of the sample using discrete grid of positions and narrowed incident beam which is moved between them. Kikuchi patterns emerging from each of the positions are analyzed by automated indexing algorithm to find the crystal orientations which generated them.

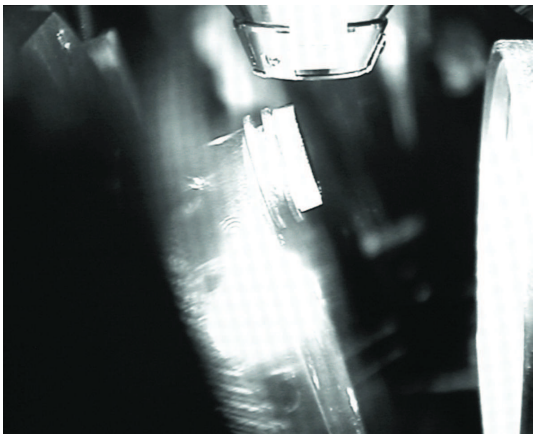

Figure 4.4: Inside SEM chamber during EBSD scan.

4.1.1 Image quality index and confidence index

On the basis of the aforementioned facts, the result obtained from EBSD analysis of selected area, referred as Orientation Imaging Microscopy – OIM map (also named as orientation map or EBSD map), is stored in the form of two or three dimensional

grid of EBSD points. In the case of TSL™ OIM acquisition software used for EBSD measurements, each point contains information about topological position in the map, crystallographic orientation given by Euler angles, phase identification parameter and two additional, but also very important, factors – image quality (or pattern quality) index and confidence index, which are related with quality and reliability of the EBSD data [110].

The first one, in a nutshell, is calculated based on the brightness difference between Kikuchi patterns and the overall background signal, therefore clear, sharp and well contrasted EBSPs have high image quality - IQ - values. In the opposite case, the IQ value is low. In some sense, this parameter is similar to signal to noise ratio.

The second one is connected with reliability of the orientation obtained on the basis of a given Kikuchi pattern is the right one. If confidence index - CI - is close to 1, then there is no orientation ambiguity, while 0 value means that there is a variety of possible orientation solutions, which fits a given EBSP, and so the final orientation chosen by the indexing algorithm is not trustworthy at all. Another possibility of low CI value is when there are at least two solutions of similar matching probability.

Usually, IQ and CI factors are connected. Low IQ value means diffused, overlapped or incomplete Kikuchi pattern thus much more orientations can be matched in the indexing algorithm. Hence, confidence index of calculated orientation is also much lower. Such correlation can be frequently observed, but it is not a general rule though. There might be a situation when CI is low despite the high IQ value due to indexing ambiguity in clear Kikuchi pattern which resulted from crystal symmetry.

4.1.2 EBSD applications

The basic principles of EBSD method remain fairly unchanged since first successful attempts of EBSPs observations performed in 1928 by Nishikawa and Kikuchi (information taken from [105]) and then first automated EBSD system proposed by Alam in 1954 [111]. However, full benefits of this approach emerged much later due to significant development of technical equipment, such as CCD cameras or SEM microscopes combined with Field Emission Gun technology, and simultaneous substantial progress in computational power, software development, data acquisition, processing and warehousing during last year's. These improvements and new analysis opportunities have been carefully reported, for instance by Dingley [112] and Randle [113]. As a result of dramatically faster acquisition of EBSPs and their automatic indexing, it is possible now to conduct investigation of material surface

with really impressive datasets as millions of orientations can be identified in less than few hours. Thereby, a window for a wide range of EBSD applications has been opened, and since then exponential increase in number of EBSD based publications is observed [23].

The list of the most important analysis tools offered by EBSD includes: local texture calculation, microstructure characterization (especially in terms of grain size/shape calculation [114, 115], but also many other grain parameters), misorientation statistics, analysis of grain and phase boundaries or phase identification. Besides these basic analyses, there are many more advanced and specialized approaches to be used like: strain mapping, investigation of phase transformations or analysis of grain boundary plane crystallography [105, 106]. Moreover, one can develop own tools to operate on EBSD data as it is done for stitching overlapping EBSD datasets [116], automatic analysis and estimation of area occupied by twins [49,117], stereological reconstruction of 3D microstructure [118], or in the case of grain reconstruction algorithm [119].

EBSD applications have been also extended in terms of scale and dimensionality of investigated area. Incorporation of Field Emission Gun - FEG, as an improved electron source, into EBSD system has increased spatial resolution so much (less than few nanometers) that it can be used to analyze sub-micrometer grains and deformation structures [120, 121] which previously could be investigated only by TEM (Transmission Electron Microscopy) observations, whereas EBSD in conjunction with Focused Ion Beam is used to characterize 3D microstructures [122, 123]. An important link between EBSD and simulation of deformation as well as recrystallization and related annealing phenomena should be also emphasized. For instance, lattice-based modeling like Monte Carlo simulations, employs directly imported 2D and 3D EBSD grid data as initial microstructures (see chapter 5).

There are also EBSD applications strictly connected with estimation of level of recrystallization progress in thermo-mechanically treated sample, especially fraction of recrystallized grains is the main point of interest. Appropriate methods have been described by Humphreys [124]. One of the possible approaches is to make use of EBSD image quality factor (in the case of TSL^{TM} OIM Software) in order to calculate minimal recrystallized fraction [125], whereas the other employs local misorientation calculations [126, 127]. Besides the recrystallized fraction, other recrystallization parameters can be determined. For example, an interesting algorithm has been proposed by Wu and Juul Jensen [128] for automatic estimation of the interfacial area density separating the recrystallization grains from the as-deformed

microstructure.

Another advantage of improved and rapid EBSD data acquisition is an opportunity for quasi in-situ observations. For instance, it is possible to put small testing machine inside SEM and perform EBSD investigation during tensile test. Surely the applied strain has to be paused for a while until EBSD scan is accomplished, but then deformation can be continued. Such an approach gives step by step information about deformation mechanisms taking place in chosen grains.

Recently, a specially designed annealing stage has been also used for in-situ recrystallization studies [129]. Similarly, EBSD in-situ annealing experiment has been performed by Kim et al. 2014 [130].

4.1.3 Comments on practical aspects of EBSD measurements

EBSD measurement procedure seems to be quite straightforward and simple for novel users at the first glance. However, after a while, one can realize that there are important difficulties and measurement practical rules which are not so obvious at the beginning. Part of them is related to statistical relevance of obtained data, whereas others concern data reliability.

In the first case, parameters such as number of acquisitioned grains and measurement step size have to be carefully analyzed. Both are connected with each other. The number of grains should be sufficiently large, especially for texture investigation, and so EBSD step size has to be a compromise between overall measurement time, map dimensions and map resolution.

In the second case, it is necessary to check if microscopic parameters (accelerating voltage, probe current), Hough transform parameters, EBSPs image processing procedure and position of the sample in the microscope as well as sample reference system are the same for each EBSD scan, especially when several scans of several samples are performed. For example, accelerating voltage and probe current have an impact on EBSD spatial resolution [131]. The IQ value, in turn, is strongly affected by the varying background images as well as application of automatic contrast during image processing procedure. The same situation is observed through variation of Hough transform parameters. As a result, IQ analysis may be error charged or even impossible to conduct between samples. Deviation from appropriate sample alignment, in turn, leads to difficulties in orientation and texture analysis as sample reference system is not correctly aligned. Another important issue connected with data reliability is the condition of the sample surface. This problem will be discussed

in detail below (in the next subsection).

In the both mentioned cases, general advices have been suggested [120, 132]. Nevertheless, each EBSD analysis of particular material is governed by its own rules. That is why appropriate amount of time has to be spent on initial tests to reach optimal measurement and processing strategies.

4.1.4 Sample surface preparation

EBSD technique is very sensitive to a condition of sample surface due to low electron penetration depth and other effects like: unfavorable dispersion of electrons or beam shadowed regions of analysis caused by surface roughness. Also, there is an effect of EBSPs image distortions when measured surface is not exactly parallel to the x-y plane of the stage due to wrongly performed polishing procedure [109]. Finally, surface defects introduced by preparation method may affect obtained results.

Therefore, a proper sample preparation method which ensures strain free and flat surface in a repeatable manner has to be settled. This is really important step for EBSD measurements which has a great impact on quality and reliability of the final data. Unfortunately, in some cases it is very time consuming, difficult or even impossible task to be accomplished.

Assuming that specimen is already cut, general approach in the preparation of the sample surface for EBSD measurements consists of grinding with silicon carbide (SiC) abrasive paper using different grades, next additional polishing with diamond past or active oxide polishing suspensions, then an electropolishing is used to remove remaining of abrasive machining. Ion polishing can be also applied as final step, if needed [133–135].

Apart from sample surface preparation, financial costs and, in some cases, measurement time are the most important problems which have to be taken into account during experiment.

4.2 X-ray texture (pole figure) goniometer

In this common method used for crystallographic texture measurements an experimental setup, in a general view, consists of diffractometer equipped with an X-ray tube as a radiation source, pole figure goniometer (like Eulerian cradle) and detection system. As in all modern techniques, there is also a computer unit responsible for configuration, positioning, control and programmed acquisition.

Texture in this case is measured in the form of set of pole figures. Mostly, it is done using reflection configurations, because they provide much better statistics in comparison to transmission mode. The one considered here is named Bragg–Brentano geometry ($\theta - 2\theta$); flat sample is placed in the middle of diffractometer, symmetrically between X-ray tube and detector, θ angle is given by direction of incoming beam and sample surface, whereas 2θ is the angle between incoming and diffracted beams (Figure 4.5).

While θ angle is changing in a specified range, the Bragg's reflection condition is fulfilled by different families of crystallographic planes $\{h, k, l\}$, as follows [102]:

$$n\lambda = 2d_{hkl} \sin\theta, \tag{4.2}$$

where n is an integer value, λ is wavelength of incident wave, d_{hkl} is the interplanar spacing.

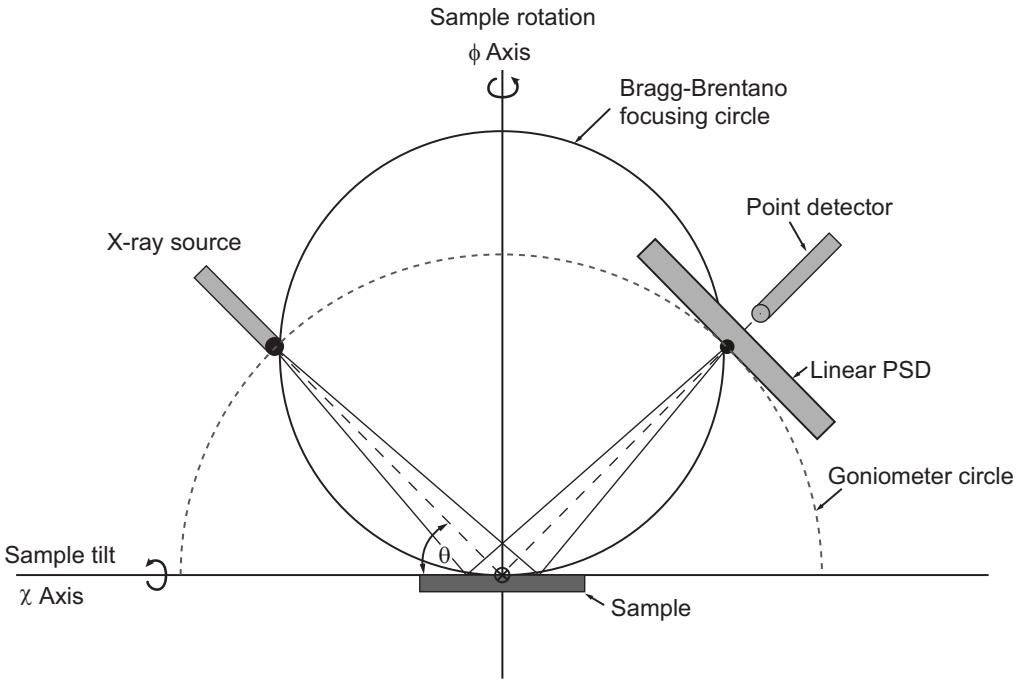

Figure 4.5: Schematic representation of Bragg-Brentano ($\theta - 2\theta$) geometry of pole figure measurement.

Consequently, diffraction peak is observed on the plot presenting detected intensity of radiation versus 2θ angle - called diffractogram. It is assumed that investigated material has a diffractogram containing well shaped intensity peaks separated from each other as well as from background intensity.

For measurement of $\{h, k, l\}$ pole figure, θ angle is fixed to a position of diffraction peak corresponding to $\{h, k, l\}$ crystallographic planes. Then, the intensity of diffracted beam is recorded while sample is rotated and tilted using goniometer (Eulerian cradle in this thesis) - see sketch presented in the Figure 4.5. These rotations are linked with orientation of diffracting grains defined in the sample reference system. Therefore, obtained intensities directly correspond to a pole figure value at a given angular position (α, β). It should be noted that in this way no information on spatial arrangement of orientations is available apart from information about "volume" fraction of grains being in the diffracting position.

Obtained pole figures (2D) are only a part of the whole information about texture, which is fully characterized by three dimensional Orientation Distribution Function – ODF. On that account, there was a strong need to develop mathematical methods in order to determine the ODF using measured pole figures, and analyze quantitatively the obtained texture. There are several available approaches right now to be used, such as WIMV algorithm [136], harmonic series expansion method proposed by Bunge (1982) [137], vector method by Vadon and Ruer (1982) [138] or Arbitrary Defined Cells (ADC) method proposed by Pawlik (1986) [139] and implemented in Labotex software [140]. The last one is an example of direct method which is free from errors generated by series expansions approach. In addition, ADC provides two types of errors which can be used to estimate the reliability of performed experiment.

Unfortunately, there are some disadvantages of the described X-ray pole figure goniometer method. First of all, only partial pole figures can be measured as the reasonable maximum tilting angle is around $60° - 85°$ due to distortion of beam projected on the sample surface [80]. Another problem is connected with corrections which are necessary to determine pole figure accurately, like absorption and intensity corrections, and especially the one connected with defocusing error which arises from the fact that diffraction peaks are broadened at the expense of much lower intensity with increasing tilting angle.

4.3 EBSD vs pole figure goniometer measurements of hexagonal textures

The influence of defocusing error can be minimized by applying the correction data which comes from the measurement of the appropriate powder sample. Even though, the pole figure goniometer allows only to measure incomplete pole figures, as already mentioned in the previous paragraph. This is an important issue in the case of hexagonal textures as some of them have maxima above the highest measurable pole distance. For example, texture of titanium or zirconium usually has maxima located at the top (north pole) and the bottom edge (south pole) of pole figures: $\{10\bar{1}0\}$ and $\{11\bar{2}0\}$. This implies that such textures are very difficult to be measured without additional samples specially cut to obtain another measurement planes. However, such solution is usually impossible in practice, especially in highly deformed samples.

On the other side, there is EBSD technique which allows to calculate directly textures from discrete orientation points. Yet, in this case information is gathered from local area of the sample. Also, penetration depth of electron beam is much lower than in the case of X-ray radiation. Despite that, it has been shown that even if EBSD information is taken from much lower number of grains, it is still possible to describe volume (bulk) texture with reasonable accuracy. The only issue is an appropriate number of sufficiently large EBSD maps which ensure statistical relevance of the calculated texture [80, 141, 142]. This is especially important for annealed samples.

There is an attractive reward for the efforts connected with extensive EBSD measurements, because one of the most significant advantages of EBSD over X-ray approach is the possibility of texture analysis which takes into account information about microstructure. For example, the textures of grains with particular size or orientation gradient within can be easily investigated.

In the light of above arguments, the EBSD technique seems to be an indispensable tool for an analysis of texture evolution in titanium and zirconium.

4.4 Stored energy measurements

Stored energy is a material parameter which is extremely desirable in the experimental investigation of primary recrystallization as well as computer simulation of this process. Unfortunately, it is quite difficult to measure or calculate exact value of

the stored energy. One of the possibilities is to analyze changes in diffraction peaks (shape broadening, shift of the position) which are caused by accumulated strain. However, such changes are very subtle thus high intensity and good collimation of the diffracting beam is necessary to observe them accurately. This implies application of synchrotron or neutron radiation for that purpose [86, 143, 144]. Based on that, stored energy can be estimated.

Going back to the experimental methods which are described and applied in this thesis, there are some attempts to use X-ray diffractometer for similar diffraction peak analysis in order to designate stored energy [145, 146]. However, it has to be kept in mind that the obtained result may be a strong approximation since intensity of radiation generated by X-ray tube is usually not high enough as well as beam focus is too broad. Nevertheless, the newest X-ray detectors have been improved significantly thus they offer much better intensities registered. Hence, application of X-ray diffractometer to estimate stored energy can be feasible in the newest equipment.

An alternative way is based on EBSD technique. There are few methods used for stored energy estimation in this case. They are divided between two main approaches according to the influence of plastic deformation, which is EBSD pattern degradation and pattern rotation.

Dislocations or crystalline lattice imperfections encountered during beam scan strongly affect registered Kikuchi patterns. Information about this influence, which appears as diffusion and degradation of EBSPs, is processed and saved in the EBSD data in the form of image quality factor. Based on the assumption that dislocations density is linked with EBSPs image quality, the stored energy values have been calculated and used in experiments and simulations [147–149]. However, this approach requires a deeper insight as image quality can be affected by wrong surface preparation as well as EBSPs acquisition and indexing settings.

Geometrically necessary dislocations - GNDs - accumulated in the grains are also connected with lattice rotation, which implies orientation gradient within the grains. Such gradients can be analyzed using calculations of local misorientations or average grain misorientations performed on EBSD map in order to obtain GND densities [150–154]. This method is also used for plastic deformation mapping [155, 156].

There is also so-called sub-grain method [157, 158] in which structure of dislocations is treated as structure of sub-grains located inside a grain. Each of the sub-grains can be analyzed in terms of size and boundary energy which is assumed to depend only on boundary misorientation (according to Read-Shockley formula –

Equation 5.6 in chapter 5). Then, stored energy can be calculated for each of the EBSD points.

Based on the presented description, it is concluded that EBSD may appear as more useful than X-ray diffraction approach in terms of estimation of the stored energy distribution. EBSD offers different methods, which can be easily compared. Each of them allows to relate stored energy with every single orientation, which is present in EBSD map. In contrary, such statistics is not possible to be obtained from X-ray approach, where stored energy is calculated only for a number of orientations. In addition to this, the results from EBSD methods can be analyzed in terms of topology using stored energy maps.

CHAPTER 5

Computer modeling of recrystallization and grain growth

As it is shown in the previous chapters, experimental techniques such as EBSD give nowadays exceptional insight into material characterization, especially in terms of recrystallization and grain growth studies. However, such investigation possibilities as well as an access to the necessary equipment and analysis tools were rather out of reach in the past. Today, many modern laboratories are already equipped with EBSD systems including FIB gun, which allows 3D microstructure measurements, but still this is a quite new method. This is why only recent reports use such data, whereas most of the conclusions published in the literature are based on 2D cross-sections of material.

For this reason, precise investigation of grain growth phenomenon, which is inherently three-dimensional, could not be carried out experimentally for many years and only theoretically derived description has been proposed. Other key points of interest, as far as experimental approach is concerned, are: high financial costs of laboratory time, samples, preparation products, technical equipment as well as high risk of unsuccessful experiment resulting in unsatisfactory or pure quality data.

Therefore, apart from quite limited theoretical approach, an alternative research way has been demanded and looked for to describe evolution of microstructure and texture during thermo-mechanical, treatment and analyze fundamental physical processes connected with this evolution. The idea behind this new research way is to make use of possibilities given by more and more popular computer simulations, and

so various computer models have been proposed. It should be noted that general context as well as development conditions for such methods were very encouraging since computer computational power increases every constant period of time (18 months as described by the famous Moore's law [159]). In addition, progress in programming languages and libraries has facilitated significantly implementation of theoretical models in the form of computer simulations. As a result, a novel analysis tool has been given to explore phenomena studied in material science such as deformation, recrystallization and grain growth. What is really important is the fact that this tool offers exceptional research possibilities as in the field of simulation almost every hypothesis can be proposed, tested and compared with experimental results.

Abovementioned comparison is the best way in which computer models can be validated. However, in some cases, conclusions withdrawn from simulation were ahead the experimental one which means that simulations also may be a good inspiration for experiments.

Despite that fact, it should be emphasized that they are still just a strong approximation of the real physical process. Hence, they cannot be treated as engineering tool used to predict final microstructure and texture obtained after heat-treatment of any material. Much remains to be accomplished in order to bridge the gap between current research models and the future predictive models. Nevertheless, computer models have been successfully used and verified for simulation of recrystallization and grain growth. Therefore, they have gained recognition in scientific community as complementary method to experimentation.

In this connection, one of the main goals of this thesis is to explore and overview simulation approach in order to lay out and implement appropriate computer model which can be used for simulation of recrystallization and grain growth with a special attention paid on a hexagonal crystal symmetry of investigated material.

5.1 Overview of computer methods used to simulate primary static recrystallization and grain growth

There are different computer models specially tailored to simulate recrystallization process and related annealing phenomena. The variety of concepts and ideas staying behind these models is really impressive. Most of them have been drawn from physics, mathematics and computer sciences, and then appropriately adapted to

materials science context. From technical point of view, they can be distinguished between statistical, front-tracking (Vertex, Surface Evolver), final elements and discretized lattice models.

The latter is represented by very popular and most recognized models, such as Monte Carlo (Potts), Cellular Automata and Phase Field models, and so this group is the one which attract the most of interest in the subject of mesoscopic simulation of static recrystallization and grain growth since couple of years. However, it should be mentioned that recently the Surface Evolver and other front-tracking models have evolved enough to be a more suited approaches in particular cases of isotropic grain growth simulations.

Mentioned groups of simulation methods have been described and compared [4, 160–165]. Hence, only brief summary of the most popular approaches is presented further. It includes lattice based models: Monte Carlo (Potts), Cellular Automata and Phase Field as well as front-tracking models as reference.

In the first case microstructure is digitally represented by discrete lattice of sites. Such an approach allows to use EBSD maps directly as input microstructure for the model. Each site within the lattice can be found in one of the finite number of possible states which can be given simply by scalar value or more complex set of parameters. Grains are distinguished using sites with the same state, whereas grain boundaries are not explicitly mapped, and are considered artificially as interfaces separating the grains. Therefore, grain boundary motion in lattice models proceeds due to state change of sites adjacent to boundary area.

In Monte Carlo Potts model (labeled as MC), a concept of minimization of the global energy of the lattice site system is applied. The general rule can be included in formulation that in the behavior of the whole system, the site states leading to a reduction in the total energy of the system will be preferred. In practice, it is realized by random selection of sites which then are allowed to change its state in a probabilistic way. Therefore, appropriate transition function has to be defined. In the simplest case, the change is only accepted if lower energy is achieved in result. The energy is calculated on the basis of interaction with neighboring sites. From that point of view, it is clear, that stochastic elements are strongly involved in MC model.

The MC model is fast and straightforward in implementation, both in 2D and 3D. It is highly flexible, versatile and universal thus it can be used to simulate recrystallization, grain growth and many related phenomena as well. Moreover, it is popular and well documented. Simulation results can be thus quite easily compared

with the literature. Also, an open source programming code for MC grain growth model is distributed – Parallel Grain Growth 3D (PGG-3D) Software [www-GGsoft].

The Cellular Automata (CA) is another lattice based model. It is very similar to MC model as far as practical aspects are concerned and so both these models share similar advantages and disadvantages. Nevertheless, there is a significant difference between MC and CA models which lies in the general concept behind these methods. MC is clearly a stochastic model since it is based on the use of pseudo-random numbers and transition function given by Boltzmann probability. CA, in turn, is much more deterministic. It employs physically derived rules to determine propagation rate of simulated transformation process. Those rules in the case of recrystallization are specially designed to obtain appropriate relationship between boundary migration rate and driving force which entails the migration. In consequence, one of the practical differences between MC and CA models is the way how sites are updated. In MC model all sites have to be selected in a random fashion during one simulation step, which is time consuming, while in classical CA all sites are updated sequentially. This generally implies better efficiency favored to CA.

Both models have been compared in detail by Rollett and Raabe (2001) [166], and Sieradzki and Madej (2013) [167]. It is argued that classical CA allows a little better control of kinetics of recrystallization. Hence, it is well suited to deal with the influence of high stored energy as a driving force for boundary velocity. On the other hand, it turns out that curvature driven grain growth cannot be correctly simulated in CA due to the abovementioned update approach thus it has to be way round in a more complex way.

In the end, CA model has not gained so much attention and popularity as MC model. It seems to be also less universal in terms of variety of possible applications.

Phase Field model is greatly different in assumptions from the both above models. MC and CA are considered as sharp interface models due to the fact that grain boundaries are considered as zero thickness interfaces between discretized grains, whereas boundary motion is realized by jumping form transitions of particular site from one grain to another.

Phase Field model, in turn, is described as diffuse interface approach in which simulated domain is considered as continuum field variables system that continuously changes across grain boundaries. Grains in microstructure are thus described by different phase-field variables, depending on space and time, called order parameters, whereas grain boundaries are regions of smooth variation in order-parameter values.

Once an explicit expression for the free energy of the system is defined, the evolution of such system is simulated using Ginzburg–Landau type equations.

Unfortunately, in practice, it involves a large number of nonlinear differential equations to be numerically solved based on discretization method. Therefore, a lattice of sites is still needed. Moreover, it has to be lattice of high resolution since grain boundaries are not sharp anymore and only smooth gradients of order parameters are permitted in the model. As a consequence, high computational power is required as well as the number of simulated grains is not so large as in the case of CA and MC models, which means that statistical analysis of the obtained results may be harder to perform.

Recent developments of Phase Field model focus on reduction of order parameters to overcome this limitation. It should be noted that apart above description, there is also alternative approach referred as multi–phase field model.

One of the main disadvantages that results from lattice representation is high difficulty in precise calculation of local grain boundary curvature. Therefore, curvature-velocity relationship, known from grain growth rate theory, is not explicitly accounted. In alternative approach of front-tracking models the general idea is to focus on explicit representation of grain boundaries which then is used to simulate boundary motion under well-defined theoretical formulation. Therefore, such methods are in some sense complementary to lattice one, where the main accent is on the grain interior, whereas grain boundaries are implicitly introduced.

There are several models belonging to the category of front-tracking models. The main criterion to distinguish them is the way how precisely grain boundaries are represented by them. The basic 2D vertex model is considered as the simplest one. The grain boundary topology is approximated by network of vertices (or nodes). The main assumption of this model is that only vertices related to boundary intersections are considered, whereas the remaining part of the boundary is simply visualized using segments of straight lines. It means that in this approach local curvature of grain boundary cannot be adequately determined. Simulation is performed by a movement of vertices which is driven by physical equations derived for boundary junctions. In an improved approach, sometimes vertex name is also used, additional vertices are placed along the boundaries, and used for calculation of the curvature. This allows focusing on the movement of boundary segments in addition to the movement of boundary junctions.

In the case of more demanding 3D simulations, front-tracking models make use of further discretization, where grain boundary interfaces are approximated by basic

triangulation [168].

The final refinement step in representation of microstructure in front-tracking approach leads to application of complete finite element method thus grain boundaries can be represented mostly by triangular mesh. Such representation allows employing Surface Evolver method developed by Brakke (1992) [169] in order to simulate microstructure grain growth evolution driven by mean curvature motion [170]. Technically, the grain boundary surfaces are evolved to obtain minimal energy based on gradient descent method.

What is common for all these models is the fact that movement of grain boundary is accompanied by special topological transformations such as the recombination of triple junctions or shrinking and disappearance of grain. They are needed to be dealt with, otherwise proper simulation cannot be performed. Therefore, such situations have to be appropriately detected and solved.

This is the main difficulty for implementation, especially in 3D, due to the increasing number of the complex topological changes to be analytically defined and incorporated in the model. Another disadvantage lies in the fact that direct use of EBSD data, as an input, is rather impossible in this case. Such models are also not well suited for recrystallization, however, there are attempts to use it even in this case [171].

On the other hand, front-tracking approach has an advantage in grain boundary representation which, in connection with well-defined theoretical equations, gives the ability to capture up precisely the influence of grain boundary curvature as well as other topological features on grain boundary mobility. This is important for grain growth phenomena as it allows to simulate more realistic movement of the boundary.

Each of the mentioned models has its specific features, advantages and disadvantages, and so particular applications. Therefore, it is important to consider and point out strong and weak attributes of each of them. Also, as application development (logic, structure, implementation, testing) is demanding and time consuming process, it is more convenient to focus only on one model. Based on the above overview and other circumstances such as previous experience in programming Monte Carlo simulation, the Monte Carlo Potts model is chosen for implementation in this thesis.

5.2 Classical Monte Carlo Potts model

Fundamental publications of Anderson et al. (1984) [172] and Srolovitz et al. (1984, 1986) [173, 174] have become a milestone in the field of mesoscopic computer simu-

lation of recrystallization and grain growth phenomena based on Monte Carlo approach. This is clear when one simply takes a look on citations. Almost every publication in this domain contains references to their work.

The origin of inspiration for the MC model presented by Anderson is placed in physics, where Ising model has been invented to study ferromagnetism using discrete lattice of two-states spins (up or down spins). This method has been then simply extended on the case of multiple possible states of the spin which is referred as Q-state Monte Carlo model or, more commonly, the Potts model. It was a starting point when it has been realized that a domain of the same spin value in the Potts model can be treated like a grain in the microstructure. What is even more important, it has been noticed that the process of energy release during recrystallization and grain growth can be simulated similarly to the procedure used for energy minimization of the system in the Ising model which is realized on the use of Monte Carlo method and computers. The final step was to transform energy Hamiltonian of the Ising spins according to the needs of annealing phenomena.

The classical 2D Q-state Potts model is defined in the following way. The polycrystalline microstructure is represented by discrete lattice of N sites. Each site i is allowed to have couple of attributes. The most important is a number s_i, referred here as a spin, which corresponds to one of all Q possible orientations. The spin is the basis for grain-grouping algorithm. It means that neighboring sites of the same spin are considered as being within the same grain, whereas the rest of the sites have to be located in other grains depending on the spin. It should be noted that in such a view there is no possibility to precisely represent grain boundaries. Hence, they are treated as artificial interfaces or lines lying between sites of unlike spin (see Figure 5.1).

The MC method is based on the use of pseudo-random numbers generated in computer. In a simulation loop a lattice site is chosen in a random fashion, and then it is attempted to reorientation procedure in which the spin of the chosen site is changed. The new spin is randomly selected from the set consisting of all the spins that are different from the considered one. Reorientation procedure then leads to evolution of energy of sites system.

This is due to the fact that each site contributes energy E_i to the whole system. This energy, in the general case of recrystallization, consists of two terms, as shown in the below equation:

$$E_i = H_i + J_i. \tag{5.1}$$

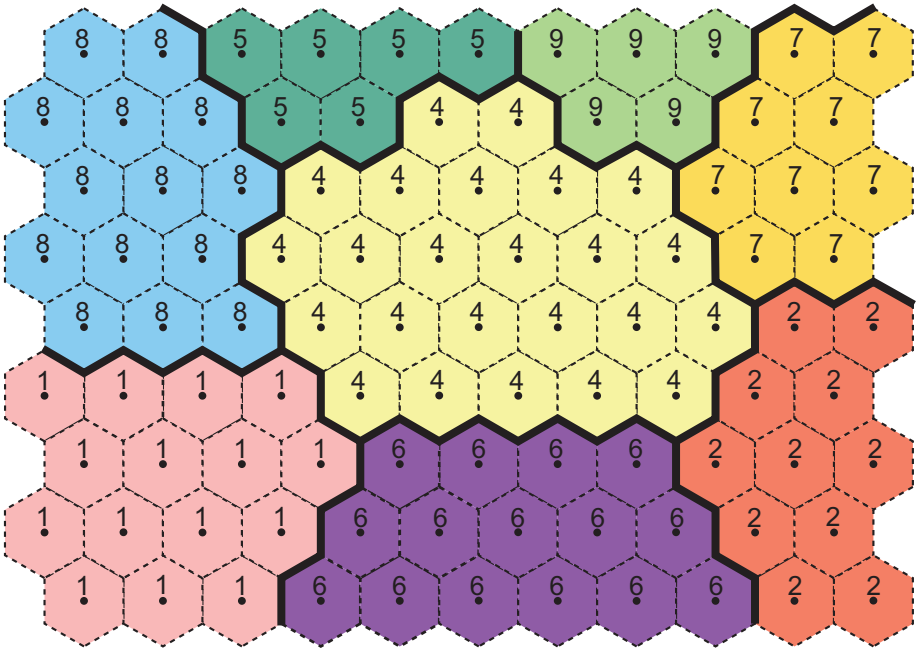

Figure 5.1: Example of hexagonal lattice of sites used in MC simulations. Note that each site is represented by hexagon. Black lines correspond to grain boundaries separating different grains which are distinguished based on spin values.

The first one, represented by H_i, is the stored energy normalized to unit area which is related to dislocation density at site i. If the site is deformed, the H is a positive constant, otherwise it is equal to 0. The second, represented by J_i, corresponds to the grain boundary energy which is considered as interaction between neighboring lattice sites thus it is expressed in the following way:

$$J_i = \sum_{j=1}^{n} \gamma\left(s_i, s_j\right), \tag{5.2}$$

where: n is the number of neighboring lattice sites, and $\gamma\left(s_i, s_j\right)$ is a parameter which should be proportional to grain boundary energy related to unit area between two sites.

However, it is assumed in a basic version of the model that $\gamma\left(s_i, s_j\right) = \delta_{ij}$, where Kronecker's delta function δ_{ij} is used to ensure that only unlike spins make an energetic contribution to grain boundary energy. Such definition of $\gamma\left(s_i, s_j\right)$ implies isotropic energy of grain boundary between different sites.

Based on that, total energy of the system E_{total} can be expressed by following equation:

$$E_{total} = \sum_{i=1}^{N} E_i = \sum_{i=1}^{N} \left(H_i + \frac{1}{2} \sum_{j=1}^{n} \gamma \left(s_i, s_j \right) \right), \tag{5.3}$$

where $\frac{1}{2}$ is due to double summation of the same elements: $\gamma \left(s_i, s_j \right) = \gamma \left(s_j, s_i \right)$.

Consequently, during MC simulation of recrystallization the energy difference ΔE, introduced by spin modification mentioned above, is calculated in the following way:

$$\Delta E = E_i^* - E_i, \tag{5.4}$$

where E_i^* is the new energy associated with the reoriented site.

According to the principle of energy minimization the reorientation is accepted if $\Delta E \leq 0$. In the other case, the spin is changed with the probability defined by Arrhenius function:

$$P = e^{(-\Delta E/kT)}, \tag{5.5}$$

where T is called lattice temperature or simulation temperature. However, despite the name, it is not related with temperature of simulated process.

Such probability allows site orientation to be changed as a result of thermal activation process thus kT term can be described as thermal energy of simulation.

Time in the MC simulation is given in Monte Carlo Step (MCS) unit which is arbitrary defined using number of reorientation attempts such that one MCS corresponds to N attempts.

Primary recrystallization is initialized thanks to nucleation. In the simulation, the nucleus of recrystallization is represented by site (or small groups of sites) for which stored energy is assumed to be 0.

There are two general ways to incorporate nucleation. Site-saturated nucleation is when all the nuclei are already located in the deformed microstructure, and the creation of new one is forbidden, whereas the other, named constant-rate nucleation, assumes that nuclei appear during annealing. Then, simulation is continued until all deformed grains are consumed.

In the case of pure grain growth simulation, input microstructure consists only of recrystallized, stored energy free grains. Hence, H is equal to 0 for all the sites as well as nucleation is omitted.

It can be found in some publications that calculation of energy difference is described by the use of full Hamiltonian in which energy of each of all the lattice sites

is added up. According to Equation 5.1 and Equation 5.2, energy assigned to each site is calculated on the basis of neighboring sites. It means that during each iteration, when only one lattice point is reoriented, the remaining sites do not contribute toward a change in energy. Therefore, mentioned Hamiltonian even if is an elegant definition of wholes system energy, is not used in practice.

Boundary conditions

As in many computational methods one needs to consider a method which deals with sites located at the boundary of the simulation box, which have to be treated differently than the internal one. In particular, how nearest neighbors should be determined in this special case. The most common approach is to use periodic boundary conditions, where neighbors missing due to finite dimensions of the lattice are respectively assigned from the opposite lattice side. In consequence, a grain located nearby one side of the lattice can interact with the grains located on the facing side.

3D model

One of the main advantages of the proposed MC model is a fairly simple extension to a 3D case, which is highly desirable since simulated phenomena are three-dimensional in their nature. In fact, MC model is independent from dimensions of space. It means that the algorithm is constructed in a way that allows separation of the model procedures from the lattice structure on which it works on. Software developer can write a general code responsible for simulation process which then can be applied to different lattices without additional modifications. Some difficulties can be encountered during preparation of 3D input microstructures rather than in MC model itself. It is, therefore, natural that Anderson et al. (1989) [175] have proposed a 3D MC model in a short time from first successful grain growth simulations of 2D microstructures, done by them.

5.3 On the development of Monte Carlo Potts model

Significant work, rich in new concepts and interesting ideas, has been done to modify and improve Monte Carlo modeling of recrystallization and grain growth. In fact, the present version is very different from Anderson's prototype. Therefore, there must be a good reason why the classical definition of MC model is recalled above instead of contemporary one, which is presented in the next chapter.

From one point of view, the introduction is more consistent if the description of classical version appears first as it facilitates to understand the close connection of MC model with Q-state Ising model mentioned at the beginning.

However, the most important advantage resulting from the above description is that it is a reference point which can be used to follow the way how the model has been evolving during last years. Hence, it is possible to analyze directly these model elements which attracted the most of scientific interest and efforts undertaken in order to overcome main weaknesses of the method. Such observation gives better understanding of the features and parameters of the modern version of the MC model as well as the knowledge about features which are still missing. This knowledge is then necessary when one has to develop and extend own simulation tools tailored according to special needs and particular applications.

5.3.1 Lattices

It is evident that lattice of sites is a fundamental skeleton for a whole Monte Carlo simulation. Hence, it is an issue of most the interest which has to be carefully implemented. Both, the structure of sites as well as the neighbor selection procedure need special attention since discrete nature of the lattice leads to non-physical effects, which can affect significantly simulation results. In the worst scenario, the structure of lattice is closely reflected in grain shapes as well as grain growth process can be even wrongly interrupted. The main problem comes from the fact that energy of grain boundary per unit length is anisotropic on the lattice and depends on surface angle [176, 177]. This in connection with the simulation condition of system energy minimization, realized by reduction of grain boundary length, results in tendency to place boundaries along lattice facets. Therefore, such effects of lattice-pinning have to be mitigated in the simulation.

There are two most common approaches used to minimize the influence of intrinsic lattice anisotropy [176, 178]. The first one is to include more interacting sites from, for example, second and third neighboring shell in grain boundary energy calculations as well as extending of the definition of the nearest neighbors in some particular types of lattice. The second one suggests to increase the simulation temperature in order to activate thermal fluctuations which, in turn, roughen the boundaries and introduce noise into the system. However, it should be noted that too high temperature may result in disordered system. More details about influence of this parameter as well as procedure to find optimal simulation temperature have

been presented recently by Zöllner (2014) [179].

There are two basic 2D lattices to be considered in MC simulations, the square one and the triangular one. Both can be extended to 3D lattice.

In the first case, the structure is much easier to implement. The simplicity of this solution, however, is paid with problems of high anisotropy, mainly caused by insufficient number of the nearest neighbors which is 4 (so-called von Neumann neighborhood). Therefore, additional neighbors are taken into account, as mentioned above, which results in optimal number of 8 nearest neighbors (so-called Moore neighborhood) in 2D and 26 in 3D, respectively. Such an approach seems to be slightly odd from general point of view since the distance between the central site and the nearest neighbors is varying, for instance in square lattice the distance from diagonal sites is $\sqrt{2}$ times higher than from side one. Nevertheless, it works well in MC model. More details concerning the influence of neighbor sites arrangement in cubic lattice can be found in the publication of Solas et al. (2004) [180].

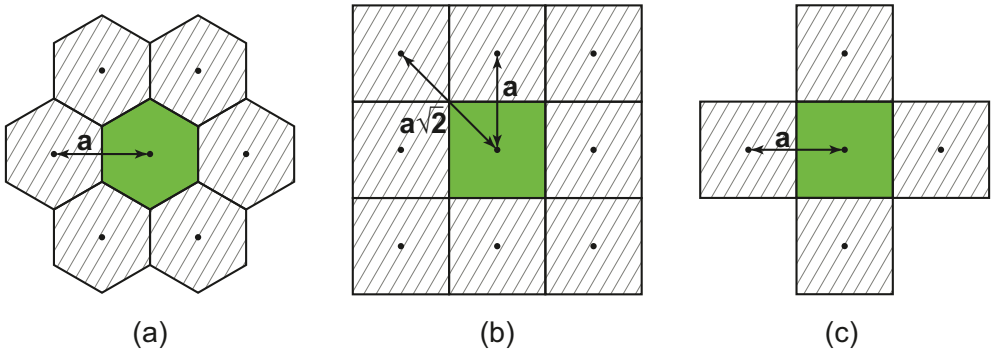

Figure 5.2: Nearest neighboring sites in the case of 2D hexagonal lattice (a), and 2D square lattice: von Neumann neighborhood (b), Moore neighborhood (c).

In the second case, the implementation is more difficult, especially in 3D, but, on the other hand, all the nearest neighbors are equally spaced. In addition, it is argued that triangular lattice is better suited to deal with grain boundary triple junctions. Nevertheless, pinning effect also occurs in this lattice which, in turn, may lead to inhibited grain growth. It has been also mentioned that construction of triangular lattice is complex in 3D, particularly determination of nearest neighbors can cause problem. Some studies in this field have been presented by Kim et al. (2005) [181].

It is generally concluded that if the uniform grain boundary energy is assumed, then triangular lattice is well suited for 2D simulation, whereas the cubic one with 26 nearest neighbors is a preferred one in three dimensions. Nevertheless, for special

purposes one may need to analyze the influence of lattices in order to find the most appropriate one. Some clues can be found in the publication of Rollet (1997) [162].

Regarding the question of lattice type to be chosen, it should be also noted that final decision may be enforced by format of experimental data, if such are used in simulation.

5.3.2 Code and efficiency optimization

The basic version of MC model is not optimized in terms of simulation time. This issue is crucial especially in 3D, where simulation containing large number of points is very time consuming, and so some limits of lattice dimensions had to be imposed. From another point of view, the construction of the classical modeling gives in some cases a rise to non-physical behavior of the system during simulation. For example, inappropriate probability function leads to unrealistic grain nucleation in another grain and disordered microstructure in a final result. Therefore, much attention has been paid on development of modifications which increase computational speed and can be physically justified at the same time [182–184].

Selection of the new orientation during reorientation step

During a reorientation attempt a new orientation is chosen from all the other orientations existing in the microstructure. Such approach applied in the first recrystallization simulations resulted in odd nucleation, unrealistic behavior and longer simulation time. Therefore, the algorithm can be improved in such a way that only local orientations are considered. It means that a new orientation is randomly taken from the one of these neighboring sites which are non-deformed ($H = 0$). The reason for such improvement can be found in the real grain boundary migration which is driven by movement of atoms from one grain to a neighboring one. In addition, a further modification has been proposed by Yu and Esche (2003) [183] to reduce list of neighboring orientations to those which are different from the one of attempted site.

Selection of the lattice sites subjected to reorientation attempt

In the classical MC model all the algorithm steps and calculations are always performed, no matter which site is chosen. This is obviously highly inefficient and unnecessary in most of the cases because simulation proceeds only due to reorientation of sites adjacent to grain boundaries, whereas orientation of sites inside the

grains cannot be changed. Hence, the algorithm should be continued only when grain boundary site is chosen [185]. Otherwise, selection of a new lattice site should be performed. As a fraction of grain boundary sites is much lower in comparison to grain interior sites, the number of algorithm steps is highly reduced thus simulation is significantly speeded up. This modification is also physically motivated and follows the mechanisms of grain boundary migration.

Parallel MC model

Significant increase in computational computer power has been gained using parallelization concept of coupling of several calculation cores, placed in processors or graphic cards, and so computational load can be shared between them. To take benefit from this method, the computer program has to be specially designed. In the case of Monte Carlo model such modification attempts have been already performed [186]. Two main approaches are known: the sub-domain one and the checkboard one [187]. Parallelization results in shorter simulation time which, in turn, allows to perform several MC simulation trials thus ensuring better statistics of obtained results.

5.3.3 Refinements connected with the physics and nature of the simulated phenomena

According to grain growth rate theory (chapter 2), the local velocity of grain boundary migration is assumed to depend on at least three factors, which are: grain boundary energy, mobility and curvature. It can be noted that none of them is explicitly defined in the first version of MC model. Despite that, it has been shown, on simple examples, that this model encapsulates physics of boundary motion in its nature. One of them is almost isotropic shrinkage of circular grain inserted in the center of uniform matrix, which is driven by grain curvature. In addition, kinetics law obtained in MC simulations obeys the theoretical one for isotropic grain growth. However, it is an important necessity to precisely incorporate parameters responsible for grain boundary motion in the model equations in order to perform more complex simulations and extend model applications in terms of modeled phenomena.

Euler angles

First of all, it has to be noted that simple approximation of the site orientation by scalar spin, dictated by computational limits in the past, is insufficient to model more advanced interactions between grains. Similarly, problems arise when orientation dependent stored energy distribution, local misorientations and orientation spread within the grains have to be taken into account. Therefore, it is more convenient to use dedicated definition of the orientation such as Euler angles (ϕ_1,Φ,ϕ_2) or any other equivalent.

Euler angles have this advantage that they are usually employed in experimental microtexture data. Hence, it is easier to import experimental microstructures into the model if Euler angles are implemented. The most important benefit of this approach is that it allows to directly calculate a misorientation between two sites, and thus to modify $\gamma(s_i, s_j)$ and introduce mobility parameter as explained in the next paragraph.

General refinements

More advanced version of the MC model incorporate Read–Shockley formula derived for low angle grain boundaries comprising of a regular array of dislocations [188]. Consequently, the energy of grain boundary separating sites i and j having spins: s_i, s_j and orientations: g_i, g_j is given by the following equation:

$$\gamma(s_i, s_j) = \gamma(g_i, g_j) = \gamma(\omega) = \begin{cases} \gamma_m \dfrac{\omega}{\theta_m}\left[1 - ln\left(\dfrac{\omega}{\theta_m}\right)\right] & ,\omega \leq \theta_m \\ \gamma_m & ,\omega > \theta_m \end{cases}, \tag{5.6}$$

where ω is misorientation angle between orientations g_i and g_j, whereas γ_m and θ_m are energy and misorientation of high angle grain boundary.

There is also grain boundary mobility parameter M to be included which is commonly approximated by relation examined by Humphreys (1997) [5]:

$$M(\omega) = M_m \left[1 - e^{-B\left(\frac{\omega}{\theta_m}\right)^n}\right]. \tag{5.7}$$

Please note that above equation was already discussed in chapter 2. Here, it is additionally noted that $B = 4$ and $n = 5$, also in this thesis.

Both relations for energy and mobility are shown in the Figure 5.3.

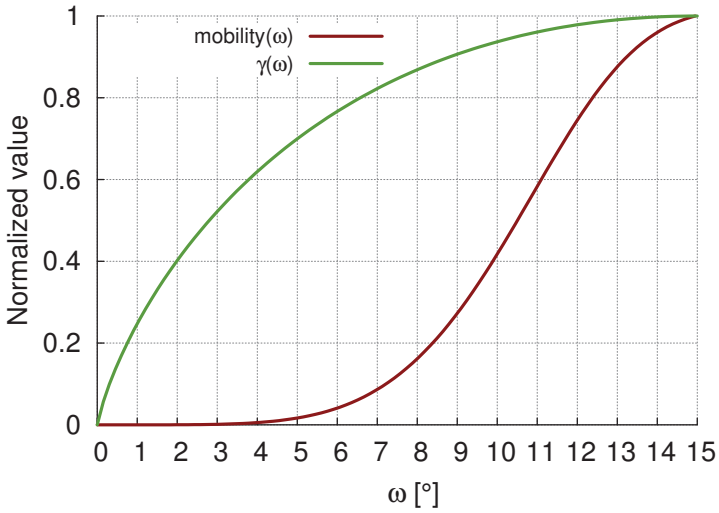

Figure 5.3: Grain boundary energy and mobility functions.

The presented boundary energy and mobility are important quantities that should be included further in the reorientation probability:

$$P = \begin{cases} \dfrac{M(\omega)}{M_{max}} \dfrac{\gamma(\omega)}{\gamma_{max}} & , \Delta E \leq \theta \\ \dfrac{M(\omega)}{M_{max}} \dfrac{\gamma(\omega)}{\gamma_{max}} e^{(-\Delta E/kT)} & , \Delta E > \theta \end{cases}, \tag{5.8}$$

where M_{max} and γ_{max} are maximal mobility and maximal boundary energy, respectively, used for normalization.

Based on this formula, it is clear that successful reorientation attempt depends strongly on the boundary misorientation. It has been also proposed to add another case in the expression (Equation 5.8), and thus change the probability from 1.0 to 0.5, when $\Delta E = 0$ [189].

Concerning recrystallization and nucleation processes, it is evident that even with this extended definition of transition probability, the driving force effect on grain boundary mobility caused by differences in stored energy is in fact not strictly incorporated. On the contrary, the corresponding probability function defined in the case of Cellular Automata model contains linear dependency of stored energy [166].

Therefore, it has to be kept in mind that MC model is limited in terms of possible stored energy values. If H/γ_m is too high, then ΔE is almost always below zero, and so the problem of unrealistically rough recrystallization front arises due to the fact that almost every reorientation attempt is accepted despite the topological

constraints. Introduction of additional parameter, so-called shape factor, seems to be some kind of solution in such case [190]. Another remedy has been proposed in the form of calibrated MC model [191].

On the other hand, if H/γ_m is too low, then nucleation and grain growth can be highly inhibited. Therefore, critical embryo sizes have been described according to a given lattice and neighboring sites since these both factors affect ΔE calculations [166]. In addition, the influence of H/γ_m on evolution of texture and microstructure in recrystallized copper has been examined by Tarasiuk et al. (2004) [149].

Anisotropy of grain boundary energy and grain boundary mobility

Normal isotropic growth of the grains leads to equiaxed microstructures, which are often observed experimentally. However, in many cases, significant anisotropy of grain growth may occur, mainly due to differences in energy between various grain boundaries. This effect is partially incorporated in the Monte Carlo model in the form of Read-Shockley potential, where non-constant energy is assigned to low angle grain boundaries. Still, all high angle grain boundaries ($\omega > 15^\circ$) are strictly isotropic since all of them have constant energies, which are typically equal to 1.

Therefore, further extensions and improvements of the model have been investigated to account energy anisotropy of grain boundaries. In particular, Holm et al. (2001) have changed the misorientation cut-off value between high and low angle grain boundaries in Read-Shockley formula to analyze misorientation distribution during simulation of anisotropic grain growth [178]. Similar approach has been presented by Yu et al. (2002) [192] and Hui et al. (2003) [193]. Ono et al. (1999), in turn, have modified Read-Shockley equation to include the effect of lower energy attributed to coincidence site lattice boundaries (CSL) in cubic metals [194].

On the basis of simulations presented by Yu et al. (2009) [195], it has been shown that despite various anisotropic energy potentials assigned to grain boundaries, grain size and grain shape distributions remain time invariant during grain growth as well as the kinetics of this growth is described by parabolic law, similarly to the isotropic case. However, different grain growth exponents as well as inhomogeneous and not-equiaxed microstructures are obtained due to increasing anisotropy. Allen et al. (2013) [196] have proposed another approach to estimate grain boundary energy which is based on Wulff plots.

Boundary energy is the first significant factor based on which it is decided in the model whether the chosen site can be reoriented or not. The second one is grain boundary mobility which in most cases is even more important as it was already

mentioned when Equation 5.8 was presented. Therefore, it should be emphasized that in standard MC model all high-angle grain boundaries have the same mobility equal to one. Such assumption seems to be rather unrealistic. The simplest way to overcome this problem is the modification of mobility equation, where a parameter has been added to ensure anisotropy of HAGB mobility [197]. Another way is to distinguish particular types of high angle grain boundaries in terms of mobility, similarly to the approach presented in the case of energy of CSL boundaries.

Fjeldbergand and Marthinsen (2010) have investigated the influence of anisotropy of both grain boundary parameters: mobility and energy [198]. They have analyzed grain size distributions resulted from simulations of several systems, each of them is different in terms of grain boundary properties starting from completely isotropic system, through mixed one and anisotropic system at the end.

Caleyo et al. (2002), in turn, have adjusted anisotropy of grain boundary mobility and energy in accordance with experimental observations in order to simulate recrystallization in Fe-50%Ni alloy [199].

In the publication of Ivasishin et al. (2003) anisotropy of the both described boundary parameters is also incorporated [200]. However, in this case, they are not considered separately thus effective mobility is proposed, and calculated on the basis of boundary energy.

Grain boundary inclination in 3D MC simulations

Since normal grain growth basically depends on grain boundary intrinsic properties, a need arises to mimic real motion of boundaries in the simulations. Unfortunately, complete information about all grain boundary parameters as well as their influence on grain boundary mobility is generally not available experimentally. Hence, strong approximations are imposed. The spatial orientation of grain boundary plane is completely neglected and only misorientation dependence is considered, as it is shown just above in the previous sub-paragraphs.

This was a motivation for Ivasishin et al. (2009) who developed a method of 3D microstructure analysis in order to determine geometrical relation between grain boundary plane and adjacent grains – so called grain boundary inclination [201]. This information is then included in their model in the form of effective mobility. Taking into account the inclination results, they have shown microstructure evolution similar to the one observed during texture-controlled grain growth.

Limited mobility of grain boundary junctions

In classical Potts model of normal grain growth it is assumed that movement of grain boundaries depends only on internal grain boundary parameters, whereas other factors connected with structural elements of grain boundaries topology are simply neglected. This assumption seemed to be valid for many years as there was no contradictory evidence from experiments. However, recent results concerning this topic emphasize that boundary migration kinetics can be significantly changed in some cases due to drag effect caused by limited mobility of the grain boundary junctions such as triple lines, triple points and quadruple points.

Such features of grain boundaries topology cannot be precisely incorporated in MC model since even the boundaries are not physically represented due to lattice basis. However, it is still possible to select small groups of adjacent points in the vicinity of real boundary junctions and modify their behavior to mimic function played by related boundary junctions.

Dana Zöllner has proposed a modification to Potts model [202, 203] which takes into account the influence of reduced mobility of particular grain boundary configurations on grain growth mechanisms occurring in nanocrystalline grain microstructures. Starting from different simulation conditions, parabolic, linear and exponential grain growth regimes have been observed depending on simulation time and the role played by triple junctions, respectively: classical grain growth driven by grain boundary curvature, grain growth driven by triple junctions and grain growth driven by quadruple points.

Physical parameters in MC simulation

One of the main objections against MC model is the lack of physical meaning of used parameters such as time, length or energy. All of them are dimensionless, which of course is a common approach in performing any computer simulation. However, the physical unit is not recovered in the final results. Few approaches have been proposed to find the link between MC parameters and SI model. For instance, MC kinetics has been scaled by Raabe (2000) according to rate theory [204], whereas Zhang et al. (2012) have developed calibrated MC model to account physical grain boundary properties obtained from experiment [191].

5.4 Monte Carlo simulation of recrystallization in titanium and zirconium

Monte Carlo method has been applied many times to investigate influence of annealing treatment on cubic materials, especially in steels, but also in copper or aluminum. However, in the field of simulations of recrystallization or grain growth taking place in hexagonal titanium and zirconium there are only few works on this subject in the literature.

Concerning cold-rolled commercially pure titanium, in comprehensive publication of Chun et al. (2006) [197] experimental data coming from EBSD technique have been used to simulate microstructure and texture evolution during the static recrystallization. Monte Carlo framework applied in this case included: stored energy estimation based on the IQ analysis, two nucleation mechanisms varying in terms of spatial distribution, incorporation of recovery process as well as anisotropy of grain boundary energy and mobility and, finally, strain-induced boundary migration model of recrystallization front movement. Several simulation conditions have been considered. It is concluded that site saturated nucleation, associated with the high stored-energy regions, which are heavily fragmented grains in this case, in connection with non-uniform stored energy distribution and anisotropy of grain boundary properties as well as possibility of recovery leads to results correlating well with JMAK kinetics obtained experimentally. Also, microstructure and texture evolution simulated using this model is equivalent to the real case.

Texture evolution in titanium has been also simulated by Sawina et al. (2007) [205]. However, in this case only grain growth is considered. Apart of Cellular Automata model, three dimensional MC model is used by the authors with synthetic microstructure as an input. It is noted that the number of grains in the simulated microstructure is decreasing during grain growth. Hence, to avoid the problem of reduced statistics a sequential approach is applied in which the microstructure is rescaled after each run. It means that current texture has to be statistically reassigned from the previous step. The question how it should be done is analyzed. This is a very important issue since initial texture associated with the microstructure is also statistically reproduced from EBSD measurements. Obtained results reveal the role of correlation between grain size and orientation. It means, for example, that orientations of the biggest grains in 3D microstructure should correspond to texture of the biggest grains in EBSD map. Only in this case simulated texture

evolution is reflected in the experiment.

Finally, Yang et al. (2000) have presented three dimensional Monte Carlo simulation applied in order to predict grain structure evolution in the complex case of GTA welded commercially pure titanium [206].

In the case of zirconium, Yu et al. (2005) have investigated microstructure evolution caused by equal channel angular pressing (ECAP) and further annealing [207]. Apart of experimental techniques – EBSD and X-ray texture measurements, they have employed Monte Carlo modeling as a complementary analysis tool. Changes of grain boundary misorientation angle distributions are accurately reproduced in grain growth simulation using EBSD data of recrystallized state as initial microstructure.

Seo et al. (2008) have pointed out that plastic deformation is highly heterogeneous. In spite of that fact, stored energy distribution cannot be uniform [208]. In particular, it should not be constant within grains. Also, a special role of grain boundaries in strain accommodation is emphasized. As a result, it has been assumed by them that stored energy changes gradually from very low values in the center of the grain toward the highest values associated with grain boundaries. Such situation is much realistic in cold-rolled zirconium, where orientation gradients have been observed inside the grains. Therefore, stored energy gradients have been defined and introduced to the MC model. This is a very interesting concept, which should be exploited further. Unfortunately, only recrystallization kinetics and grain size distributions are analyzed by the authors, whereas an influence of the proposed modification on microstructure and texture evolution is not further investigated.

5.5 Concluding remarks

Starting from first successful idea to combine Monte Carlo computer simulation with modeling of recrystallization and grain growth phenomena, significant work connected with further developments and improvements of run-time and accuracy has been done.

The presented journey over most important steps of the evolution of MC model indicates undying interest in this approach, and shows how much popular and acknowledged it is. In addition, there is still a continuous need to use and develop it further.

MC model is relatively simple in assumption and not too complex in implementation, and so it can be easily integrated with other computer models. Monte Carlo simulations coupled with Cellular Automata [166] or final element model of de-

formation [209, 210] can be mentioned as an example. Experimental data can be directly used as well, which is non-negligible since modern experimental techniques like EBSD allow to obtain real 3D microstructures.

It should be also noted that computational efficiency of the model is high enough to simulate large microstructures over long time intervals, which allows to statistically analyze the obtained data.

On the other hand, a problem arises from the fact that parameters which play the most important role in the MC model equations are difficult to measure experimentally. However, some theoretical efforts have been already undertaken to deal with this issue. The proposed model description of grain boundary energy and mobility seems to be a satisfactory solution in many cases.

Flexibility as well as many other advantages of the MC model entail wide spectrum of applications. In addition to static recrystallization and normal grain growth, related physical processes have been simulated in this way, such as dynamic recrystallization [162], anisotropic and abnormal (sub-) grain growth [178, 211], texture-controlled grain growth [200], influence of second phase particles [184,198] and Zener drag effect [212].

Despite many applications, the idea to use MC model in recrystallization and grain growth study of hexagonal metals has not been widely exploited yet, and so it is an interesting topic to be further explored.

CHAPTER 6

Implementation of Monte Carlo model

6.1 Simulation framework

COMPUTER modeling of recrystallization involves several steps to be performed. In fact, appropriate development, implementation and testing procedures of Monte Carlo model are one of the elements necessary for simulation approach. It means that there are also other simulation elements to be considered and developed. MC model constitutes the core of the final program, whereas input microstructure, analysis and input-output algorithms as well as visualization tools are the surrounding layers. All of them have to match exactly and stick together in order to accomplish a simulation investigation. Therefore, the most important simulation elements are discussed in the following text.

6.1.1 Input microstructure

Preparation of realistic microstructures for MC simulation is a difficult and demanding task, especially in 3D. The most common ways to deal with this problem can be divided into experimental microstructures and synthetic (or simulated) microstructures.

In the first case, EBSD maps are used as real starting microstructures [147, 157, 197, 199, 213]. Hence, it allows exact description of real material texture and microstructure to be included in the simulation. This is important for the simulation of primary recrystallization to be performed with realistic conditions, where EBSD

data can be used to estimate stored energy distribution. Certainly, such an approach gives an exceptional possibility to compare, in detail, simulations with experimental observations.

Moreover, this method is simple and straightforward in 2D, where EBSD data are almost ready to use in the model. 3D case, in turn, needs much more attention due to difficulties on the experimental part. However, the development of FIB-EBSD technique greatly facilitated experimental measurements of 3D microstructures which are obtained by reconstruction from series of 2D sections [122, 123] (chapter 4).

In the second case, computer simulation methods have to be employed to generate the microstructure. Such situation is common when necessary information can be taken only from the literature, or when only 2D EBSD data are available, whereas 3D simulation has to be performed. The main motivation behind such cases comes from the fact that a synthetic microstructure, which reflects in statistical manner some of the most important material parameters like texture and grain boundary misorientations, can sufficiently approximate the real microstructure. For instance, Miodownik et al. (1999) have developed an algorithm to map desired texture and grain boundary misorientation functions into 3D equiaxed microstructure obtained from Monte Carlo grain growth simulation [214].

One step further goes a method proposed by Saylor et al. (2004) [215] and improved then by Brahme et al. (2006) [118]. This method makes use of packing of ellipsoids, representing 3D grains, combined with Voronoi tessellation to reconstruct statistically representative 3D microstructure from two perpendicular EBSD cross-sections.

Another method in the synthetic approach is connected with crystal plasticity and finite element models which, in result, can provide deformed microstructures for the MC model [216, 217]. What is relevant, is the fact that such models predict stress states and dislocations density thus stored energy can be estimated and used in MC simulation.

In all the abovementioned methods, the microstructure is generated to substitute the experimental one. However, there are investigations where synthetic microstructure is used on purpose. For example, evaluation of theoretical description concerning isotropic grain growth phenomenon is done using equiaxed synthetic microstructures with random texture.

It should be noted that in such a case MC model itself can be used to generate simple initial microstructure due to the fact that grain growth simulation of completely random system leads to microstructure comprising of equiaxed grains.

Finally, synthetic approach is well suited and commonly used for procedures testing the MC model.

Both presented cases are used in this thesis. EBSD 2D maps obtained from an experiment can be directly imported to MC model, whereas synthetic microstructures can be generated using either Dream3D software [218] or simple grain growth procedure.

6.1.2 Grain reconstruction algorithm

Generally, once the microstructure is prepared, it has to be analyzed first in terms of grains structure. Therefore, special algorithm is needed to reconstruct grains based on the information stored in lattice sites. This important procedure is frequently used to calculate number of grains as well as grain size distribution. Both are necessary to investigate grain growth kinetics. Moreover, in advanced Monte Carlo models an information about site location is required, whether it is inside grain interior or nearby grain boundary.

To reconstruct the grains an algorithm similar to flood-fill or seed-fill methods in computer graphics is used. It is assumed that there is a lattice site attribute which allows to distinguish the grains. It can be an orientation given by Euler angles or just an integer value such as spin described in the classical version of MC model.

The algorithm consists of following steps, presented below, which are performed during a loop over all lattice sites.

1. For a given site s it has to be firstly checked if it is already assigned to one of the grains. If not, a new grain g is created with s site inside. Otherwise, further steps are omitted and next site in the loop is analyzed.

2. Information about nearest sites neighboring to s is collected. Then it is decided which of the neighbors should be assigned to the grain g. The most common criterion is misorientantion value between s and the neighbor: all the neighbors with misorientation lower than arbitrary chosen threshold (typically 15°) are added to the grain. The alternative solution is to compare spins. In this case, neighbors with the same spin as the s site are included. It is important to notice that neighbors which are already inside the grain g, as a result of previous iterations in the loop, should not be added again.

3. If there are new sites, which were added in the previous step, then the step 4 is executed. In the opposite case, grain g is completely reconstructed thus

next iteration in the algorithm loop is performed.

4. Operations analogous to those from the step 2 are applied to all the new sites. The purpose of this step is to find a next group of new sites assigned to the grain. When it is finished, the algorithm goes back to the step 3.

6.1.3 Input/Output procedures

From the viewpoint of data treatment, computer models are usually described as "black boxes" equipped with input and output connections. The only role of end-user is to provide input data and analyze the outcome. Hence, no knowledge about internal procedures of the model is needed. This is why a good simulation framework should contain a wide range of input/output procedures. Also, the more input file formats that can be imported, the easier to apply and more universal model is.

Following input/output operations have been implemented:

- import and export of EBSD data in the form of *osc* and *ang* file formats,
- import and export of Euler angles,
- import and export of configuration files, used to control the MC model and entire simulation framework,
- import of input microstructures generated by Dream3D software,
- export of microstructures in *vtk* file format,
- export of information about process kinetics,
- export of log files containing messages such as errors or warnings and other informations generated by simulation procedures.

6.1.4 Implementation of MC model

The MC model developed in the thesis has been implemented using C++ programming language combined with object-oriented paradigm and design patterns. Briefly, abstract class is used to represent object from real life, its state, behavior and interaction with other objects. The main purpose behind this idea is to provide a way for easier maintenance, evolution, testing and better reusability of code structure of an application. Therefore, the obtained C++ code of MC model is efficient and

flexible at the same time. In addition, OpenMP interface [www-OpenMP] has been employed to improve the efficiency even further thanks to program parallelization.

On the basis of the overview presented in the previous chapter, following features of MC model have been considered.

1. Remind that developed MC model has to be applied in particular case of hexagonal metals. The main purpose is thus to analyze texture and microstructure evolution during recrystallization and grain growth in these metals, whereas kinetics of these processes is not a key point of interest. From that point of view, only the most relevant refinements presented in the previous chapter are incorporated. Also, all the optimizations of code efficiency and some of the physics modifications are included.

2. The most general version of MC model consists of several simulation steps which are: recovery, nucleation, recrystallization and grain growth.

   a) Recovery is neglected in this model. However, if there is a suspicion that strong recovery occurs in the simulated material, an appropriate input microstructure is used to account for this effect.

   b) The nucleation phenomenon is usually necessary in MC model to start simulation of primary recrystallization. It can be simply implemented. Stored energy of lattice site, which is considered as a candidate for being a nucleus, has to be zero. Depending on desired nucleus size, additional neighboring sites may be taken into account. Obviously, such definition of nucleus is different from the real one due to size inconsistency. The nucleus in the model has at least few micrometers, whereas the real one has barely few nanometers. Therefore, it is difficult to observe it experimentally. Nevertheless, the nuclei in the model can be treated as small grains emerging from the real nuclei.

   c) As mentioned in the previous chapter, there are two possible nucleation mechanisms: site saturation and constant rate. Nucleation in this model is imposed to be governed by site saturation mechanism, which means that all the possible nuclei have to be present in the microstructure before simulation starts. Despite this important choice, there are still several ways to perform this process. It has to be considered what the preferable place for nucleus is. For example, it can be a random position, position close to grain boundaries (particular types can be imposed here) or areas

of the highest (smallest) stored energy. The other question is the orientation of nucleus. It can be inherited from a site that became the nucleus or from one of its neighbors, or even randomly chosen from all the possible orientations in the lattice. Mixing all of these conditions leads to many possible ways of nucleation to be simulated.

d) Recrystallization and grain growth are usually separated. It means that grain growth is assumed to start once recrystallization is finished. On the other hand, it does not have to be the only one solution. Such processes may proceed simultaneously. These both mechanisms can be investigated in this model.

3. Square 2D, triangular 2D, cubic 3D and triangular 3D are the possible lattices to use. In addition, different nearest-neighbors arrangements have been incorporated such as von Neumann and Moore neighborhood.

4. Each site lattice has several attributes, the most important are:

   a) orientation given by Euler angles,

   b) stored energy,

   c) position in the lattice given by integer numbers,

   d) position in the real space,

   e) site id,

   f) id of a grain to which site is assigned.

5. Grain boundary energy is calculated using Read-Shockley equation. Different ranges of neighboring sites can be taken into account.

6. Grain boundary mobility is calculated according to Humphrey's relation.

7. Anisotropy of HAGB properties, if necessary, can be simulated.

8. A novel analysis of grain boundary curvature is also proposed in order to facilitate Monte Carlo modeling (see more details in the next chapter).

9. General algorithm of the MC model, that has been elaborated on the basis of the above assumptions, is schematically described using block diagram presented in the Figure 6.1.

10. Three different situations can be simulated:

- pure recrystallization; apart of nuclei, all sites are deformed thus the stored energy is higher than 0 ($H \neq 0$),
- pure grain growth; all sites are recrystallized therefore they do not possess the stored energy ($H = 0$),
- simultaneous recrystallization and grain growth.

11. Hence, main loop condition, used to decide whether simulation is continued or stopped, may be defined in one of the following forms:
    a) if material is completely recrystallized,
    b) if number of grains reached desired value,
    c) if average size of grains reached desired value,
    d) if number of MCS reached desired value.

There are two major versions of the MC model developed in this thesis. The first one is presented above. The second one incorporates modifications proposed by Yu and Esche (2003) [183]. There are three of them, namely: modification I, modification II and modification III.

Modification I is already included in the basic version of the model. Briefly, sites that are inside the grain cannot be attempted for reorientation.

According to modification II, during reorientation attempt only those neighboring orientations should be considered, which are different from orientation of selected site. This implies faster simulation since probability of successful reorientation is greatly increased.

Modification III concerns the way how sites are chosen from the lattice. It turned out that classical MC model allows multiple selection of one lattice site during one MCS. It means that some of the sites are attempted multiple times for reorientation, whereas the others not at all. To overcome this problem at least two solutions are available.

The first one utilizes a vector which at the beginning of every MCS has to be filled with all lattice sites. Once site is randomly chosen from the vector, it is removed from this container thus it cannot be chosen again.

In the second solution sites have Boolean flag that describes its state: already chosen or not chosen. At the beginning of every MCS all the sites are not chosen. During MCS a site can be selected only if it is permitted by its Boolean flag.

These both solutions have been implemented. However, only the second one is used as it is the faster one.

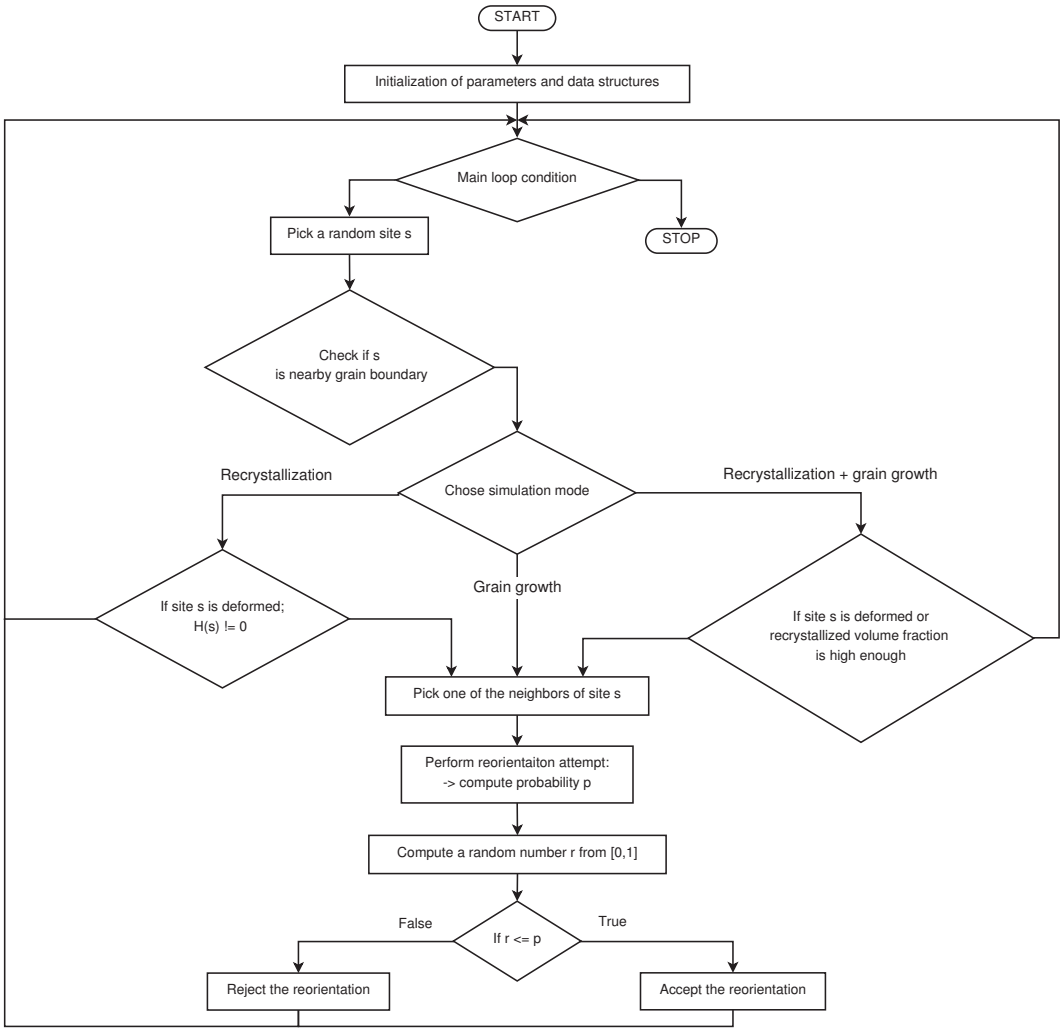

Figure 6.1: Block diagram of the algorithm used for simulation of recrystallization and grain growth.

6.1.5 Structure of main program classes

Implementation of the MC model in the form of C++ application appeared as rather extensive project which has involved thousands of code lines. Therefore, more details about the developed software, including UML diagrams as well as list of classes and functions, can be found in the online documentation published on the Internet [www-Documentation].

6.1.6 Graphical User Interface

A GUI application has been developed to facilitate the maintenance and control over simulation steps and parameters (Figure 6.2). The idea is to represent these parameters in user-friendly form with additional help description. All the simulation settings chosen by user can be then saved to configuration file, which, in turn, is imported into the simulation application. Another benefit of this approach comes from the fact that after many simulation trials each of them can be checked out by the user in terms of applied settings. It can be done using the presented GUI application by loading a configuration file. After that, all the settings stored in the configuration file will be shown.

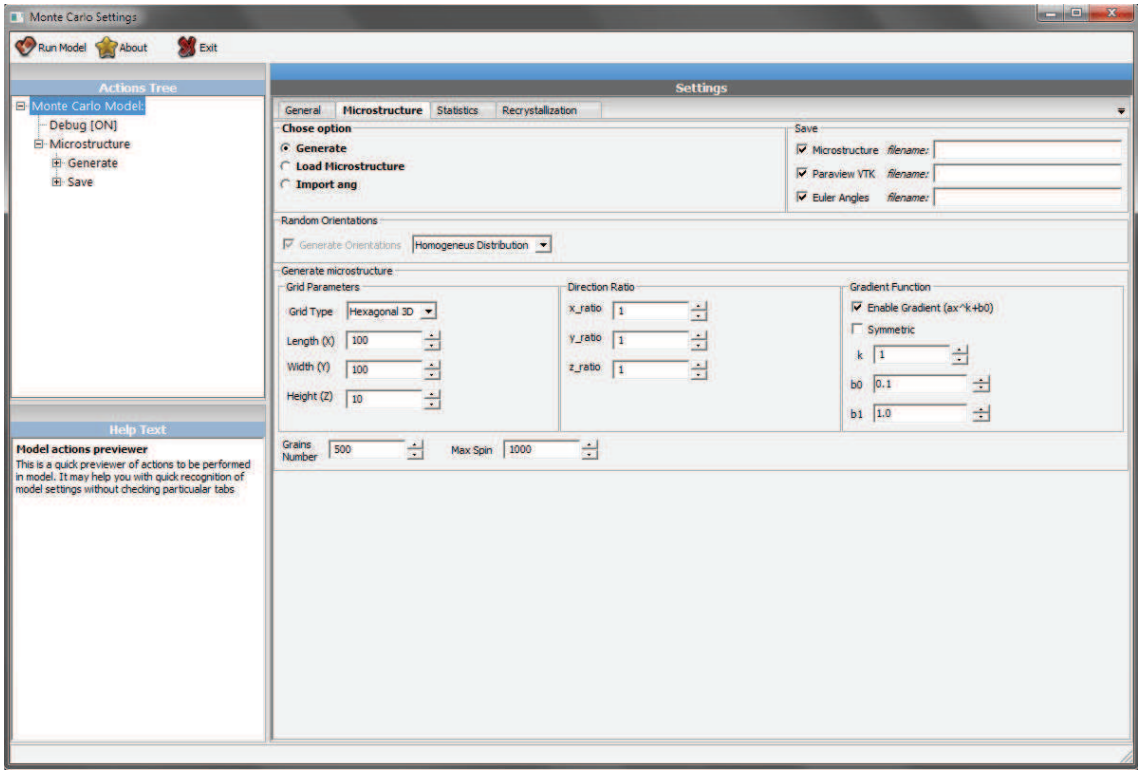

Figure 6.2: Graphical user interface developed to facilitate MC simulations.

6.1.7 Visualization and analysis of the microstructures

Microstructures obtained during simulation can be exported in EBSD data formats or in *vtk* file format. The first one provides a possibility to present and analyze the results with dedicated TSL^{TM} OIM Software [www-OIM], whereas the second is used for visualization and graphical treatment. This is important in 3D, where the microstructure can be rotated, sliced, thresholded, clipped and so on. For instance, the freeware Paraview software [www-Paraview] can be used for that reason. Unfortunately, working with large number of simulated microstructures is rather inconvenient in this program. Also, it turned out that some functionality dedicated to the author needs is still missing.

Therefore, own visualization program has been developed by the author. The main advantage of this software is the ability to show particularly chosen grains using either points or smoothed surfaces. The main parameters to be used for the grains separation are: the stored energy and the grain id. Figure 6.3 presents an example of microstructure visualized in this program.

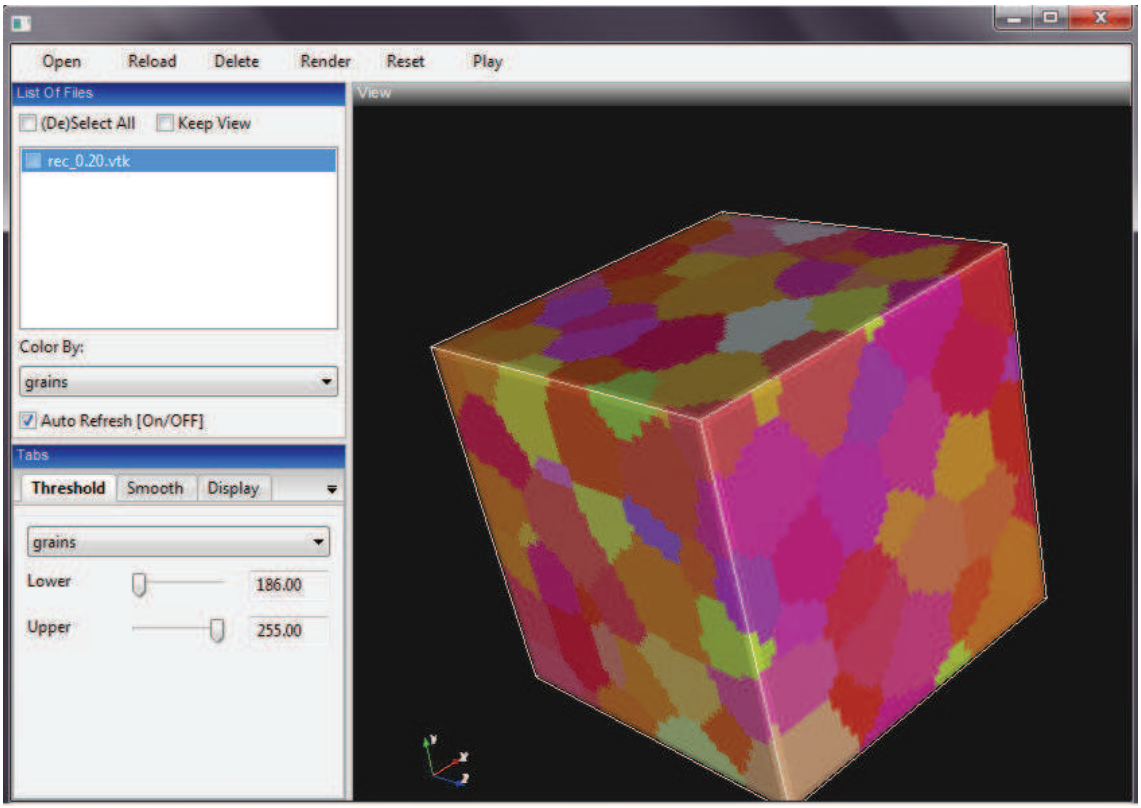

Figure 6.3: Software developed to visualize simulated microstructures.

6.2 Testing procedure of the developed MC model

The developed MC Potts model has been verified using synthetic tests which are linked with isotropic grain growth theory and primary recrystallization theory: parabolic law and JMAK model, respectively. It means that testing procedures are designed in such a way that they allow to reproduce behavior predicted by both these models. Based on that, it is possible to check if the Potts model is correctly implemented as well as to analyze the impact of the most important model parameters on simulation results. In all the following tests grain boundary energy and mobility are always equal to 1.0 according to the abovementioned assumption of GB isotropic properties.

6.2.1 Shrinkage of isolated circular grain in 2D microstructure

One of the most commonly used tests relies on the analysis of shrinkage of one grain which is placed in the center of infinite matrix. Since the boundary of this grain is convex and equally spaced from the grain center, it is expected that it will collapse evenly during grain growth process until it disappears completely. It means that the grain area should decrease linearly in time hence a decrease of the grain radius should be given by square root function. However, a deviation from this behavior should be also expected due to the lattice effects as well as simulation temperature. The impact of these parameters is one of the major key points to be investigated in the following simulations.

Generally, the radius is calculated on the basis of grain area. Such definition can be insufficient in some cases. It has been observed that despite a correct decrease in grain radius (or grain area), the overall shrinkage is not isotropic. This is a situation when the center of decreasing grain is shifted from the center of the lattice. Therefore, another parameter d_{GB} is proposed in order to show such a process. This parameter is defined as average distance between grain boundary points and the center of the lattice. It means that d_{GB} value is different from 0 if the grain did not disappear exactly in the center of the lattice.

Simulation 1: Influence of the lattice

Settings:

- different lattice types:
  - square with 4 nearest neighbors (square-4),
  - square with 8 nearest neighbors (square-8),
  - hexagonal with 6 nearest neighbors (hex-6),
- different lattice resolutions:
  - 50×50 sites; initial grain radius = 20,
  - 500×500 sites; initial grain radius = 200,
- $kT = 0$.

Results. For each lattice, three curves are presented: d_{GB}, R and R_{TH}. First two correspond to decrease of d_{GB} or R parameter over simulation time, whereas R_{TH} is presented as a reference since it corresponds to decrease of radius calculated according to the theoretical model.

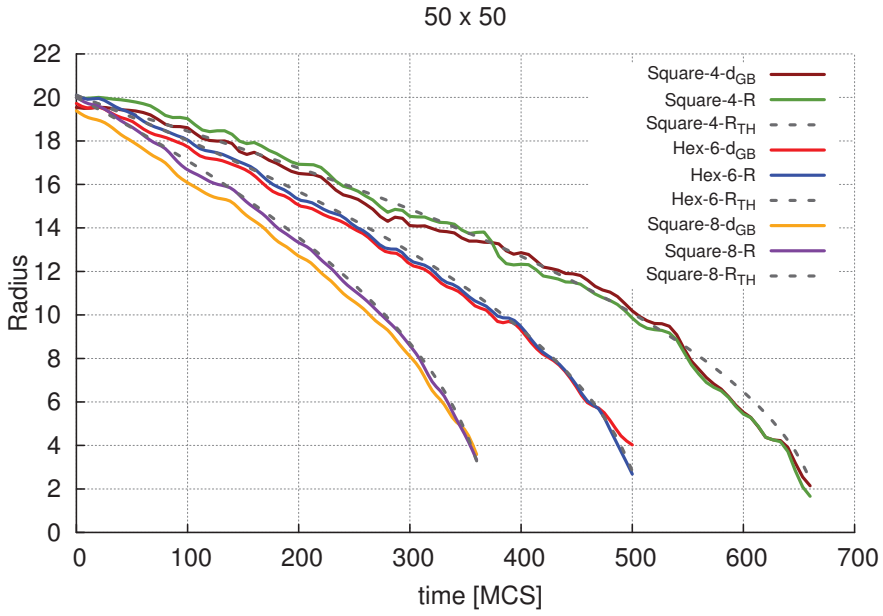

Figure 6.4: Shrinking of isolated grain depending on the used lattice (resolution: 50 x 50).

In the light of the results presented in the Figure 6.4, it can be concluded that in the case of lattice having small resolution (50×50) the difference between simulated and theoretical curves are clearly noticeable. For the square lattice with 4 nearest neighbors the differences between simulated grain shrinkage and isotropic one are the highest. Also, application of this lattice results in the longest simulation time. That is why it should rather not be used in the MC simulations. Hexagonal-6 and square-8 lattices, on the other hand, give similar and much better results.

Much higher resolution of the applied lattice (500×500) leads to almost ideal curves (Figure 6.5) which are almost the same as for the theoretical shrinkage. Again, square-8 lattice seems to provide the best outcome.

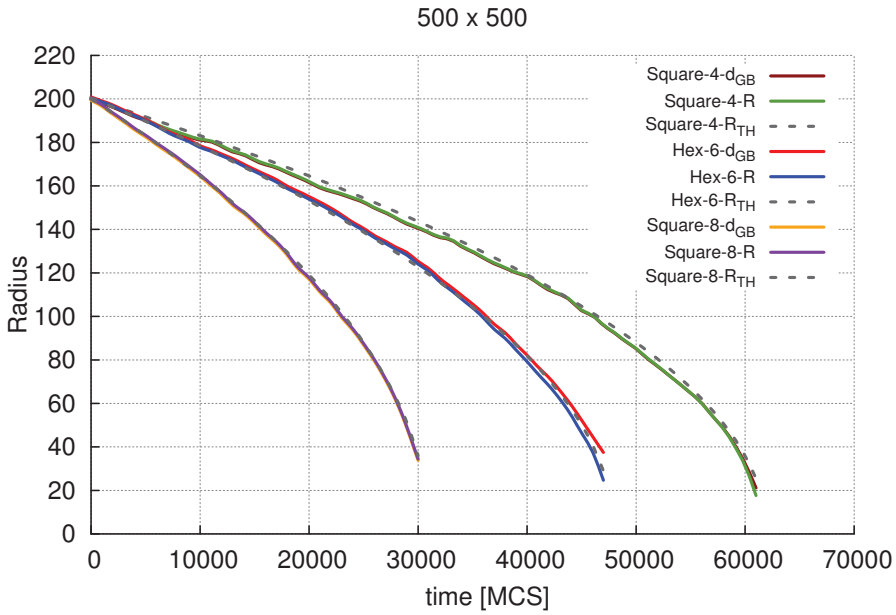

Figure 6.5: Shrinking of isolated grain depending on used lattice (resolution: 500x500).

To compare quantitatively these two lattices, following estimators are introduced:

$$S_{R1} = \sum_{i=1}^{N} \frac{|R_i - R_{THi}|}{R_{max}}, \qquad S_{R2} = \sum_{i=1}^{N} \frac{|R_i - R_{THi}|}{R_{THi}}, \tag{6.1}$$

where R_{max} is initial grain radius, R_i, R_{THi} are the values of these radii at i-th MCS, and N is total number of MCS.

Based on the proposed parameters, following comparison of investigated lattices

is presented in the table below.

Table 6.1: Quantitative comparion of lattice induced anisotropy in the simulation of isolated grain shrinkage. The final result for each lattice is averaged over several simulation trials.

Lattice	S_{R1}	S_{R2}
Square-8-50x50	0.015	3.72
Hex-6-50x50	0.017	3.99
Square-4-50x50	0.021	5.08
Square-8-500x500	0.008	0.07
Hex-6-500x500	0.008	1.26
Square-4-500x500	0.011	1.95

Simulation 2: Influence of the simulation temperature

Settings:

- lattices:
  - square with 8 nearest neighbors (square-8),
  - hexagonal with 6 nearest neighbors (hex-6)
- lattice resolution: 250×250 sites; initial grain radius = 80,
- various kT values: 0.0, 0.5, 1.0, 2.0, 5.0.

Results. Increasing simulation temperature is one of the solutions which is used to deal with lattice anisotropy. As a result, grain boundary becomes more and more rough. However, too high temperature can introduce disordering behavior in the simulation.

A good example of such situation is shown in the Figure 6.6, where R and d_{GB} curves obtained for $kT = 5.0$ are significantly different from the isotropic grain shrinkage. Also, in the case of hexagonal lattice the grain center is highly shifted from the center of the matrix, especially at final shrinkage stage.

Moreover, hexagonal and square lattices have been also compared using the introduced S_{R1}, S_{R2} parameters, which are computed for simulations varying in terms of kT value (see following Table 6.2 and Table 6.3).

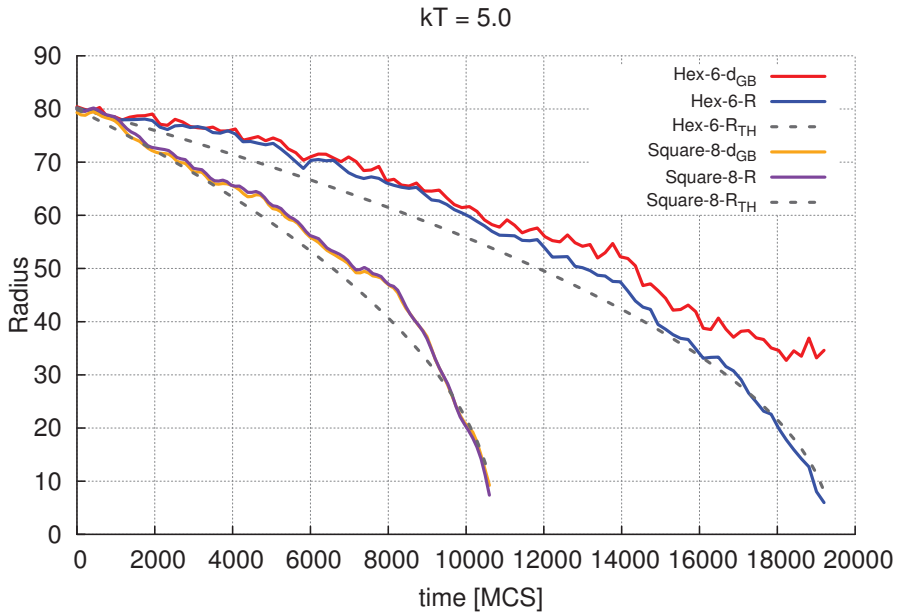

Figure 6.6: Shrinking of isolated grain influenced by high lattice temperature ($kT = 5.0$).

Table 6.2: S_{R1} calculated for different lattices and kT values.

	$kT = 0.0$	$kT = 0.5$	$kT = 1.0$	$kT = 2.0$	$kT = 5.0$
Square Lattice	0.012	0.009	0.010	0.013	0.030
Hexagonal Lattice	0.016	0.011	0.013	0.015	0.035

Table 6.3: S_{R2} calculated for different lattices and kT values.

	$kT = 0.0$	$kT = 0.5$	$kT = 1.0$	$kT = 2.0$	$kT = 5.0$
Square Lattice	3.41	1.66	2.17	2.74	6.02
Hexagonal Lattice	3.87	1.67	2.54	3.39	6.21

Finally, the difference in roughening of grain boundary, caused by different kT values, is qualitatively presented in the Table 6.4 for the both investigated lattices.

Table 6.4: Shape of the shrinking grain influenced by various kT values.

	$kT = 0.0$	$kT = 1.0$	$kT = 5.0$
hexagonal lattice			
	$t = 4800$ MCS	$t = 8200$ MCS	$t = 15200$ MCS
square lattice			
	$t = 1800$ MCS	$t = 3800$ MCS	$t = 8200$ MCS

Conclusion.

On the basis of the considered results, it is shown that curvature driven shrinkage of one grain is correctly simulated using the developed model. It can be also concluded that higher resolution of applied lattice provides more reliable results. Moreover, simulation temperature and lattice type are important factors which need to be carefully adjusted.

Presented calculations of S_{R1}, S_{R2} parameters (Table 6.2, Table 6.3) suggest that square lattice with 8 nearest neighbors is the one that possesses the lowest intrinsic anisotropy, which is consistent with the results already published in the literature (see chapter 5). However, it has to be kept in mind that this conclusion is based on very simple test thus a more detailed analysis of lattice impact, especially in terms of grain shape, has to be performed in the case of more advanced applications.

6.2.2 2D grain growth of random microstructure

Next step in the validation of the implemented model is to start much more advanced test, in which interaction between various grains is allowed. Therefore, 2D non-textured microstructure, which comprises of small equiaxed grains, is synthetically prepared and then used as an input for isotropic grain growth simulation (Figure 6.7).

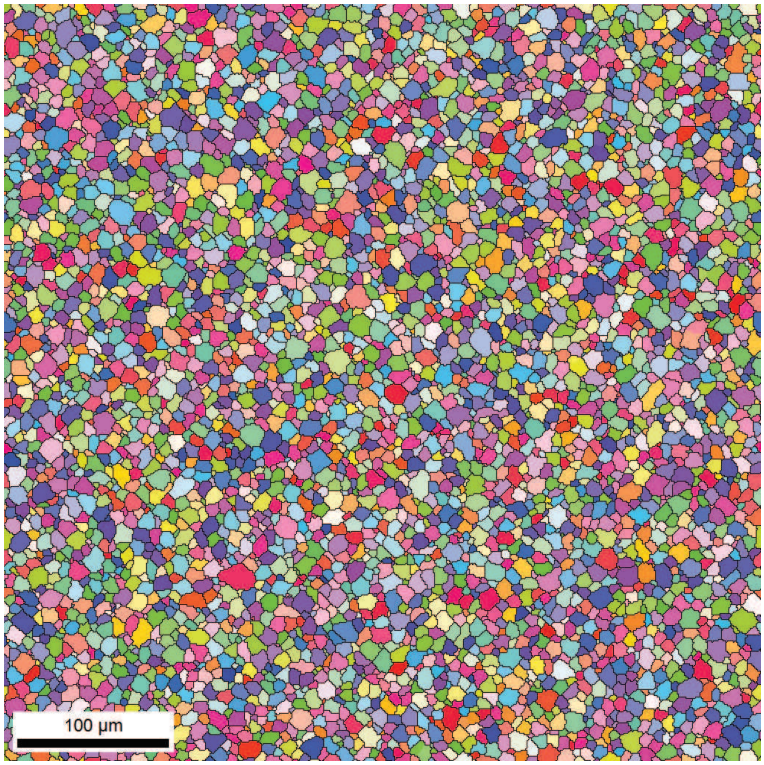

Figure 6.7: Initial synthetic microstructure used for 2D grain growth simulations.

A linear increase of average grain size as well as self-similarity character of grain size distributions is expected over time. In addition, texture should remain random.

Simulation 1: Influence of the lattice, neighboring sites and temperature

Similarly to the previous tests, the influence of lattice type and simulation temperature is investigated. In addition, another type of test is presented, where extended number of neighbors is taken into account during calculations of boundary energy in order to overcome lattice effects.

Settings:

- lattices:
  - square with 8 nearest neighbors (500×500 sites) – square-8,
  - square with 4 nearest neighbors (500×500 sites) – square-4,
  - hexagonal with 6 nearest neighbors (500×577 sites) – hex-6
- various kT values: 0.0, 0.5, 1.5, 2.0,
- number of neighbors considered during calculations of boundary energy:
  - 8; square-8-8,
  - 24; square-8-24,
  - 4; square-4-4,
  - 6; hex-6-6,
  - 17; hex-6-17,
- simulation is stopped when number of grains is less than 100.

Results. From general point of view, it can be concluded that almost all of the obtained curves, shown in Figure 6.8 and Figure 6.9, which present dependency of average grain area versus simulation time, are approximately linear functions.

This is also quantitatively confirmed by the linear correlation coefficient, which is higher than 0.99. Therefore, only small oscillations around linear trend can be noticed, especially after longer growth when number of grains is highly decreased.

Square-4-4 configuration is the only exception. In this case, the curve is flat, while the linear correlation coefficient is equal to 0.26.

Regarding grain growth kinetics, a significant difference between obtained results can be noticed in terms of applied lattice. Clearly, more time is needed to finish simulation if hexagonal lattice is used than in the case of square-8 lattice, whereas in the case of square-4 lattice the grain growth process is inhibited so much that it is eventually stopped.

Moreover, it can be stated that grain growth rate can be significantly increased if more sites are taken into account in the procedure of boundary energy calculation. For both considered lattices, simulation time is almost two times shorter in comparison to the standard case.

Finally, based on the provided figures, it appears that temperature impact on grain growth rate is relatively low. All the simulations performed with kT less than 1.0 result in very similar kinetics. This may be explained by high resolution of the lattice, which means that at lower resolutions growth kinetics can be more noticeably affected by the high value of kT factor.

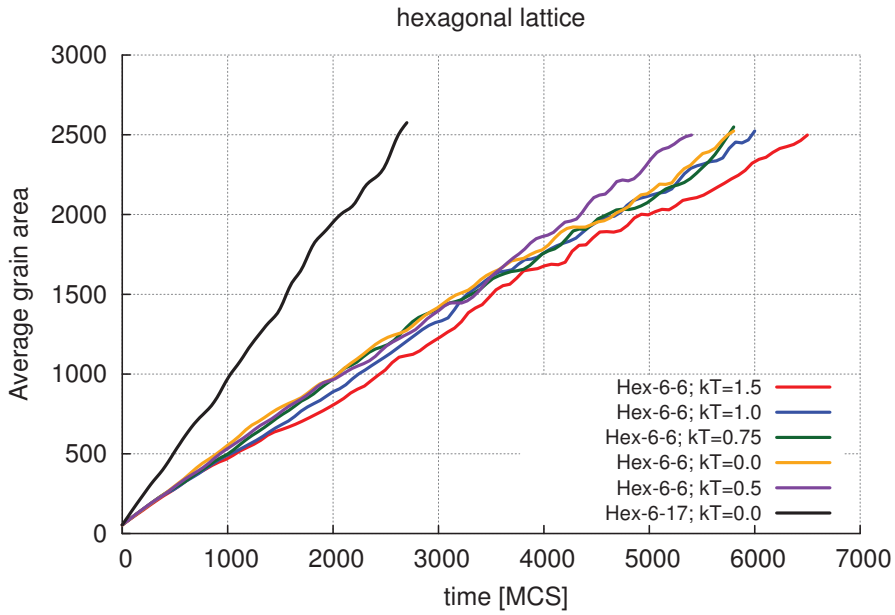

Figure 6.8: Average grain area versus time simulated using hexagonal lattice.

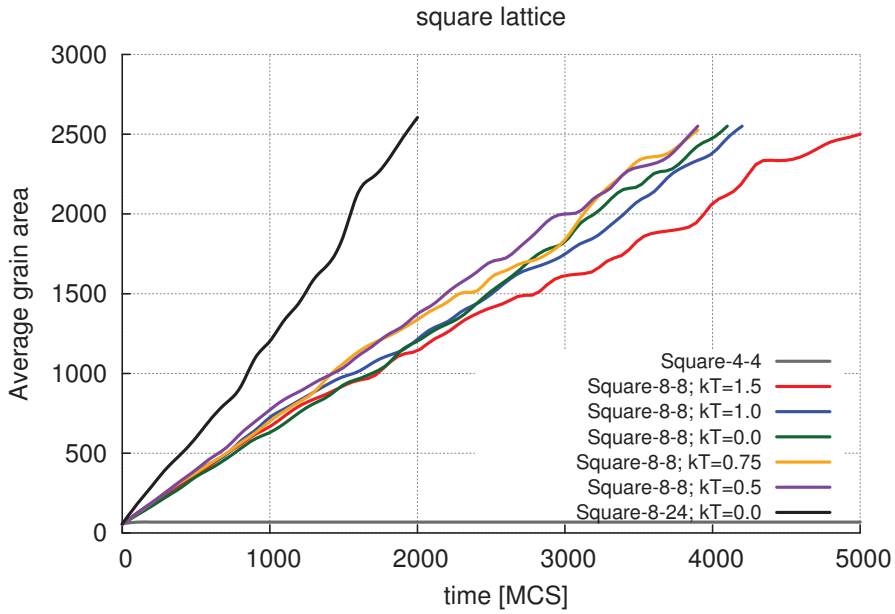

Figure 6.9: Average grain area versus time simulated using square lattice.

Nevertheless, the most important role connected with simulation temperature should be looked for in the simulated microstructure. Lattice symmetry is strongly reflected in the grain shape and grain boundary topology if simulation is performed in zero-temperature (see comparison shown in the Figure 6.10).

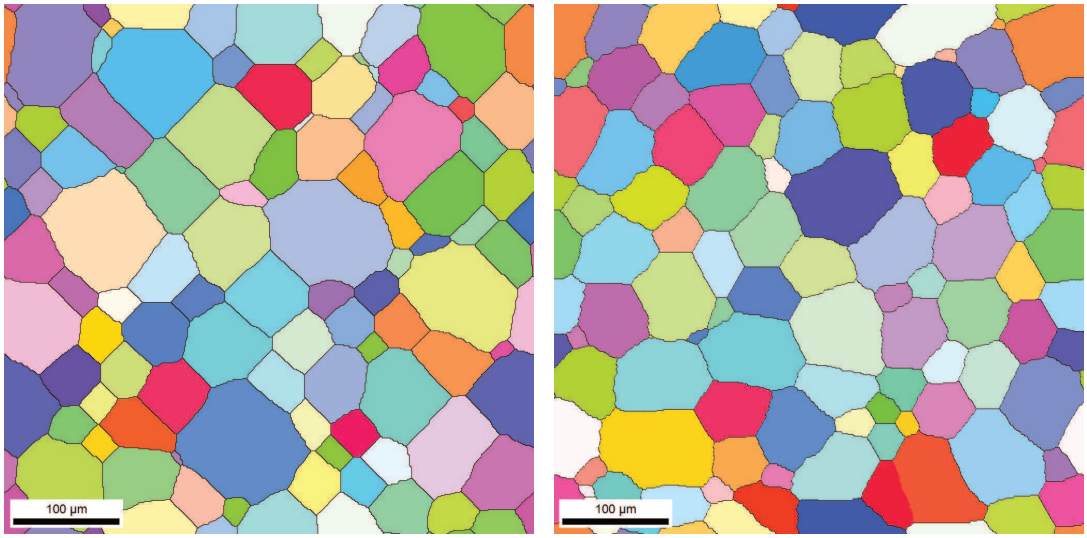

(a) square lattice **(b)** hexagonal lattice

Figure 6.10: Microstructure obtained at the end of 2D grain growth simulation which was performed at $kT = 0.0$ using square (a) and hexagonal (b) lattices.

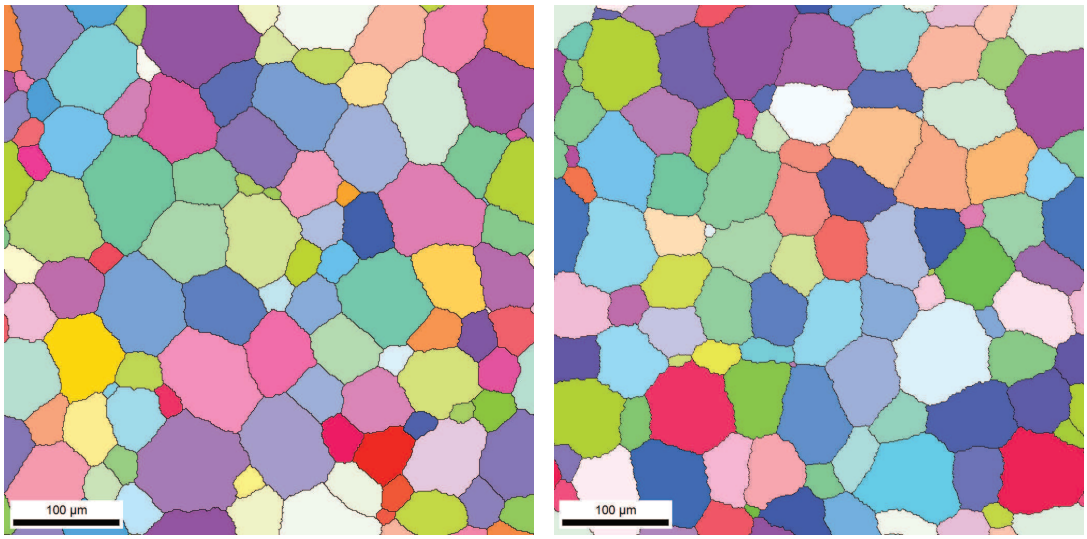

(a) square lattice **(b)** hexagonal lattice

Figure 6.11: Microstructure obtained at the end of 2D grain growth simulation which was performed at non-zero simulation temperature ($kT = 0.75$) using square (a) and hexagonal (b) lattices .

Application of square lattice results in rectangular grains thus grain boundary segments often meet at an angle of 90°. Hexagonal lattice, on the other hand, provides more hexagonal grains and large number of triple points, where straight fragments of grain boundaries are connected at an angle of 120°.

Such lattice effects are undesired and unfavorable since they can artificially slow down the grain growth. Therefore, one needs to take advantage of the fact that higher, but also carefully estimated, simulation temperature makes grain boundary appropriately rough. In consequence, they are more curved instead of being straight, while grains appear to be less regular (Figure 6.11 on the previous page).

To make sure that the test is positively passed, an analysis of the simulated microstructures is presented.

Figure 6.12 presents grain diameter distributions calculated for particular MC steps. To compare them effectively, grain diameters (horizontal axis) are divided by average grain diameter. The obtained curves can be well approximated by log-normal distribution. Also, they present self-similarity over simulation time.

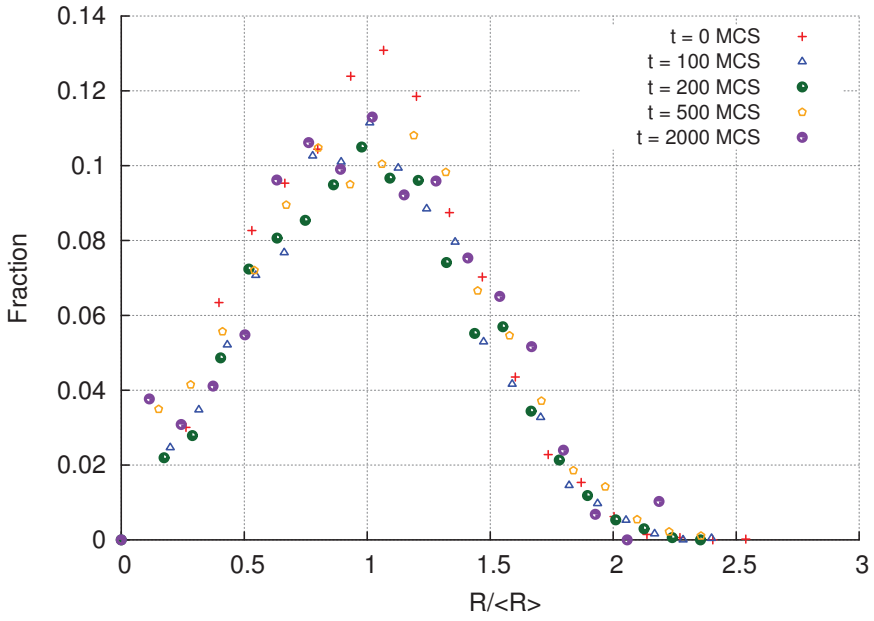

Figure 6.12: Grain diameter distributions obtained at various Monte Carlo steps (simulation has been performed using hexagonal lattice and $kT = 1.0$).

Figure 6.13, in turn, presents misorientation distribution, which remains random during simulated grain growth, as expected.

Therefore, it is concluded that 2D grain growth phenomenon can be appropriately simulated.

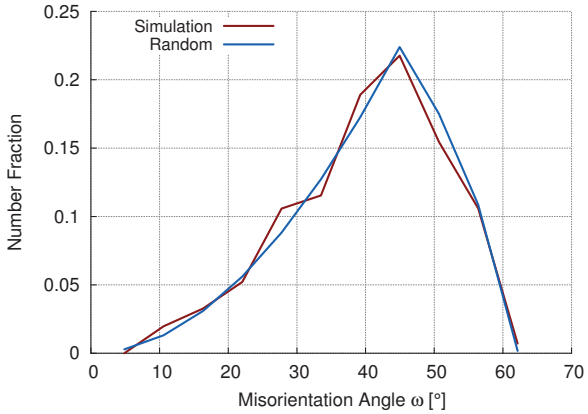

Figure 6.13: Misorientation distribution obtained at the end of 2D grain growth simulation which has been performed using hexagonal lattice and $kT = 1.0$.

Simulation 2: Influence of model modifications and efficiency improvements on grain growth curves

There are two major modifications which are incorporated in the MC model: modification I and modification II. Both are described in the implementation section. This test is designed to check if they are correctly implemented.

Settings:

- lattice:
  - hexagonal with 6 nearest neighbors (500×577 sites) and 6 neighbors considered during calculations of boundary energy,
- kT value: 1.0,
- tested modifications:
  - modification I (Mod1),
  - modification II (Mod2),
  - modification I and II (Mod1Mod2),
  - modification I combined with parallel computing (Parallel Mod1),
- simulation is stopped when number of grains is less than 100.

Results. As it can be seen in the Figure 6.14, one of the most significant advantages provided by both incorporated modifications is the dramatic increase in grain growth rate. This is very important in the case of large and time-consuming 3D simulations. Moreover, modifications do not change linear increase of areas size of the grains, so it can be assumed that simulated physical phenomena are not negatively affected by their application. Similarly, parallelization procedure is also positively verified because it gives almost the same results (blue curve) as standard simulation (green curve).

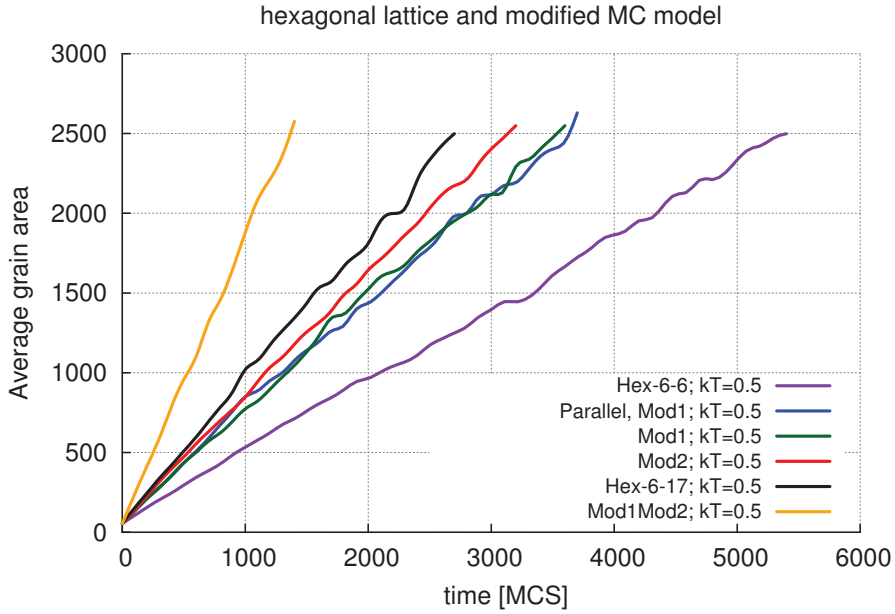

Figure 6.14: Average grains area versus time simulated using hexagonal lattice and modified version of Monte Carlo Potts model.

6.2.3 3D grain growth of random microstructure

Similarly to 2D grain growth, a 3D isotropic grain growth is investigated.

Settings:

- cubic lattice - $200 \times 200 \times 100$; random microstructure,
- kT value: 0.75,
- applied modification I,
- applied modification II,

- enabled parallel computation.

Results. In this type of simulation an average volume V of the grains is obtained at given MCS, whereas it is more convenient to analyze average area A. Therefore, it is calculated in a simplified form as: $A = V^{\frac{2}{3}}$.

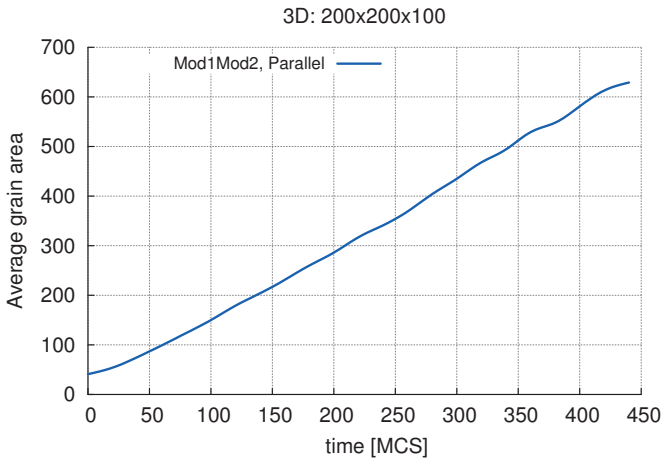

Figure 6.15: Relation between average grain area and time during 3D grain growth simulation.

Resulted $A(t)$ curve is almost linear (see Figure 6.15), which means that 3D isotropic grain growth is correctly simulated.

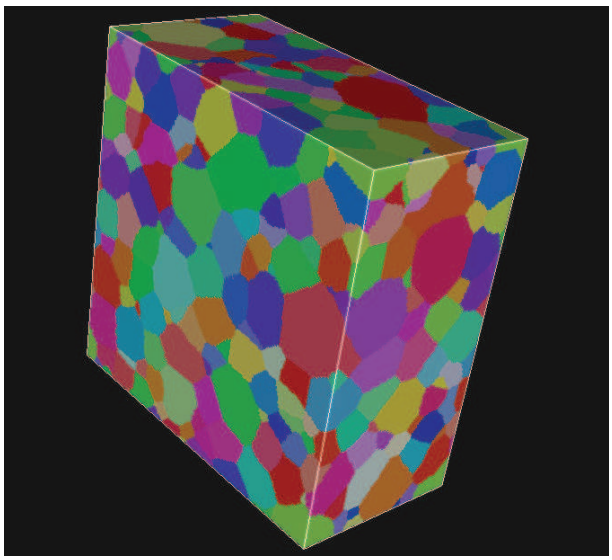

Figure 6.16: 3D microstructure obtained after 300 MCS of grain growth simulation.

In addition, a middle cross-section ($z = 50$) of the simulated 3D microstructure (Figure 6.16) has been analyzed in terms of general structure and misorientation distribution (see Figure 6.17). As it can be seen, the distribution remains random during simulation thus texture is also random, which means that there is no preference in terms of growth of particular orientation.

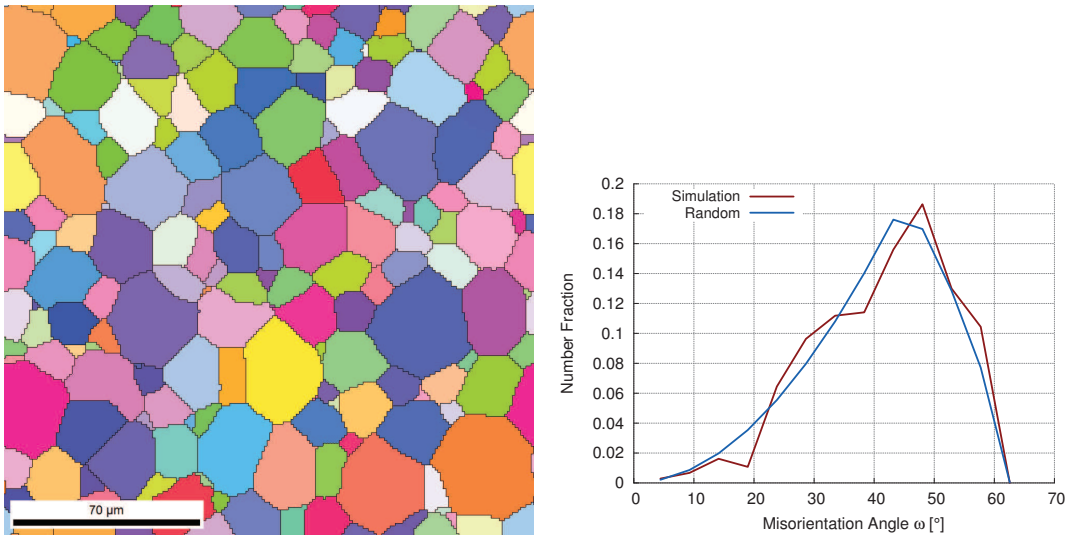

(a) **(b)**

Figure 6.17: 2D cross-section ($z = 50$) of 3D microstructure (a) obtained after 300 MCS of grain growth simulation and corresponding misorientation distribution (b).

To summarize, taking into account the presented results of 3D grain growth kinetics as well as misorientation distribution, it can be concluded that the developed MC model is capable to simulate 3D grain growth process properly.

6.2.4 2D simulation of recrystallization using random microstructure

2D synthetic microstructure, the same as in the 2D grain growth test, is used in order to simulate primary recrystallization and compare the obtained results with JMAK model.

Settings:

- hexagonal lattice - 500×577, random microstructure,
- $H = 2.0$, stored energy is constant for all the grains,

- $kT = 1.0$,
- site saturated nucleation, number of nuclei is 100,
- position and orientation of nuclei is assigned in a random fashion,
- applied modification I.

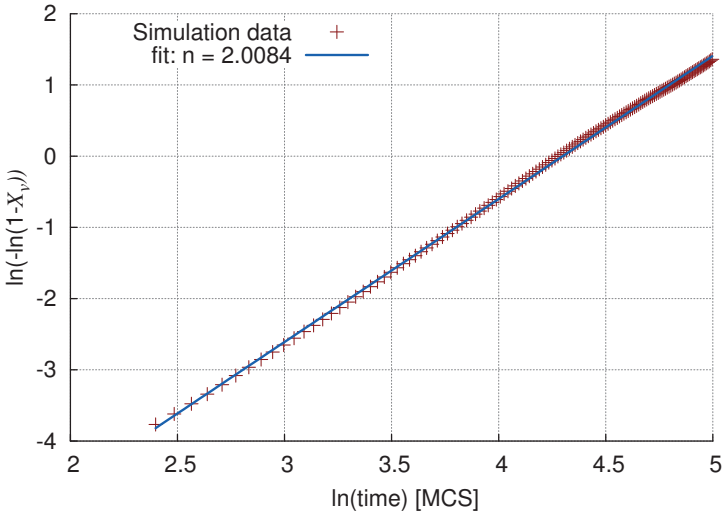

Figure 6.18: JMAK plots obtained from 2D simulation of recrystallization.

Results: Since site saturated nucleation is imposed, the Avrami exponent should be equal to 2, which is confirmed by the presented JMAK plots ($n = 2.008$) thus simulation is positively verified.

6.2.5 3D simulation of recrystallization using random microstructure

Again, expansion from 2D to 3D microstructure is considered in order to simulate recrystallization in 3D.

Settings:

- cubic lattice - $100 \times 100 \times 100$; random microstructure,
- $H = 4.0$, stored energy is constant for all the grains,
- $kT = 1.0$,

- site saturated nucleation, number of nuclei is 10,
- position and orientation of nuclei is assigned in a random fashion,
- applied modification I.

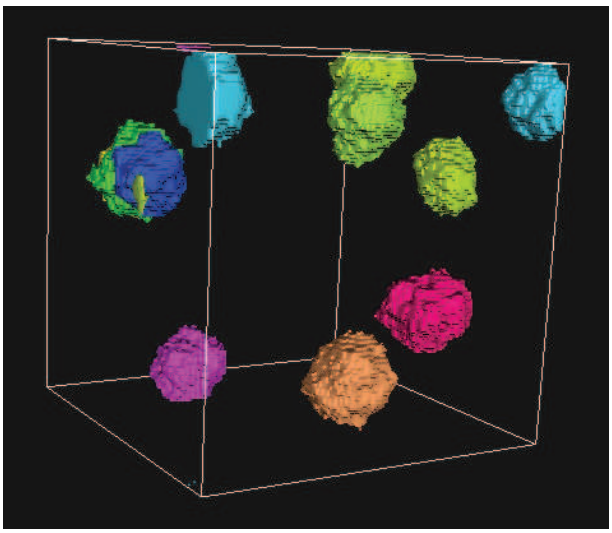

Figure 6.19: Recrystallization grains emerging during simulation.

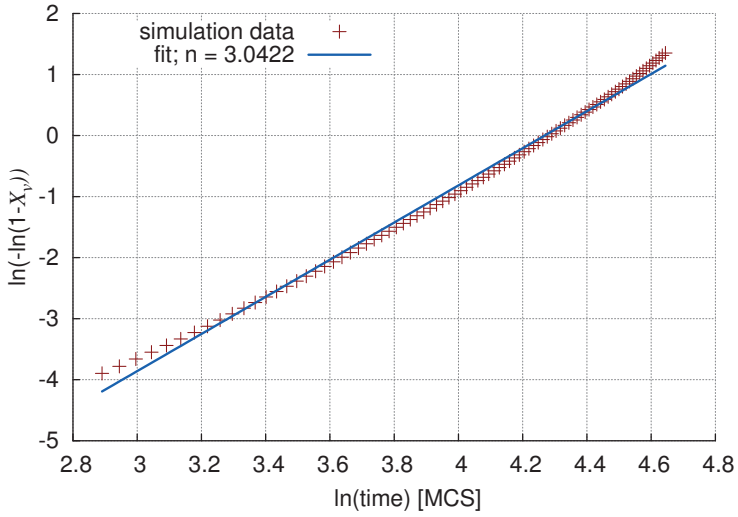

Figure 6.20: JMAK plot obtained from 3D simulation of recrystallization.

Results: Based on the Figure 6.20, it is shown that MC model works well in terms of 3D simulation of recrystallization as the resulted Avrami exponent (3.04) is in very good agreement with the theoretical value (3.0).

6.3 Concluding remarks

Taking into account successful results of the presented testing cases and also many other simulations performed during development process, but not shown in the thesis, it is concluded that the proposed MC model is correctly implemented. Therefore, it can be applied to simulate the primary recrystallization and grain growth phenomena in real microstructures.

CHAPTER 7

New method of grain boundary representation and characterization

Grain boundaries (GBs) are a broad research topic in the materials science, for the whole bunch of reasons, even if they are only interfaces separating grains. Despite the fact that GBs occupy much smaller area in the microstructure comparing to the grains, GBs play significant role during deformation and recrystallization. Therefore, in some cases they affect the final material properties in the greatest manner.

As shown in the previous chapters, GBs are strongly linked with accumulation of dislocations, whereas during annealing they appear as preferable place for recrystallization nuclei. Moreover, GB energy, mobility as well as topology have strong impact on the grain growth process.

In the light of the abovementioned facts, extended knowledge about GB structure and parameters as well as satisfactory theory of GBs evolution is still being looked for.

The development of EBSD technique has facilitated significantly the GB investigations. Even if EBSD devices cannot give an insight at the scale of few nanometers, which is required to characterize GB internal structure, it is still possible to take advantage of the fact that EBSD map contains information about orientation points adjacent to GBs. Therefore, particular GB misorientation (axis and angle) as well as overall grain boundary misorientation distribution can be calculated without application of extreme resolution in measurements.

Then, based on misorientation angle criteria, different grain boundary types, such as HAGB and LAGB, special CSL boundaries or twin boundaries, can be distinguished on EBSD map.

Another analysis, founded on the use of misorientation angle, concerns estimation of fractions of given grain boundary types. This research possibility has led to refinement of novel concepts, as it was in the case of Watanabe's idea [219] of GB network design, which evolved now into new material science domain called grain boundary engineering – GBE [220, 221].

It has been proved that appropriate thermo-mechanical treatment can be used to redesign Grain Boundary Character Distribution (GBCD) and GB network structure in order to improve polycrystalline material properties such as resistance to intergranular stress-corrosion cracking, thermal coarsening or precipitation [220].

The key point of GBE processing is to replace the network of random GBs by the network of so-called special GBs. This is usually done by the use of annealing twins. Therefore, validation of grain boundary engineered materials involves evolution of the abovementioned special GB fractions.

Next example of GB investigations concerns determination of GB plane using stereological approach, or three dimensional microstructures reconstructed from EBSD scans obtained by serial sectioning [222]. This is a part of extensive research on five-parameter grain boundary distributions.

Regarding experimental and simulation techniques presented in the last two chapters, EBSD technique and Monte Carlo modeling seem to be a totally opposite investigation tools. However, it should be noted that in both cases GBs are represented in the same way which is called Line Segments Method (LSM) in the thesis. Therefore, next paragraph presents short description of LSM and its potential application when EBSD data is concerned. Furthermore, in the thesis, alternative approach of GB characterization has been proposed by Jedrychowski et al. (2013) [223, 224], namely Point Method (PM). The introduced PM has been originally developed for EBSD data, but it can be used in MC model as well, which is proven by the examples at the end of this chapter.

7.1 Grain boundary representation in 2D EBSD map – Line Segments Method

In 2D EBSD map, grain boundaries (grain boundary traces, strictly speaking) are visualized by line segments separating adjacent EBSD points which are associated with specific misorientation ranges; for instance:

- high-angle grain boundary (HAGB) segments are usually associated with misorientation higher than a threshold, typically set at 15°,
- low-angle grain boundary (LAGB) segments are associated with misorientation between 5° and 15°;
- in addition, line segments associated with misorientations lower than 5° can be considered as intragranular boundaries (IBs) or dislocation cell boundaries.

The name Line Segments Method (LSM) is implicated due to the fact that this approach is based on GB line segments representation, where line segment is understood as an edge between two neighboring EBSD points, or lattice sites from general point of view.

One of the main results given by LSM is the fraction (length or number fraction) of a particular GB type. Based on [110], it is explained below how such a quantity is calculated. Considering the number fraction of HAGBs as an example, it can be given by the following equation:

$$f_{HAGB} = \frac{N_{HAGB}}{N_{th}}, \tag{7.1}$$

where f_{HAGB} is the fraction being looked for, N_{HAGB} is the number of HAGB line segments and N_{th} is the number of line segments obtained using misorientation angle higher than some limit (1° or 2°).

It is important to realize that N_{th} may vary between results obtained from two different EBSD maps, even if the same map size and grid step are used during measurements. Hence, the direct comparison of f_{HAGB} should be performed carefully with strong attention paid to variation of N_{th}.

Alternatively, one may extract information about N_{HAGB} and normalize it by map size or by total number of all possible line segments which are present in the map.

7.2 A new approach in grain boundary characterization – (EBSD) Point Method

LSM description can be satisfactory for some EBSD analyses like in the case of the abovementioned GBCD investigation. Nevertheless, an alternative approach in GB analysis is proposed and described in this chapter. The motivation to do so comes from two main reasons.

First reason is connected with the fact that in the less ideal case of deformed microstructure the GB is a region of transition between two crystallographic orientations which is rich in various types of dislocations, particularly in geometrically necessary dislocations, often arranged in cell blocks with geometrically necessary boundaries. Hansen & Juul Jensen (1999) [225] have shown from transmission electron microscopy that a grain boundary of misorientation angle close to 15° can be a dislocation filled area of a width higher than 10 µm. Therefore, GB representation based on thin line or edge is inadequate in this case.

On the other hand, even for a very thin and narrow GB (like the one in a fully recrystallized material), a discretized grid of EBSD measurement does not ensure the correct representation. In this respect, as the real GB is not located exactly in the line segment separating two EBSD points, the GB characterized using EBSD should be also interpreted as a region within which the real grain boundary may lie.

The second reason, equally important as the first one, is implied by the fact that the number of possible GB analyses can be greatly increased using another GB representation. To recall, LSM itself allows investigating GB fractions or connectivity of GB topology, whereas important information contained in EBSD points is only used in limited manner to calculate misorientations. As a consequence of above arguments, in the thesis, a complementary method of grain boundary representation has been developed which focuses on the grain boundary area (GBA). In contrast to the LSM, these areas, which in general case should be adjacent to the GB line segments, are represented by EBSD points. Hence, names like the point method (PM) or alternatively the GBA representation are used as a reference to this concept.

Such an approach gives the possibility to use the information associated with the EBSD points contributing to the regions which include real boundaries and thus it provides some new ways to analyze and characterize the material. Note that this method is not a new definition of GB. As stated above, it is an alternative idea of the way how grain boundary can be analyzed using lattice of orientation points.

In the proposed PM, the selection of EBSD points that belongs to different GB areas can be realized in various ways.

One of the possibilities to be considered is 'edge' criterion which means that the EBSD point is assigned to a particular GB area type only if one (or more of its edges) is a particular line segment from the LSM. This approach is suitable for HAGBs since their topology can be approximated by well-defined network of relatively narrow lines.

The more advanced approach is to select EBSD points on the basis of extended Kernel Average Misorientation (eKAM) parameter. The standard KAM value is calculated as the average of misorientation angles between a considered EBSD point and all its neighbors with the proviso that only misorientations lower than some threshold value (usually 5°) are included in the average [110]. This restriction is set up to limit the determination of misorientation angles to intragranular values and to exclude those associated with grain boundaries. The extended KAM, in turn, is calculated without restricting the averaging procedure to low misorientation values. Therefore, all nearest neighbors of a given point are taken into account in the eKAM determination, including those points that may belong to a neighboring grain.

The equation below gives the mathematical formula describing the eKAM value for a given EBSD point j:

$$\mathrm{eKAM}(\mathrm{point}\, j) = \frac{1}{N}\sum_{i=1}^{N}\omega(g_i, g_j), \tag{7.2}$$

where N is the total number of neighbors of point j, $\omega(g_i, g_j)$ is the misorientation value between orientation of i-th neighbor point - g_i, and orientation of j point itself - g_j.

By selecting appropriate ranges for the eKAM value, different GB types can be distinguished. Similar approach has been already shown above in the case of LSM, where three boundary categories are identified based on misorientation angle. It is thus possible to represent the same categories of GB areas based on the fact that they are associated to different eKAM ranges.

Note that the values of eKAM ranges are arbitrary and depend on: material state, measurement grid type and analysis assumptions thus they have to be carefully estimated. For instance, the possible scenario is that HAGBs of relatively low misorientation, around 15°, can be partially determined by eKAM if the imposed limit is too high. In contrary, if the limit is too low, then some of LAGB areas can be recognized as HAGBs.

To overcome this problem, a mixed criterion (eKAM and edge) can be applied as the solution. For example, it can be imposed that an EBSD point contributing to HAGB area should have at least two edges determined as HAGB by LSM or eKAM value which is high enough.

The last step in the PM is the cleaning procedure used to remove isolated GB points.

It can be concluded, on the basis of the presented description, that PM is highly flexible. What is more, it can be easily modified according to particular point of interest, whether it is comparison of HAGBs, LAGBs and IBs or investigation of special boundaries like CSL one.

7.3 Comparison of PM and LSM methods

The comparison of both described methods: PM and LSM is presented using model situations.

In the first case (Figure 7.1), two grains are considered: the yellow one and the blue one, which are separated by HAGB. On the left side, a set of grey points, which corresponds to HAGB area (calculated by PM), is shown. On the right side, in turn, HAGB is represented by red line segments given by LSM.

In the second case (Figure 7.2), IB is visualized inside one grain (blue points). Again, grey points correspond to IB area (PM), while red lines are supposed to represent IB (LSM).

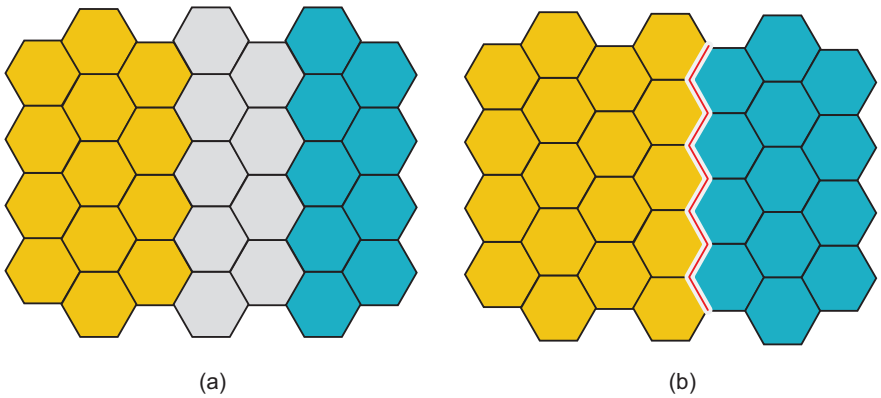

Figure 7.1: GB area (grey points) separating two grains - a) and boundary segments (red lines) separating two grains - b).

These idealized cases have been next validated using experimental EBSD data

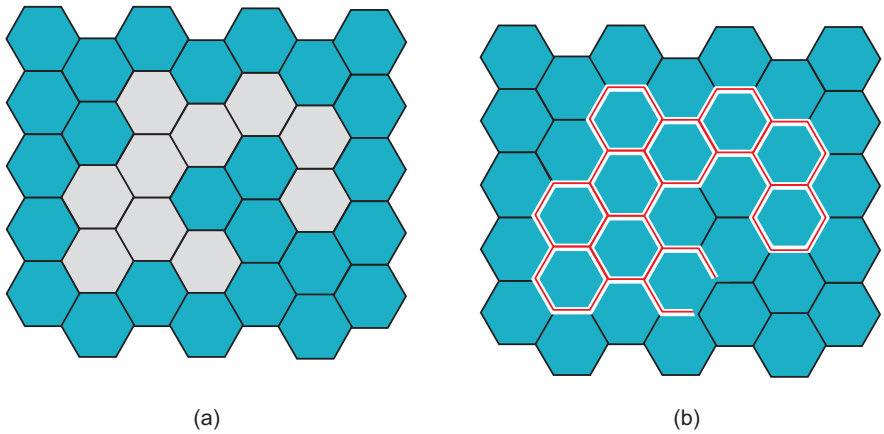

Figure 7.2: Characterization of Intragranular Boundaries using GBA method (grey points) - a) and LSM (red lines) - b). Blue points mean one grain.

obtained from zirconium measurements. Two zirconium states are compared, recrystallized and deformed one, in terms of HAGBs, LAGBs and IBs visualization given by PM and LSM (see figures below).

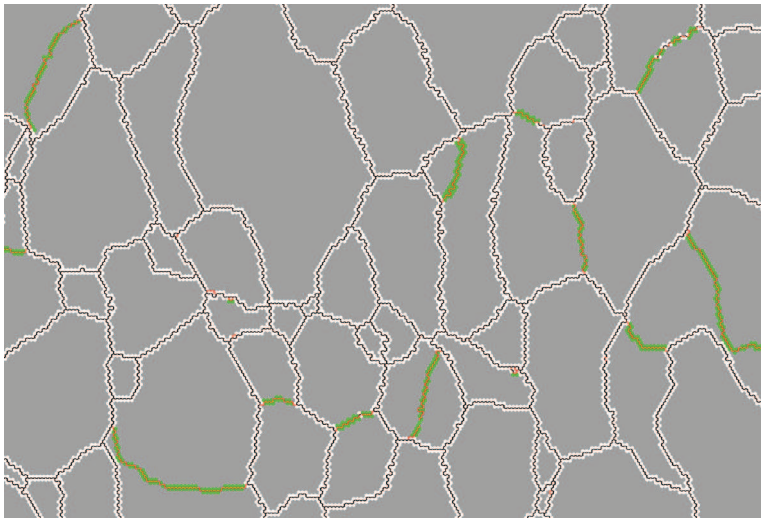

Figure 7.3: Grain boundary map for the recrystallized state of zirconium. HAGBs, LAGBs and IBs are represented by lines from the LSM (black and red) and by areas visualized by points from PM (white and green).

In the case of PM, IBs and LAGBs areas are determined using eKAM parameter, whereas a mixed (eKAM + edge) condition has been used for HAGBs areas.

Figure 7.3 presents GB map obtained for recrystallized state of zirconium. It is confirmed that PM works, as it is expected, since HAGB and LAGB line segments lie exactly in the areas identified and visualized by the PM.

In the Figure 7.4, where deformed state is shown, situation is quite similar as far as HAGBs and LAGBs are concerned. However, significant differences are observed in the case of IBs.

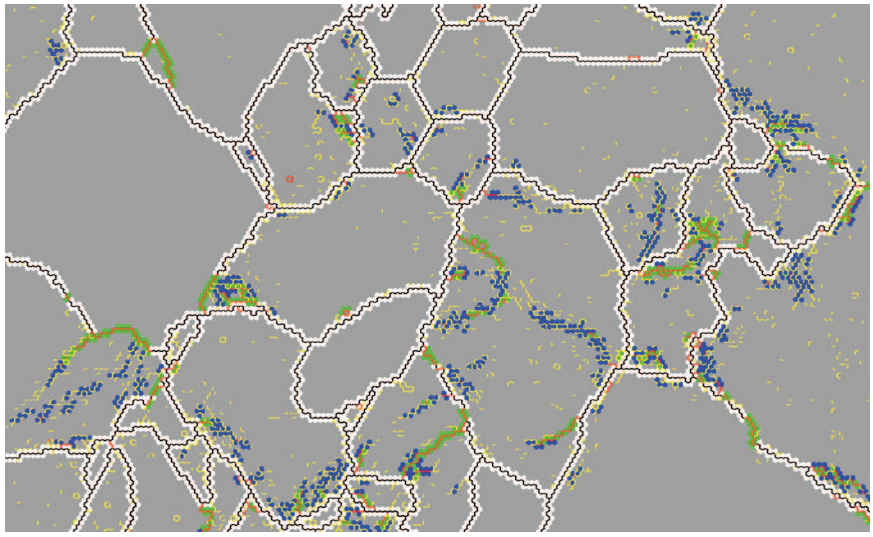

Figure 7.4: Grain boundary map for the deformed state of zirconium. HAGBs, LAGBs and IBs are represented by lines from the LSM (black, red and yellow, respectively) or by areas visualized by points from the PM (white, green and blue). LSM is not well suited to identify properly some specific IBs structures which tend to gather in wider areas. This results in small groups of isolated yellow lines which seem to be randomly distributed.

It is clear that line segments are less convenient for the description of the IBs in the deformed zirconium (see Figure 7.4). This is due to the fact that IBs tend to concentrate in the form of broader regions which consist of many neighboring EBSD points.

Moreover, in the LSM method, the characterization of a boundary segment is based on very local and limited information, namely the comparison of only two EBSD points. As a result, a lot of isolated IB line segments are determined. Such segments seem to be randomly distributed and are thus difficult to analyze. Because IBs have a very low misorientation, it is also highly possible that these segments may result from errors in the orientation measurements.

Conversely, using the boundary area, a clearer structure of IBs can be seen inside the grains. The effect of isolated or incorrectly determined boundaries is reduced as more information about boundary surroundings is taken into account since all the neighbors are accounted during eKAM calculation.

To conclude, the proposed point representation is more appropriate in this case

as IBs are indeed regions of lattice defects accumulation.

7.4 Possible applications of the GB area representation in EBSD investigation

The main benefit of the proposed GB representation comes from the fact that EBSD points linked to particular GB area can be analyzed statistically.

Based on the crystallographic orientation stored in EBSD point, it is possible to calculate texture of GB areas. Certainly, in many cases it may appear that the texture of a given boundary type is random or similar to the texture of the whole sample. However, in some other cases the textures between various GB areas can be different. In addition, they may evolve differently during thermo-mechanical treatment, which, in turn, provides new insight into understanding of the ongoing process.

The difference between textures of GB areas has been observed in steel deformed up to 50% of strain by cold rolling [224]. It has been shown that global texture of investigated steel has two main maxima. Then, it has turned out that one of them correlates with texture of HAGB areas, whereas the other is linked to textures of LAGB areas – see Figure 7.5.

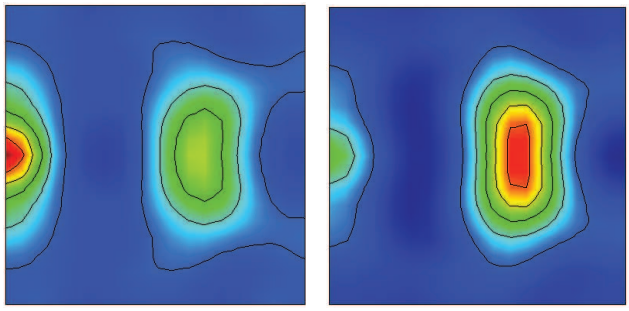

(a) **(b)**

Figure 7.5: ODF cross-section for $\phi_2 = 0°$ presenting HAGB (a) and LAGB (b) textures in deformed steel.

Please note that level values between both ODF cross-sections are different since the main purpose of this comparison is to prove that main texture orientations of HAGB and LAGB areas are separated.

Application of the PM can be useful especially for an analysis of GBs in two-phase material. Using the LSM, it is very difficult, or even impossible, to determine the

number of GBs between grains of different phases or boundaries between grains of the same phase [226]. In contrary, the EBSD points in the GBA representation naturally contain information about the phase thus it is much easier in this case to estimate the number of all possible grain boundary types present in a two-phase material.

Next information to be explored in the GBA approach is Image Quality or Confidence Index associated to different GB types. Such investigation may shed a light on dislocation accumulation in particular GBs.

Another benefit is the alternative way of estimation of GB fraction. In the proposed method the GB fraction can be described as a portion in two dimensions of the total area of the EBSD map. Direct determination of GBA fractions can be helpful in the analysis of GB evolution, especially when the results are compared between EBSD maps (with the same grid step) that were obtained for different states of deformation and recrystallization.

Finally, PM can be used to analyze material parameters which are connected with GBs. The statistical analysis of dislocations is presented as an example. Kamaya (2012) [156] has shown that comparison of the average KAM value of the grain with KAM values obtained from near grain boundary regions may give topological information about concentration or localization of dislocations. If these two values are similar, then dislocations should be uniformly distributed in the grain. In the opposite case, when KAM value calculated for near grain boundary regions is much higher than the average KAM of the grain, then dislocations should be located mainly in grain boundary regions.

Another approach, developed in order to analyze dislocation concentrations, may be adapted with the GBA representation combined with the KAM analysis. However, instead of a topological investigation of each of the grains, a more general approach can be proposed. The main idea is to focus on orientations of the IB regions covered by particular density of geometrically necessary dislocations. PM is, therefore, used to extract all IB regions from EBSD map. For each EBSD point included in IB areas, a KAM value can be calculated. All IB area points and their KAM value can be thus used to calculate special type of texture, in which intensities of orientations are proportional to the KAM. Based on that, it is possible to determine orientations of the grains, in which IB have the highest or the lowest KAM value. As a result, a scenario about dislocation density in grains of various orientations can be proposed.

7.5 Application of the grain boundary point method in MC modeling – a new method for estimation of grain boundary curvature

As stated in the introduction, the proposed concept of GBA representation is universal thus it can be applied to every microstructure mapped on lattice of sites. Hence, apart from EBSD maps, discretized microstructures used in Monte Carlo modeling can take advantage of the developed method.

However, the new possibilities in grain boundary analysis, which are described in the previous paragraphs, are directed mainly to EBSD investigations. From MC model point of view, they seem to be less useful. Nevertheless, there is an application of GBA representation, non-discussed yet, which may appear as very important for MC simulations. It concerns estimation of grain boundary curvature.

It has been shown that boundary migration driven by GB curvature is well embedded in the nature of MC grain growth simulations despite the fact that there is no strict curvature parameter defined in the model. The main difficulty to incorporate such a parameter arises from the fact that GBs are treated as lines between grains, which does not allow to calculate the necessary curvature.

A remedy solving this problem can be found in point representation. First, the idea how it can be used to estimated boundary curvature is described. Then, the proposed method is applied to experimental data. The obtained results are presented on a few examples.

A n-sided grain g from MC discretized microstructure (or EBSD map) is considered, which means that there are n neighboring grains. Note that overall GB of grain g is divided into n fragments which are connected by boundary junctions. Each GB fragment separates grain g from one of the neighboring grains (Figure 7.6). Therefore, each fragment has own local curvature, which is being looked for.

Grain g consists of similarly oriented lattice sites which can be distinguished on those located in the grain interior and those which are adjacent to grain boundary area. The latter are called GB sites.

GB sites can be sorted in terms of topological position. To create an ordered list of GB sites, a site adjacent to one of the boundary junctions has to be chosen as the first one. Then, all remaining sites are added site by site during a clockwise or counter-clockwise movement along grain boundary (see Figure 7.7). Based on

the obtained list, it is possible to extract information about neighboring boundary junctions which, in turn, allows to separate GB sites contributing to different GB fragments.

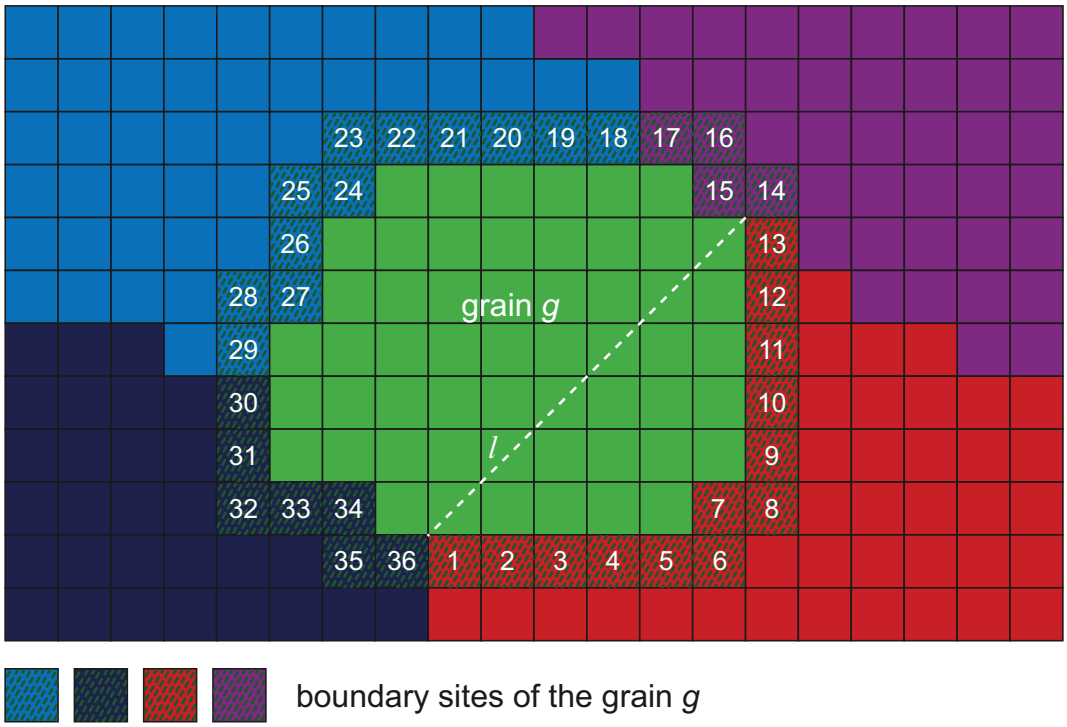

Figure 7.6: Example of GB sites sorting procedure.

In the next step, the curvature of one of the GB fragments, denoted as f, is considered. The two boundary junctions which define fragment f can be connected with straight line l. If GB sites, which represent GB fragment f, are placed on the line l (white dashed line), then it means that fragment f is flat, and thus has zero curvature. In contrary, the considered GB fragment is curved when corresponding GB sites are far away from l. In addition, it can be convex or concave depending on the way how GB fragment sites are positioned in reference to the line l. It is explained schematically on the following examples.

The red line represents GB sites which contribute to convex GB fragment, whereas the blue line represents GB sites of concave GB fragment (Figure 7.7).

Situation 1 describes convex GB fragment, while *situation 3* describes concave case. In addition, there is *situation 2* - the convex case, where center of the grain - *COG* is between line l and GB fragment.

It is necessary to find out which GB sites are under line l (red line in convex case)

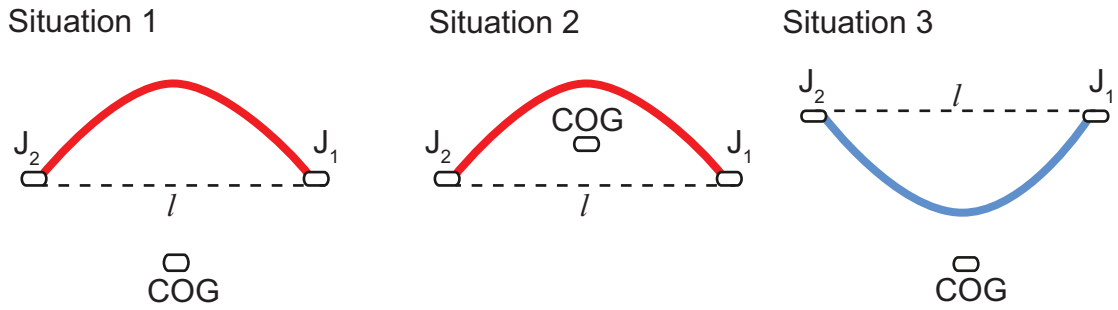

Figure 7.7: Explanation of the way how grain boundary curvature is determined.

or below (blue line in concave case), as it implies which GB fragments are convex or concave. Therefore, the following algorithm is proposed:

1. Center of the grain (COG) is calculated. Obtained coordinates are given below:

$$\begin{aligned} x_{COG} &= \frac{1}{N}\sum_{i=1}^{N} x_i, \\ y_{COG} &= \frac{1}{N}\sum_{i=1}^{N} y_i, \end{aligned} \tag{7.3}$$

   where (x_i,y_i) are coordinates of i - site and N is total number of sites in the grain.

2. Each of GB sites associated with the considered GB fragment is analyzed using three vectors **L**, **C**, **S**:

$$\begin{aligned} \mathbf{L} &= (x_2 - x_1, y_2 - y_1), \\ \mathbf{C} &= (x_2 - x_{COG}, y_2 - y_{COG}), \\ \mathbf{S} &= (x_s - x_2, y_s - y_2), \end{aligned} \tag{7.4}$$

   where (x_s,y_s) is a position of a particular GB site - s, $(x_1, y_1) = J_1$ and $(x_2, y_2) = J_2$.

3. Based on vector product $\mathbf{C} \times \mathbf{L}$, it is settled which of the three possible situations (1,2,3) takes place:

   a) *situation 1* or *2*, if $\mathbf{C} \times \mathbf{L} > 0$,

   b) *situation 3*, if $\mathbf{C} \times \mathbf{L} < 0$.

4. If *situation 1* or *situation 2* is selected from the above condition, then another vector product $\mathbf{S} \times \mathbf{L}$ is used to decide whether analyzed GB site is above line l or below:

   a) *situation 1*, if $\mathbf{S} \times \mathbf{L} > 0$,

   b) *situation 2*, if $\mathbf{S} \times \mathbf{L} < 0$.

5. Then, the distance d between the site s and line l can be calculated using below equation:

$$d = \frac{|Ax_s + By_s + C|}{\sqrt{A^2 + B^2}}, \tag{7.5}$$

   where A, B, C are constants from definition of line l:

$$l : y(x) = Ax + By + C. \tag{7.6}$$

To conclude, the above algorithm provides an information about the distance of GB sites from line l as well as the type of curvature of GB fragment.

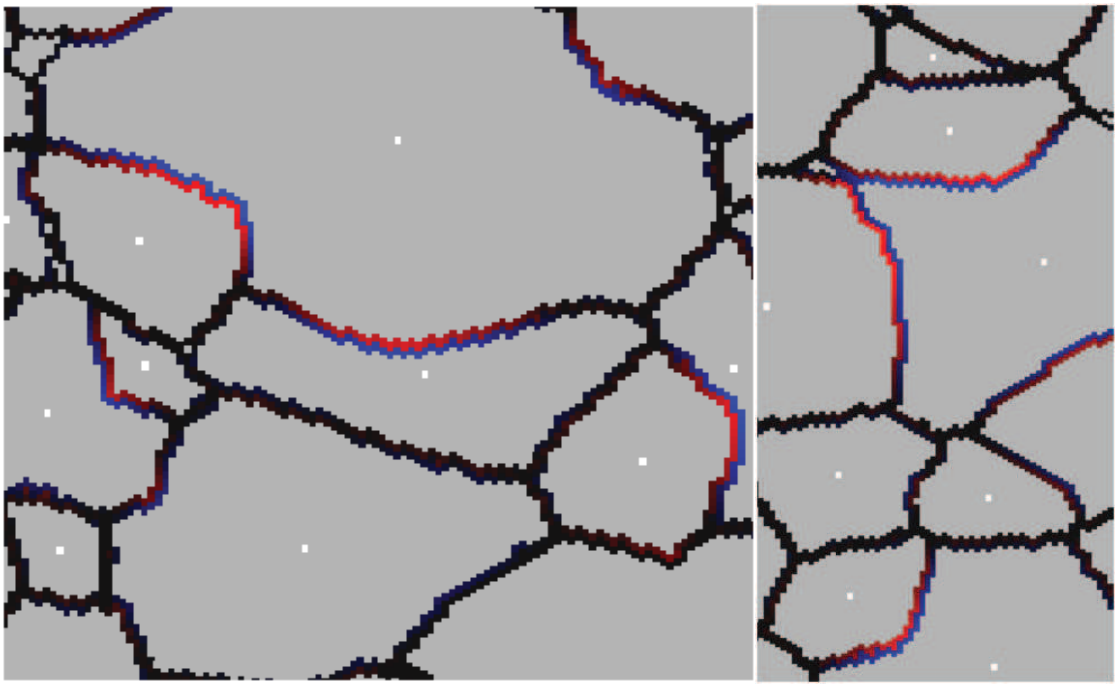

Figure 7.8: Examples of grain boundary curvature determined by the proposed algorithm.

Examples are given to show how the proposed algorithm works in practice (Figure 7.8). On the presented maps white points corresponds to COG of the grains. Curvature

degree is visualized using color gradient. Black color means that GB fragment is flat. Gradient from black to red represents increasing curvature of convex boundary, whereas gradient from black to blue corresponds to increasing curvature of concave boundary.

7.6 Concluding remarks

1. A new method of grain boundary representation is proposed in which grain boundaries are represented by EBSD points (or lattice sites).

2. This concept may be more compatible with a real microstructure, especially after deformation in which most of the boundaries, particularly intragranular boundaries, are indeed areas of lattice defect accumulation.

3. Such an approach allows to perform new types of analysis like: textures, phase or IQ statistics of GB areas, which may give interesting information about GB evolution. This method gives also a new possibility of GB fraction estimation using area occupied by particular GB.

4. In addition, GB point representation has been used as a basis for algorithm of boundary curvature determination which is important for MC simulations as well as grain growth investigations.

CHAPTER 8

Investigation of recrystallization and grain growth in commercially pure titanium based on EBSD measurements and Monte Carlo modeling

INVESTIGATION presented in this chapter is mainly focused on characterization and analysis of recrystallization and grain growth phenomena taking place during annealing of cold rolled titanium. As already noted, the most thorough studies linked with this subject have been conducted in the case of highly deformed microstructures, wide 80% of thickness reduction.

Therefore, complementary experiment was performed as a contribution to the abovementioned scientific efforts. Accordingly, EBSD analysis of three deformation steps, namely 20%, 40% and 60%, subsequently annealed, is carried out in order to elucidate mechanisms of recrystallization and grain growth in the case of less deformed microstructures.

EBSD topological maps, comprised of a very large number of acquisitioned orientation points, have been used to characterize and understand texture and microstructure evolution activated by the imposed thermo-mechanical treatment. A part of this work focuses on twin formation in the deformed state and their role on early stages of recrystallization.

The obtained conclusions are then confronted with the extensive modeling studies.

In this context, the investigation of grain boundary curvature should be noticed as it is a good example of application capabilities of the approach presented in chapter 7.

8.1 Experimental material and procedure

HCP titanium (grade 2) in a fully recrystallized state was used to prepare a set of samples subjected to the recrystallization and grain growth investigation. Deformation was introduced by cold-rolling in several passes along initial Rolling Direction – RD (Figure 8.1). Following thickness reduction ratios have been achieved: 20%, 40% and 60%. Sample reference system is thus defined by Rolling Direction (RD), Transverse Direction (TD) and Normal Direction (ND).

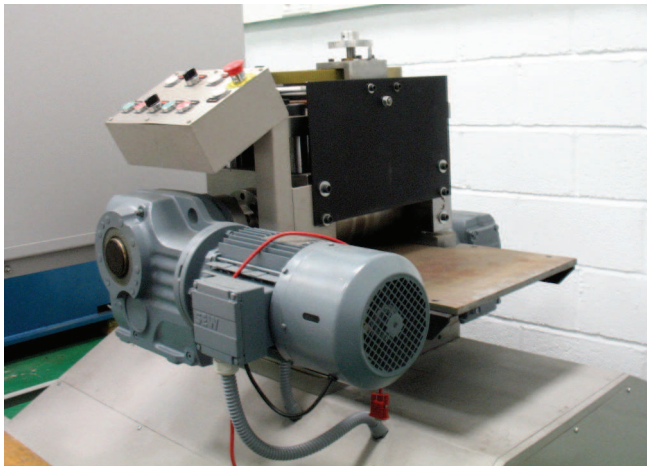

Figure 8.1: The rolling mill used in the thesis.

Then, heat-treatment was conducted in air atmosphere at various annealing temperatures (500 °C, 600 °C, 715 °C, 750 °C) and times (5 min, 15 min, 1 h, 4 h, 12 h) in order to achieve partly-recrystallized, recrystallized and grain growth states. Also, part of them was used to observe nucleation behavior. The degree of recrystallization progress in material was initially estimated based on microhardness parameter measured using well-known Vickers method (Figure 8.2). As an example Figure 8.3 is presented which shows that in the case of sample deformed by 40% of thickness reduction, further annealing over 1h in 600 °C results in microhardness comparable with the initial state, whereas annealing over 1h in 500 °C seems to be insufficient to finish recrystallization process.

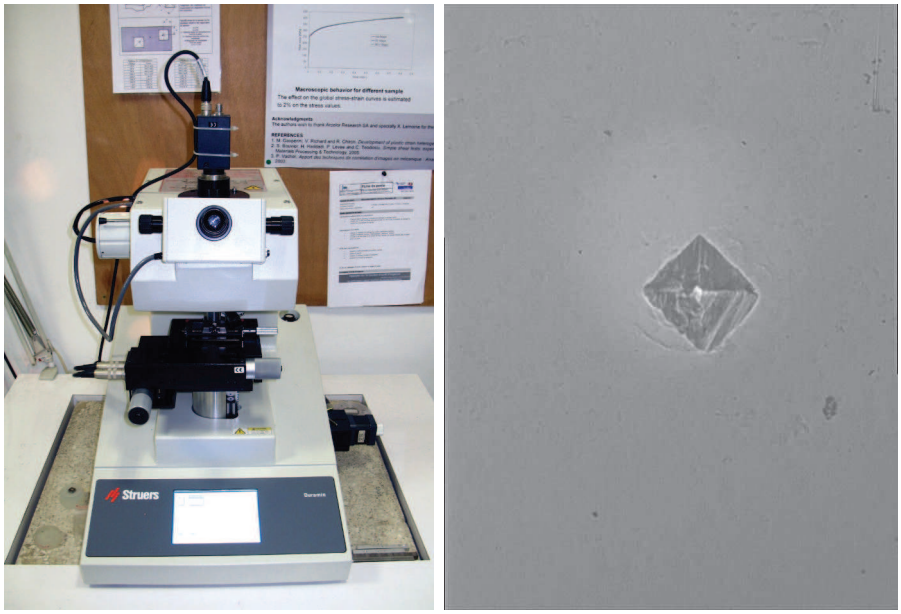

(a) (b)

Figure 8.2: Equipment applied for microhardness measurements (a) and example of image presenting rhomboidal indentation used in the Vickers method (b).

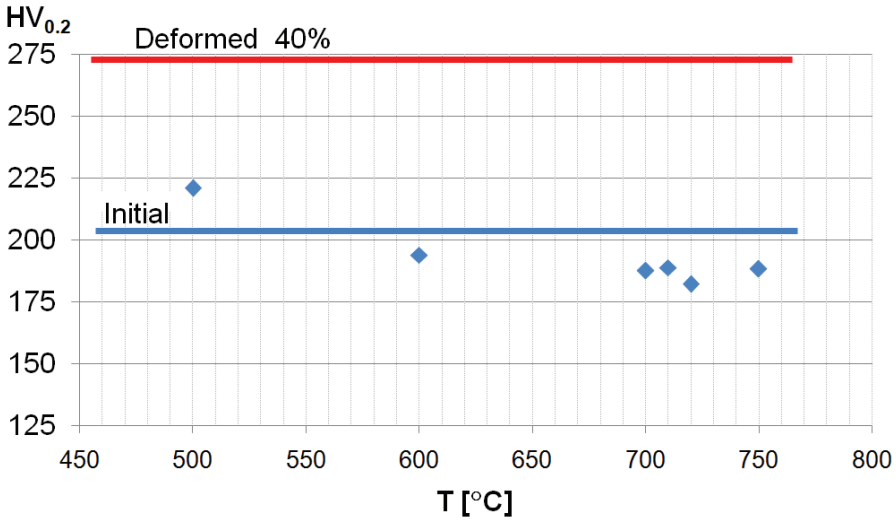

Figure 8.3: Evolution of microhardness parameter with annealing temperature in sample deformed by 40% of thickness reduction. Annealing time was 1h. The blue line corresponds to microhardness of initial state, while red one is related to deformed state.

Both, deformed and annealed states, were then examined by EBSD technique using Cambridge S360 (WGUN) scanning electron microscope (Figure 9.5 in the next chapter) and Carl Zeiss Supra VP - Ultra High Resolution FEG-SEM (Figure 4.1

provided in chapter 4), both equipped with TSL/EDAX Data Acquisition software.

The surface preparation procedure, required by EBSD, consisted of several steps: grinding with silicon carbide paper down to grade 4000, then grinding with OPS solution from Struers, and finally electropolishing under 40 V with an A3 solution from Struers, which approximately consists of 5% perchloric acid and 95% methanol. This preparation may appear complex, but it is necessary for the elimination of surface hardening or remaining defects caused by mechanical polishing.

EBSD topological maps were measured on RD-TD and RD-ND surfaces. The measurements were carried out in the middle cross-section of each sample to avoid the influence of potential surface effects. Moreover, special attention was given to reach statistically representative and trustworthy data. Total number of captured grains was at least 10 000 for each sample. In this context, complementary measurements of texture pole figures were performed using X-ray diffractometer with Bragg-Brentano configuration.

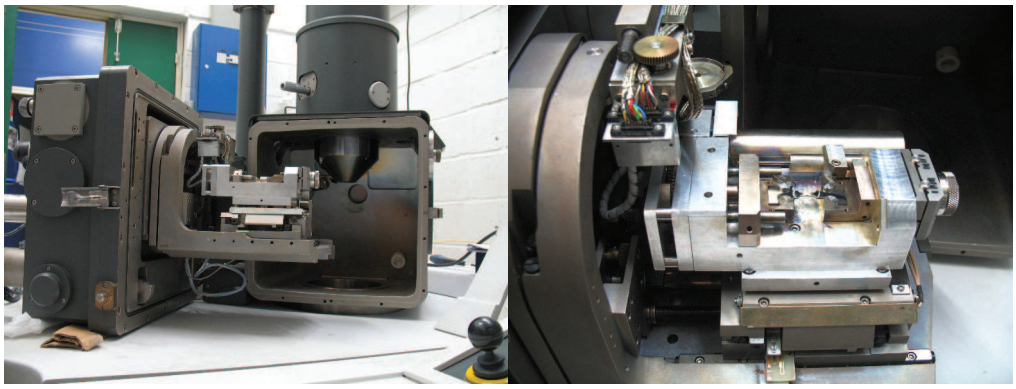

Figure 8.4: Equipment used for in-situ tensile test.

Additional in-situ EBSD measurements were performed to provide a wider perspective on deformation mechanisms operative in the considered Ti. In this case, initial sheet was specially cut out to prepare samples which were tensile tested along RD. The test was conducted inside Cambridge S360 microscope (Figure 8.4) using a unique attachment – the small testing machine developed in LSPM laboratory – University Paris 13 (Figure 8.5). Thanks to that, an extraordinary possibility can be gained for experimental observations of microstructure area performed simultaneously with the proceeding deformation or annealing. In this part, EBSD maps were collected at few steps of deformation, for instance 0% (initial area), 7%, 11%. After the highest deformation, heat-treatment (600 °C - 715 °C, 1h) was introduced inside the microscope chamber using tiny furnace placed below the sample in order

to observe formation of recrystallization grains, however, no satisfactory results were obtained.

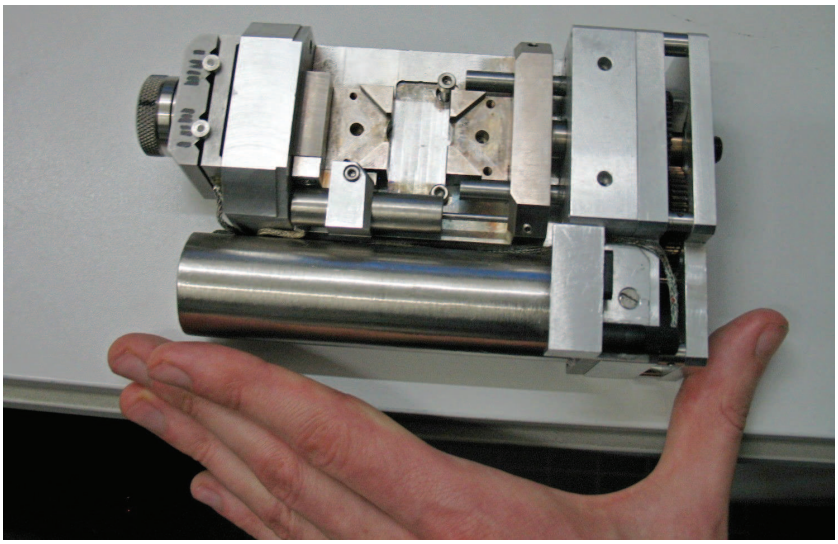

Figure 8.5: Tensile test machine used for in-situ EBSD observations. Scale is given by the size of the author's hand.

All the obtained EBSD data were analyzed with the OIM Analysis v5.3 Software from TSL [www-OIM], MTEX software [227] and author own programs.

To sum up this subsection, Table 8.1 is presented to provide a list of all examined samples, including their final reduction and applied annealing treatment. Also, some information about the chosen naming convention is given.

As it can be seen, the rolled samples will be denoted as TiRoll, whereas further annealed will be denoted as TiRex or TiGG depending on interplay between recrystallization and grain growth processes, respectively. Samples used in the tensile test will be called TiTen. In all these cases, there is a number attached which refers to the degree of deformation which is understood either as percentage of thickness reduction in rolling or strain obtained in tension. Then, some brief information about heat-treatment conditions is provided for annealed samples.

Table 8.1: List of titanium samples.

Sample	Deformation mode	Deformation degree	Annealing conditions	Final state
Init	-	-	-	Initial
TiRoll20			-	Deformed
TiRex20-600-30m			600 °C, 30 min.	Partial recrystallization
TiRex20-715-05m			715 °C, 5 min.	Partial recrystallization
TiRex20-715-15m	Rolling	20%	715 °C, 15 min.	Recrystallization
TiGG20-715-1h			715 °C, 1 h	Grain growth
TiGG20-715-4h			715 °C, 4 h	Grain growth
TiGG20-715-12h			715 °C, 12 h	Grain growth
TiRoll40			-	Deformed
TiRex40-500-1h			500 °C, 1 h	Partial recrystallization
TiRex40-600-1h	Rolling	40%	600 °C, 1 h	Recrystallization
TiGG40-715-1h			715 °C, 1 h	Grain growth
TiGG40-715-4h			715 °C, 4 h	Grain growth
TiRoll60			-	Deformed
TiRex60-600-30m			600 °C, 30 min.	Recrystallization
TiGG60-715-1h	Rolling	60%	715 °C, 1 h	Grain growth
TiGG60-715-4h			715 °C, 4 h	Grain growth
TiGG60-715-12h			715 °C, 12 h	Grain growth
TiTen11		11%	-	Deformed
TiTen12	Tensile	12%	-	Deformed
TiTen15		15%	-	Deformed

8.2 Analysis of EBSD data

The obtained EBSD data have been analyzed using several tools provided by the TSL software. The following text gives a review on them.

1. Inverse Pole Figure maps (or orientation maps). These are color coded maps, where color of an EBSD point is assigned on the basis of the transformation of

a chosen direction specified in sample reference system into crystal reference system. For instance, in the case of hexagonal crystal symmetry [001] IPF map indicates how sample Normal Direction is aligned between $[2\bar{1}\bar{1}0]$, $[10\bar{1}0]$, [0001] crystal directions which, in turn, are presented in the form of color triangle, as shown in the Figure 8.7. Note that this IPF legend is used for all the presented IPF maps in this chapter.

2. Topological maps, generated based on Image Quality parameter (chapter 4).

3. Specialized maps which are generated as combination of orientation/topological map and particular point of interest being analyzed. Maps presenting local misorientations or grain boundaries can be mentioned here, for instance.

4. Statistics that are related with characterization of grains in terms of their size and internal orientation spread. In this context, the grain size is specified by an area which is calculated as number of EBSD points included in the grain multiplied by size of one point, or by diameter which is determined as $2 \cdot \sqrt{\frac{area}{\pi}}$. Grain Orientation Spread (GOS), in turn, is grain based measure of local misorientations. It is calculated as the first central moment of the orientation distribution of the EBSD points constituting a particular grain: it corresponds thus, for one grain, to the average of all misorientations between an average representative grain orientation and the orientations of all EBSD points inside the considered grain. Mathematically, the GOS is given by the following expression:

$$\mathrm{GOS}(\mathrm{grain}_G) = \frac{1}{N_G} \sum_{i=1}^{N_G} \omega(g_i, \overline{g_G}), \tag{8.1}$$

where N_G is the total number of EBSD points inside a given grain G, $\overline{g_G}$ is the average orientation of grain G, g_i is the orientation of a given EBSD point within grain G, and $\omega(g_i, \overline{g_G})$ is the misorientation between orientations g_i and $\overline{g_G}$.
Similarly to the KAM (local misorientations - see chapter 7), the GOS can also be considered in order to estimate plastic deformation.

5. Statistics that concerns misorientation angle within (i.e. local) or between grains; the first one is calculated on the use of KAM parameter, the second gives information about distribution of misorientation angle in the whole sample. Those are usually compared with Mackenzie plot, which corresponds

to Misorientation Angle Distribution calculated for a random set of orientations [228]

6. More detailed misorientation statistics which takes into account both: misorientation angle and corresponding misorientation axis.

In spite of misorientation angle statistics, they are calculated in two ways. One, called correlated (or texture derived), considers only misorientations between a point and the nearest neighbors thus it can reveal special orientation relationship between grains. In contrary, uncorrelated one takes all possible misorientation pairs into account therefore it is often used in order to reduce texture effects inherently incorporated in the correlated distribution.

The mentioned calculations can be done on the use of Misorientation Distribution Function – MDF [229,230], which can be considered as equivalent of texture function – ODF, but defined for misorientation parameter. Consequently, so-called texture reduced MDF can be given as correlated MDF divided by uncorrelated MDF. All MDFs in this work have been calculated using harmonic method from TSL Software.

In addition, there is another way to investigate axis/angle misorientations which is discrete version of MDF. In this case, distribution of axes is shown for a given range of misorientation angle. This type of analysis gives similar results to texture reduced MDF plots if it is imposed that a particular angle corresponds to the minimal possible misorientation.

It has to be noted that one of the important steps in analysis of EBSD dataset is to employ grain grouping algorithm that transforms sets of connected and similarly oriented points into grains. For that reason two parameters have to be specified: Minimal Grain Size – that is minimal number of points in a set which should be regarded as a grain, and Grain Tolerance Angle which corresponds to a misorientation threshold needed to separate differently oriented grains with grain boundary. Obviously, this definition can introduce strong ambiguity between results obtained using different grain recognition parameters. Also, it is emphasized that special care has to be paid if analysis is performed on several maps measured with various grid step sizes. In this work, minimal grain size is set as 10 points, while grain tolerance angle is fixed at 15°. The latter means also that grain boundaries, which are shown further on EBSD maps, are classically determined by a 15° misorientation critical value and are thus HAGBs.

Regarding textures, they are analyzed based on Orientation Distribution Functions - ODF's - and {0001} pole figures, both have been calculated from EBSD

data using harmonic method incorporated in TSL Software. MTEX software is also employed for that purpose. Bunge's definition of Euler angles (φ_1, Φ, φ_2) is used to describe orientation [137] (Figure 8.6). Crystal coordinate system is defined as follows: $X = [2\bar{1}\bar{1}0]$, $Y = [01\bar{1}0]$, Z=[0001]. Please note that this definition leads to a shift of 30° in the φ_2 comparing to the results which were cited in chapter 3.

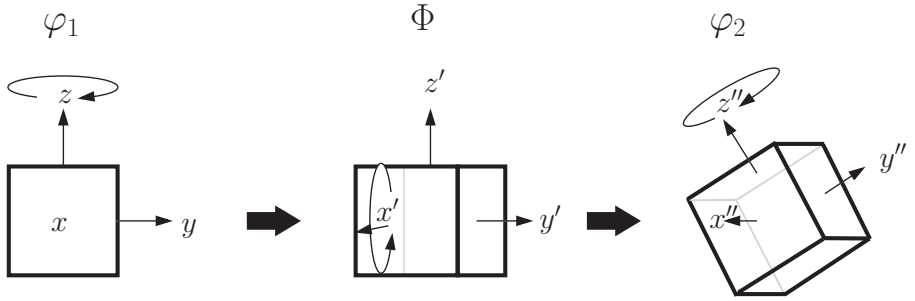

Figure 8.6: Sketch presenting three rotations related to the chosen definition of Euler angles.

Orthotropic sample symmetry was not imposed during calculation procedure. Then, only two ODF cross-sections ($\varphi_1 = 0°$ and $\varphi_1 = 180°$) were analyzed in more details instead of whole three-dimensional ODF because, in general, they contain the most important information about changes taking place in the texture. In addition, {0001} pole figures are provided to give information about stereological projection of grains *c*-axes.

Finally, it is noted that most of the obtained EBSD maps were directly analyzed, and only the one measured after highest deformations have been corrected by cleaning procedure which is usually used to remove wrongly indexed EBSD points.

8.2.1 Microstructure of initial state

Initial state microstructure of the investigated titanium comprises of fully recrystallized, equiaxed grains, whose average diameter grain size is 22 µm (540 µm^2), according to computations performed on RD-TD surface. Apart of this general view, there are also more subtle features to be discussed.

It appears that area of the initial grains is slightly larger in RD-TD cross-section than in RD-ND. In the latter case, the average grain size is equal to 20 µm (420 µm^2). Also, some of regions in RD-TD cross-section exhibit noticeable inhomogeneity in terms of shape and size. Three different examples are shown. One corresponds to a normal case (Figure 8.7), then two maps with grains significantly larger than average are presented (Figure 8.8).

The first one reveals a gradual increase of grain size. Moreover, the largest grains contain a pronounced fraction of triple junctions and quadruple points which are connected by straight boundaries (see right side of the Figure 8.8a). The second (Figure 8.8b), in turn, is more related with curved and convex boundary segments of the largest grains.

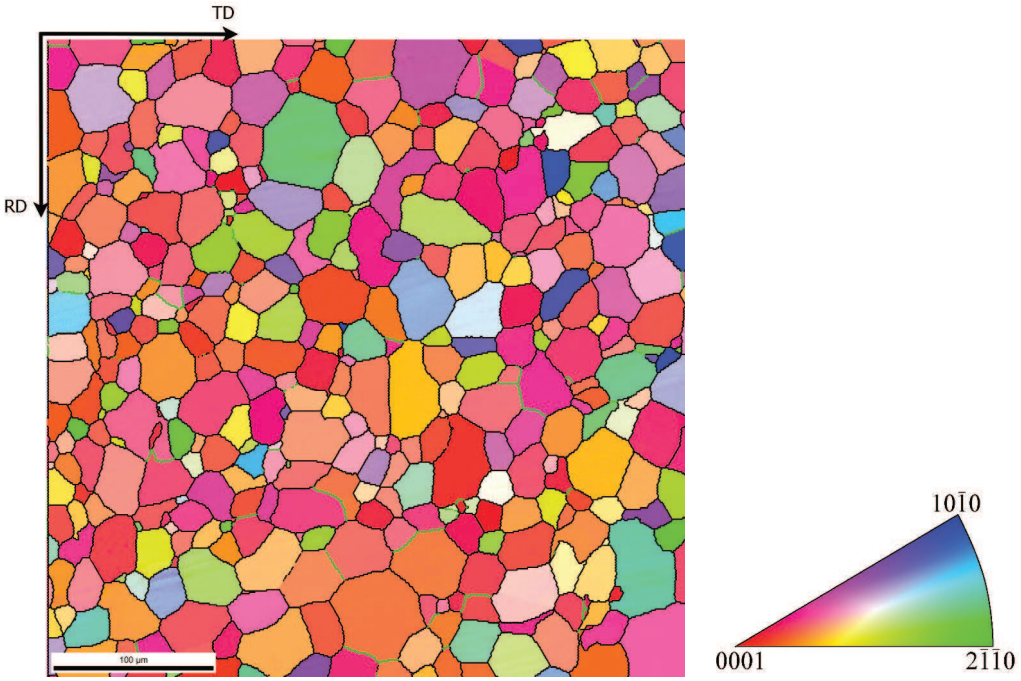

Figure 8.7: EBSD IPF [001] map of initial Ti microstructure (RD-TD plane). RD is parallel to vertical axis, while TD is parallel to horizontal axis.

In RD-ND cross-sections these trends are also present (see Figure 8.9), but in a lesser extent; there are only few grains which are much larger than the rest. On the other hand, an interesting effect can be observed in this case. The following maps clearly show that some of the grains are constrained and grouped together along vertical axis in form of long "tapes", especially in the center of Figure 8.9b. Most probably, they were created as a result of grain growth taking place inside lamellar deformation structures.

Concerning grain boundaries, all the maps show that, besides HAGBs, LAGBs are also present in the microstructure of the initial state.

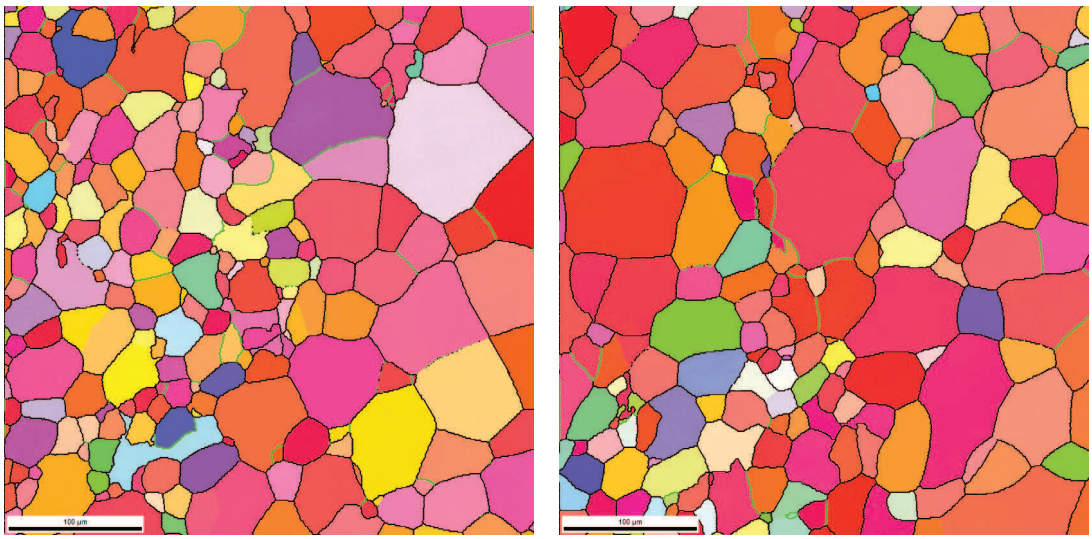

(a) (b)

Figure 8.8: EBSD IPF [001] map presenting selected features of initial RD-TD section.

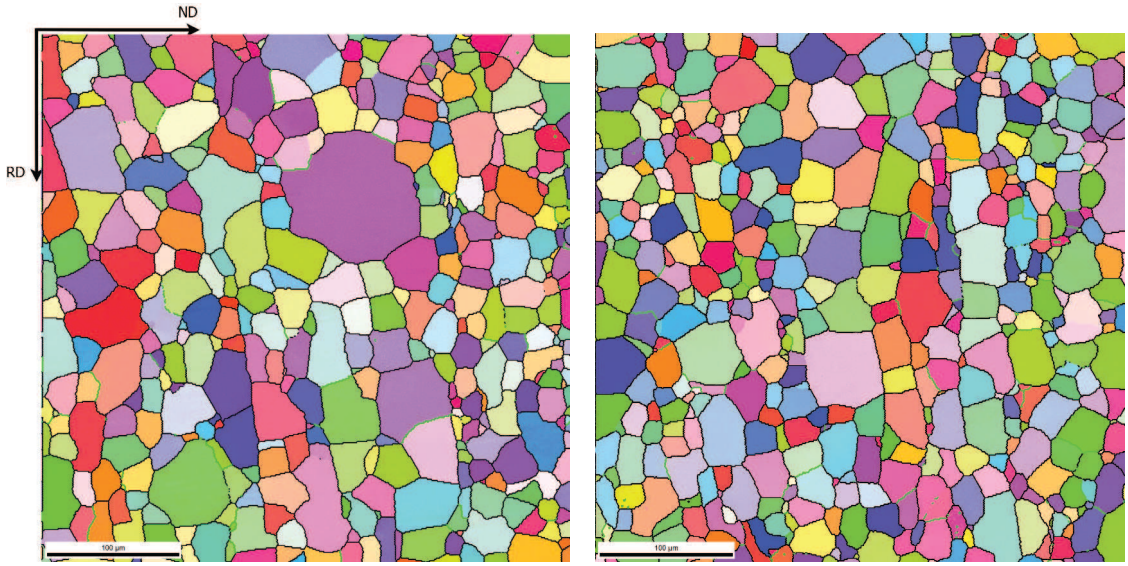

(a) (b)

Figure 8.9: EBSD IPF [001] map presenting selected features of initial RD-ND section.

Next analysis deals with misorientations. There is one distinctive maximum in the correlated misorientation distribution, which is centered at 30° (Figure 8.10). At the same time, the uncorrelated one indicates that this maximum is texture derived in a principal manner.

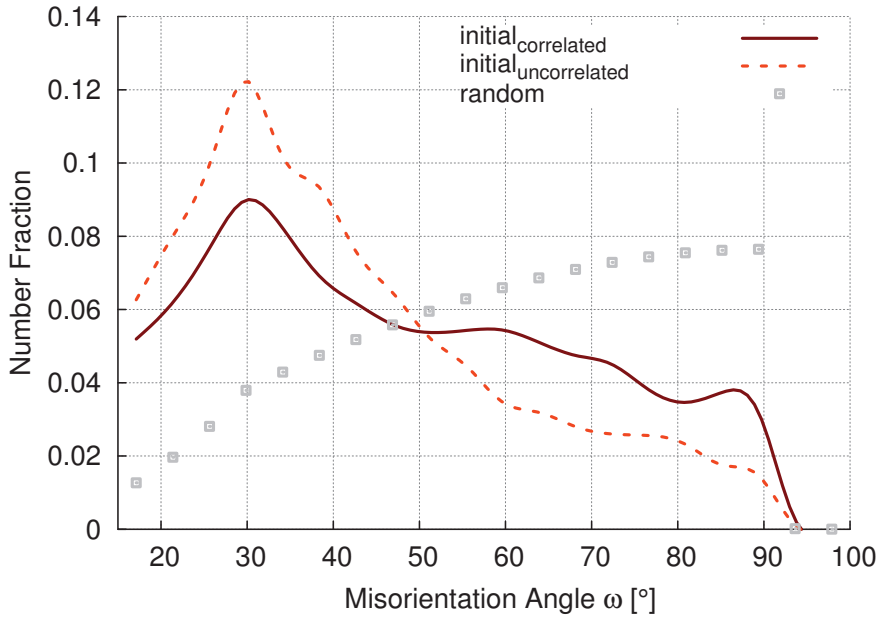

Figure 8.10: Correlated and uncorrelated misorientation distributions in the initial state.

Finally, based on [001] IPF map, it can be noticed that most of the grains have their *c*-axis almost parallel to sample ND, which is manifested by IPF color similar to red or orange in the case of RD-TD surface (Figure 8.7, for instance). Further texture analysis of the initial state is included in the separated subsection 8.2.4.

8.2.2 Microstructure of the deformed state after cold-rolling. Influence of twinning

Obtained EBSD maps reveal that in titanium the beginning of rolling induced deformation is mainly governed by twinning deformation mode.

Consequently, in the sample TiRoll20, significant number of twins is observed in the microstructure. They appear in the form of narrow and highly elongated grains. Moreover, it can be seen that secondary twins are also created in the most of already twinned grains (Figure 8.11). Without doubts, twinning plays crucial role in accommodation of externally imposed strain in this case.

However, it should be also noted that some of the grains are resistant to twinning. Instead, they exhibit slight color gradients. This, in turn, indicates the presence of local misorientations, which are connected with accumulation of dislocations inside internal grain structure.

The next deformation step - TiRoll40 - is, in some sense, a transition point, where microstructure heterogeneity is developed in a more significant manner (Figure 8.12 and Figure 8.15). On one side, already twinned grains are further refined, whereas, on the other side, higher orientation gradients are incarnated in grains unfavorably oriented to twinning.

As a consequence of this tendency, further deformation leads to a high fragmentation of most of the grains, while the rest appear as wide and broad oval regions of continuous orientation gradient which, most probably, were produced by slip deformation mode.

Therefore, the microstructure obtained after 60% of thickness reduction - sample TiRoll60 - is highly heterogeneous. The RD-TD section can be described in terms of big isolated orientation gradient islands surrounded by a sea of extremely fragmented areas (Figure 8.13a, Figure 8.14). In the case of RD-ND section, untwined areas are much more elongated thus lamellar structure is formed (Figure 8.13b).

Examples of extremely large grains which exhibit high orientation gradients are presented in Figure 8.16 and Figure 8.17 for both described surfaces. Also, misorientation profiles are shown for a chosen path across particular grains. It is noted that local (i.e. between neighboring points – red curve) misorientations are usually smaller than 10°, however, at larger distances they gradually increase to reach even 35° (blue curve).

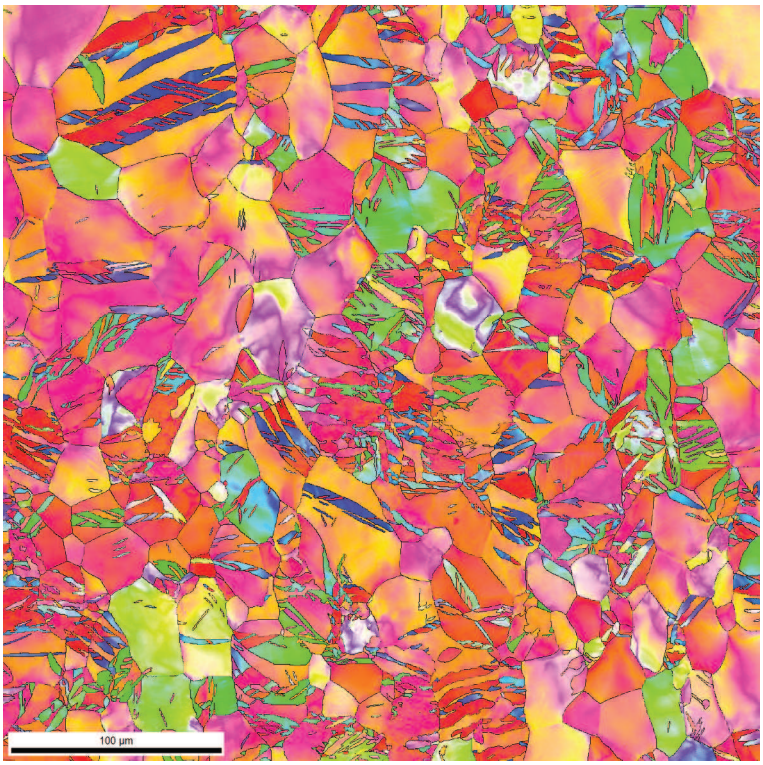

(a) RD-TD surface

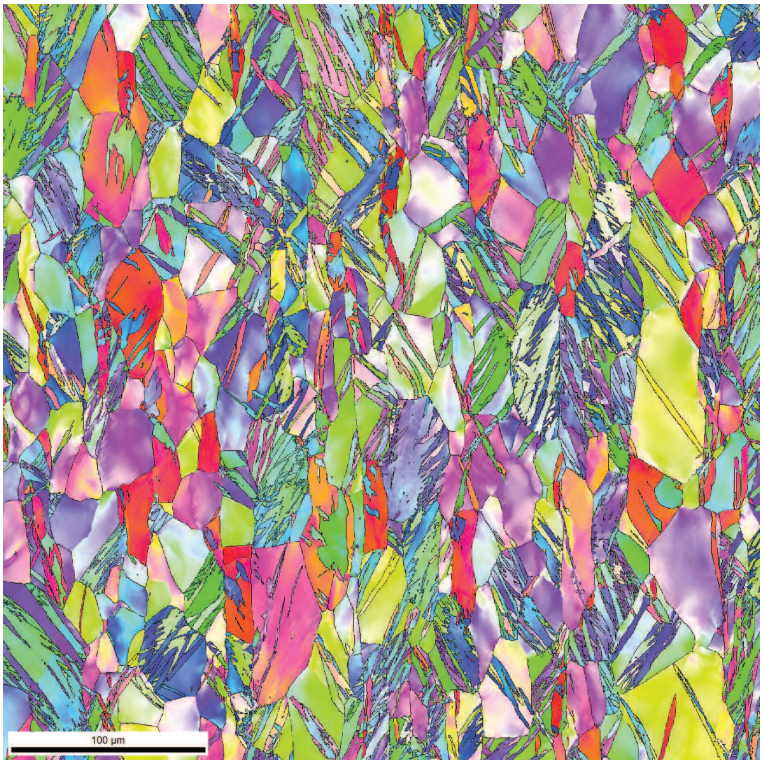

(b) RD-ND surface

Figure 8.11: EBSD IPF [001] maps (400 µm x 400 µm) presenting microstructure of the TiRoll20 sample. The black lines represent high angle grain boundaries. RD is parallel to vertical axis, while TD (a) and ND (b) are parallel to horizontal axis.

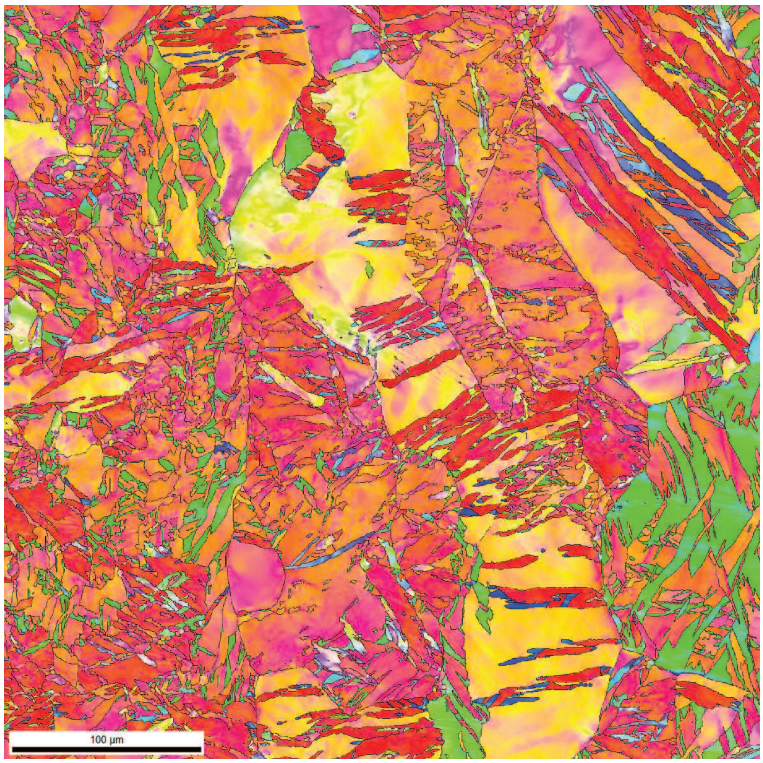

(a) RD-TD surface

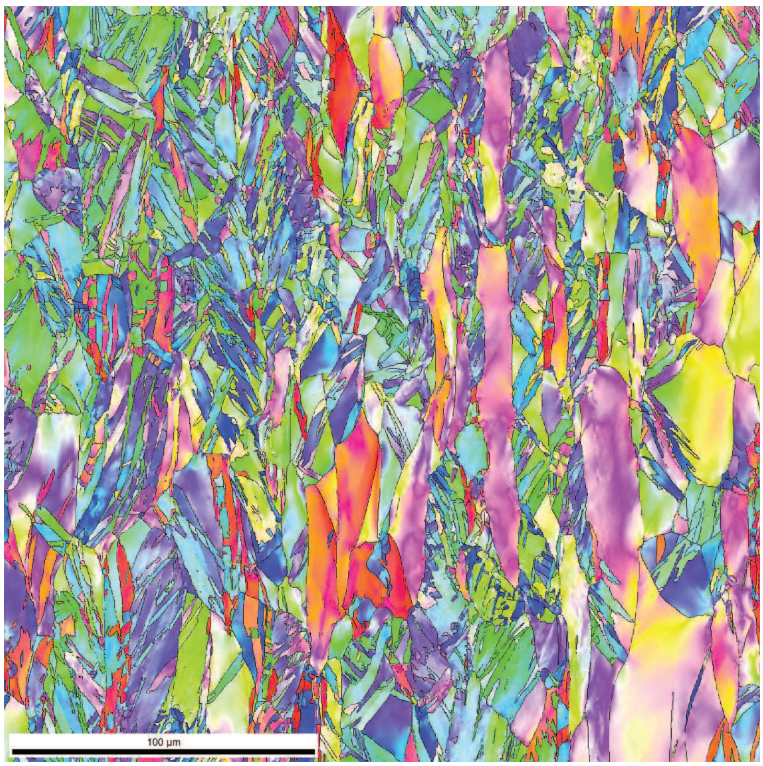

(b) RD-ND surface

Figure 8.12: EBSD IPF [001] maps (400 µm x 400 µm) presenting microstructure of the TiRoll40 sample.

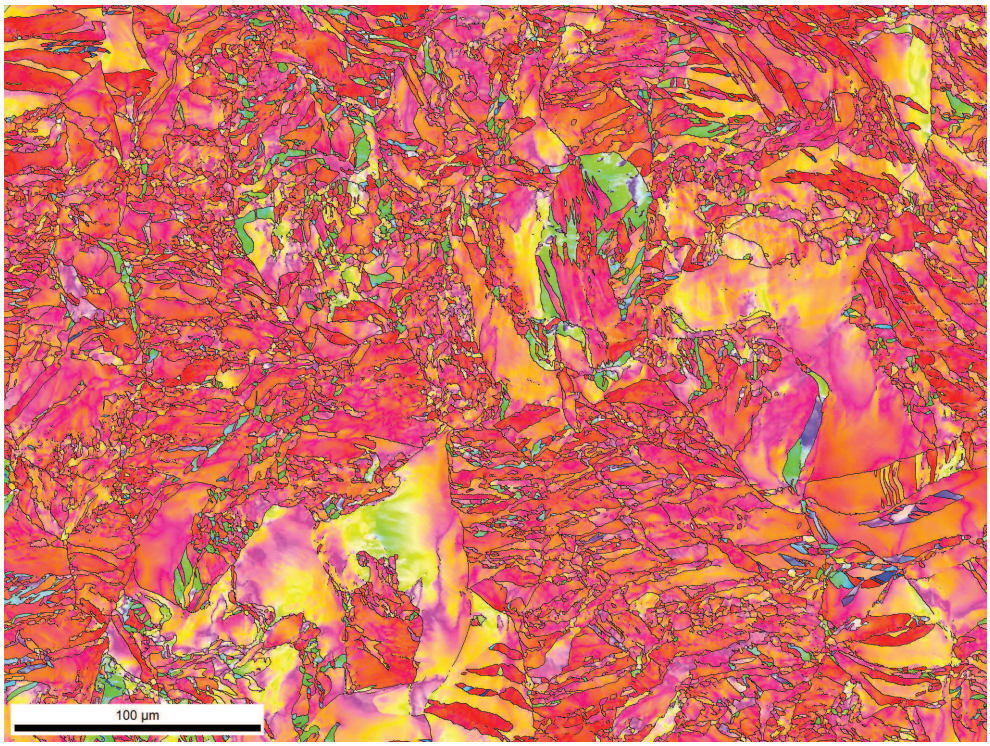

(a) RD-TD surface

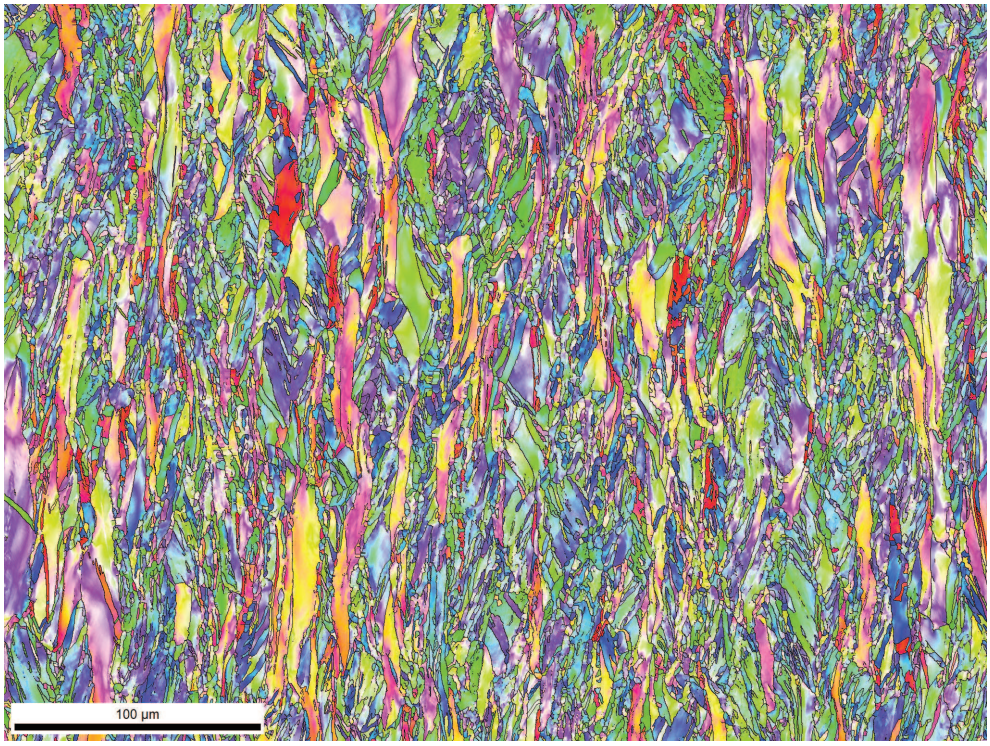

(b) RD-ND surface

Figure 8.13: EBSD IPF [001] maps (400 µm x 300 µm) presenting microstructure of the TiRoll60 sample.

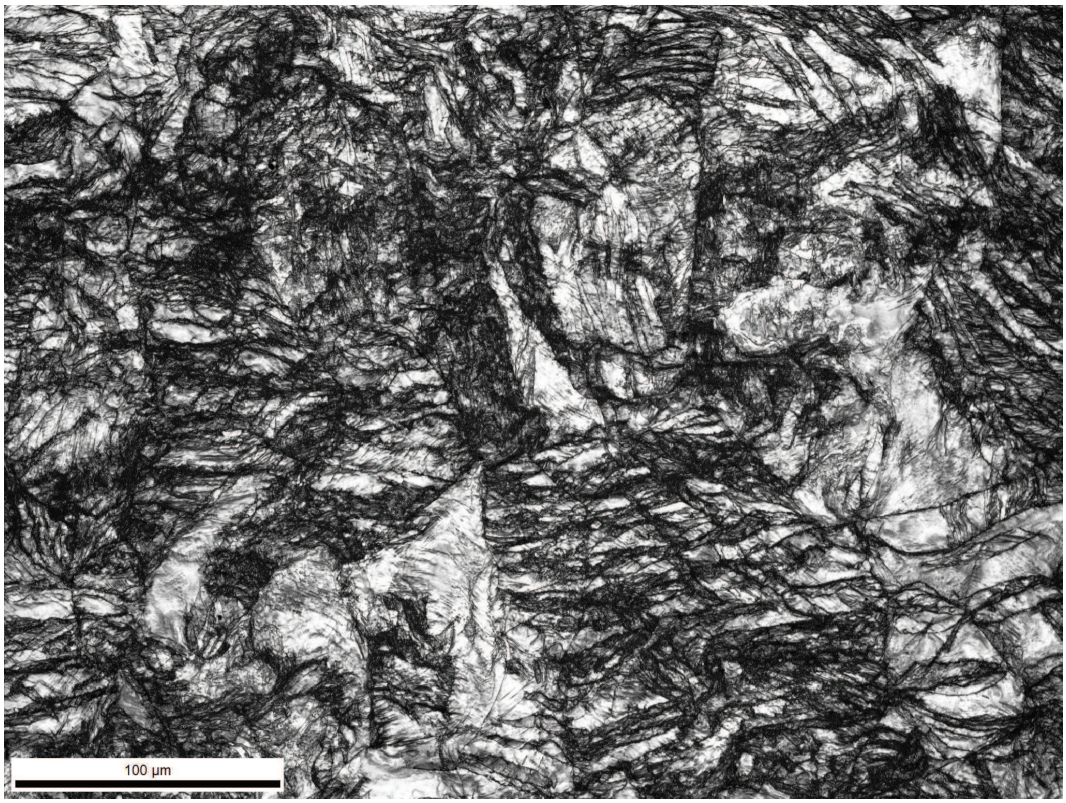

Figure 8.14: IQ map of the TiRoll60 sample, corresponding to IPF map presented above in the Figure 8.13a.

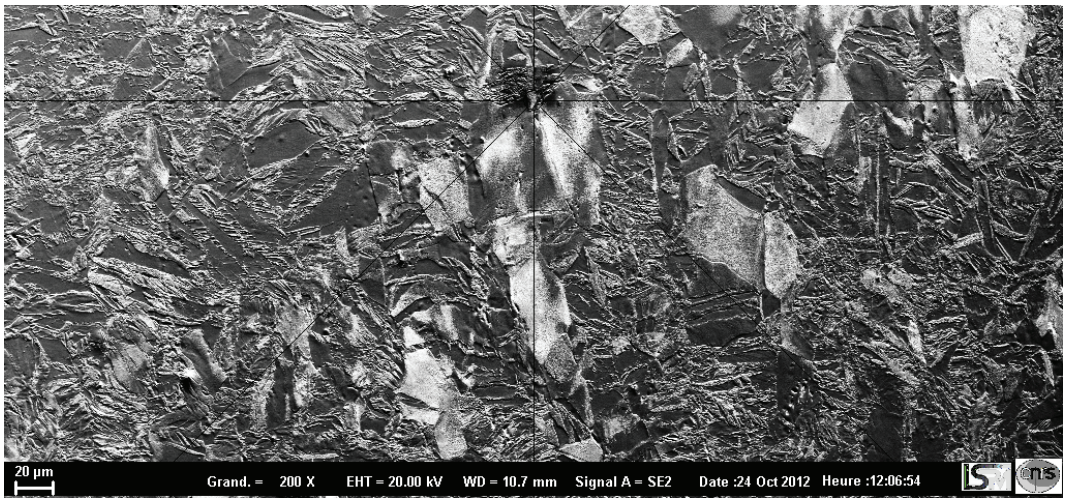

Figure 8.15: SEM image of TiRoll40 sample presenting increased heterogeneity of the deformed microstructure.

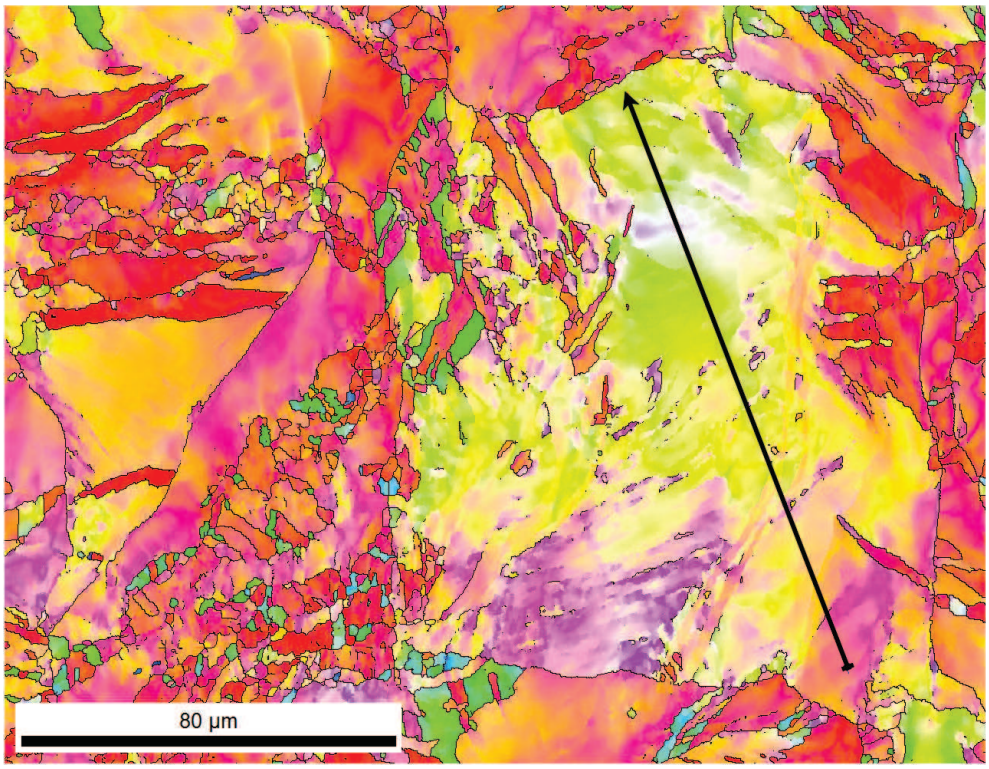

(a)

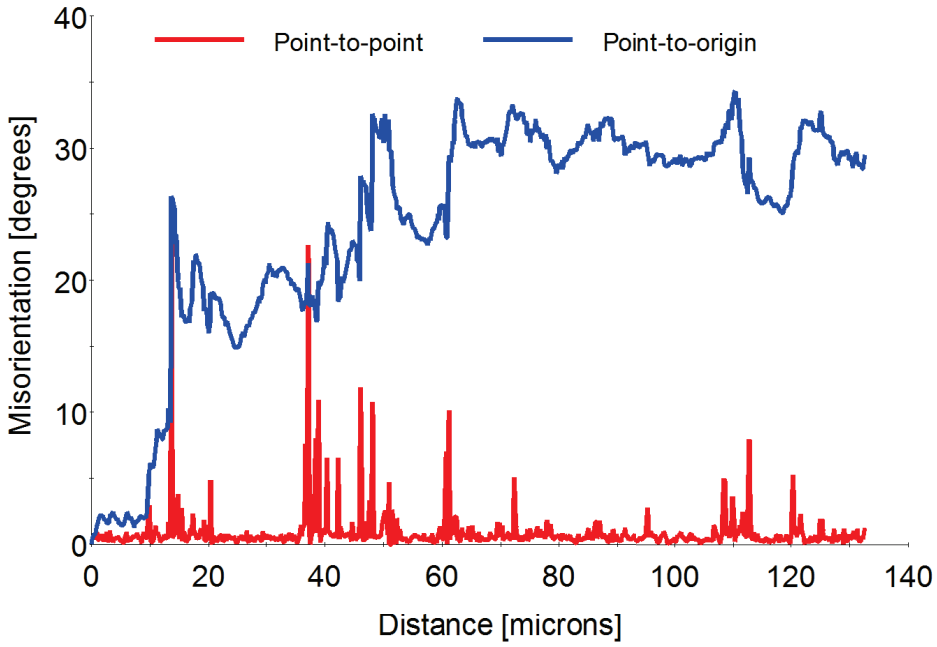

(b)

Figure 8.16: Misorientation profile (b) across a large grain of high orientation gradient (a) in the case of TiRoll60 sample (RD-TD plane).

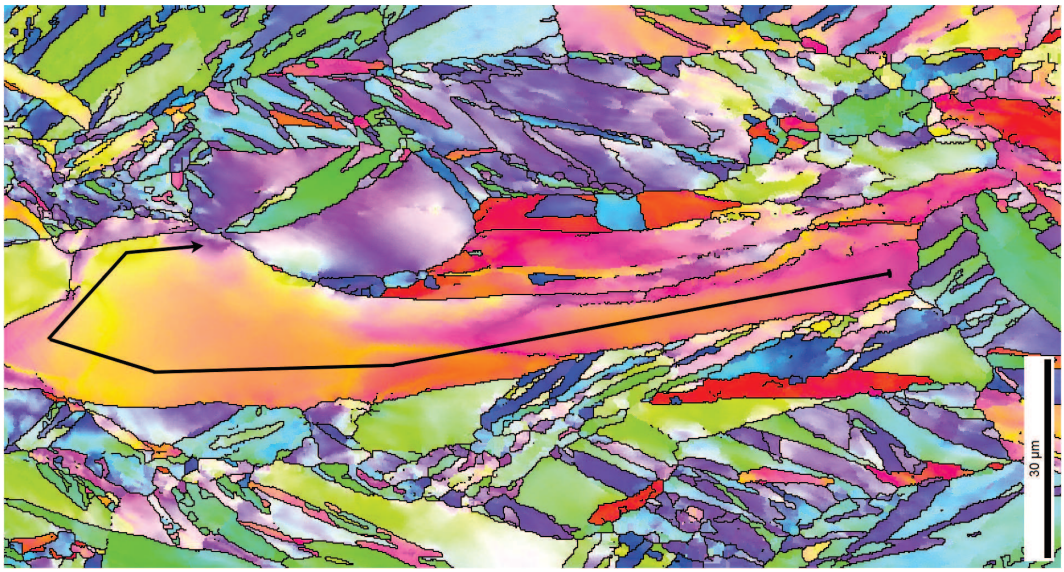

(a)

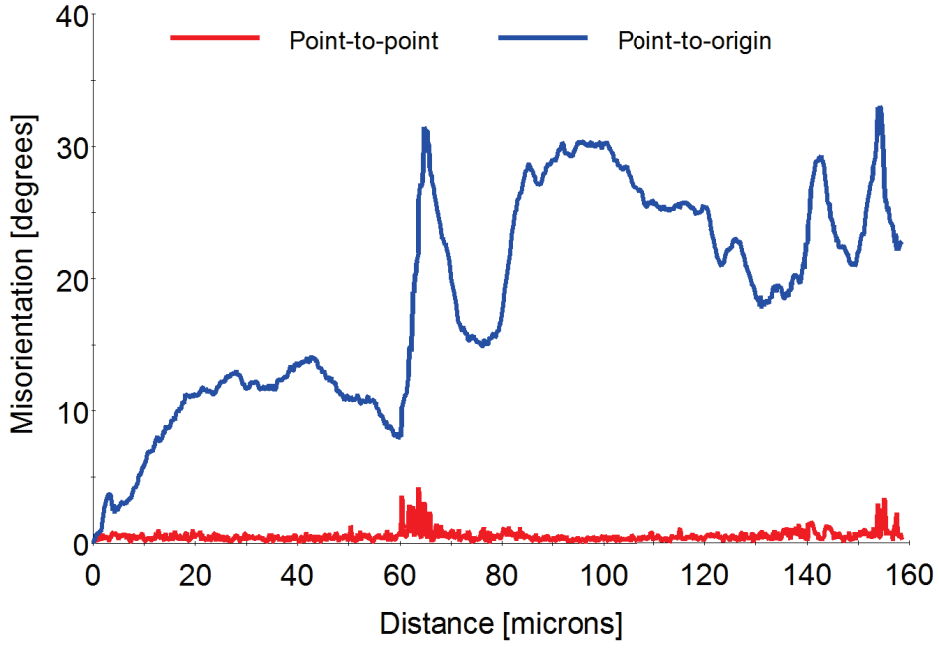

(b)

Figure 8.17: Misorientation profile (b) across a large grain of high orientation gradient (a) in the case of TiRoll40 sample (RD-ND plane).

Analysis of twinning

Activation of twinning can be investigated using analysis of misorientations. Figure 8.18 presents distribution of the misorientation angle calculated for all deformed samples.

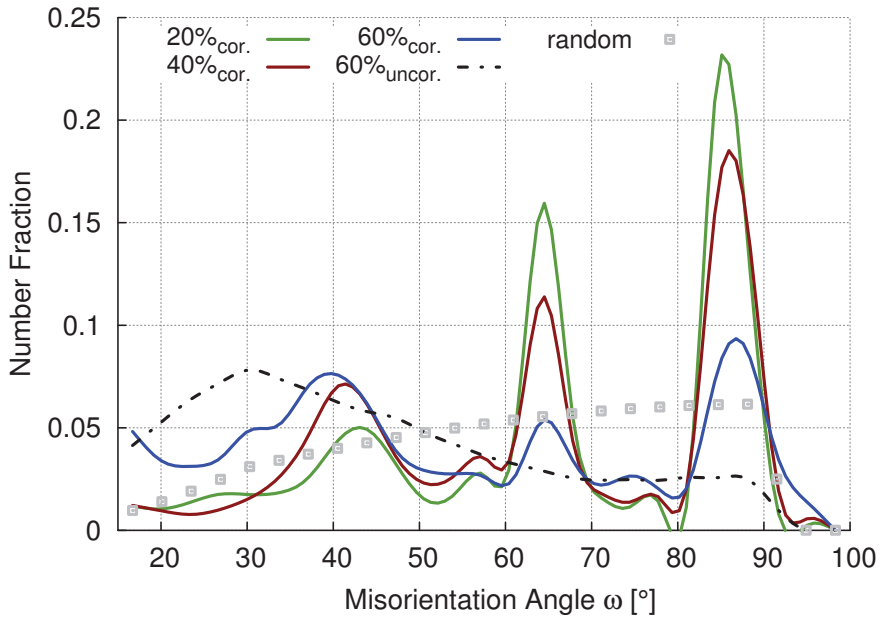

(a) RD-TD surface

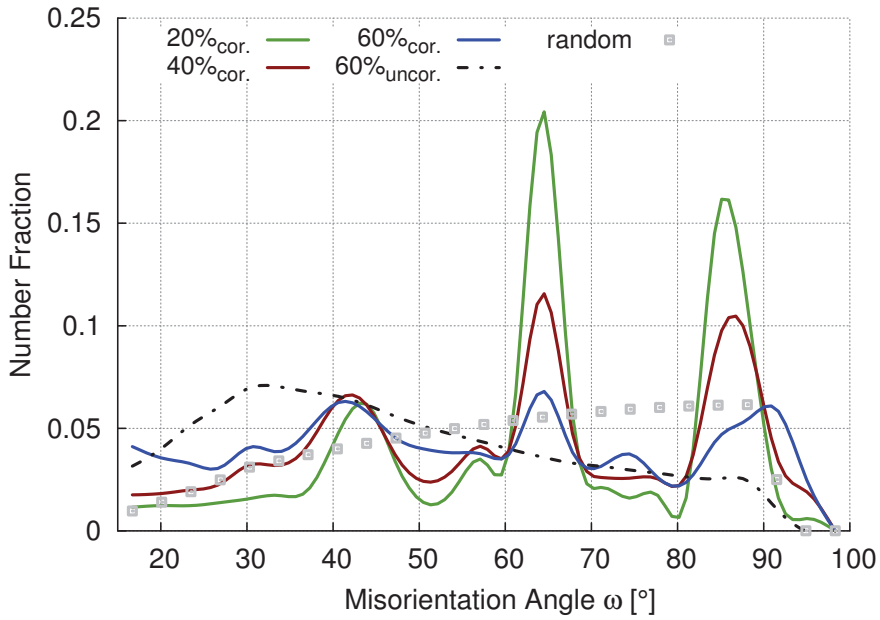

(b) RD-ND surface

Figure 8.18: Misorientation angle distribution at various deformations: 20%, 40%, 60%.

Figure 8.19, in turn, shows texture reduced MDF obtained for TiRoll20.

Based on them, well known tensile $\{10\bar{1}2\}<\bar{1}011>$ (85° around $<2\bar{1}\bar{1}0>$ axis) and compression twins $\{11\bar{2}2\}<\bar{1}\bar{1}23>$ (65° around $<10\bar{1}0>$ axis) are identified in the case of TiRoll20 sample, since activation of these two is connected with maxima observed in the provided figures. Moreover, it can be noted from RD-TD cross-section of this sample that fraction of 85° misorientation angle is much higher in comparison to 65°, whereas opposite situation is encountered in RD-ND cross-section. The observed difference provides some clues about shape and dimensions of the created twins. For instance, tensile twins are expected to occupy much larger area on RD-TD surface, but at the same they are more narrow on RD-ND surface.

The observed difference provides some clues about shape and 3D dimensions of the created twins. For instance, tensile twins are expected to occupy much larger area on RD-TD surface, but at the same they are more narrow on RD-ND surface.

As deformation proceeds further, fraction of compression and tensile twin misorientations is decreased. Based on the previously presented IPF maps, the most probable scenario, to be proposed, is that the ideal axis/angle relation for twin misorientation is lost due to process of extreme fragmentation combined with activation of crystallographic slip.

Another observation concerns a smaller peak around 41° which is slightly increasing, and then is quite stable until the highest strains. Unfortunately, it is difficult to analyze this misorientation using texture reduced MDF since the uncorrelated and correlated distributions are overlapping in this region. However, application of discrete axis/angle distribution, which has been calculated for the minimum angle misorientation, clearly shows that there are axes linked with 41° which are concentrated in the vicinity of one particular direction (Figure 8.19).

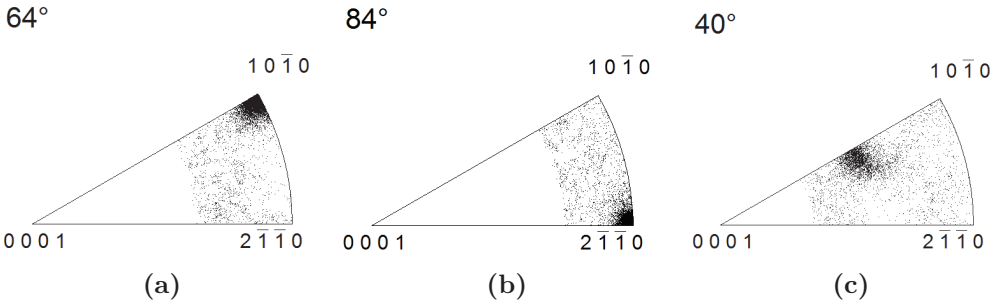

Figure 8.19: Axis-angle distribution for chosen misorientation values obtained for TiRoll20 sample (rolled by 20°).

This is consistent with observations performed by Bozzolo et al. (2010), who have found the same peak in misorientation angle distribution, and identified it as 41° <5$\bar{1}\bar{4}$3> misorientation resulted from tensile twinning {10$\bar{1}$2} inside compression one {11$\bar{2}$2} [53].

Following from that fact, IQ map has been prepared in order to confirm that misorientations defined as 41° <5$\bar{1}\bar{4}$3> (with slight spread, i.e., tolerance equal to 5°) really exist in the heavily twinned regions of the investigated samples (Figure 8.20).

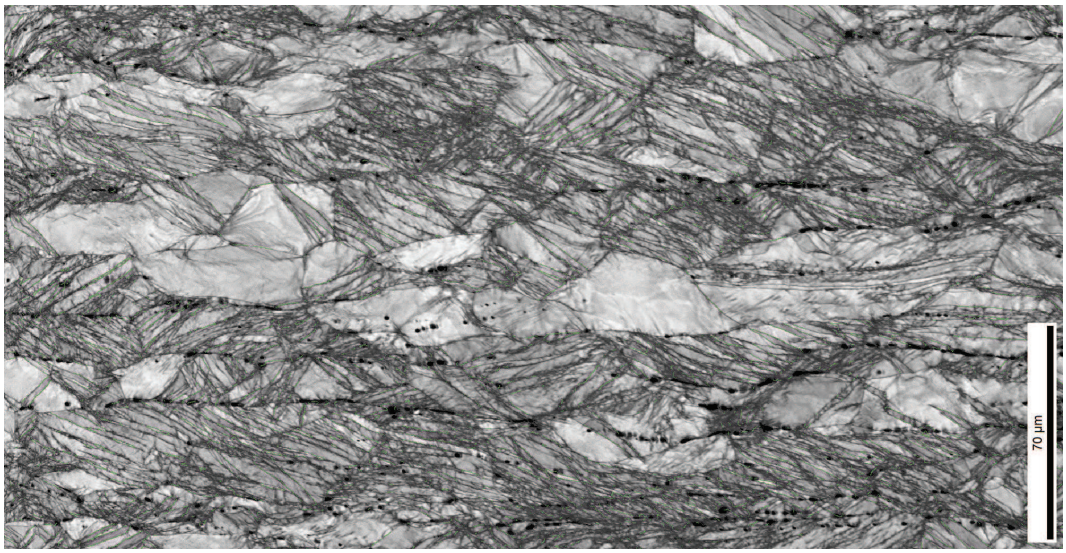

Figure 8.20: IQ map presenting location of 41° <5$\bar{1}\bar{4}$3> misorientations in the sample TiRoll40 (rotated RD-ND plane).

Taking into account the obtained results, it can be argued that decreasing fraction of primary tensile and compression twins, in a significant manner, is connected with further twin fragmentation introduced by double twinning.

In-situ tensile test

Additional analysis of microstructure evolution observed during in-situ tensile test is performed in order to get a wider view on deformation mechanisms taking place in the investigated titanium.

Certainly, comparing tensile deformation with rolling cannot be fully justified since only elongation direction – that is RD - is in common between them, whereas important strain component parallel to ND is externally imposed only in the latter case.

Nevertheless, a possibility to observe another way of microstructure evolution when the mentioned strain component is not active is exactly what is desired at this

point, especially that all the changes can be followed in terms of step by step in-situ procedure.

Four EBSD scans have been conducted during tensile test experiment. One for initial area (Figure 8.21), chosen to observe further, and three for deformation stages: 5%, 10% and 15% of strain, respectively. For the last two, the obtained IPF maps (Figure 8.22) have been rescaled in order to facilitate direct comparison between initial state, 10% and 15% of deformation. Then, SEM images are shown for the case of the finally achieved strain – 20% (Figure 8.23), as a reference.

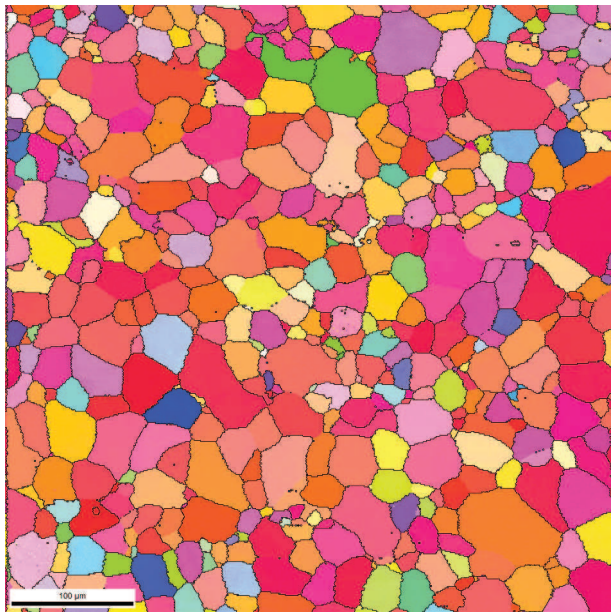

Figure 8.21: Initial area (500 µm x 500 µm; RD-TD plane) investigated by the in-situ tensile test.

It is pointed out that no twins are created during tensile test. Therefore, it can be concluded that accommodation of strain along ND is the reason why twins are formed in such extensive manner during rolling, as expected.

Therefore, grains rather retain their shape instead of being fragmented. Also, strong color gradients appear in many of them due to domination of slip mode. At 15% of strain, these orientation gradients result in HAGB interruption. Examples are shown in the Figure 8.22b. It means that deformation in this case makes grains similarly oriented, at least in the regions located nearby grain boundary, which, in turn, leads to aggregation of smaller grains into larger areas. Such behavior corresponds closely to large untwined areas of continuous orientation spread which are seen in cold rolled samples, and, to some extent, explains their origin.

(a) 10% of strain (560 µm x 470 µm) **(b)** 15% of strain (640 µm x 440 µm)

Figure 8.22: In-situ tensile deformation of the titanium microstructure (RD-TD plane). Please note that the presented IPF maps have been rescaled in order to facilitate direct comparison of grains. Also, on the right side, there are regions marked using white ellipses, where grains start to merge because of interruption of HAGBs caused by orientation gradients.

(a) Detector of secondary electrons (SE)

(b) Detector of backscattered electrons (4QBSD)

Figure 8.23: SEM images presenting Ti microstructure obtained after 20% of elongation along RD.

8.2.3 Microstructure evolution during recrystallization and grain growth of cold-rolled samples

A wide range of applied annealing conditions has allowed to capture several recrystallization and grain growth stages, namely:

- 25% - 30% of recrystallization:
  - TiRex20-600-30m,
  - TiRex40-500-1h,
- 65% of recrystallization: TiRex20-715-5m,
- 90% - 95% of recrystallization:
  - TiRex20-715-15m,
  - TiRex40-600-1h,
  - TiRex60-600-30m,
- further grain growth states:
  - Ti20GG,
  - Ti40GG,
  - Ti60GG.

In this context, it has to be mentioned that the very beginning of recrystallization (i.e. first emerging grains) is difficult to follow and analyze. The main problem arises from the pure statistics related with small number of the recrystallization grains. Also, there is an uncertainty about the origin of nucleating grains as there are two possibilities: the observed grain is really a growing nucleus located in the measured area, or, in the other case, it is a cross-section of much larger grain which grows from a nucleus located somewhere else in the deformed microstructure.

Therefore, 25% of recrystallization is chosen as the first stage of annealing treatment to be analyzed. The following EBSD maps (Figure 8.24, Figure 8.25) present examples of the way how recrystallization grains are formed in deformed microstructure of TiRoll20 and TiRoll40 samples.

In the first one, recrystallization grains are hard to distinguish from surrounding microstructure thus two separated partitions are presented: recrystallized and deformed one. The separation has been achieved using GOS analysis, where grains

with the lowest GOS are recognized as the recrystallized one. Based on that, it is shown that newly created equiaxed grains emerge in particular areas of the sample instead of being homogeneously distributed. Such behavior seems to be linked with significant decrease of twins, which is also confirmed by distribution of misorientation angle (not shown here). At this point, average grain size of recrystallized partition is equal to 11.5 µm.

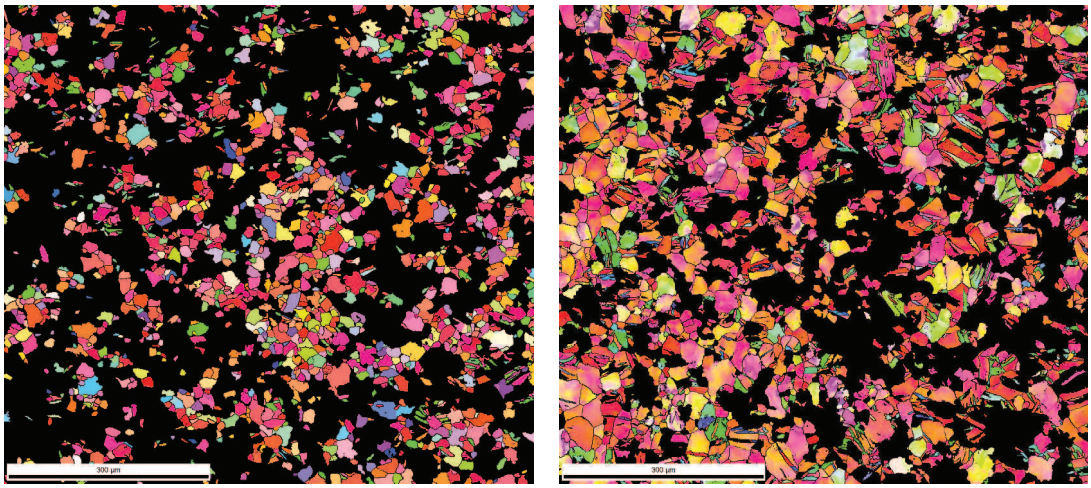

(a) recrystallized partition **(b)** deformed partition

Figure 8.24: Microstructure of the TiRex20-600-30m sample.

For the second sample, IQ maps are precise enough to see clearly the microstructure evolution during annealing (Figure 8.25). In this case a tendency of grains to grow in preferred areas is much stronger since they gather in the form of clusters localized in highly fragmented areas. From this point of view, it is obvious that microstructure heterogeneity developed during cold-rolling has the most important impact on further recrystallization and grain growth phenomena. Among others, it means that recrystallized volume fraction will vary depending on observed area; the more fragmented region, the higher probability of nucleation and thus increased progress of recrystallization. This can be seen by comparing the presented examples (Figure 8.25a and Figure 8.25b).

It is, therefore, expected that number of successfully nucleated grain will increase with prior deformation degree, which affects, in turn, grain size. Indeed, in the considered TiRex40-500-1h sample (remind only 30% of recrystallization), the average size of recrystallization grains is equal to 4.5 µm, which is 2.5 times less than for corresponding TiRex20-600-30m sample. At the same time, it is emphasized that almost recrystallized state obtained after annealing of the highest deformation state

(TiRex60-600-30m sample) exhibits only slightly higher value of average grain size – 5.5 µm.

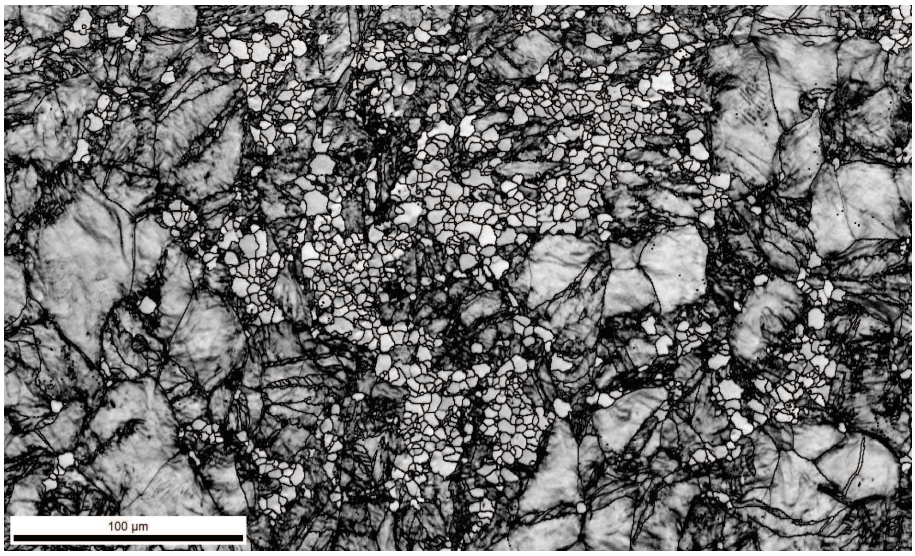

(a)

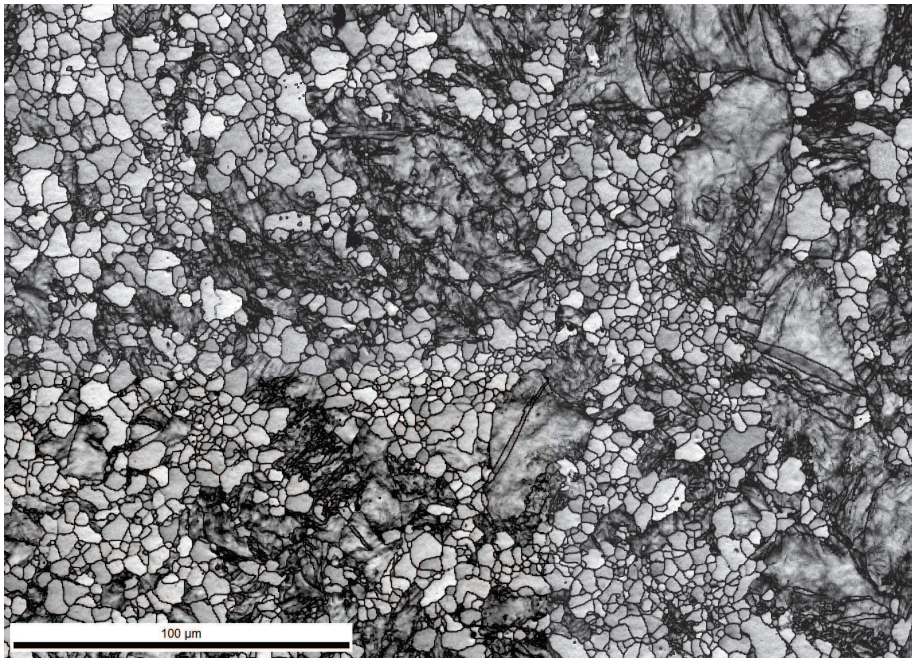

(b)

Figure 8.25: Microstructure of the TiRex40-500-1h sample.

Finally, as a consequence of the discussed nucleation mechanism, large, untwined and still deformed grains are replaced by the population of new grains at final stage of recrystallization, as demonstrated on the following examples (Figure 8.26).

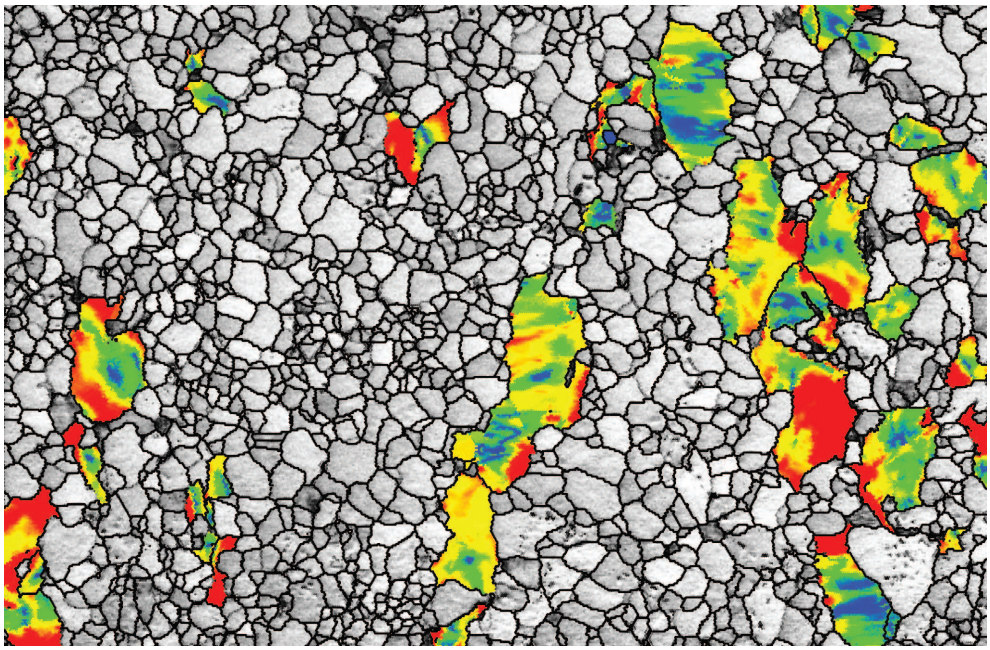

(a) TiRex40-600-1h, unrecrystallized grains are marked by color gradients

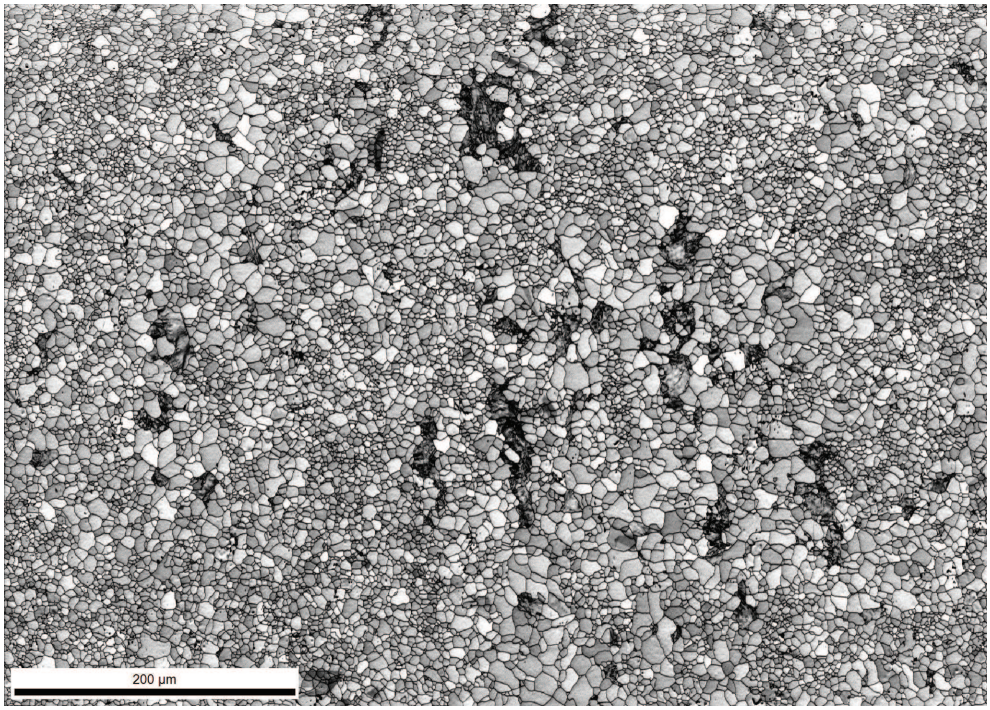

(b) TiRex60-600-30m

Figure 8.26: IQ maps presenting the very end of recrystallization process including the remaining of last deformed grains.

It should be noted that the described microstructure evolution is consistent with the observations reported for highly rolled titanium (see chapter 3).

Analysis of grain size obtained after grain growth

In the next step, the mentioned influence of the prior deformation degree, and related microstructure heterogeneity, on grain size after grain growth is shown qualitatively (Figure 8.27) and quantitatively (Figure 8.28) using data obtained with the same annealing conditions, i.e. TiGG20-715-1h, TiGG40-715-1h, TiGG60-715-1h samples.

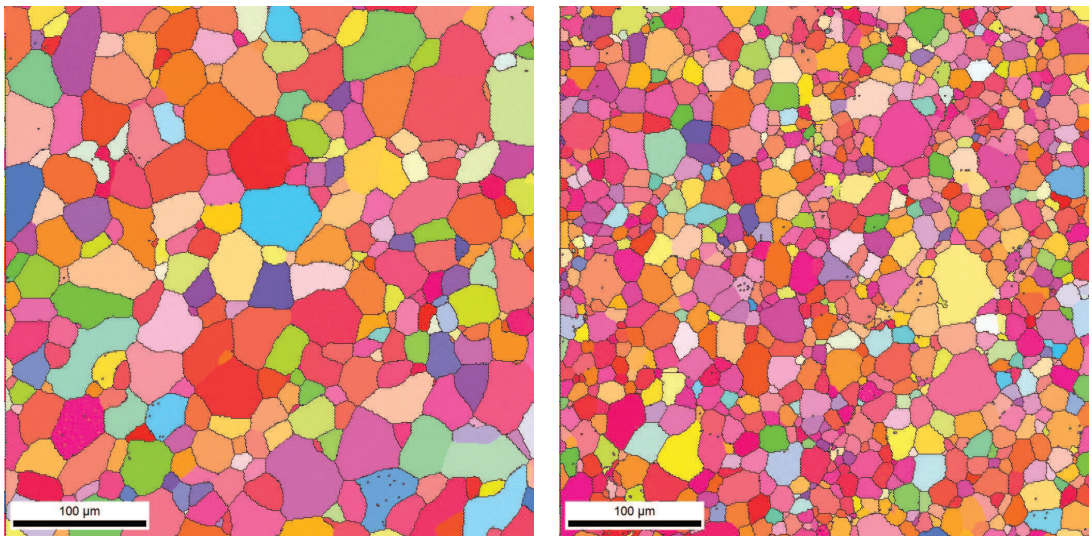

(a) **(b)**

Figure 8.27: Qualitative comparison of grain size obtained after annealing in 715°C over 1h between TiGG20-715-1h (a) and TiGG60-715-1h (b) samples.

Average grain size has been calculated on both measured surfaces for all the three mentioned samples in order to compare them in a quantitative way (Figure 8.28). Based on that, it is clear that there is a link between the degree of deformation and the size of grains obtained after grain growth. Moreover, only for higher prior deformation - 40%, 60% - the average grain size after grain growth is almost the same on both planes, which suggests that real 3D grains can be approximated by spheres in these cases, whereas in initial state and TiGG20-715-1h sample they are more like ellipsoids.

This significant difference between TiGG20-715-1h and TiGG60-715-1h samples has lead to additional analysis of grain size which has been performed for several stages of grain growth (Figure 8.29). This time grain size is given by an average diameter since it allows to compare the obtained results with the literature.

Clearly, in the TiGG20 sample grains are so large just after recrystallization that further grain growth is significantly inhibited. In contrary, in TiGG60 sample grains

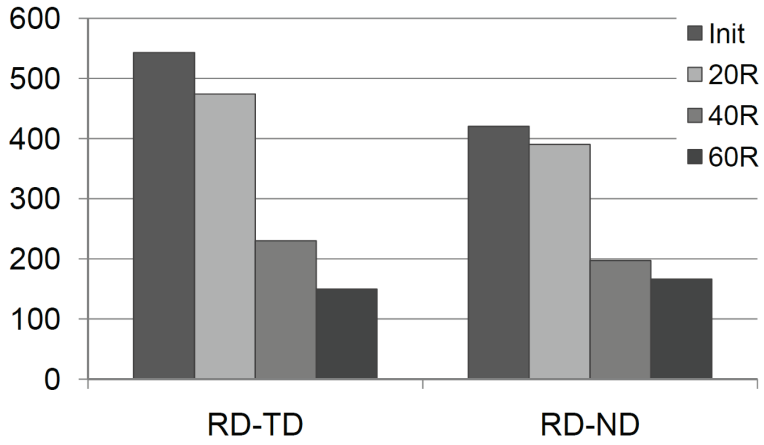

Figure 8.28: Average area grain size [in μm^2] calculated for both planes (RD-TD and RD-ND) of annealed samples (715°C, 1h).

have much higher possibility to grow further; after 12 h of annealing the average grain diameter increased from 5.5 µm to 22.5 µm.

In addition, a glimpse on the nature of grain growth phenomenon can be gained in this case. It appears that grain diameter follows parabolic law of time. This is in a good agreement with already published results [68, 90]. On the other hand, grain growth exponent, estimated as 0.25, indicates that there are factors hindering the growth in the investigated TiGG60 samples, and thus it can not be considered as completely isotropic process.

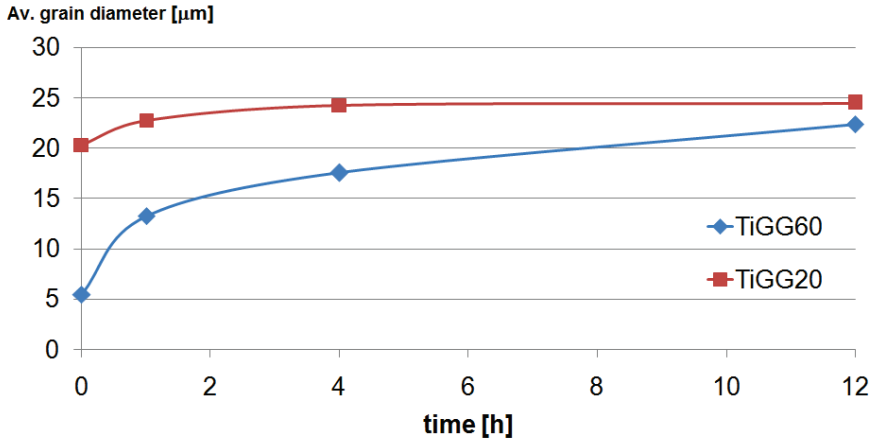

Figure 8.29: Average grain diameter over grain growth process.

Microstructure evolution during grain growth of Ti60GG samples.

On the basis of the presented results, and also taking into account the conclusions withdrawn on the texture evolution (discussed in the next subsection), it is

concluded that TiGG60 samples are the most worthwhile and promising from grain growth point of view thus they are analyzed deeper in terms of misorientations as well as grain size self-similarity. Short discussion about microstructure heterogeneity is also presented.

Distributions of misorientation angle (Figure 8.30) as well as grain diameter (Figure 8.31) have been compared between recrystallized state (TiRex60_600_30m) and three stages of grain growth, namely:
TIGG60-715-1h, TIGG60-715-4h, TIGG60-715-12h.

Analysis of misorientations reveals an interesting effect. The rapid changes are observed for uncorrelated distribution of misorientations (solid lines), whereas the correlated one is stable during grain growth (dashed lines). Also, it should be strongly emphasized that the most significant evolution of uncorrelated distribution takes place until 4 h of annealing, then it is not changed despite long heat-treatment – 12 h. Hence, sample TiGG-715-12h is not shown. Moreover, it is clear that the mentioned evolution is stopped, when both correlated and uncorrelated distributions are nearly the same.

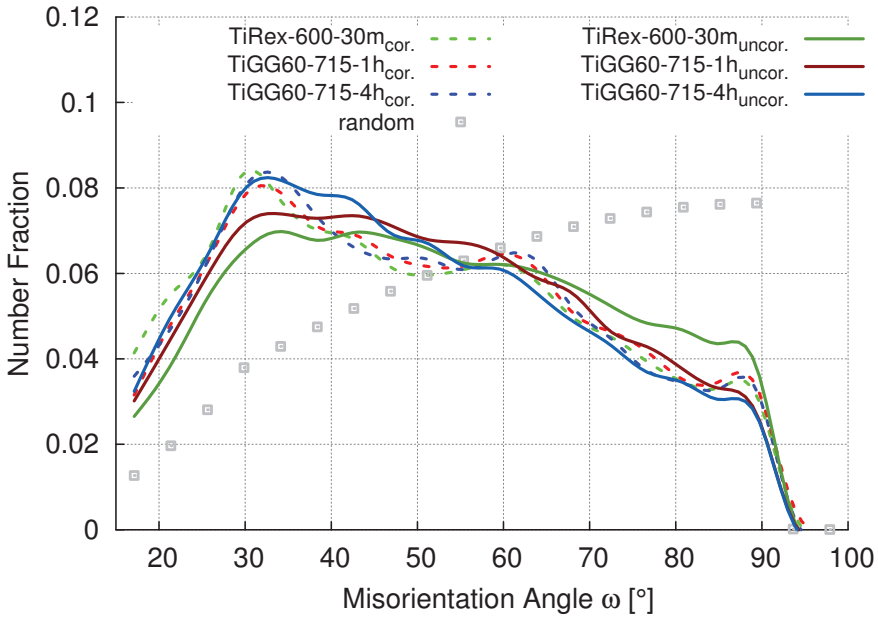

Figure 8.30: Evolution of correlated (cor.) and uncorrelated (uncor.) distributions of misorientation angle observed during grain growth of the Ti60 sample.

The described behavior correlates well with the already presented evolution of average grain diameter which also can be characterized by more dynamic increase in the same annealing regime.

Therefore, it can be assumed that as long as local arrangement of grains is different from the global one, the grain growth is not hindered.

Another conclusion that concerns grain growth process in the investigated samples is self-similarity property of grain size distribution which is confirmed in the following Figure 8.31. It is shown that between different stages of grain growth almost the same distributions are obtained for normalized $D/<D>$ diameter value.

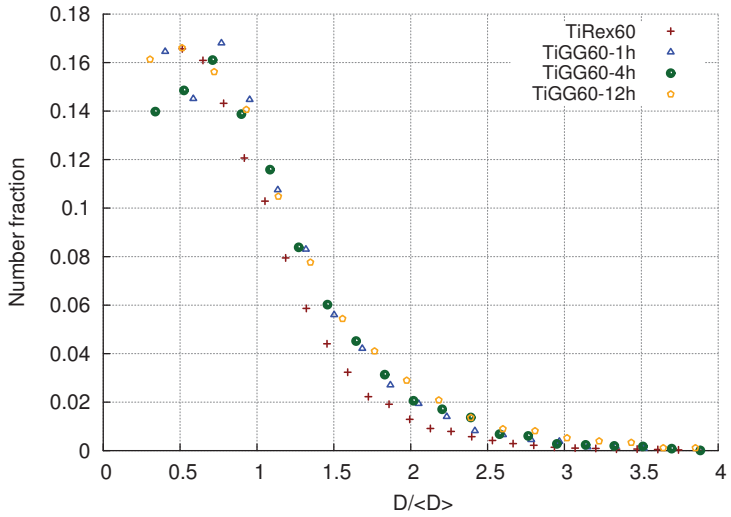

Figure 8.31: Grain diameter distributions during grain growth of Ti60GG sample.

This is consistent with detailed observation of microstructure which indicates that there are no significant differences in terms of size or shape between grains, as it was in the case of some regions in the initial state.

Therefore, the only issue to be mentioned in this context is the influence of heterogeneity of deformed microstructure, especially on RD-TD surface.

As shown above, large areas of orientation spread resist to recrystallization thus they are consumed at the end by growing recrystallization front located nearby. This implies, in turn, that some of the recrystallization grain have to be much larger than the one developed in highly fragmented areas. Consequently, microstructures obtained after further grain growth have also such features; the most extreme example is presented on the right side of the Figure 8.32.

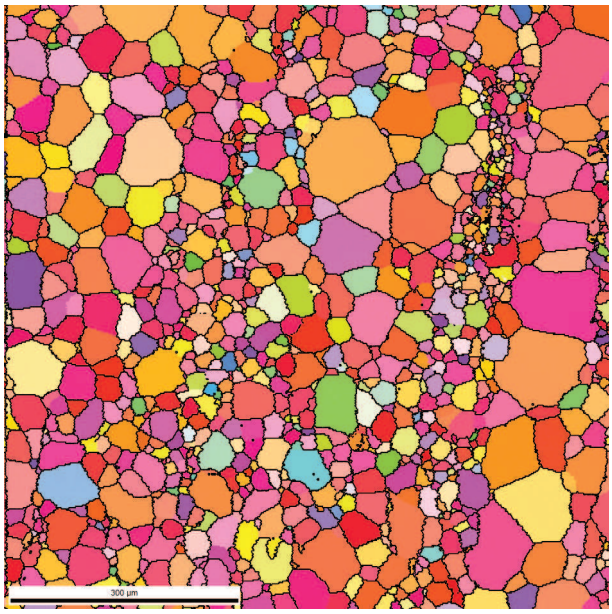

Figure 8.32: Special arrangement of large and small grains observed in the microstructure of Ti60-714-12h sample.

8.2.4 Texture evolution during deformation, recrystallization and grain growth of titanium samples

Following from the fact that in the considered titanium the microstructure evolution is highly dependent on the degree of thickness reduction and associated heterogeneity, it is interesting to explore how the latter can affect texture evolution during deformation, recrystallization and grain growth processes.

Texture of initial state is shown in the Figure 8.33. It is shown that majority of the grains have c-axis oriented almost parallel to ND. Hence, texture maxima are located at the top of ODF cross-sections (Figure 8.33b). They can be described by two orientations: (0°, 10°, 30°) and (180°, 10°, 30°). However, it should be noted that {0001} pole is clearly shifted from the center towards left side of the pole figure (Figure 8.33a), whereas no symmetrically equivalent pole is present on the right side.

Analysis of the deformed state reveals that this asymmetry is further strengthen due to imposed rolling (Figure 8.34). Therefore, only one {0001} pole (and lack of maximum on $\varphi_1 = 180°$ ODF cross-section) is observed in the TiRoll60 sample. Moreover, this effect has been also confirmed by complementary X-ray measurements of pole figures.

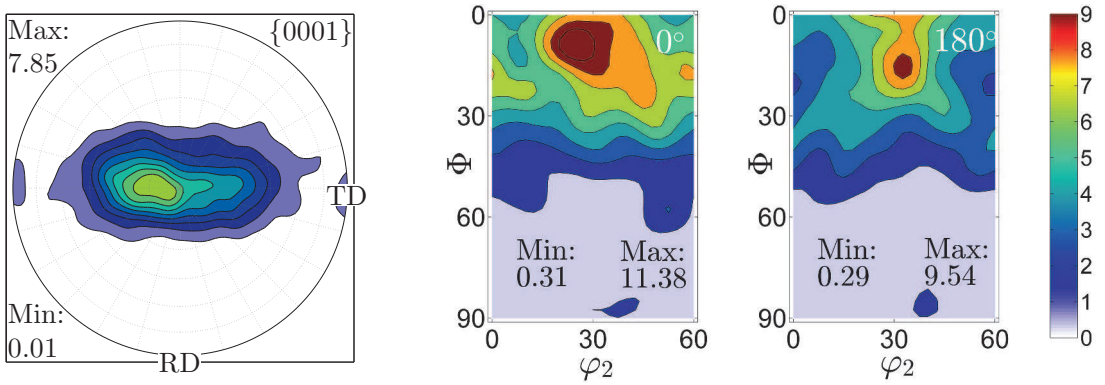

(a) (b)

Figure 8.33: {0001} pole figure - a) and ODF cross-sections ($\varphi_1 = 0°$, $\varphi_1 = 180°$) - b) of the titanium initial state.

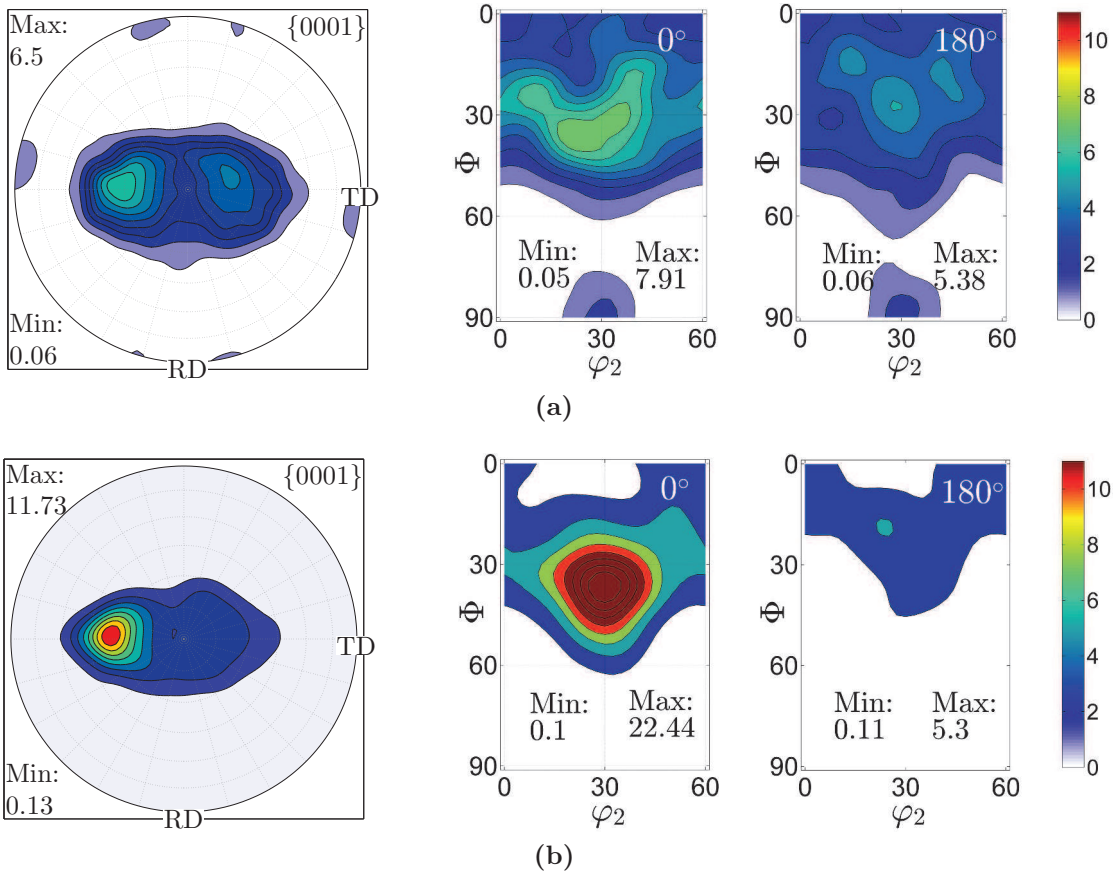

(a)

(b)

Figure 8.34: Evolution of texture during deformation: a) sample rolled by 20%, b) sample rolled by 60%. {0001} pole figure is shown on the left, whereas ODF cross-sections ($\varphi_1 = 0°$, $\varphi_1 = 180°$) are on the right.

It is an interesting and slightly surprising evolution because classical rolling texture, as shown before, comprises of two main orientations positioned between ND and TD, that means two {0001} poles located symmetrically: one on the left side, and second on the right side.

Further analysis of deformation texture reveals that the main component is shifted from initial position toward TD thus ODF cross-section shows maximum at (0°, 35°, 30°) which is continuously strengthen until 60% of thickness reduction - Figure 8.34b. It is so-called tilted {0001}<10$\bar{1}$0> deformation component.

Regarding recrystallization and grain growth phenomena, partially recrystallized samples are analyzed first. It is concluded that, in all the investigated cases, texture of newly created grains is very similar to the prior deformation texture (for instance, compare Figure 8.35a and Figure 8.34a).

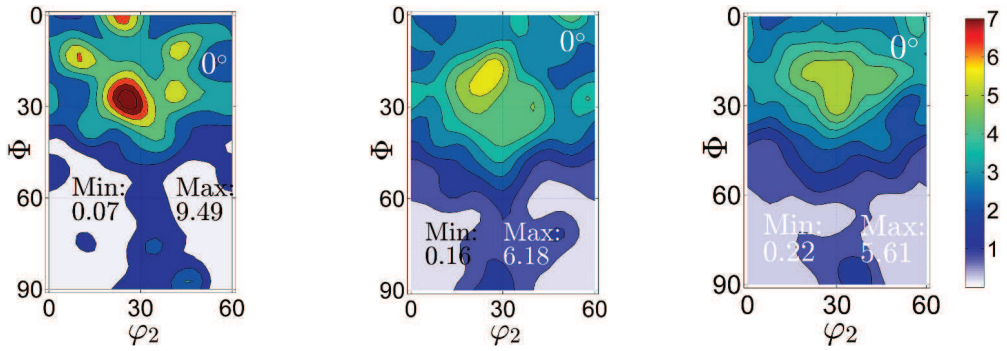

(a) 600 °C, 30 min. Rex. area fraction = 30%

(b) 715°C, 15 min. almost recrystallized $< D > = 21$ µm

(c) 715 °C, 1 h Grain growth $<D>= 23$ µm

Figure 8.35: ODF cross-sections ($\varphi_1 = 0°$) presenting textures of sample rolled by 20% and subjected to different annealing conditions. The information about annealing treatment and obtained average grain diameter $< D >$ is also provided.

As a result, textures obtained just after primary recrystallization do not change much in comparison to the deformed state. Main maximum is only slightly moved toward the top of ODF cross-section. Also, ODF maxima have lower value due to texture randomization, which is usually observed after annealing. Another observation deals with texture of the large unrecrystallized areas in almost recrystallized state. It is concluded that these regions exhibit main orientation located close to (0°, 40-45°, 30°) which has been already reported in the literature [89].

Texture evolution during grain growth is more absorbing since it depends strongly on the way how recrystallized state has been developed. This, in turn, is connected with the amount of stored energy and microstructure heterogeneity in the

deformed samples. Two distinctly different cases are shown, 20% and 60%, respectively (Figure 8.35 and Figure 8.36). In less deformed sample (TiRoll20) grain growth does not lead to important texture evolution, which can be connected with the fact that overall microstructure is almost unchanged during this process.

In contrary, in the case of higher deformation (TiRoll60) there is a continuous rotation of orientations from (0°, 30°, 30°) to (0°, 30°, 0°) over grain growth process, which corresponds to formation of the so-called tilted {0001}<11$\bar{2}$0> grain growth component.

Another result, which is mainly related with the heat-treatment of the highest deformation, is the abovementioned texture asymmetry which is significantly reduced after annealing (Figure 8.36). Nevertheless, it is still present in the texture.

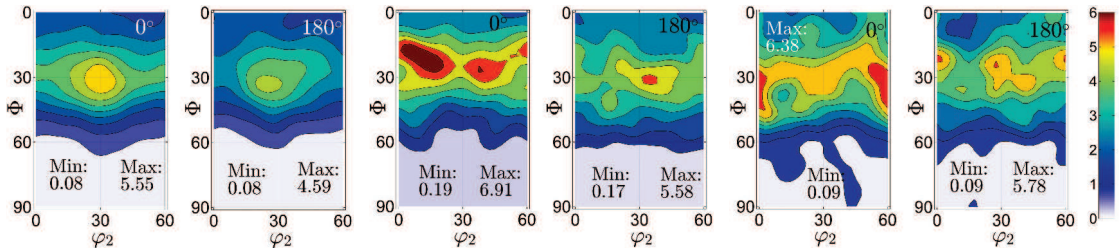

(a) 600 °C, 30 min. almost recrystallized <D> = 7 µm

(b) 715 °C, 4 h grain growth <D> = 18 µm

(c) 715 °C, 12 h grain growth <D> = 23 µm

Figure 8.36: ODF cross-sections ($\varphi_1 = 0°$, $\varphi_1 = 180°$) presenting textures of sample rolled by 60% and subjected to different annealing conditions. <D> is average grain diameter.

Therefore, partial textures have been calculated using the largest and the smallest grains in order to understand this effect. This approach reveal an important difference between them in the TiGG sample (Figure 8.37).

Based on that, it is clear that asymmetry of global texture is caused by the largest grains. Going deeper, it appears that the largest grains are also responsible for (0°, 20°-30°, 10°) orientation significantly pronounced on the ODF cross-section (Figure 8.36b). In contrary, the smallest grains exhibit a texture which can be approximated by (0°, 30°, 0°-60°) and (180°, 30°, 0°-60°) fibers combined with a strong presence of (180°, 30°, 0°) orientation.

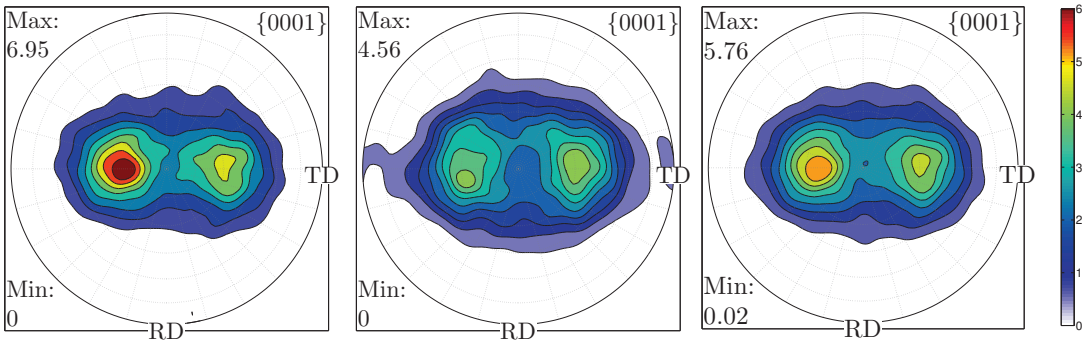

(a) the largest grains **(b)** the smallest grains **(c)** all the grains

Figure 8.37: {0001} pole figures showing influence of large grains on final texture obtained after grain growth – TiGG60-715-4h sample.

8.2.5 Analysis of grain boundary curvature

Microstructure of the TiGG60-715-4h sample appears as an important step in the microstructural evolution since it is the moment when grains are much larger in comparison to the recrystallized state. Moreover, there are first signs of more pronounced texture evolution. Therefore, it is analyzed in terms of grain boundary curvature, which is expected to play the most significant role as a driving force for further growth.

The curvature is estimated using algorithm and boundary representation explained in chapter 7. Obtained results are divided into the most concave and the most convex grain boundary fragments. Then, partial textures are calculated for each of them and presented in the Figure 8.38.

Based on that, it can be assumed that concave boundaries are mostly linked with the largest grains since they also exhibit strong (0°, 20°, 10°) orientation. In contrary, main orientations of areas adjacent to convex boundaries are located along the same fibers which were identified above for the smallest grains in the TiGG60-715-4h sample.

Further comparison of the obtained partial textures with the texture of the Ti60GG-715-12h sample leads to a surprising observation that orientations of smaller grains (and convex boundaries) are developed further during grain growth. However, this might be just a coincidence related to statistics of partial textures.

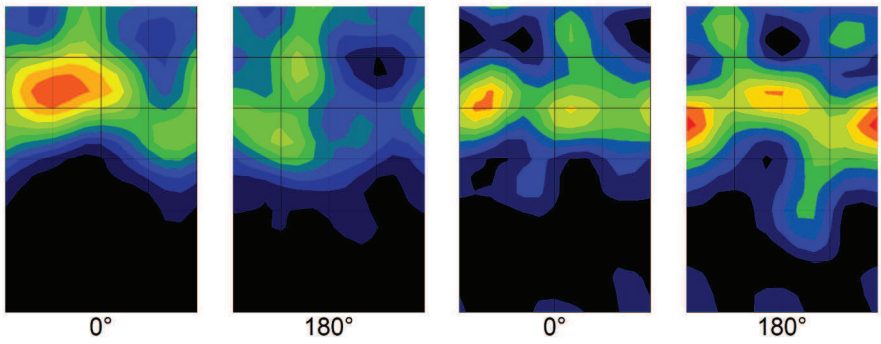

(a) concave boundaries **(b)** convex boundaries

Figure 8.38: Texture analysis of concave (a) and convex (b) grain boundaries. Two ODF cross-sections are presented for each case: $\varphi_1 = 0°$ and $\varphi_1 = 180°$. The color scale is separeately adjusted. Maximum ODF value is equal to 11 - a) and 9 - b).

8.3 Simulations of recrystallization and grain growth

The objectives of this section are two-fold. First, the potential of the developed MC model can be estimated using real experimental data instead of synthetic tests. Secondly, conclusions obtained from EBSD analysis can be confronted with simulations which, in turn, can provide valuable information for further refinements of the mechanisms being involved during recrystallization. Moreover, simulation of normal grain growth is performed in order to shed more light on the texture evolution observed in Ti60GG samples.

8.3.1 Simulation of recrystallization of TiRoll60 sample

As it is shown in the previous sections and also in the literature overview, beginning of recrystallization in cold-rolled titanium is strongly connected with severely fragmented areas which are preferable place for nucleation.

Following from that fact, it is assumed in the applied physical model that these areas exhibit the highest stored energy. Consequently, the stored energy distribution is accordingly prepared using local misorientations in such a way that promotes sites from the fragmented regions. It means that they exhibit the highest misorientation value. Then misorientation of each site in the MC lattice was rescaled in order to obtain desired range of stored energy – $(0 - 4.5)$ in this case. Example of the resulting stored energy distribution is presented in the Figure 8.39.

Simulation is performed using square lattice comprising of 1000×751 sites, corresponding $kT = 0.5$.

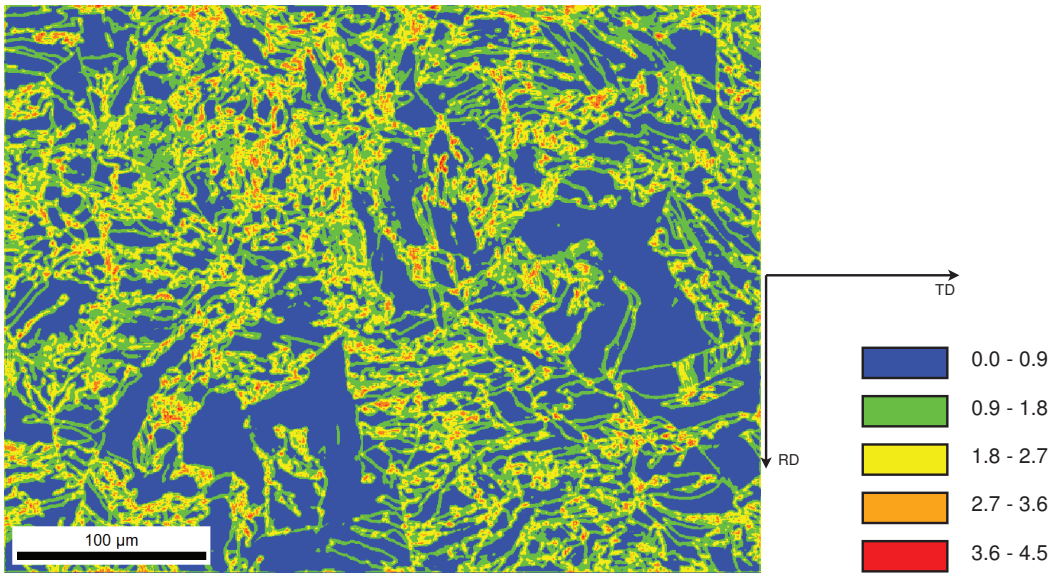

Figure 8.39: Example of stored energy distribution used in simulation of recrystallization of TiRoll60 sample.

As shown in the next figure, such an approach, combined with site saturated nucleation in the regions of the highest stored energy, leads to clustered nucleation at the beginning of simulation.

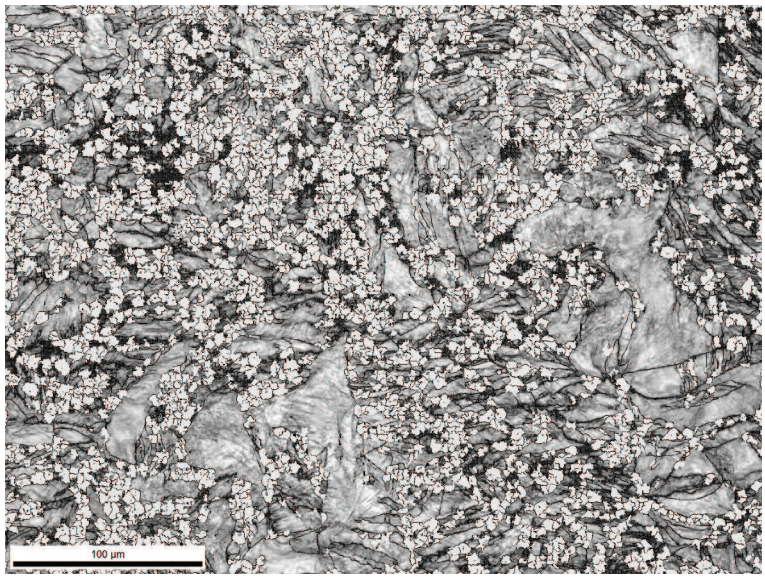

Figure 8.40: Clustered grains emerging during simulation of recrystallization of TiRoll60 sample.

Moreover, large untwined grains remain in the microstructure until last stages of the simulation, then they are finally consumed. Such situation is presented in the Figure 8.41, where black regions are still unrecrystallized. They can be easily compared with IQ map from the Figure 8.40 in order to confirm that they are indeed large areas of orientation spread.

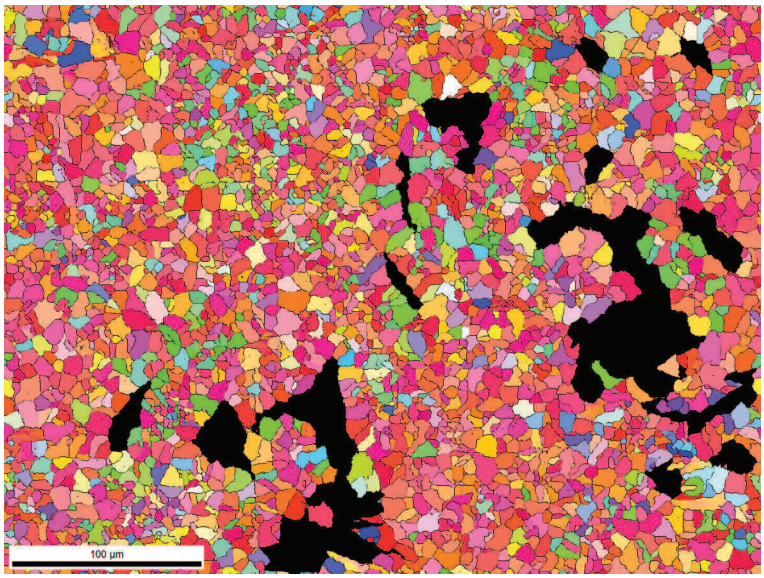

Figure 8.41: Recrystallized partition of the titanium microstructure obtained at the end of the simulated recrystallization process.

The obtained results are in very good agreement with experimental observations. This conclusion is also further confirmed by comparison of grain size distribution and texture with the TiRex60 sample. As it can be seen in the Figure 8.42, the simulated and the experimental grain diameter distributions are very similar, whereas the provided $\varphi_1 = 0°$ ODF cross-section contains (0°, 30°, 30°) main component, already described in the experimental part.

Nevertheless, apart of these very promising results, there is one parameter to be mentioned which is difficult to reproduce in simulation, namely misorientations. Figure 8.43 presents distributions of misorientation angle obtained from two different simulations.

Simulation 1 is the one discussed above, where orientation of potential nuclei site is inherited from the deformed site. In this case, the experimentally observed difference between correlated and uncorrelated distributions is well modeled. However, the highest number fraction is attributed to 50° misorientation angle, which is not correct. Similar situation is encountered using microstructure from RD-ND section.

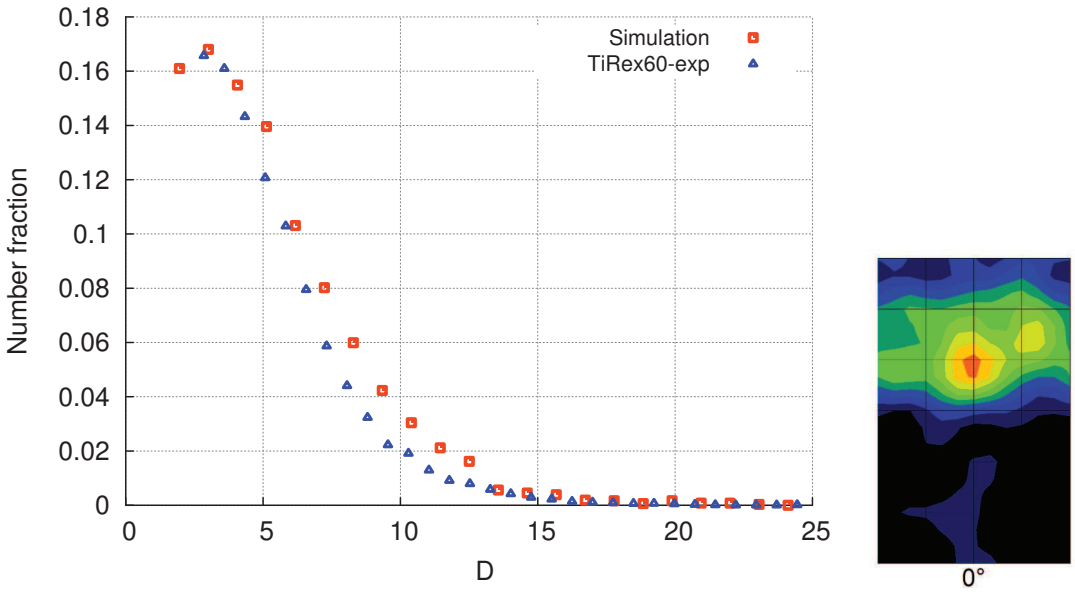

Figure 8.42: Comparison of modeled and experimental grain diameter distributions (left) and $\varphi_1 = 0°$ ODF cross-section calculated from simulation data (right).

In contrary, simulation 2 is performed assuming that orientation of nuclei site is randomly chosen from global deformation texture. This approach yields much better fraction of 30° misorientation angle, but at the same time the mentioned difference between correlated and uncorrelated distributions is lost.

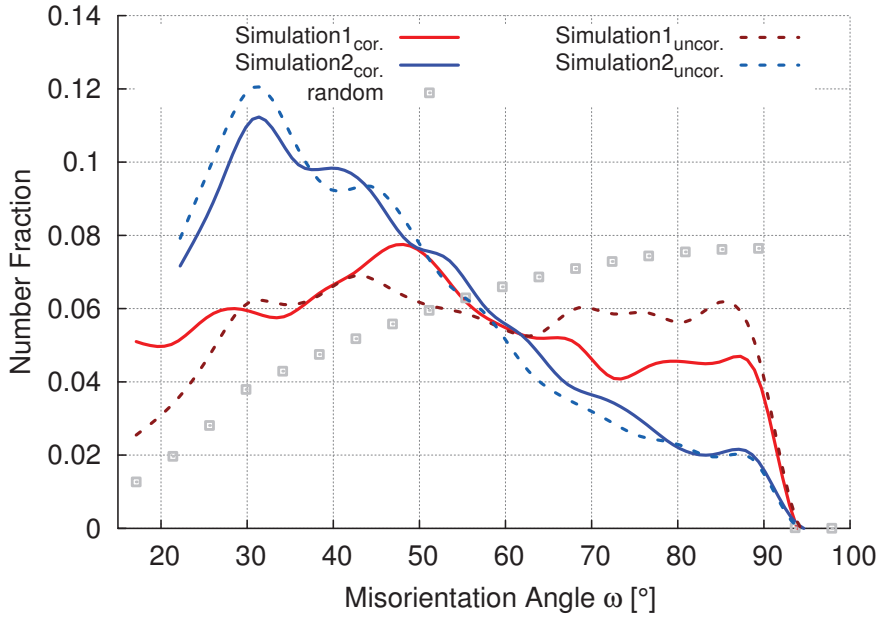

Figure 8.43: Comparison of misorientation angle distributions between two simulation cases.

All these problems arise from the fact that highly fragmented areas in the deformed microstructure have the worst EBSD indexation thus they can be highly influenced in terms of local misorientations. Also, such microstructure has to be slightly coarsened in order to reduce the size of MC lattice and corresponding simulation time. This, in turn, has an unfavorable impact on misorientations.

Therefore, it can be concluded that procedure of nucleation in highly deformed microstructures has to be carefully analyzed in terms of texture.

8.3.2 Simulation of grain growth

Modeling approach and the developed simulation framework have been also employed in order to analyze grain growth process observed in TiGG60 samples. Texture evolution and grain growth kinetics are the key points of interest in this case. Four scenarios are considered which are different in terms of anisotropy of mobility and energy of HAGBs.

The anisotropy is introduced by varying the θ_m parameter in mobility and energy equations (see chapter 5).

Consequently, following simulations are performed:

simulation 1, $\theta_m = 15°$,

simulation 2, $\theta_m = 30°$,

simulation 3, $\theta_m = 45°$,

simulation 4, $\theta_m = 60°$.

In all these cases, the same EBSD map of the TiRex60 sample is used as the initial microstructure.

The examined grain growth kinetics is shown in the Figure 8.44. It can be noted that simulation 2 provides the best outcome in reference to the experimental results. Grain growth is more rapid at the beginning, and then it is slightly suppressed. Although, the estimated grain growth exponent - 0.4 - is still different from the real one.

Further analysis of texture evolution confirms that simulation 2 is the most interesting scenario. Only in this case a transition between deformation and grain growth components is observed, when grain diameter is equal to 21 µm, as shown in the Figure 8.45. In addition, ODF cross-section of texture resulting from simulation 1 is presented as a reference.

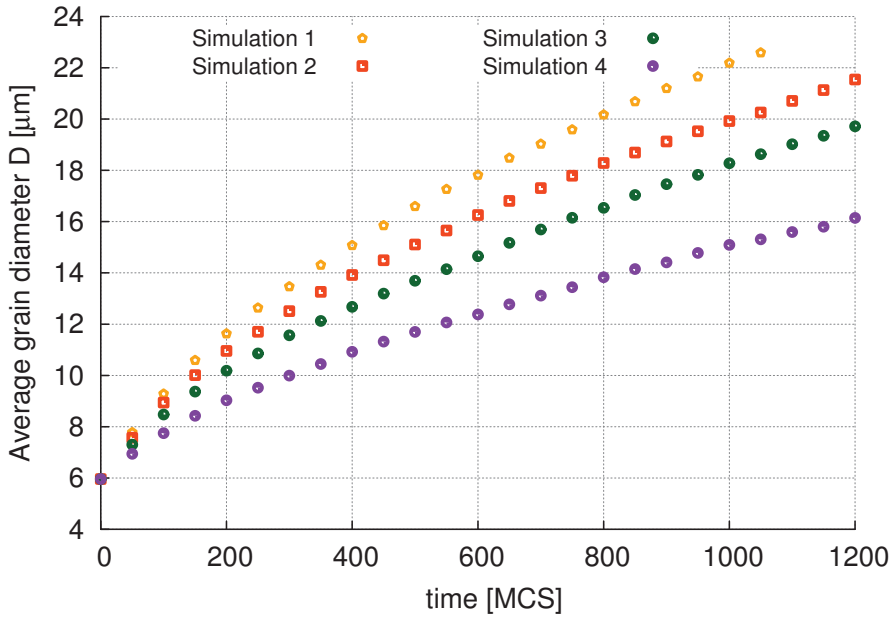

Figure 8.44: Comparison of grain growth kinetics between four simulation cases.

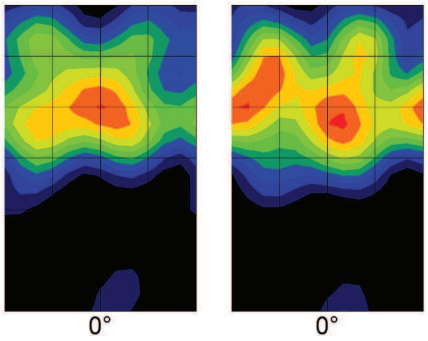

(a) simulation 1 **(b)** simulation 2

Figure 8.45: Texture analysis of the simulated grain growth process.

Based on the obtained simulation results, it can be concluded that the mechanism of grain growth in which HAGBs with misorientation angle lower than $\theta_m = 30°$ have much lower energy and mobility is highly possible thus it should be investigated in more details, especially on the use of real 3D microstructures. Nevertheless, it can be noted that more advanced physical model of the investigated grain growth phenomenon should be refined in the future.

8.4 Summary and conclusions

This work focuses on the investigation of texture and microstructure evolution of commercially pure HCP-Ti caused by cold rolling and subsequent heat-treatment.

The examined set of samples includes three steps of the imposed deformation, it means 20%, 40%, 60% of thickness reduction, as well as a wide range of annealed samples. Such an approach gives an opportunity to capture in details the moment when more significant changes occur in microstructure and texture. The mentioned evolution is expected based on the literature survey, in which thorough research has been reported for the case of highly cold-rolled and heat-treated titanium.

It is confirmed that compression and tensile twins play significant role at early stages of deformation, then microstructure is put toward high heterogeneity caused by severely fragmented regions and large areas of significant orientation spread. The latter, as revealed by additional in-situ tensile test, are most probably formed by adjacent grains of similar orientation which, due to local misorientations, are not delimited by HAGBs anymore.

Appropriate heat treatment leads to equiaxed microstructures. It is shown that parameters important from the viewpoint of final properties, such as grain size and texture, are strongly related with the level of the prior deformation. The size of recrystallized grains decreases with rolling reduction degree, which is consistent with the conclusion that highly fragmented areas obtained by higher deformations constitute a preferable place for nucleation.

Regarding texture evolution, the most important conclusions concern grains created at the beginning of recrystallization process as well as texture changes observed during advanced grain growth. It is shown that only in the case of long annealing of sample rolled by 60% the transition from tilted $\{0001\}<10\bar{1}0>$ into tilted $\{0001\}<11\bar{2}0>$ is activated, whereas only slight evolution is observed after recrystallization.

Another interesting issue is the asymmetry of $\{0001\}$ pole figure observed in the investigated samples, especially after deformation, which results in the fact that the most important information is included only in the $\varphi_1 = 0^\circ$ ODF cross-section. It is also concluded that the higher deformation, the less texture asymmetry is seen after grain growth.

The presented microstructure and texture evolution is in a very good agreement with the conclusions presented in the literature overview (chapter 3).

Finally, it can be emphasized that the developed software for MC modeling of recrystallization and grain growth phenomena is capable to deal with real problems encountered in the experiment. In this context, both conducted simulations of recrystallization and grain growth give satisfactory results.

Regarding recrystallization phenomenon, the important role of clustered nucleation in highly fragmented areas it taken into account. Therefore, stored energy distribution is appropriately estimated. Such mechanism allows to predict with a good precision the overall microstructure evolution and related distribution of grain size. Obtained texture is also positively verified in this case.

Grain growth, in turn, is modeled using various degrees of anisotropy of boundary energy and mobility. Simulations indicate that 30° misorientation is the best threshold value which separates more mobile HAGBs from the rest since only in this case texture evolution as well as grain growth kinetics are approaching to the reality.

CHAPTER 9

Investigation of recrystallization in zirconium (Zr702α) based on EBSD measurements and Monte Carlo modeling

The main purpose of this chapter is to relate early stages of plastic deformation with subsequent recrystallization of hexagonal zirconium. In order to achieve this goal, an EBSD investigation is performed on several zirconium samples which were variously channel-die compressed in two perpendicular directions: normal direction (ND) and transverse direction (TD) of initial material sheet, and then briefly annealed to reach partly recrystallized state. Such an approach gives a possibility to distinguish statistically these grains which are consumed first by recrystallization front, and these which are the most resistant to recrystallization. As a consequence, it allows to explore various scenarios concerning mechanisms of accumulation of dislocations and related sub-grain formation.

EBSD data are thus analyzed in terms of texture evolution associated with thorough description of microstructure features, including local misorientations, orientation gradients, twinning, grain size distributions, grain boundaries. It should be noted that the latter are also characterized based on the approach presented in chapter 7.

A part of this work deals with the mechanisms of accumulation and rearrangement of intragranular substructure, as macroscopically there is some difference in the mechanical response of the investigated zirconium depending on the compression

direction. This, in turn, can be important from recrystallization point of view.

The obtained results and proposed hypotheses are compared further with predictions provided by simulation approach in order to withdraw general conclusions.

9.1 Experimental material and procedure

Commercially pure zirconium (Zr702α) was used to prepare several samples to be subjected to two alternative deformation routes. The starting material was furnished as a metal sheet in a rolled and annealed state.

The metal sheet was then cut using an oil-cooled wire saw into parallelepipedic samples of dimensions 8.12 mm, 6.30 mm, 6.30 mm for channel-die compression, with the longest dimension parallel to the initial rolling direction (RD) of the sheet.

One sample was then left as a reference for the initial state. All other samples were mechanically polished on one side to fit the width of the compression channel (approximately 6 mm), and then coated in Teflon tape, and compressed in a channel die using an Instron 1195 testing machine (Figure 9.1).

Figure 9.1: Instron 1195 testing machine.

Three samples were compressed along ND, while three other samples were compressed along TD. In both cases, elongation was restricted to RD (see Figure 9.2), and the surface subjected to the load had the same dimensions (8.12 mm x 5.94 mm).

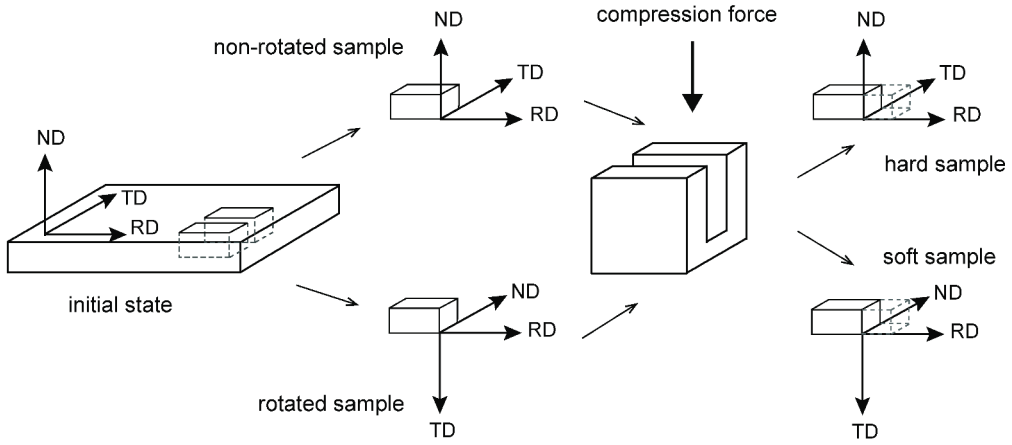

Figure 9.2: Reference systems and deformation geometry for compressed samples.

Final reduction ratios of 7%, 12% and 17% (for ND), and 9%, 10% and 17% (for TD) were achieved.

It was observed that compression along ND required a slightly higher force than compression along TD. Because of that, the samples deformed in ND will be called hard (H) samples, and those deformed in TD will be called soft (S) samples.

Table 9.1 contains a list of all deformed samples, their final reduction, and some information about the maximum applied compression force.

Table 9.1: List of deformed samples and associated compression parameters

Sample	Maximum applied force at final strain [kN]	Final strain ϵ
H17D	53	0.17
H12D	48	0.12
H07D	41	0.07
S17D	46	0.17
S10D	39	0.10
S09D	37	0.09

All samples in this work will be denoted according to compression plane (H or S) and deformation percentage: for example, H17D refers to a hard sample (RD–TD plane) deformed to 17% of strain, while H17R means that the H17D sample was further annealed.

It has to be mentioned that these experiments are quite close to those performed by Francillette et al. (1998) [62], which revealed the strong influence of the initial texture on the activated slip systems, resulting hardening curve and level of

macroscopic stress.

As already noticed by Francillette et al. (1998), the soft samples correspond mainly to the activation of easy prismatic glide systems, and the resulting hardening curve is almost linear in this case. Conversely, the hard samples are associated with the activation of prismatic glide and secondary hard systems thus the hardening curve has a parabolic shape in this case.

Nevertheless, maximal strains considered in this thesis are much lower than those applied by Francillette et al. (1998), which means that activation of secondary slip systems is very unlikely. Therefore, slightly different deformation mechanisms can be expected in this work even if the obtained stress/strain curves seem to confirm the abovementioned conclusions (see Figure 9.3).

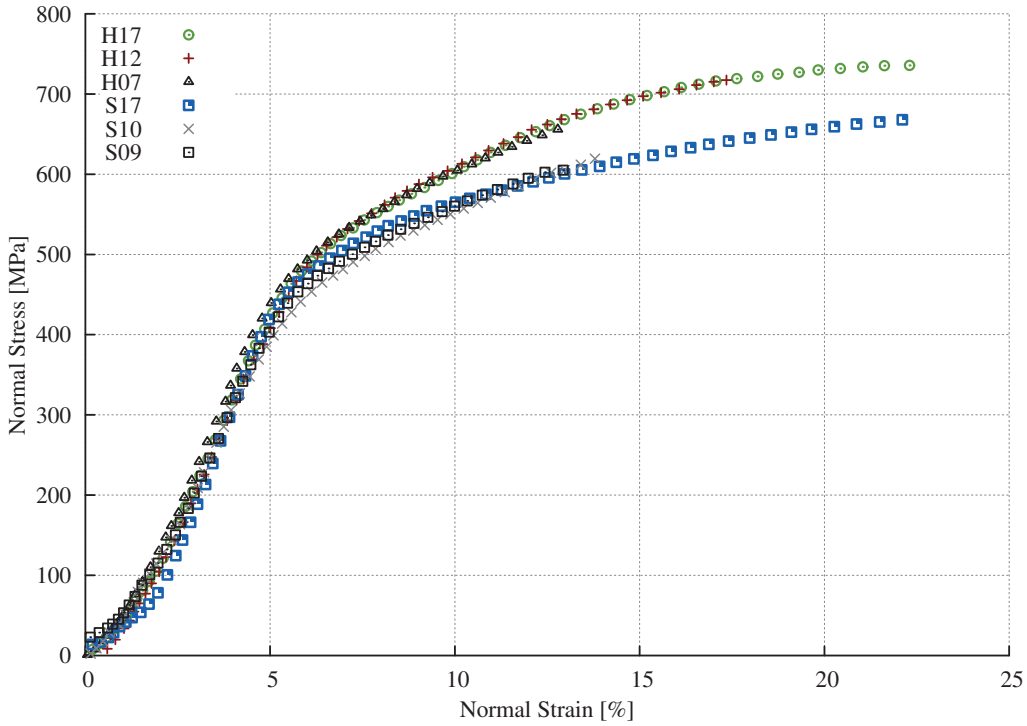

Figure 9.3: Experimental compression curves for the H and S samples. Note that the beginning of the curve is affected by slight discrepancy between sample dimensions and channel width as well as by compression of the Teflon used for lubrication.

Each sample was then cut into two parts. The cutting plane was taken perpendicular to the compression direction. Based on microhardness measurements (Figure 9.4), one part was annealed at 615 °C for 15 min. to achieve partly recrystallized state, whereas the second part was left in the deformed state.

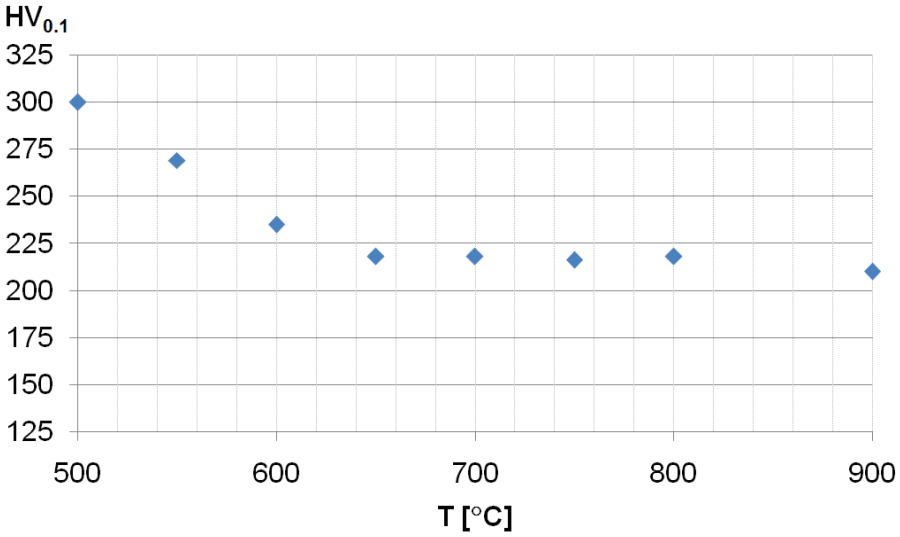

Figure 9.4: Zirconium microhardness after annealing over 15 minutes at various temperatures. The presented values were obtained using Vickers hardness test.

Hence, the following sets of samples were prepared for EBSD analysis:

1. initial state: H00, S00,
2. deformed state: H07D, H12D, H17D, S09D, S10D, S17D,
3. annealed state: H07R, H12R, H17R, S09R, S10R, S17R.

Figure 9.5: Initial state of zirconium measured by EBSD equipment combined with Cambridge S360 microscope.

For EBSD measurement and analysis, almost identical procedure was applied as in the case of titanium (chapter 8). H samples were measured on the RD-TD plane of the initial sheet, whereas S samples were measured on the RD-ND plane of the initial sheet. Total areas covered by EBSD maps was at least 1 mm^2 for each sample. Example of one of the performed EBSD scans is presented above in the Figure 9.5.

9.2 Analysis of EBSD data

All the obtained EBSD maps were subjected to slight cleaning procedure, if such was necessary.

The same color scale is used for all the presented IPF maps thus only Figure 9.6contains example of the color triangle.

EBSD grains were determined as structures of similar orientation comprising of at least 10 EBSD points (assuming that EBSD lattice step is equal to 1.2 µm), and separated by boundary interface with misorientation higher than 15° from the surroundings. Grain size was calculated using diameter and area methods.

Similarly to titanium, textures are analyzed using Euler angles. The crystal coordinate system is defined as $X = [2\bar{1}\bar{1}0]$, $Y = [01\bar{1}0]$, Z=[0001]. Again, it is noted that such convention results in the difference of 30° on φ_2 in respect to publications that concern investigation of zirconium (chapter 3). Also, no special sample symmetry was imposed for texture calculations, i.e. triclinic one was used.

9.2.1 Initial state

The initial microstructure, presented in the Figure 9.6 and Figure 9.7, consists of completely recrystallized and equiaxed grains with an average area grain size of 240 μm^2 (or equivalent diameter of 16 µm).

Based on the IPF [001] map (Figure 9.6), it can be noted that most of the grains have *c*-axis located in the vicinity of ND. Further texture analysis revels domination of tilted $\{0001\}<2\bar{1}\bar{1}0>$ component which appears in this case as strong symmetrical maxima $(0°, 30°, 0°)$ and $(0°, 30°, 60°)$ – see Figure 9.8a. However, it should be noted that corresponding $(180°, 30°, 0°)$ and $(180°, 30°, 60°)$ are less pronounced (Figure 9.8b), which is also clearly shown by the slight asymmetry of basal poles in the 0001 pole figure (Figure 9.8c).

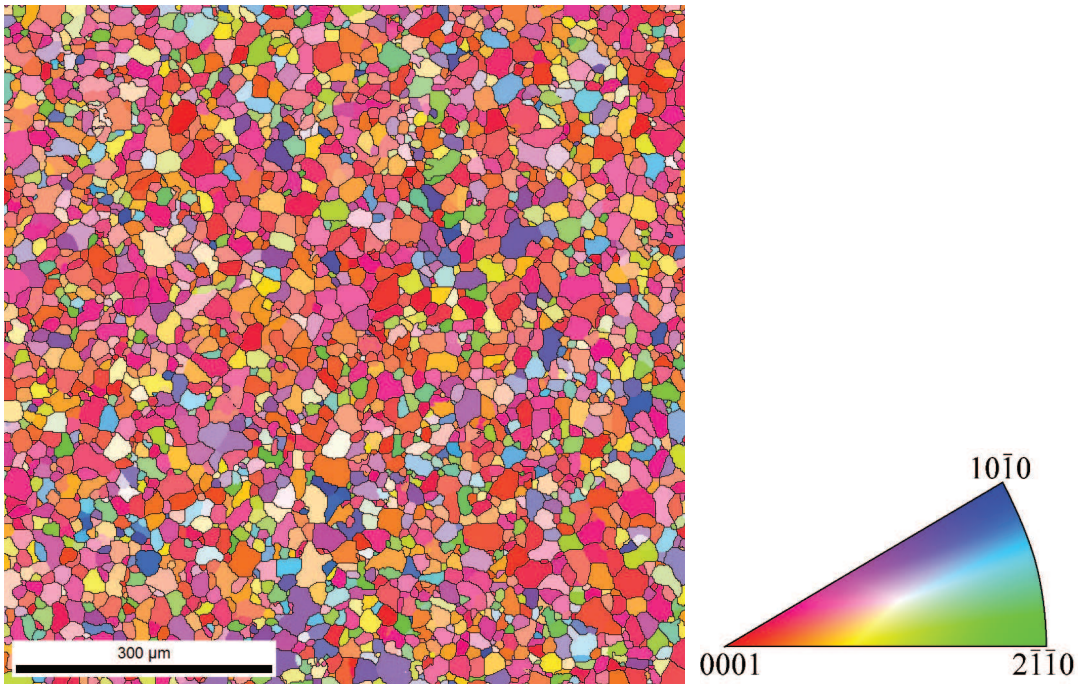

Figure 9.6: EBSD IPF [001] map of initial Zr microstructure (RD-TD plane).

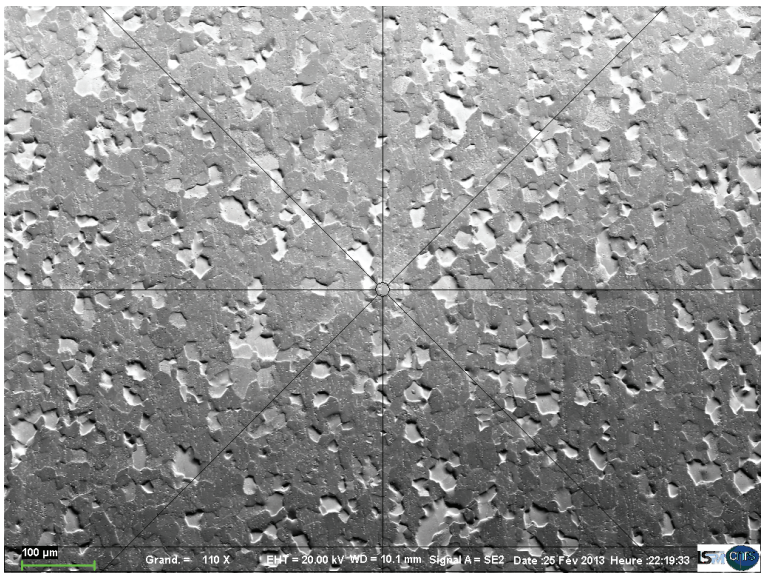

Figure 9.7: SEM image of initial state of the investigated zirconium.

Finally, there is an additional component to be noted, approximately given by (0°, 30°, 30°), which is located in between the main maxima.

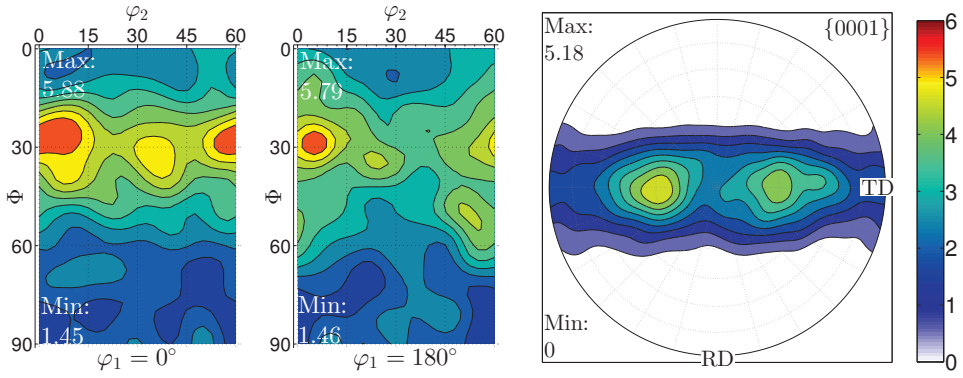

(a) **(b)** {0001}

Figure 9.8: Texture of the Zr initial state, ODF cross-sections (a,b) and pole figure (c).

9.2.2 Deformed state

Some representative EBSD maps of the deformed states are shown in the Figure 9.9 for the H and in the Figure 9.10 for the S samples. Note that, on these maps, and in those shown further for the annealed state, grain boundaries are classically determined by a 15° misorientation critical value and are thus HAGBs.

In both deformation directions, it can be seen that some orientation spread appears within the grains (visualized by the color variations) with increasing strain, because of the formation of misorientations of a few degrees, which are associated with build up of intragranular dislocation substructures. The misorientation angles of these substructures can further increase during deformation because of different orientations within different parts of the grain.

Moreover, it can be mentioned that, on the first glance, overall shape and size of the grains are not changed significantly over compression in comparison to initial state. This can be explained by the abovementioned fact that grains are rather deformed by misorientation accumulation instead of undergo heavy fragmentation.

Concerning the latter, the presented maps (Figure 9.9, Figure 9.10), where black lines represent high angle grain boundaries, whereas white lines fulfill axis/angle condition for tensile twins boundaries, show that twinning deformation mechanism, which is usually responsible for structure refinement, is not very active in the investigated samples. However, some subtle mechanisms have to be discussed.

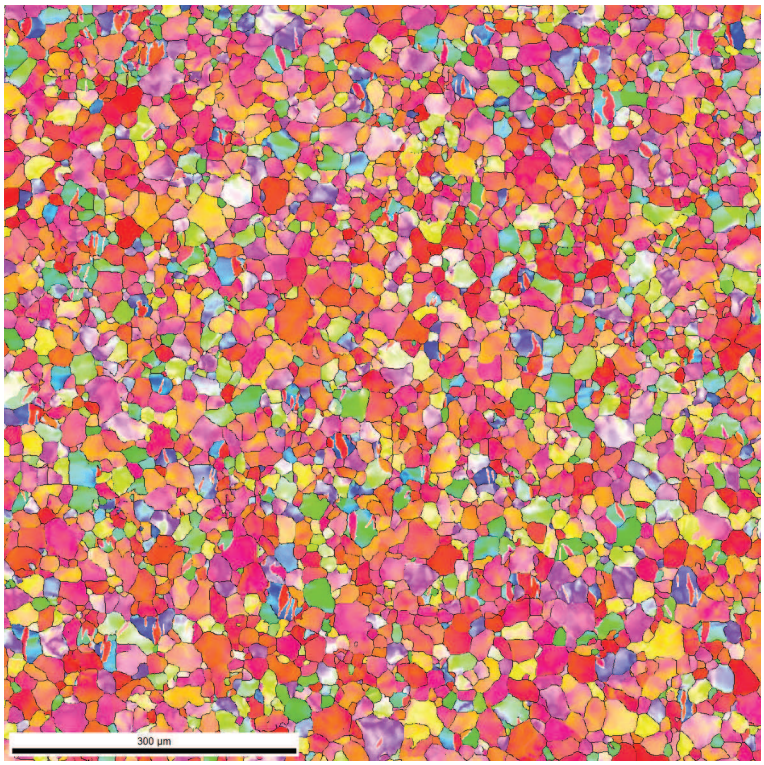

(a) H07D

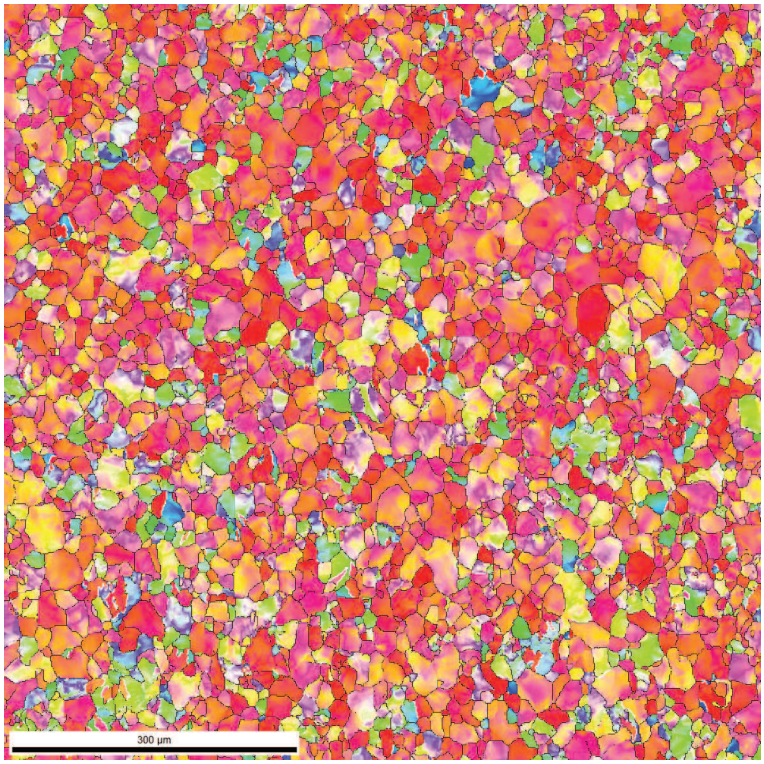

(b) H17D

Figure 9.9: EBSD IPF [001] maps (800 µm x 800 µm; RD-TD plane) of the deformed state of the sample H07D (a) and H17D (b).

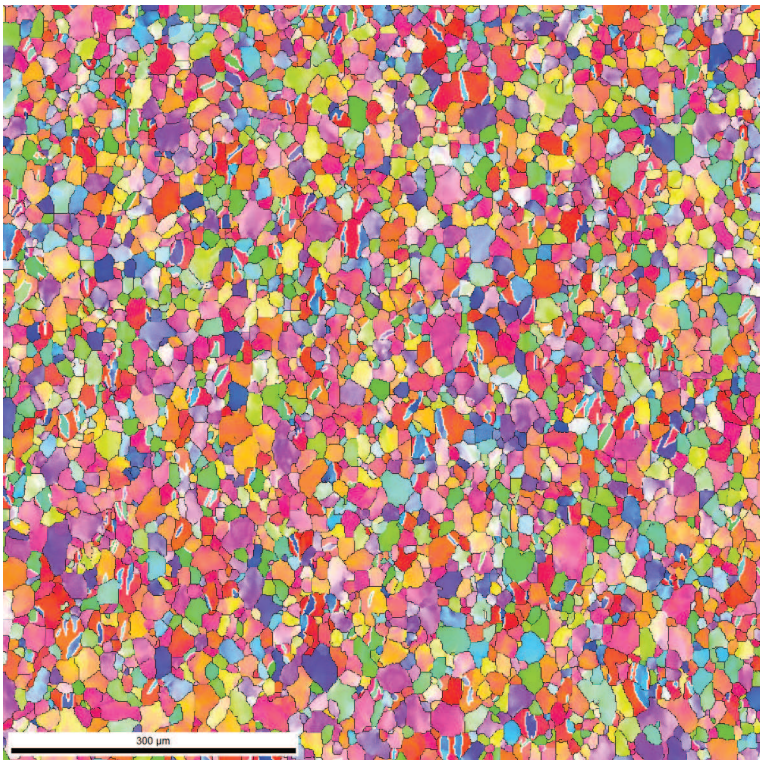

(a) S09D

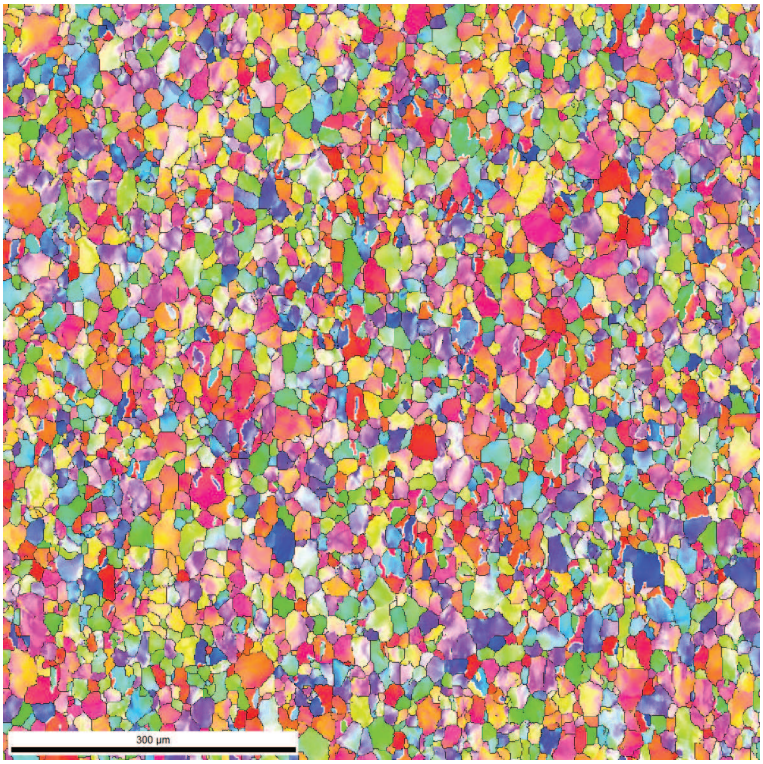

(b) S17D

Figure 9.10: EBSD IPF [010] maps (800 µm x 800 µm; RD-ND plane) of the deformed state of the sample S09D (a) and S17D (b).

Comparison of H07D and S09D sample in terms of formation of tensile twin boundaries suggest that twinning is more frequent at early stages of TD compression. This is also confirmed in topological structure presented by SEM image of the S09D sample (Figure 9.11).

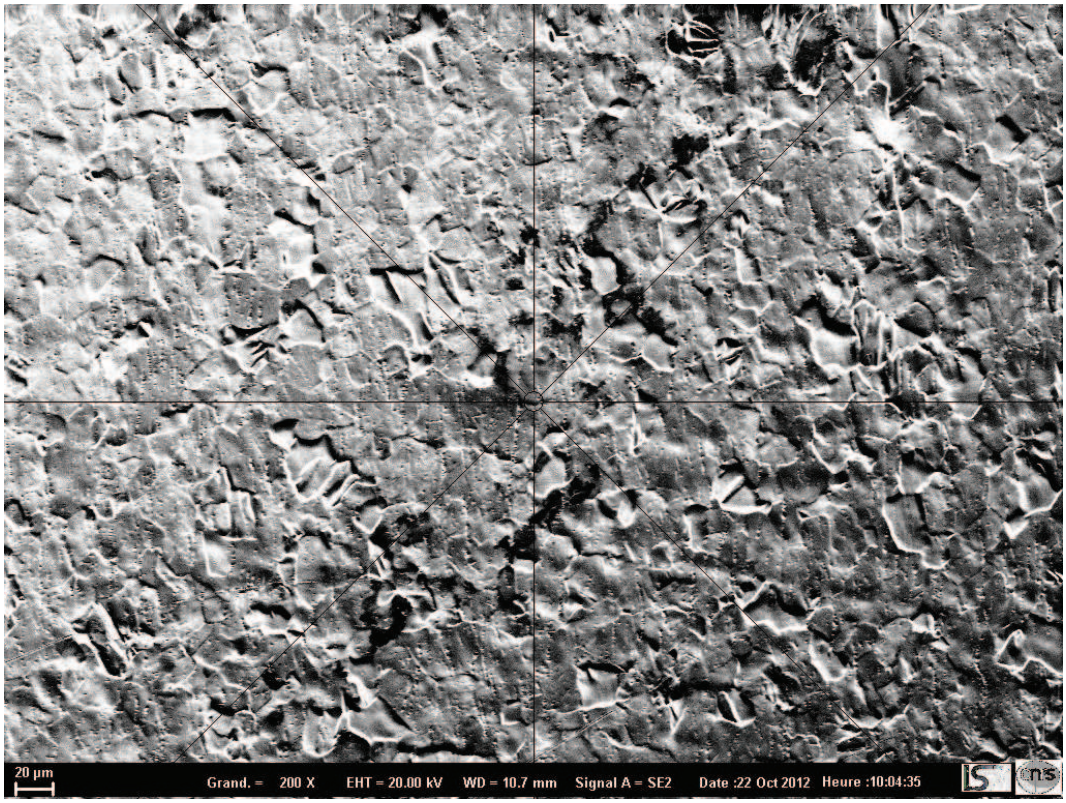

Figure 9.11: SEM image of S09D sample presenting activation of lenticual tensile twins in some of the grains.

Misorientation angle distributions and MDF are used in order to analyze this observation in a more quantitative way.

Obtained results show the formation of the maxima associated with tensile twin misorientation which is not texture derived (Figure 9.12).

Complementary analysis of texture reduced MDF confirms that this misorientation is really linked with tensile twin axis – $<2\bar{1}\bar{1}0>$, as shown by the example (Figure 9.13).

Based on the Figure 9.12, it is clear that twinning is the most active in S09D sample, whereas further deformation along TD direction leads to the decrease of tensile twin misorientation, which suggests that crystallographic slip becomes more dominant at higher strains.

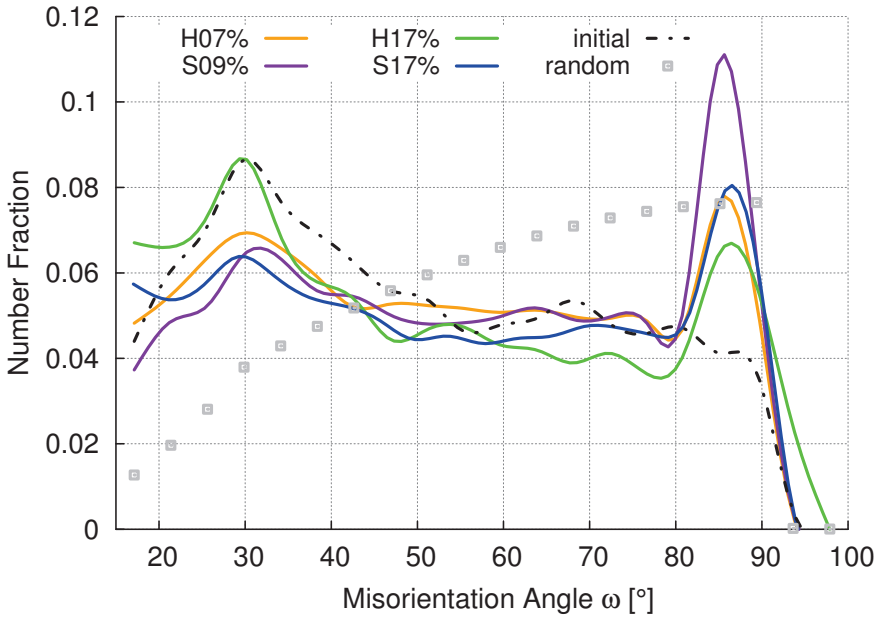

Figure 9.12: Evolution of correlated misorientation angle distributions during deformation. Please note that correlated and uncorrelated misorientations are very similar in the range of $15° - 75°$ thus the distributions for the latter are not shown in the figure.

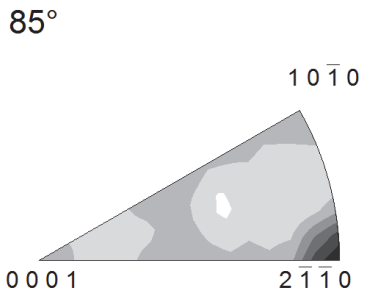

Figure 9.13: MDF plot for twin misorientation angle in the case of S09D sample.

Regarding the observation that concerns orientation gradients and local misorientations, both are investigated using GOS and KAM calculation methods, which were already described in the previous chapters. The obtained GOS and KAM distributions can be further averaged over the whole sample; such data are presented in the Figure 9.14 for some of the investigated Zr samples.

The two parameters reveal the same trend, namely an increase of both local and grain misorientations with strain in all deformed samples, resulting in part from accumulation and rearrangement of dislocations.

However, both parameters seem to increase faster in H samples than in S samples. Starting from the beginning of the deformation process: the H07D sample presents a higher averaged KAM value and a higher averaged GOS value than the S09D sample. At highest strain level (17%), in turn, it is shown that both analyzed parameters are higher in H17D than in S17D. Such a distinction is most probably a direct consequence of different active deformation mechanisms and resulting hardening curves in S and H samples.

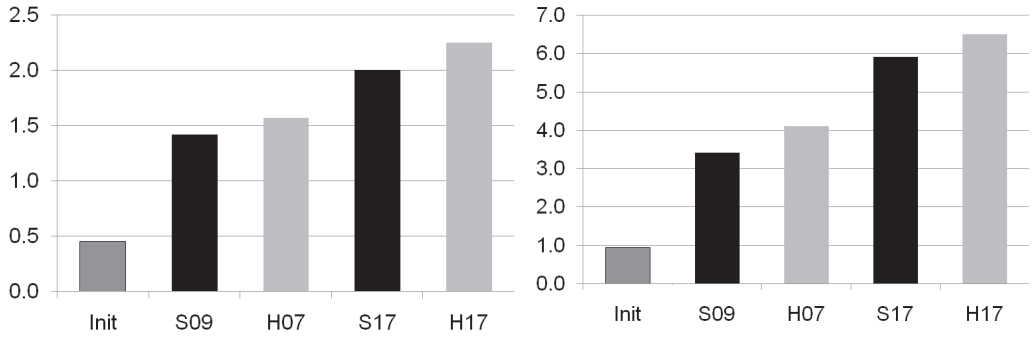

(a) Average KAM [°] **(b)** Average GOS [°]

Figure 9.14: Averaged KAM (a) and GOS (b) values obtained for deformed Zr samples.

Therefore, Schmid Factor has been calculated for prismatic slip in order to shed more light on the mechanisms of slip activation. It appears that the considered Schmid Factor is almost stable during compression along RD, whereas in TD it increases significantly with strain (see Table 9.2).

Table 9.2: Average Schmidt Factor calculated for initial and deformed Zr samples

	Initial state	H07D	H17D	S09D	S17D
Schmid Factor	0.63	0.63	0.60	0.69	0.72

In consequence, from geometrical point of view, prismatic slip can be more easily run in the S samples. In H samples, in turn, grains are not so well oriented for easy glide system thus they are harder to deform, which imply accumulation of local misorientations and related orientation spread inside grains.

This observation, in connection with a higher twinning activity at early stages of deformation in S samples, may be responsible for the mentioned discrepancy in

hardening regime.

The described orientation spread, local misorientations and slight influence of twinning in S samples have together a visible reflection in final size of deformed grains. The analysis of the latter includes average grain area as well as average grain diameter, which were calculated for lower and higher strains. The obtained results are summarized in the Table 9.3.

Table 9.3: Average grain size for initial and deformed Zr samples

Average grain size	Initial state	H07D	H17D	S09D	S17D
Area method [µm^2]	240	240	312	200	245
Diameter method [µm]	16.0	15.2	17.0	14.0	15.5

As it can be seen, there are few issues to be discussed. The most significant decrease of grain size is only seen in S09D sample, which can be reasonably explained by the described presence of tensile twins. In corresponding H07D sample, average grain size is not changed at all. Then, there is a surprising issue that large grains have to be formed during further compression to justify increasing average grain size, especially in H17D sample.

Therefore, an analysis of H17D sample is performed in order to understand this effect. The microstructure has been divided into the largest grains and the rest using threshold value of grain size equal to 1250 µm^2 (40 µm in diameter), which corresponds to the largest grains in the initial state. Average grain size of subset containing smaller grains is equal to 245 µm^2 (15.7 µm), whereas in the case of the largest grains, value of 2125 µm^2 (51 µm) is obtained.

In the next step, the average GOS has been calculated for each subset. Larger grains exhibit average orientation spread equal to 12.5°, whereas it is much less in the smaller grains - only 6.5°. Based on this strong difference, it can be concluded that the largest grains are formed during deformation due to significant concentration of orientation gradients.

Example of this process is shown in the Figure 9.15, which presents EBSD maps (IPF map and Unique Grain Color map; the latter is created by assigning various colors only to distinguish the grains) of the largest grain identified in H17D sample by grain recognition algorithm.

It is revealed that this extremely big grain (visualized by purple color) is, in fact,

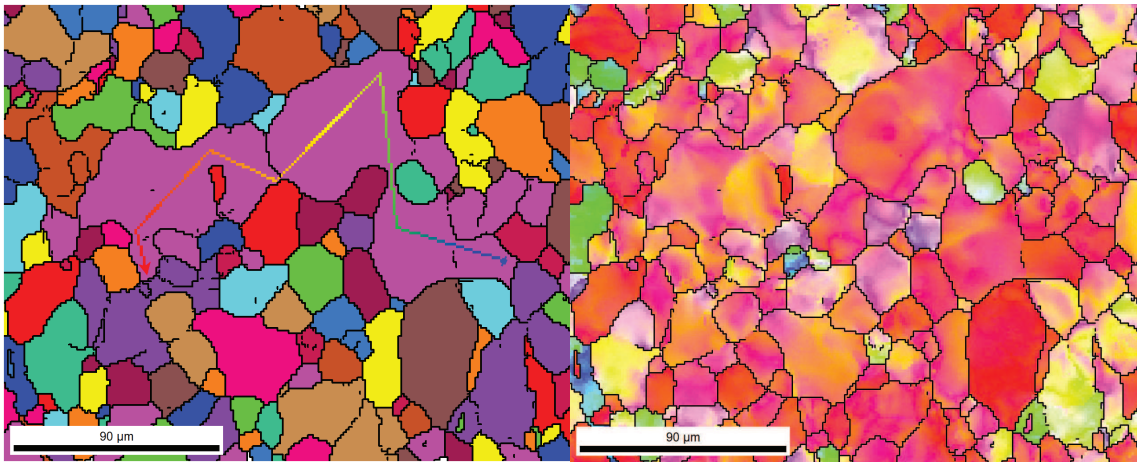

(a) Unique Grain Color map **(b)** IPF map

Figure 9.15: Fragment of H17D microstructure containing the largest grain (purple color). The black lines correspond to HAGBs.

area which comprises of "partial-grains" delimited by low angle grain boundary (Figure 9.16).

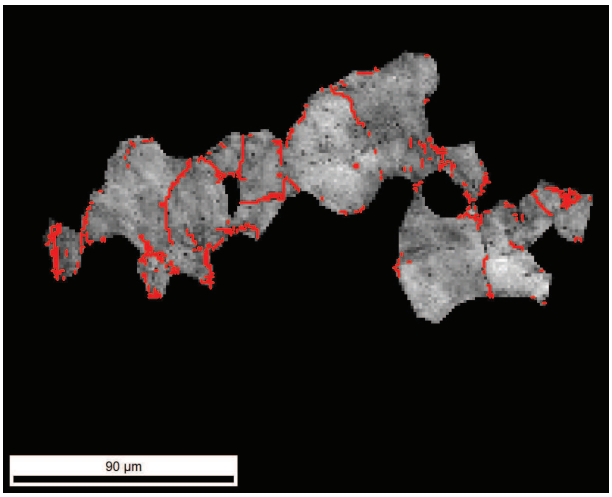

Figure 9.16: IQ map of extremely large grain with red lines corresponding to LAGBs.

Also, misorientation profile (Figure 9.17), which has been calculated for the trace marked in the Figure 9.15, shows that such large grain has indeed significant orientation spread since misorientation from one point to another can reach 35°, and despite that it is still treated as a single grain.

Therefore, it can be concluded that local misorientations are responsible for transition from HAGB to LAGB which, in turn, leads to sticking of the partial-grains.

This is also confirmed in some of the regions inside the considered grain, where this process is not finished resulting in interrupted HAGBs.

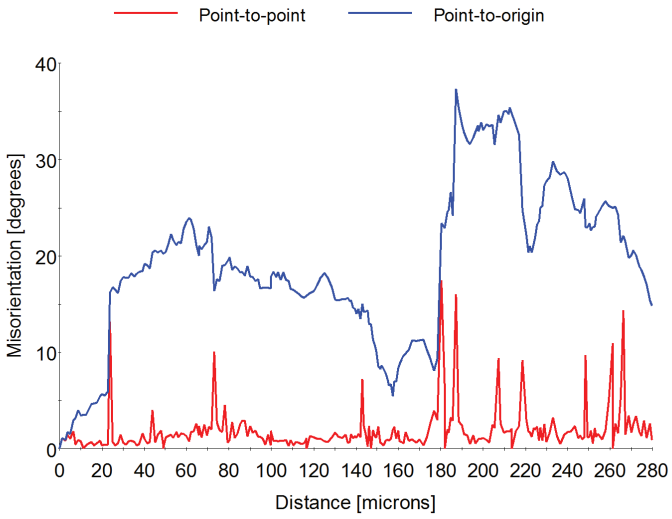

Figure 9.17: Misorientation profile across the large grain. It has been calculated for the trace presented in the Figure 9.15a.

On the other hand, it has to be mentioned that there are examples where HAGB is partly connected only due to mismatch of just few points. Such cases can be regarded as wrongly determined, or artificial, large grain which actually consists of separated grains.

Nevertheless, the described overall tendency of merging grains into large areas is still valid even if threshold misorientation used for grain determination is changed to lower value – 10° for instance.

Next analysis employ special approach developed and described in this thesis (chapter 7) in order to characterize area fractions of regions adjacent to particular types of grain boundaries. HAGB, LAGB and IB (intragranular boundaries) regions are considered.

The area fractions determined for the deformed state are presented in the following Figure 9.18. Based on that, the situation seems to be quite clear; an increase of LAGB and IB fractions during deformation, as expected. Although, there is a difference between the investigated types of samples. In H samples, LAGBs and IBs are generated more easily, whereas the population of HAGBs is almost constant and equal to the initial state. On the other hand, in S samples, a notable increase of HAGB fraction is seen at the beginning of deformation – this is linked with twinning activity - then the fraction is stabilized due to predominance of slip. Consequently,

at higher strain, S sample has more HAGB areas than corresponding H sample, in which accumulated misorientations facilitate transition from HAGB to LAGB.

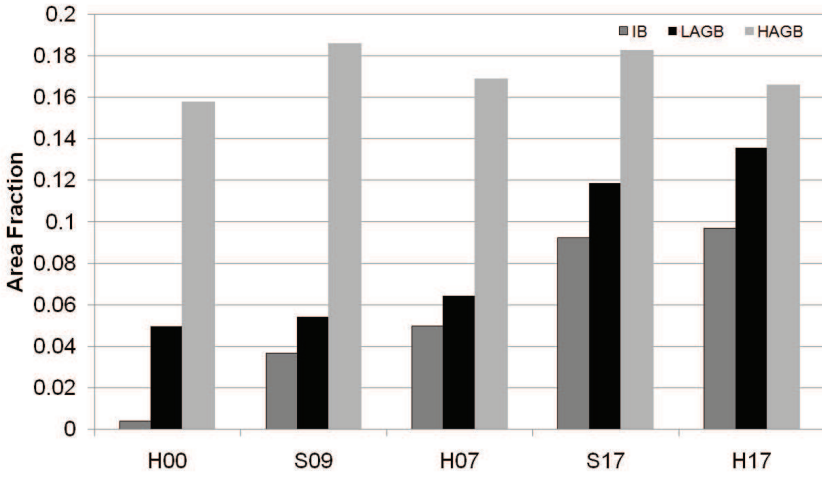

Figure 9.18: IB, LAGB and HAGB area fractions obtained using the GBA approach for initial and deformed samples.

These results are thus confirmed to be in a very good agreement with the discovered mechanisms of strain accommodation in Zr samples.

The described observations on evolution of Zr microstructure during compression resemble investigation performed on tensile tested titanium, in which author of this thesis have actively participated. This work will be submitted soon into publishing process. Therefore, the final conclusions are shortly reviewed. Two sets of samples have been considered: samples tensiled along RD and samples tensiled along TD. The initial state had similar microstructure and texture as the presented zirconium. Also, final achieved strains: 8% and 16%, in each direction, correspond well to these obtained for Zr.

In this study, it has been shown that samples tensiled along TD are much softer. Consequently, tensile test along TD results in almost flat curve in the hardening regime, while parabolic shape is observed in the RD case (Figure 9.19). This difference is attributed to tensile twinning. In this context, it has to be mentioned that activation of twinning in titanium is increasing between 8% and 16% of deformation, which is in contrary to the zirconium S samples. Therefore, titanium stress/strain curves have comparable character to those in the Figure 9.3 from one point of view, but at the same time there is still a clear difference in the slope of hardening regime between titanium soft samples and zirconium soft samples.

Another important conclusion regards orientation spread and local misorientations

in titanium samples tensile tested along RD. In this case, a tendency to create wide areas consisting of similarly oriented grains and interrupted high angle grain boundaries is also observed which, in turn, leads to the already presented problem of increasing average grain size over deformation.

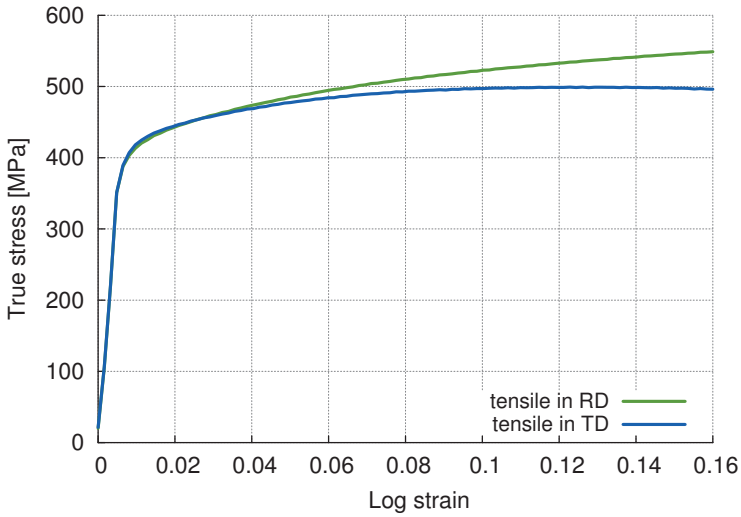

Figure 9.19: Experimental macroscopic stress (σ) vs. deformation (ϵ) measured in RD and TD direction in the case of tensile-tested titanium.

Two different microstructure evolutions observed in titanium have strong impact on subsequent recrystallization phenomenon, especially in term of kinetics of this process. Therefore, comparable situation is expected in the case of the investigated Zr samples.

9.2.3 Annealed state

After annealing, the creation of a new dislocation-free microstructure through recrystallization is only visible in the highest strain states (samples H17R and S17R). For the lowest strain levels, recovery possibly takes and thus the resulting microstructures are only locally reconstructed within the grains.

Typical microstructures obtained for the H17R sample and S17 sample are shown in Figure 9.20a and Figure 9.21a, respectively.

It is clear that recrystallization is not complete in both samples since deformation substructures still appear in some of the grains. Therefore, recrystallized fraction has been additionally extracted based on the GOS analysis and presented (Figure 9.20b, Figure 9.21b). Indeed, different deformation mechanisms results in slightly different

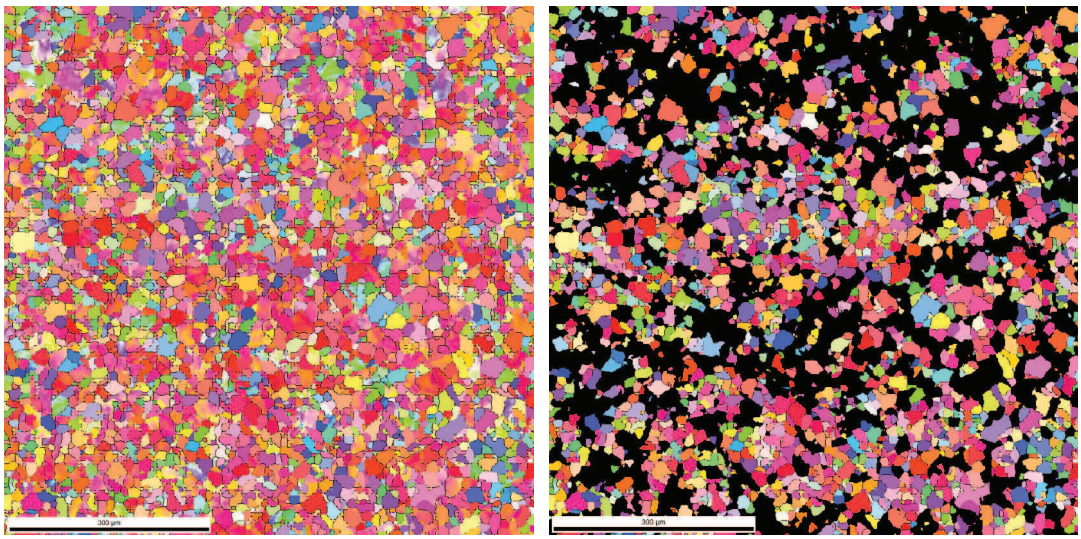

(a) (b)

Figure 9.20: EBSD IPF [001] maps (800 µm x 800 µm; RD-TD plane) of the partly recrystallized H17R sample (a) and separated recrystallized grains (b).

recrystallization kinetics between H and S samples since recrystallized area fraction is higher in the S17R sample: 0.7 in comparison to 0.58 in the H17R sample.

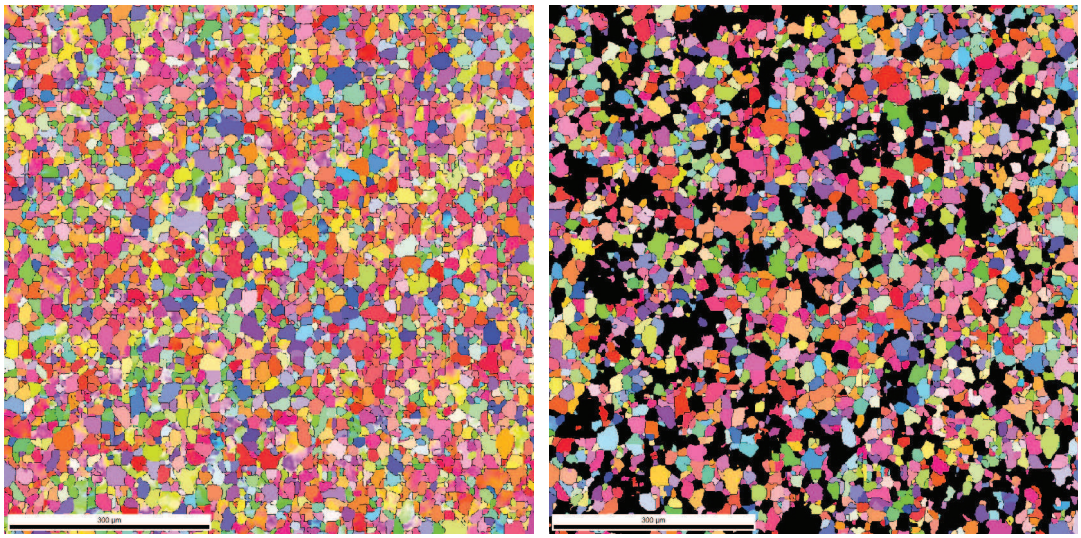

(a) (b)

Figure 9.21: EBSD IPF [010] maps (800 µm x 800 µm; RD-ND plane) of the partly recrystallized S17R sample (a) and separated recrystallized grains (b).

Also, recrystallized grains have been compared in terms of grains size and average GOS (Table 9.4). In both samples recrystallized grains have similar parameters,

which in accordance to recrystallized area fraction imply higher number of recrystallized grain in the S17R sample. Indeed, the map presented in the Figure 9.21 contains 2756 recrystallized grains, which is about 400 more than in the map from Figure 9.20.

Table 9.4: Average grain size and average GOS for recrystallized grains in sample H17R and S17R.

Average grain size	Initial state	H17R - rex. partition	S17R - rex. partition
Area method [µm^2]	240	157	162
Diameter method [µm]	16.0	12.6	12.7
Average GOS	0.95	0.87	0.87

Further investigation of recrystallized grains deals with distribution of misorientation angle in order to find influence of special boundaries. It is shown that only misorientations close to 30° have considerable fraction since it is much higher than corresponding value provided by random distribution (Figure 9.22). However, it appears that these misorientations are texture derived. Moreover, analysis of texture reduced MDF does not distinguish any dominating axis connected with 30° misorientation angle.

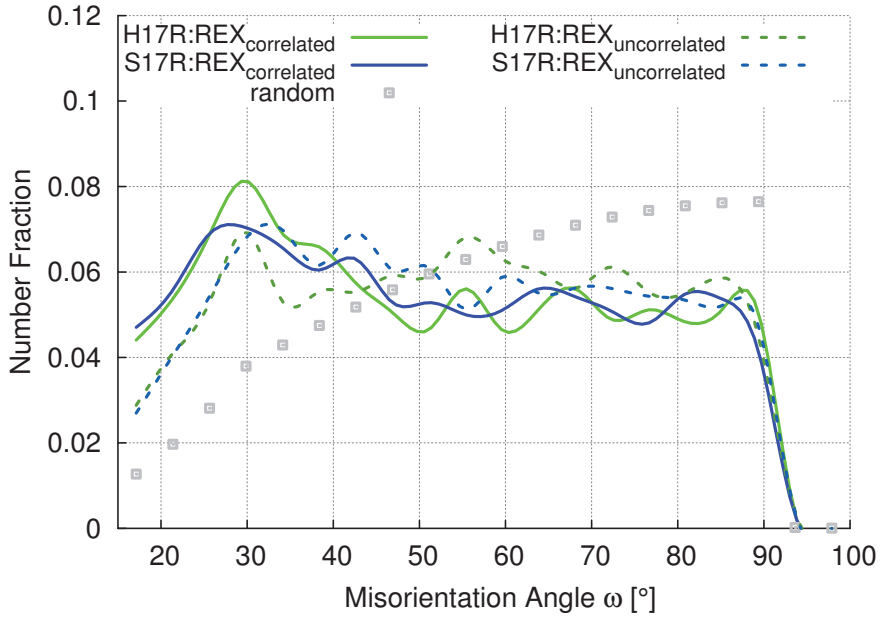

Figure 9.22: Correlated and uncorrelated misorientation angle distributions obtained for recrystallized grains in H17R and S17R samples.

9.2.4 Texture evolution during thermo-mechanical treatment

Regarding texture analysis, it is recalled that there are two sample coordinate systems due to different compression geometries; (RD, TD, ND) defined for H samples, and (RD, ND, TD) for S samples. Therefore, it was decided to rotate EBSD data obtained for S samples in order to compare more easily texture evolution between both considered sets of samples using the same reference frame. The rotation is defined as (+/-) 90° around RD axis.

Increasing strain during deformation results in strengthening of basal poles asymmetry (see example of H17 sample – Figure 9.23a), which has been described in the case of the initial state. It means that main texture maxima are located mainly on $\varphi_1 = 0°$ ODF cross-section. Only this one is, therefore, analyzed, and compared between deformed H and S samples – see Table 9.5.

In both samples, compression leads to formation of tilted deformation component located in this case along $\varphi_2 = 30°$. However, it is noted that the texture changes are much more rapid in S samples. In the H07 sample evolution is rather slight. Main maximum already observed in the initial state is shifted toward the center of $\varphi_1 = 0°$ cross-section. At higher strain – H17 sample, in turn, ODF cross-sections contain very broad maximum which can be described as superposition of four main orientations: (0°, 30°, 30°), (0°, 45°, 30°) and two symmetrically located (0°, 30°, 15°), (0°, 30°, 45°).

In contrary, in the S sample main deformation component - (0°, 30°, 30°), which is usually reported in the zirconium literature, is already formed at the beginning of deformation. Then, it evolves toward (0°, 45°, 30°), which has been reported as hard orientation in titanium.

After annealing, textures have been separately calculated for recrystallized and still deformed partitions. In the latter case, it appears that symmetry of {0001} pole figure is partially restored, especially in the H17R sample (see Figure 9.23). Hence, again only $\varphi_1 = 0°$ ODF cross-section is shown.

Based on the presented comparison, it can be assumed that most of the grains with orientation close to the main deformation components, described above, have been consumed.

Texture evolution in recrystallized partition is also very interesting and quite surprising, in fact.

1. In the H17R sample, recrystallization component (0°, 30°, 0°), i.e. tilted {0001}<$2\bar{1}\bar{1}0$> is formed despite the fact that recrystallization is not com-

pleted. It should be emphasized that this is rather rare situation since it is generally acknowledged that such component should appear only after additional grain growth process.

2. In the S17R sample, the texture is slightly more random than in the H17R sample. Although, there is also strong maximum approximately given by (0°, 70°, 35°), which means that main orientation of recrystallized grains evolved from main deformation component by tilting of *c*-axis itself, instead of using rotation around *c*-axis as in the case of the H17R sample.

These observations suggest that mechanisms responsible for development of recrystallization texture in the considered samples can be different from the one already reported in the literature. On the other hand, it has to be admitted that the results concerning textures of selected partitions can be influenced by statistical issues. Therefore, this subject needs further investigations.

Additional insight into the analyzed evolution can be provided by textures calculated for grain boundary areas extracted during investigation of the deformed state. As already mentioned in chapter 7, such data contain information about orientations of grain boundary regions. The main motivation in this context is to analyze textures of IB and LAGB areas since they provide stored energy. This, in turn, means that they can be faster replaced by recrystallization front due to increased gradient of stored energy. From that point of view, it can be also assumed that the SIBM mechanism is more active in HAGBs surrounded by these locally misoriented regions.

It is shown that in all the considered cases, the texture of HAGB area generally follows that of the whole sample. More interesting observations concern regions adjacent to LAGBs and IBs. In the H17D sample, they have main maximum located at (0°, 45°, 30°), and two slightly less pronounced centered at (0°, 30°, 30°) and (0°, 30°, 15°). Please note that deformation component (0°, 30°, 45°) in not present in this case. In S17D samples, all the GB areas have the same texture that reflects global texture.

After annealing, it is clearly demonstrated that grains having high fraction of IBs and LAGBs are disappearing first. Based on that, it can be understood why (0°, 30°, 45°) orientation have remained in the texture of still deformed grains in the H17R sample.

Therefore, a following scenario is proposed in order to explain the observed texture evolution. First, SIBM is considered as main mechanism of sub-grain formation.

Table 9.5: Texture evolution in Zr during thermo-mechanical treatment.

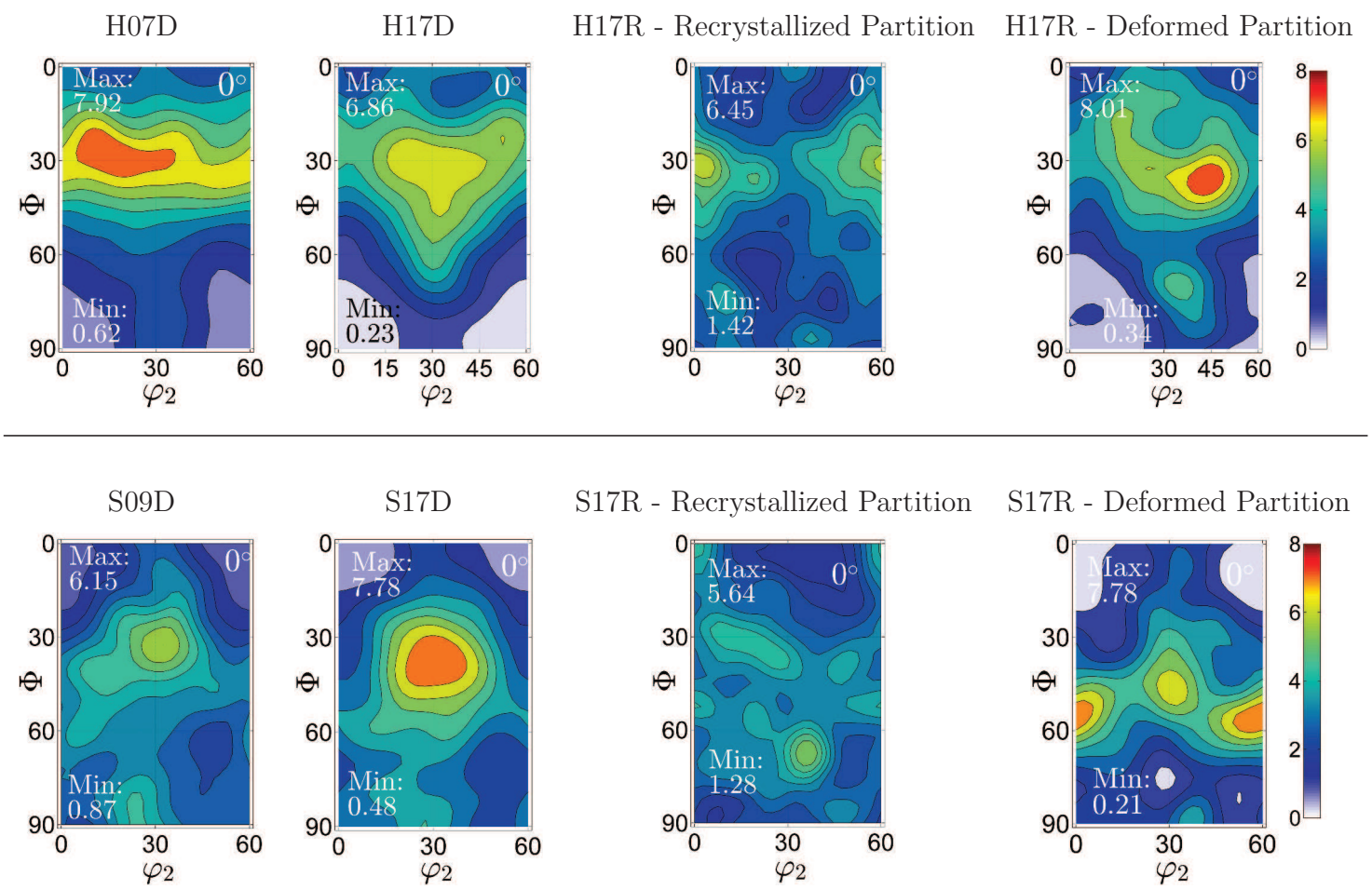

Table 9.6: Relation between textures of GB areas in deformed Zr samples and textures of deformed partition remained after brief annealing.

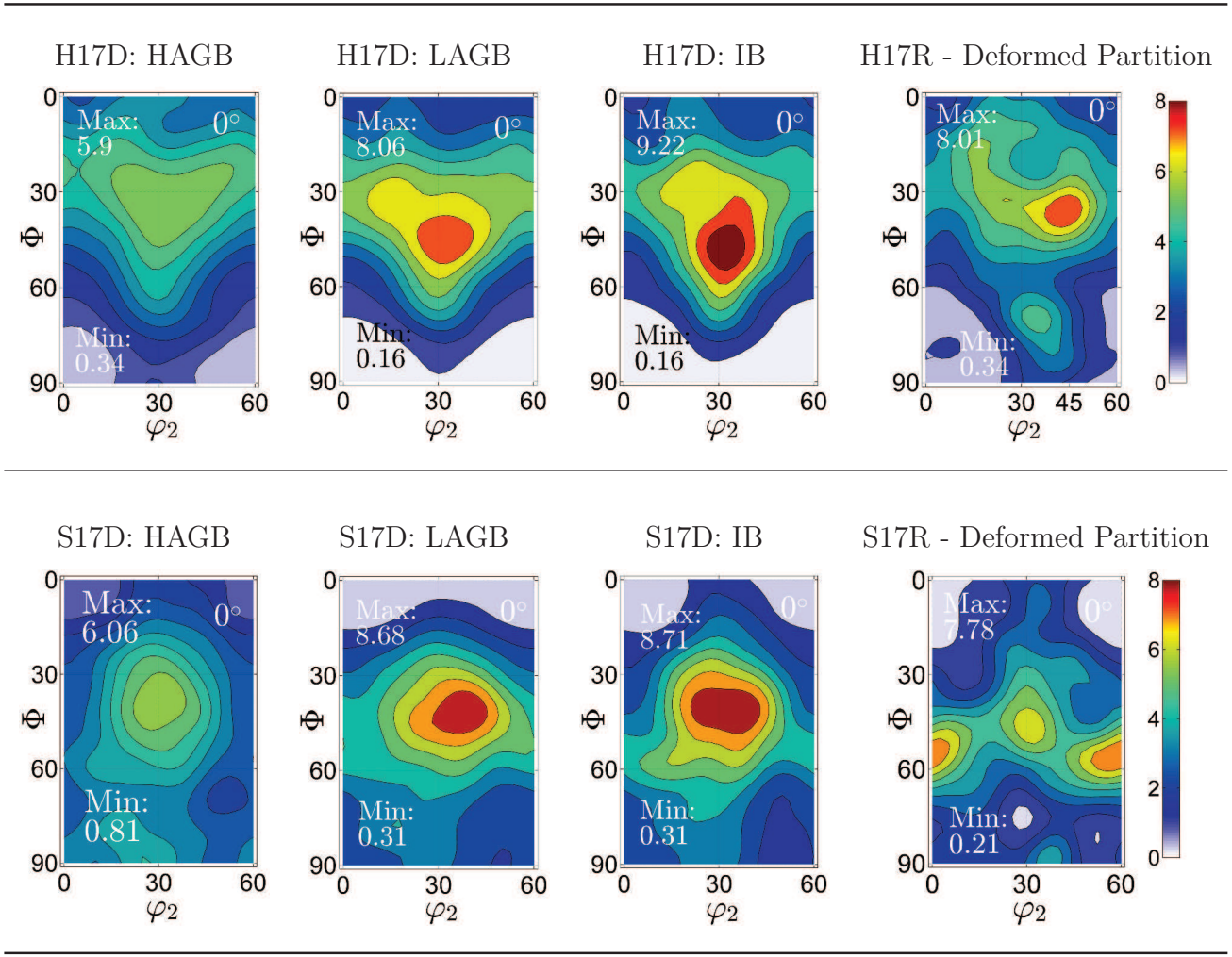

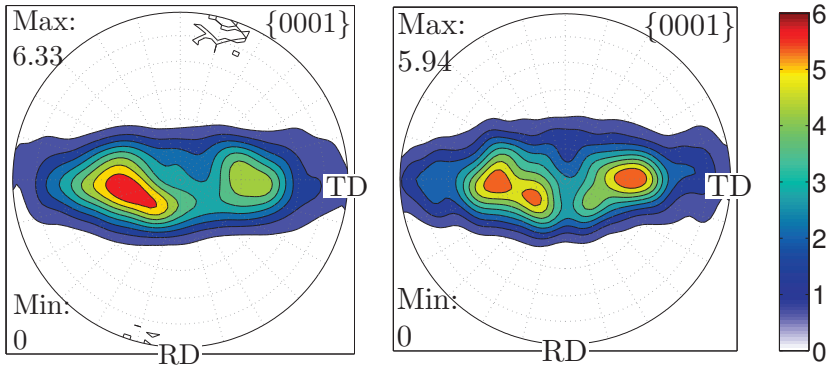

(a) **(b)**

Figure 9.23: Comparison of {0001} pole figure between H17D sample (a) and deformed partition in H17R sample (b).

Then, HAGB of grain having substantial fraction of local misorientations (IBs and LAGBs) is regarded as preferential place of SIBM activation. Consequently, they are consumed first as they exhibit the higher energy.

From this point of view, the higher fraction of HAGBs surrounded by local misorientations in the deformed sample, the more recrystallization grains after annealing. This corresponds very well with the difference in the annealing state between H17R and S17R samples.

Monte Carlo simulations are, therefore, used in order to verify the suggested hypothesis.

9.3 Simulations

Simulations have been performed using EBSD data of the deformed state as an input microstructure. That gives 666×665 sites in the lattice. Stored energy distribution has been evaluated based on local misorientatations, i.e. rescaled KAM parameter. In each considered case, anisotropy of grain boundary energy and mobility has been applied only to LAGBs. In addition, small thermal fluctuations – $kT = 0.5$ – have been introduced in order to reduce effects related with lattice anisotropy.

Several scenarios have been simulated including SIBM mechanisms, and traditional nucleation which takes place inside HAGB structure. The one connected with SIBM relies on special procedure for sub-grain formation which is allowed only in the HAGB regions of high stored energy difference. Also, probability function of reorientation depends on stored energy gradient across the boundary.

The presented simulations concern recrystallization in H17R and S17R samples.

9.3.1 Simulation of recrystallization in H17 sample

The obtained stored energy distribution is presented in the Figure 9.24. The maximum stored energy is fixed at 4.5. Areas of low and high stored energy are analyzed in terms of preferred orientation. It appears that the first one (blue color) exhibit a smooth fiber component defined as ($0° - 60°$, $30°$, $0° - 60°$), whereas the latter (orange and red colors) exhibit a texture that corresponds more to the texture of IB and LAGB areas in the H17D sample.

In the first attempt of SIBM scenario, sub-grains have been formed in the microstructure using only probability increasing with stored energy gradient.

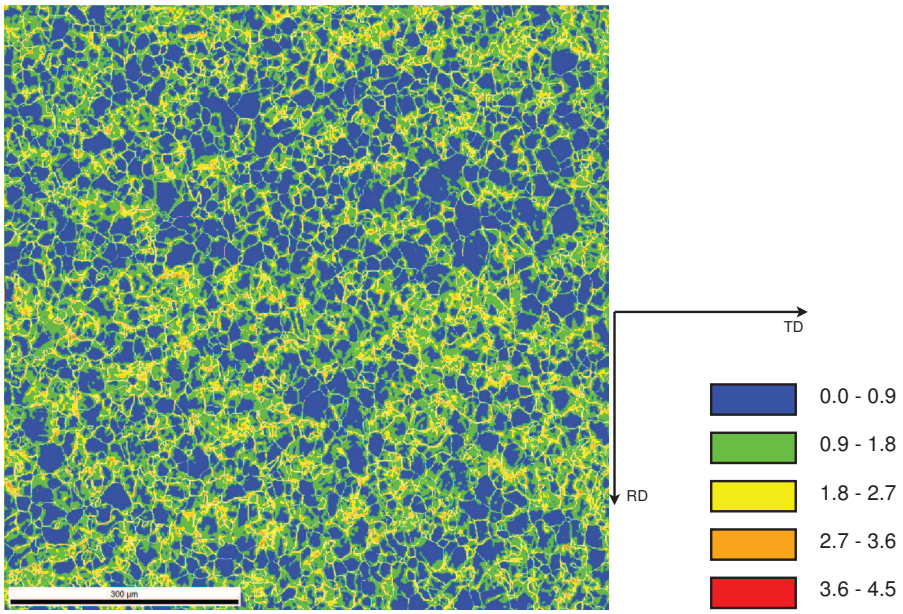

Figure 9.24: Stored energy distribution used in simulation of recrystallization of the H17D sample.

Therefore, it should be noted that this mechanism is not very strict since both: low energy and high energy areas have a big spread in terms of texture. It means that there are multiple combinations of sub-grain having orientation selected from the abovementioned fiber, and neighboring high stored energy area having many possible orientations.

Despite this highly non deterministic version of the SIBM model, a promising simulation results have been achieved. Analysis of texture evolution and microstructure characterization for this case are presented in the following figures.

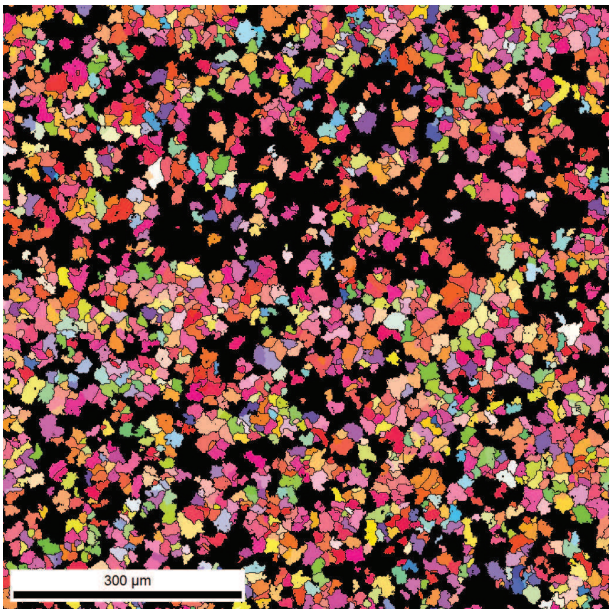

Figure 9.25: Recrystallized grains obtained from simulation performed in the case of the H17 sample.

Obtained recrystallized partition, shown in the Figure 9.25, consists of 2300 grains of average size equal to 12.5 µm. It can be noted that these grains are not homogeneously distributed in terms of spatial location. There are large still deformed regions (black areas in the Figure 9.25) and regions of rather clustered recrystallized grains. However, distribution of misorientation angle does not indicate the presence of special boundary between them (Figure 9.26).

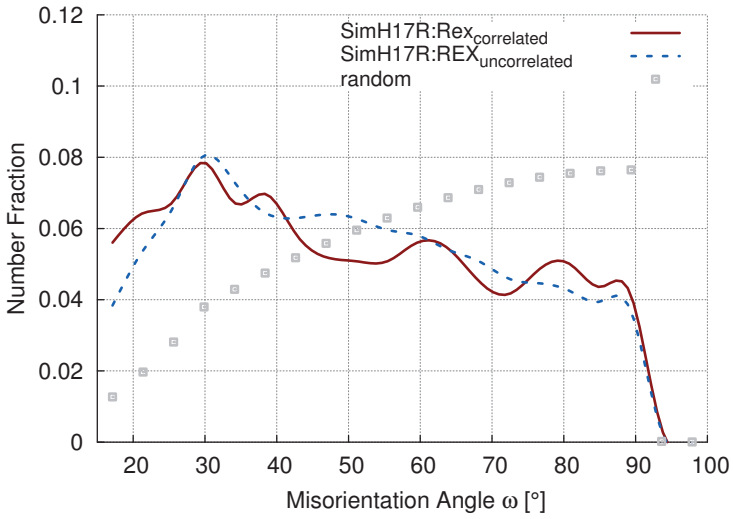

Figure 9.26: Misorientation angle distributions calculated for recrystallized grains which have been obtained from simulation performed in the H17 sample.

All these observation are in very good agreement with the experimental microstructure of annealed state of the H17R sample.

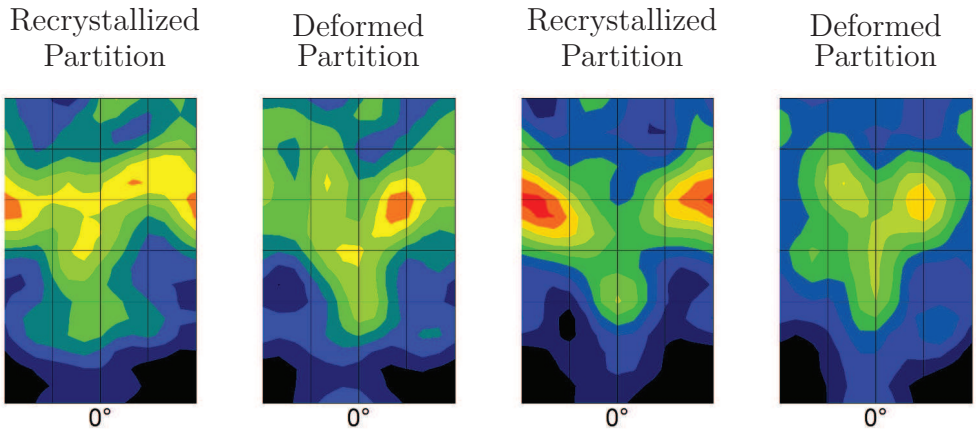

(a) general SIBM procedure **(b)** specialized SIBM procedure

Figure 9.27: Texture evolution during simulation of recrystallization in H17R sample. Maximum ODF value is equal to 7.9 (a) and 8.5 (b).

At the same time, based on the Figure 9.27a, it can be concluded that simulated texture evolution is also reproduced with a good accuracy. Strong recrystallization component is developed, and simultaneously only (0°, 30°, 45°) orientation remains in the texture of the deformed partition.

In contrary, a classical scenario, in which new strain-free grains emerge from highly deformed structures, does not match to experimental data. One of the examples is presented in the Figure 9.28. In this case, nucleation sites are also distributed in HAGBs, but they are allowed to grow without stored energy gradient. Clearly, such scenario leads to more homogeneously distributed grains in the microstructure. No significant texture evolution is noted as well.

In the next step, SIBM procedure has been refined further in order to improve model predictions from statistical point of view. In this case probability of sub-grains formation is slightly increased for those oriented in the vicinity of the recrystallized component – (0°, 30°, 0°). It can be concluded that more specialized SIBM procedure leads to the same microstructure evolution as the presented above in this subsection, whereas changes observed in the texture (Figure 9.27b) correspond even better to the experimental results.

Therefore, this version of the model has been applied further for the case of the S17R sample.

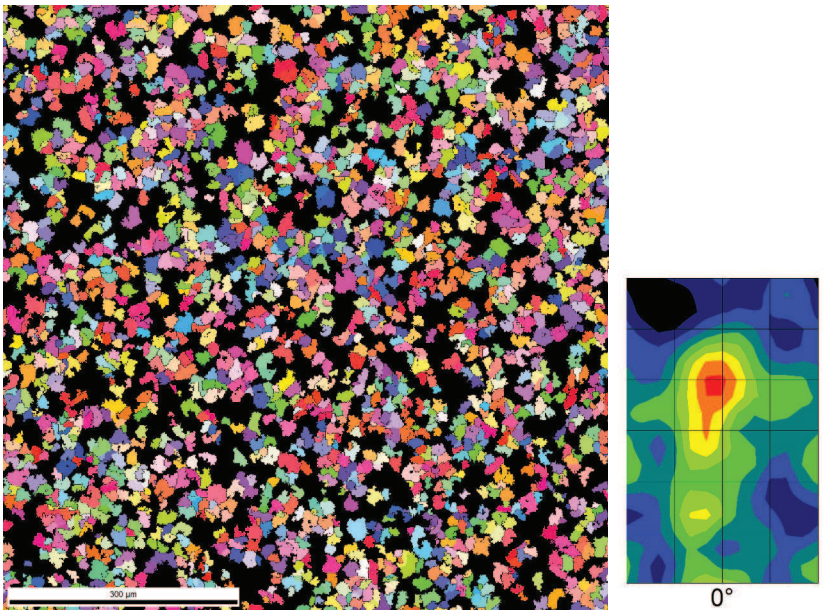

Figure 9.28: Microstructure and texture evolution (ODF max. = 8.3) obtained from simulation without incorporated SIBM mechanism.

9.3.2 Simulation of recrystallization in S17 sample

The same analysis of simulation results has been conducted for the S17R sample. It appears that most of the observations discussed in the previous H17R sample can find a corresponding equivalence in this case. Hence, only a brief review on microstructure and texture results is provided using the following figures. Then, a small summary is given.

First, it is noted that despite more advanced recrystallization (recrystallized area fraction = 0.7), the average grain diameter of the simulated microstructure (see Figure 9.29) is only slightly higher - 12.6 µm - in comparison to simulation of H17 sample. Then, analysis of misorientations is shown in theFigure 9.30 which indicates that number fraction of 30° misorientation is slightly lower than in the corresponding case of H17 sample. Finally, texture evolution is presented in order to confirm the correct developement of recrystallization component (Figure 9.31a).

In the light of the presented data, it can be concluded that simulated SIBM driven recrystallization predicts a correct microstructure and texture evolution in the case of the S17R sample.

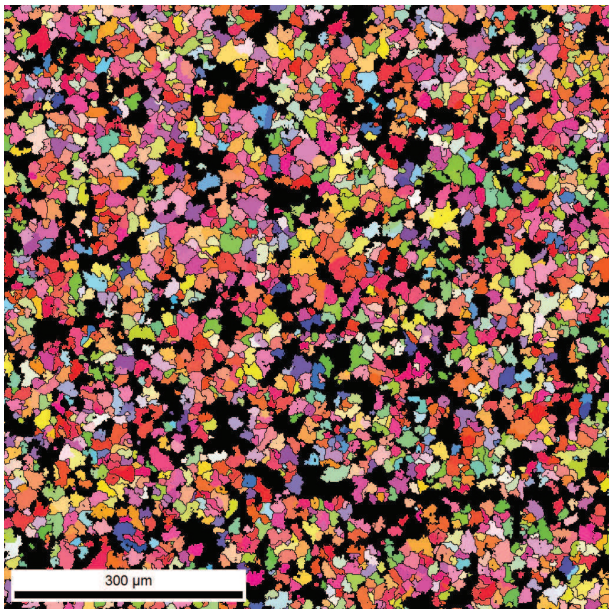

Figure 9.29: [010] IPF map presenting recrystallized partition in simulated microstructure of S17 sample. Average grain size = 12.6 µm.

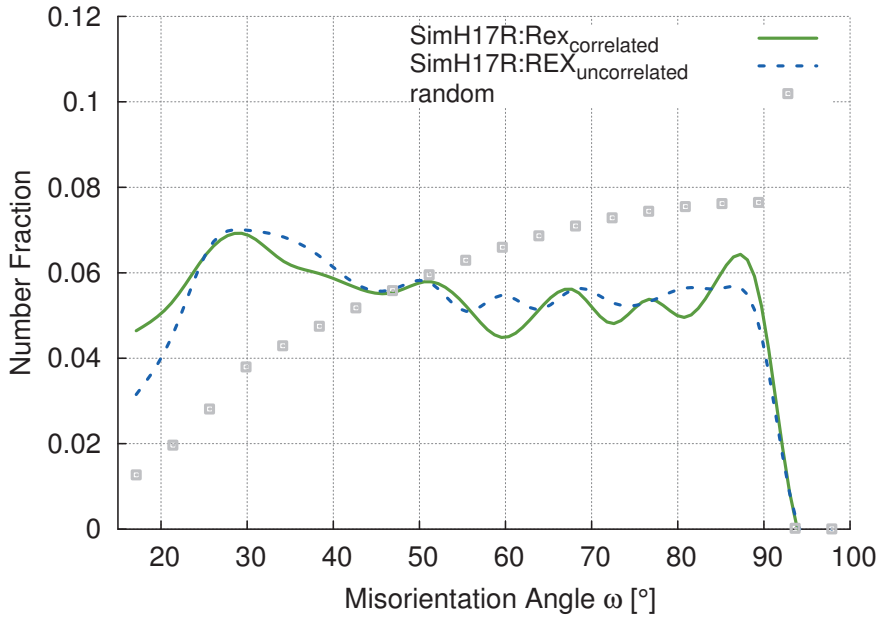

Figure 9.30: Misorentation angle distributions calculated for recrystallized grains which have been obtained from simulation performed in S17 sample.

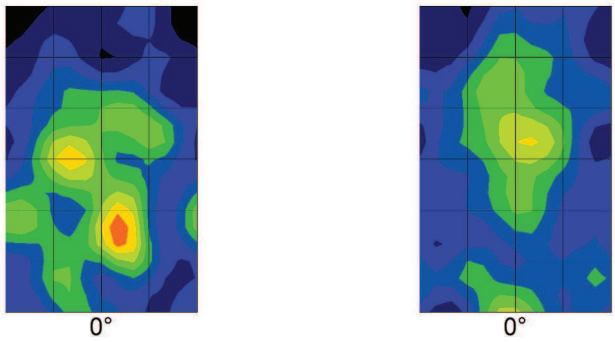

(a) Recrystallized partition **(b)** Deformed partition

Figure 9.31: Texture evolution in S17 sample after simulated partial recrystallization.

Taking into account both simulated cases: H17R and S17R, it can be summarized that recrystallization behavior in these samples can be properly explained in terms of SIBM process in which sub-grains are formed nearby grains reach in local misorientations. Moreover, it should be emphasized that the proposed physical model of recrystallization has been successfully validated using both microstructure and texture studies at the same time. The coincidence of all the investigated parameters indicates that the proposed model is highly feasible in the reality.

9.4 Summary and conclusions

Hexagonal zirconium was channel-die compressed to reach various degrees of deformation, and briefly annealed to achieve a partially recrystallized state. It is observed that compression in ND (hard samples, H) requires a higher force than in TD (soft samples, S). This has been related with Schmid factor calculations which reveal that easy glide – prismatic slip – is more favored in S samples, especially at higher strains.

On the basis of the analysis of microstructural features, i.e. twins, grains size, local misorientations, orientation gradients and grain boundary areas, performed in zirconium, different mechanisms of deformation between H and S samples are described and correlated with soft and hard character.

It is observed that deformation in the hard samples is strongly connected with the accumulation of IBs and LAGBs, whereas the population of HAGBs is almost constant. This could mean that grains are harder to deform in this case, leading to the build up of dislocation cells inside the grains, which has a reflection in increasing value of local misorientations. At higher strains the resulting local misorientatatons

and orientation spread are so high in some regions that transition from HAGB into LAGB is activated, and thus similarly oriented grains are grouped together into very large areas.

This trend is less marked for the soft samples, where grain fragmentation is easier to achieve at the beginning of the deformation due to more pronounced activity of tensile twins thus HAGBs evolve much more, and the impact of deformation on the LAGB population is less significant. However, at higher strains, grains tend to accumulate more misorientations, similarly to H samples, presumably due to much higher activity of prismatic slip. Consequently, the development of HAGBs is stopped, whereas IBs and LAGBs are massively created.

This evolution has also confirmation in GOS and KAM statistics. It is shown that the average GOS (orientation gradients) and KAM (local misorientations) values increase faster in H samples during deformation.

As a consequence of the discussed deformation mechanisms, slightly different kinetics of recrystallization process are reported between the annealed samples. Assuming domination of SIBM, this can be related with difference in HAGBs populations between H and S samples. S17D sample have more HAGBs which are necessary to start sub-grain growth driven by the stored energy gradient therefore more recrystallization grains are formed, and so higher recrystallized area fraction is obtained after 15 minutes of annealing in 610°C.

Regarding texture evolution, deformation leads to a movement from initial main component – tilted $\{0001\}<11\bar{2}0>$; (0°, 30°, 0°) - toward well known deformation component – tilted $\{0001\}<10\bar{1}0>$; (0°, 30°-45°, 30°). This trend is more pronounced in S samples, whereas in H samples higher strains are needed, and even though the main texture maximum has a large spread.

After annealing, it is emphasized that in the H17R sample a complete reverse transition from the main deformation component into main recrystallization component - tilted $\{0001\}<11\bar{2}0>$; (0°, 30°, 0°) is already observed during partial recrystallization, which is a relatively new effect taking into account the well established fact that only extensive grain growth is responsible for such evolution.

In the S17R sample, in turn, main maximum in recrystallization texture is related to the main deformation component by further tilting of *c*-axis thus (0°, 70°, 35°) orientation is formed.

An interesting insight into this evolution is provided by textures of grain boundary areas in the deformed state which reveal important role played by local misorientations located nearby HAGBs. Clearly, orientations that are present simultaneously

in the texture of HAGBs, IBs and also LAGBs disappear first during annealing. Such behavior suggest again SIBM mechanism activated nearby HAGBs due to stored energy gradient introduced by local misorientations within the grains, and related higher density of dislocation structures.

Taking into account the EBSD observations, a physical model has been formulated. It assumes SIBM driven sub-grain growth in regions containing significant difference of local misorientations. The proposed hypothesis has been positively tested using modeling approach. The obtained simulation results find very good correlation with experimental data in terms of texture as well as microstructure evolution. Based on this comparison, it can be argued that the developed model has good perspectives to be a real case scenario.

Last small note concerns applied investigation methodology. With the proposed grain boundary characterization approach, new types of analysis can be performed, like textures and fractions of GB areas, which in the case of zirconium appear to be very helpful in the understanding of the overall microstructure and evolution.

CHAPTER 10

Final summary

THIS thesis aims to make use of the research opportunities provided by experimental and modeling techniques in order to characterize mechanisms of recrystallization and grain growth phenomena occurring in hexagonal metals, in particular titanium and zirconium were considered.

Taking into account the reported research efforts in this subject, author has prepared and carried out several experiments. In this context, most of the experimental work was conducted in Laboratoire des Sciences des Procédés et des Matériaux in Paris–Villetaneuse. Titanium was cold rolled to three different degrees of thickness reduction and extensively heat-treated in order to achieve several stages of recrystallization and grain growth, whereas zirconium was channel die compressed and then briefly annealed for partial recrystallization. Then two EBSD systems were used for measurements.

EBSD technique has been chosen as the main investigation tool since it simultaneously provides unique combination of microstructural information, related microtexture and appropriate statistics of the obtained experimental data. Nevertheless, it requires much attention, mainly due to demanding surface preparation procedure, especially in hexagonal metals. Therefore, in addition to basic introduction and features of the EBSD technique, some practical aspects related with measurement procedure were discussed.

A wide range of EBSD data have been obtained and put into analysis which consisted of various dedicated methods, including: IPF maps, grain size and misorientation distributions, KAM and GOS statistics, ODF and MDF plots, partial

textures. In addition, an original approach of grain boundary characterization was proposed and successfully applied for considered zirconium and titanium. In the first case, analysis of grain boundary textures and grain boundary fractions was performed to shed more light on mechanisms of deformation and recrystallization. In the second, in turn, the algorithm of estimation of grain boundary curvature was applied in order to analyze and simulate grain growth process.

The important information stored in the EBSD map can be also used in the modeling approach. In this context, a special software has been developed from scratch. In the main part, it consists of Monte Carlo Potts model supported by additional GUI applications as well as other extensions. The provided synthetic tests showed that the obtained simulation framework is correctly implemented.

As a result, there are two complementary scientific methods applied in this thesis which, if combined together, can give powerful insights into the undertaken problems. Certainly, experimental EBSD results are the key point to observe microstructure and texture evolution during thermo-mechanical treatment, and thus to develop various hypotheses on mechanisms being involved. On the other hand, the proposed scenarios are often difficult to examine further on the use of experimental approach. This is the point at which the simulations are entering the stage. Despite some necessary approximations, the developed MC Potts model operating on real experimental microstructures can provide a wider perspective on the analyzed mechanisms. Based on that, physical models and hypotheses can be verified in more details, or even refined further.

The mentioned interplay between these scientific approaches was especially evident in the presented investigation of titanium and zirconium.

Hexagonal titanium was cold rolled along initial RD direction until 20%, 40% and 60% of thickness reduction were reached. The imposed values are related with the fact that interesting EBSD results concerning highly rolled titanium (80%) have been reported in the literature. Therefore, the aim of this study is to contribute to these previous efforts, and thus to analyze lower degrees of deformation in terms of following recrystallization and grain growth phenomena.

The main point of the conducted investigation was to analyze the link between deformed and annealed microstructures. It was observed that accommodation of strain is mainly attributed to tensile and compression twins, especially at the beginning of deformation process 20%. Then, microstructure is further fragmented. However, there are also grains which are unfavorably oriented for twinning. They evolve into large areas containing significant orientation gradients. This behavior

was confronted with additional in-situ tensile test which due to absence of twinning indicated similar formation of deformed regions.

Consequently, high microstructure heterogeneity is obtained at the largest strain which, in turn, has crucial impact on recrystallization and grain growth. All these observations are consistent with the presented literature overview. In addition, EBSD analysis described above yielded a number of new findings.

First of all, the three steps of deformation were compared in terms of further grain growth phenomenon. It appeared that 40% is a transition point, where grains can increase their size during further annealing. Nevertheless, only in the case of 60%, the obtained grain growth process is long enough to provide more significant changes in the texture, which are manifested by transition from tilted $\{0001\}<10\bar{1}0>$ component into tilted $\{0001\}<11\bar{2}0>$ component. More detailed analysis of one of the grain growth stages revealed that the described transition is mainly driven by the largest grains which exhibit tilted $\{0001\}<11\bar{2}0>$ component.

Also, it was concluded that kinetics of grain growth is correlated with the evolution of misorientations, in particular, the difference between correlated and uncorrelated distributions of misorientation angle was shown. Moreover, it was revealed that self-similarity property can be attributed to the analyzed grain growth phenomenon.

Further conclusions concern modeling approach. Sample rolled by 60% was chosen as the most interesting one. Simulation of recrystallization with incorporated mechanism of nucleation in highly fragmented areas gave satisfactory results which are comparable with experimental observations. However, it was also noted that the way how orientations are assigned to potential nucleation sites needs to be carefully examined. Simulations of normal grain growth, in turn, showed interesting results about nature of this process.

Hexagonal zirconium was channel die compressed in two perpendicular directions to rather low strains (17% is the highest obtained value) since there are already similar research attempts which have dealt with higher deformations.

At the beginning of compression process, a slight difference in twinning activity between samples compressed along ND and TD directions results in a more pronounced HAGB structure in the latter. However, twinning is rarely observed at higher strains, whereas a significant role of local misorientations, and related orientation spread within the grains, was underlined. Both are connected with formation of large areas comprising of sub-grains delimited by LAGB and interrupted HAGB. Similar tendency was revealed in the case of in-situ tensile test of titanium as well as in the rolled titanium, where large untwined regions exhibit strong orientation

gradients.

Moreover, based on the fact that local misorientations are strictly connected with density of dislocations, and taking into account analysis of grain boundary areas, the SIBM was proposed as dominating mechanism in order to explain behavior observed during partial recrystallization of zirconium.

Furthermore, the obtained physical model of recrystallization was confirmed by MC simulations. It can be emphasized that both microstructure and texture evolutions were reproduced with a good accuracy in the examined samples.

Another conclusion, which deserves much attention, concerns texture evolution in the samples compressed along ND. After 17% of deformation, the resulting texture corresponds well with classical rolling textures of titanium or zirconium. However, after partial recrystallization the main texture maxima are changed, instead of being retained, as in the case of titanium. Therefore, it appears that well the documented exchange between deformation component – tilted $\{0001\}<10\bar{1}0>$ and annealing component – tilted $\{0001\}<11\bar{2}0>$ can take place without significant grain growth process if appropriate SIBM mechanism is active during recrystallization.

It can be summed up that part of the discussed results and conclusions withdrawn in this thesis has been already published, and presented on international conferences in the form of oral and poster presentations. In this regard, it is emphasized that two posters presented by the author have been certified by the best poster award.

It is also admitted that there are still many interesting issues in the undertaken topic, not included in this thesis, which should be investigated in more details. Among them, a perspective of 3D grain growth simulations using real titanium microstructures is highly desired. Also, additional modeling aspects should be considered for both analyzed materials, including the influence of input microstructure and more advanced physical scenarios. In this context, the developed modeling software will be further improved, tested and distributed among scientific community. Cellular Automata model is also planned to be incorporated. From experimental point of view, the major microstructural feature remaining to be characterized in the future work is connected with in-situ tensile test carried out in this thesis.

Finally, it is noted that there are results and ideas in this thesis which should be reviewed and eventually reported in the literature therefore substantial part of undertaken efforts will be devoted for the publishing procedure.

List of publications published by author

1. M. Jedrychowski, J. Tarasiuk, B. Bacroix, S. Wronski, *EBSD investigation of local misorientations and orientation gradients in connection with evolution of grain boundary structures in deformed and annealed Zirconium. A new approach in grain boundary analysis*, Journal of Applied Crystallography, vol. 46, pp. 483–492, 2013

2. M. Jedrychowski, J. Tarasiuk, B. Bacroix, *EBSD investigation of cold rolled and recrystallized titanium*, Materials Science Forum vol. 753, pp. 289–292, 2013

3. M. Jedrychowski, J. Tarasiuk, B. Bacroix, S. Wronski, *An alternative method of grain boundary characterization*, Materials Science Forum, vol. 753, pp. 93–96, 2013

4. M. Jedrychowski, *Characterization of recrystallization phenomena in commercially pure titanium based on EBSD technique*, Proceedings of the ISD Workshops, eds. M. Perzanowski et al., Faculty of Physics and Applied Computer Science, AGH University of Science and Technology, Krakow, pp. 211–214, 2013

5. M. Jedrychowski, J.Tarasiuk, B. Bacroix, S. Wroński, D.Chaubert, *Investigation of deformed and recrystallized textures in zirconium*, Materials Science Forum, vols. 715-716, pp. 940–945, 2012

6. M. Jedrychowski, J. Tarasiuk, S. Wronski, B. Bacroix, *An EBSD analysis of texture evolution observed during recrystallization and grain growth of commercially pure titanium,* to be published in the proceedings of ICOTOM 17

7. M. Jedrychowski, J. Tarasiuk, S. Wronski, B. Bacroix, *Statistical relevance of EBSD microtexture data in the case of commercially pure HCP titanium*, to be published in the proceedings of ICOTOM 17

List of conferences and interships abroad

1. ICOTOM 17 - 17thInternational Conference on Textures of Materials, Drezno, Germany, 2014:
    - oral presentation: *An EBSD analysis of texture evolution observed during recrystallization and grain growth of commercially pure titanium.*
    - poster presentation: *Statistical relevance of EBSD microtexture data in the case of commercially pure HCP titanium.*
2. 5th International Conference on Recrystallization and Grain Growth, Sydney, Austalia, 2013:
    - oral presentation: *EBSD investigation of cold rolled and recrystallized titanium.*
    - poster presentation: *An alternative method of grain boundary characterization.*
3. Workshop GDR Rex 3436 - Modeling in mean field and full field contexts, Paris, France, 2013
4. Microscopy Conference, Kiel, Germany, 2011:
    - poster presentation: *EBSD characterization of deformed and recrystallized commercialy pure titanium* – Best Poster Award
5. Scientific Workshop of the Interdisciplinary PhD Studies: Zakopane 2011; Ochotnica Dolna 2012; Szczyrk 2013; Poland:
    - oral presentation: *Characterization of recrystallization phenomena in commercially pure titanium based on EBSD technique.*
6. 4th International Conference on Recrystallization and Grain Growth, Sheffield, UK, 2010:
    - poster presentation: *EBSD investigation of deformation and recrystallization in zirconium* – Best Poster Award.
7. Laboratoire des Sciences des Procédés et des Matériaux - Université Paris XIII, France (16 months).

List of Figures

List of Tables

Bibliography

[1] F. J. Humphreys, M. Hatherly, Recrystallization and Related Annealing Phenomena, Pergamon Press, Elsevier Science Ltd, Oxford, 1995.

[2] R. D. Doherty, Recrystallization and texture, Progress in Materials Science 42 (1997) 39–58.

[3] R. D. Doherty, D. A. Hughes, F. J. Humphreys, J. J. Jonas, D. J. Jensen, M. E. Kassner, W. E. King, T. R. McNelly, H. J. McQueen, A. D. Rollett, Current issues in recrystallization: a review, Mater. Sci. Eng., A 238 (1997) 219–274.

[4] F. J. Humphreys, M. Hatherly, Recrystallization and Related Annealing Phenomena, 2nd Edition, Elsevier, 2004.

[5] F. J. Humphreys, A unified theory of recovery, recrystallization and grain growth, based on the stability and growth of cellular microstructures–i. the basic model, Acta Mater 45 (1997) 4231–4232.

[6] C. Herring, Surface Tension as a Motivation for Sintering, McGraw-Hill, New-York, 1949.

[7] A. E. Lobkovsky, A. Karma, M. I. Mendelev, M. Haataja, D. J. Srolovitz, Grain shape, grain boundary mobility and the herring relation, Acta Mater. 52 (2004) 285–292.

[8] R. W. Cahn, Recrystallization of single crystals after plastic bending, Journal of the Institute of Metals 76 (1949) 121–143.

[9] R. W. Cahn, A new theory of recrystallization nuclei, Proceedings of the Physical Society 63 (1950) 323–336.

[10] P. A. Beck, P. R. Sperry, H. Hu, The orientation dependence of the rate of boundary migration, J. Appl. Phys. 21 (1950) 420–425.

[11] A. N. Kolmogorov, Sobre a teoria estatistica da cristalizacao de metais, Izv. Akademii Nauk SSSR - Ser. Matemat. 1 (1937) 355–359.

[12] A. Johnson, R. F. Mehl, Reaction kinetics in processes of nucleation and growth, Trans AIME 135 (1939) 416–442.

[13] R. A. Vandermeer, B. B. Rath, Interface migration during recrystallization: The role of recovery and stored energy gradients, Metallurgical Transactions A 21 (1989) 1143–1149.

[14] J. E. Burke, D. Turnbull, Recrystallization and grain growth, Progress in Metal Physics 3 (1952) 220–292.

[15] J. von Neumann, Written discussion of grain shapes and other metallurgical applications of topology, Metal Interfaces, American Society for Metals, Cleveland OH (1952) 108–110.

[16] W. W. Mullins, Two dimensional motion of idealized grain boundaries, J. Appl. Phys. 27 (1956) 900–904.

[17] G. Gottstein, L. S. Shvindlerman, Triple junction drag and grain growth in 2d polycrystals, Acta Mater. 50 (2002) 703–713.

[18] G. Gottstein, Y. Ma, L. S. Shvindlerman, Triple junction motion and grain microstructure evolution, Acta Mater. 53 (2005) 1535–1544.

[19] G. Gottstein, L. S. Shvindlerman, B. Zhao, Thermodynamics and kinetics of grain boundary triple junctions in metals: Recent developments, Scr. Mater. 62 (2010) 914–917.

[20] L. A. Barrales-Mora, G. Gottstein, L. S. Shvindlerman, Effect of a finite boundary junction mobility on the growth rate of grains in two-dimensional polycrystals, Acta Mater. 60 (2012) 546–555.

[21] D. Juul Jensen, Effects of orientation on growth during recrystallization, in: N. Hansen, D. J. Jensen, Y. L. Liu, B. Ralph (Eds.), Microstructural and Crystallographic Aspects of Recrystallization, Vol. 16th Riso International Symposium on Materials Science, Riso National Lab., Roskilde, Denmark, 1995, pp. 119–137.

[22] K. Sztwiertnia, Recrystalization textures and the concept of oriented growth revisited, Mater. Lett. 123 (2014) 41–43.

[23] V. Randle, Applications of electron backscatter diffraction to materials science: status in 2009, J. Mater. Sci. 44 (2009) 4211–4218.

[24] F. C. Campbell, Manufacturing Technology for Aerospace Structural Materials, Elsevier, 2006.

[25] C. Chunxiang, H. BaoMin, Z. Lichen, L. Shuangjin, Technical report: Titanium alloy production technology, market prospects and industry development, Materials and Design 32 (2011) 1684–1691.

[26] M. Yamada, An overview on the development of titanium alloys for non-aerospace application in japan, Mater. Sci. Eng., A 213 (1996) 8–15.

[27] M. Baratz, A. J. Towsen, Arthritis of the wrist and hand. Orthopaedic Surgery: The Essentials, Thieme Publishers, 1999.

[28] E. Teckhoff, Deformation mechanisms, texture and anisotropy of zirconium and Zircaloy, ASTM International, West Conshohocken, PA, 1988.

[29] K. L. Murty, I. Charit, Texture development and anisotropic deformation of zircaloys, Progress in Nuclear Energy 48 (2006) 325–359.

[30] K. L. Murty, R. Jallepalli, S. T. Mahmood, Effects of recrystallization and nb additions on texture and mechanical anisotropy of zircaloy, Nucl. Eng. Des. 148 (1994) 1–15.

[31] B. K. Kad, J. M. Gebert, M. T. Perez-Prado, M. E. Kassner, M. A. Meyers, Ultrafine-grain-sized zirconium by dynamic deformation, Acta Mater. 54 (2006) 4111–4127.

[32] W. Q. Cao, S. H. Yu, S. K. Hwang, B. Bacroix, Microstructure, texture and deformation mechanism of zr702 processed by equal channel angular pressing (ecap), Materials Science Forum 503-504 (2006) 533–538.

[33] W. Q. Cao, S. H. Yu, Y. B. Chun, D. H. Shin, S. K. Hwang, Deformation mechanism of zr702 processed by equal channel angular pressing, Metall. Mater. Trans. A 38 (2007) 2805–2814.

[34] S. Suwas, B. Beausir, L. S. Töth, J. J. Fundenberger, G. Gottstein, Texture evolution in commercially pure titanium after warm equal channel angular extrusion, Acta Mater. 59 (2011) 1121–1133.

[35] W. J. Kim, S. J. Yoo, H. T. Jeong, D. M. Kim, B. H. Choe, J. B. Lee, Effect of the speed ratio on grain refinement and texture development in pure ti during differential speed rolling, Scr. Mater. 64 (2011) 49–52.

[36] H. M. Otte, A. G. Crocker, Crystallographic formulae for hexagonal lattices, Physica Status Solidi B: Basic Solid State Physics 9 (1965) 441–450.

[37] P. G. Partridge, The crystallography and deformation modes of h.c.p. metals, Metall. Rev. 12 (1967) 169–194.

[38] R. von Mises, Mechanik der plastischen formänderung von kristallen, Z. Angew. Math. Mech. 8 (1928) 161–185.

[39] M. J. Philippe, C. Esling, B. Hocheid, Role of twinning in texture development and in plastic deformation of hexagonal materials, Textures and Microstructures 7 (1988) 265–301.

[40] J. R. Morris, Y. Y. Te, K. M. Ho, C. T. Chan, M. H. Yoo, Structures and energies of compression twin boundaries in hcp ti and zr, Philosophical Magazine A 72 (1995) 751–763.

[41] S. G. Song, G. T. Gray, Structural interpretation of the nucleation and growth of deformation twins in zr and ti - ii; tem study of twin morphology and defects reactions during twinning, Acta Metallurgica et Materialia 43 (1995) 2339–2350.

[42] S. G. Song, G. T. Gray, Influence of temperature and strain rate on slip and twinning behavior of zr, Metall. Mater. Trans. A 26 (1995) 2665–2675.

[43] J. F. Bingert, T. A. Mason, G. C. Kaschner, P. J. Maudlin, G. T. Gray, Deformation twinning in polycrystalline zr: Insights from electron backscattered diffraction characterization, Metall. Mater. Trans. A 33 (2002) 955 – 963.

[44] T. A. Manson, J. F. Bingert, G. C. Kaschner, S. I. Wright, R. J. Larsen, Advances in deformation twin characterization using electron backscattered diffraction data, Metall. Mater. Trans. A 33 (2002) 949–954.

[45] Y. B. Chun, S. H. Yu, S. L. Semiatin, S. K. Hwang, Effect of deformation twinning on microstructure and texture evolution during cold rolling of cp-titanium, Mater. Sci. Eng., A 398 (2005) 209–219.

[46] M. R. Barnett, Twinning and the ductility of magnesium alloys. part i: 'tension' twins, Mater. Sci. Eng., A 464 (2007) 1–7.

[47] M. R. Barnett, Twinning and the ductility of magnesium alloys. part ii: 'contraction' twins, Mater. Sci. Eng., A 464 (2007) 8–16.

[48] M. R. Barnett, P. Cizek, Identification and rationalization of secondary twin variants in a magnesium alloy, in: A. Rollett, B. Adams, K. Barmak, T. Bieler (Eds.), ICOTOM 2008 : Proceedings of the 15th International Conference on Textures of Materials (ICOTOM 15), Wiley, 2008, pp. 451–460.

[49] R. J. McCabe, G. Proust, E. K. Cerreta, A. Misra, Quantitative analysis of deformation twinning in zirconium, International Journal of Plasticity 25 (2009) 454–472.

[50] J. H. Chung, Development of thermomechanical processing method to enhance twinning in commercially pure zr, Scr. Mater. 61 (2009) 161–164.

[51] S. Yi, I. Schestakow, S. Zaefferer, Twinning-related microstructural evolution during hot rolling and subsequent annealing of pure magnesium, Mater. Sci. Eng., A 516 (2009) 58–64.

[52] S. K. Sahooa, V. D. Hiwarkar, A. Majumdar, I. Samajdar, P. Pant, G. K. Dey, D. Srivastav, R. Tiwari, S. Banerjee, Presence and absence of significant twinning: Effects on cold deformed microstructures of single phase zircaloy 2, Mater. Sci. Eng., A 518 (2009) 47–55.

[53] N. Bozzolo, L. Chan, A. D. Rollett, Misorientations induced by deformation twinning in titanium, J. Appl. Crystallogr. 43 (2010) 596–602.

[54] J. R. Luo, A. Godfrey, W. Liu, Q. Liu, Twinning behavior of a strongly basal textured az31 mg alloy during warm rolling, Acta Mater. 60 (2012) 1986–1998.

[55] S. Wang, C. Schuman, L. Bao, J. S. Lecomte, Y. Zhang, J. M. Raulot, M. J. Philippe, X. Zhao, C. Esling, Variant selection criterion for twin variants in titanium alloys deformed by rolling, Acta Mater. 60 (2012) 3912–3919.

[56] M. H. Yoo, Slip, twinning, and fracture in hexagonal close-packed metals, Metallurgical Transactions 12 (1981) 409–418.

[57] E. J. Rapperport, Room temperature deformation processes in zirconium, Acta Metallurgica 7 (1959) 254–260.

[58] U. F. Kocks, D. G. Westlake, Trans. TMS-AIME 239 (1967) 1107–1109.

[59] D. R. Chichili, K. T. Ramesh, K. J. Hemker, The high strain rate response of alpha-titanium: Experiments, deformation mechanism and modeling, Acta Mater. 46 (1998) 1025–1043.

[60] S. Nemat-Nasser, W. G. Guo, J. Y. Cheng, Mechanical properties and deformation mechanism of a commercially pure titanium, Acta Mater. 47 (1999) 3705–3720.

[61] N. P. Gurao, R. Kapoor, S. Suwas, Deformation behaviour of commercially pure titanium at extreme strain rates, Acta Mater. 59 (2011) 3431–3446.

[62] H. Francillette, B. Bacroix, M. Gasperini, J. L. Bechade, Grain orientation effects in zr702alfa polycrystalline samples deformed in channel die compression at room temperature, Acta Mater. 46 (1998) 4131–4142.

[63] R. Gehrmann, M. M. Frommert, G. Gottstein, Texture effects on plastic deformation of magnesium, Mater. Sci. Eng., A 395 (2005) 338–349.

[64] L. Guo, Z. Chen, L. Gao, Effects of grain size, texture and twinning on mechanical properties and work-hardening behavior of az31 magnesium alloys, Mater. Sci. Eng., A 528 (2011) 8537–8545.

[65] T. Al-Samman, Comparative study of the deformation behavior of hexagonal magnesium-lithium alloys and a conventional magnesium az31 alloy, Acta Mater. 57 (2009) 2229–2242.

[66] K. Okazaki, H. Conrad, Recrystallization and grain growth in titanium: I. characterization of the structure, Metallurgical Transactions 3 (1972) 2411–2421.

[67] H. Masayuki, Y. Hirofumi, I. Mitsuo, H. Hissaki, Recrystallization behaviour of commercially pure titanium during hot rolling, Tech. Rep. 62, Nippon Steel Technical Report (1994).

[68] P. Ganesan, K. Okazaki, H. Conrad, Characterization of recrystallization and grain growth in ti-7.4 at. pct ai (cph) and ti-15.2 at. pct mo (bcc) alloys, Metallurgical Transactions A 10 (1979) 1021–1029.

[69] F. J. Dunkerly, F. Pledger, V. Damiano, J. Fulton, Grain growth and recrystallization characteristics of zirconium, Trans. AIME 191 (1951) 1003–1024.

[70] R. J. Contieri, M. Zanotello, R. Caram, Recrystallization and grain growth in highly cold worked cp-titanium, Mater. Sci. Eng., A 527 (2010) 3994–4000.

[71] H. R. Wenk, I. Lonardelli, D. Williams, Texture changes in hcp -> bcc -> hcp transformation of zirconium studied in situ by neutron diffraction, Acta Mater. 52 (2004) 1899–1907.

[72] J. Romero, M. Preuss, J. Q. da Fonseca, Texture memory and variant selection during phase transformation of a zirconium alloy, Acta Mater. 57 (2009) 5501–5511.

[73] H. Sharma, S. M. C. van Bohemen, R. H. Petrov, J. Sietsma, Three-dimensional analysis of microstructures in titanium, Acta Mater. 58 (2010) 2399–2407.

[74] Y. N. Wang, J. C. Huang, Review: Texture analysis in hexagonal materials, Mater. Chem. Phys. 81 (2003) 11–26.

[75] C. Lebensohn, P. V. Sanchez, A. A. Pochettino, Modelling texture development of zirconium alloys at high temperatures, Scripta Metallurgica et Materialia 30 (1994) 481–486.

[76] A. Salinas-Rodriguez, Grain size effects on the texture evolution of α-zr, Acta Metallurgica et Materialia 43 (1995) 485–498.

[77] O. Castelnau, H. Francillette, B. Bacroix, R. A. Lebensohn, Texture dependent plastic behavior of zr 702 at large stain, J. Nucl. Mater. 297 (2001) 14–26.

[78] R. D. Doherty, L. C. Chen, I. Samajdar, Cube recrystallization texture - experimental results and modeling, Mat. Sci. Eng. A 257 (1998) 18–36.

[79] O. Engler, Recrystallisation textures in copper-manganese alloys, Acta Metall. Mater. 49 (2001) 1237–1247.

[80] O. Engler, V. Randle, Introduction to Texture Analysis: Macrotexture, Microtexture, and Orientation Mapping, Second Edition, CRC Press, 2009.

[81] D. Griffiths, Explaining texture weakening and improved formability in magnesium rare earth alloys, Mater. Sci. Technol.

[82] D. Chaubet, B. Bacroix, J. L. Béchade, An ebsd study of static recrystallization of cold-rolled zircaloy-4 sheets, Materials Science Forum 408-412 (2002) 797–802.

[83] K. Y. Zhu, D. Chaubet, B. Bacroix, J. L. Béchade, Microstructure and texture evolution during static recrystallization of zr-2hf alloy, Materials Science Forum 467-470 (2004) 537–544.

[84] K. Y. Zhu, D. Chaubet, B. Bacroix, F. Brisset, A study of recovery and primary recrystallization mechanisms in a zr-2hf alloy, Acta Mater. 53 (2005) 5131–5140.

[85] K. Y. Zhu, B. Bacroix, T. Chauveau, D. Chaubet, O. Castelnau, Mechanism of texture evolution during primary recrystallisation and grain growth in a zr-2hf alloy, Materials Science Forum 550 (2007) 545–550.

[86] K. Y. Zhu, B. Bacroix, T. Chauveau, D. Chaubet, O. Castelnau, Texture evolution and associated nucleation and growth mechanisms during annealing of a zr alloy, Metall. Mater. Trans. A 40 (2009) 2423–2434.

[87] B. Bacroix, J. Tarasiuk, K. Wierzbanowski, K. Y. Zhu, Misorientations in rolled and recrystallized zirconium compared with random distribution. a new scheme of misorientation analysis, J. Appl. Crystallogr. 43 (2010) 134–139.

[88] N. Bozzolo, F. Wagner, N. Dewobroto, T. Grosdidier, Recrystallization textures in some hexagonal alloys, Materials Science Forum 408-412 (2002) 901–906.

[89] F. Wagner, N. Bozzolo, O. van Landuyt, T. Grosdidier, Evolution of recrystallisation texture and microstructure in low alloyed titanium sheets, Acta Mater. 50 (2002) 1245–1259.

[90] N. Bozzolo, N. Dewobroto, T. Grosdidier, P. Barberis, F. Wagner, Grain growth texture evolution in zirconium (zr702) and commercially pure titanium (t40), Materials Science Forum 467-470 (2004) 441–446.

[91] N. Dewobroto, Bozzolo, P. N, Barberis, F. Wagner, Experimental investigations of recrystallization texture development in zirconium (zr702), Materials Science Forum 467-470 (2004) 453–458.

[92] N. Bozzolo, N. Dewobroto, T. Grosdidier, F. Wagner, Texture evolution during grain growth in recrystallized commercially pure titanium, Mater. Sci. Eng., A 397 (2005) 346–355.

[93] N. Dewobroto, N. Bozzolo, F. Wagner, Influence of deformation substructures on the early mechanism of recrystallization in cold-rolled titanium and zirconium, Materials Science Forum 495-497 (2005) 711–718.

[94] N. Dewobroto, N. Bozzolo, P. Barberis, F. Wagner, On the mechanisms governing the texture and microstructure evolution during static recrystallization and grain growth of low alloyed zirconium sheets (zr702), Int. J. Mater. Res. (formerly Z. Metallkd.) 97 (2006) 826–833.

[95] N. Bozzolo, N. Dewobroto, H. R. Wenk, F. Wagner, Microstructure and microtexture of highly cold-rolled commercially pure titanium, J. Mater. Sci. 42 (2007) 2405–2416.

[96] N. Bozzolo, G. Sawina, F. Gerspach, K. Sztwiertnia, A. D. Rollett, F. Wagner, Grain boundary character evolution during grain growth in a zr alloy, Materials Science Forum 558-559 (2007) 863–868.

[97] F. Gerspach, N. Bozzolo, F. Wagner, Recrystallisation behavior of cold rolled zr702: Influence of rolling direction and thickness reduction, Materials Science Forum 550 (2007) 459–464.

[98] F. Gerspach, N. Bozzolo, F. Wagner, About texture stability during primary recrystallization of cold-rolled low alloyed zirconium, Scr. Mater. 60 (2009) 203–206.

[99] L. Jiang, M. T. Pérez-Prado, O. A. Ruano, M. E. Kassner, EBSD Study of Annealing Rolled Zirconium, in Materials Processing and Texture (ed A.D. Rollett), John Wiley & Sons, Inc., Hoboken, NJ, USA, 2008.

[100] M. Shi, T. Umetsu, Y. Takayama, H. Kato, H. Watanabe, Microstructure and Texture Gradient in Titanium Severely Strained by Friction Roll Processing and Subsequent Annealing, in Materials Processing and Texture (ed A.D. Rollett), John Wiley & Sons, Inc., Hoboken, NJ, USA, 2008.

[101] Y. B. Chun, S. K. Hwang, Static recrystallization of warm-rolled pure ti influenced by microstructural inhomogeneity, Acta Mater. 56 (2008) 369–379.

[102] C. Hammond, The Basics of CrystallCrystal and Diffration (Third Edition), Oxford University Press, 2009.

[103] V. Randle, Microtexture determination and its applications (2nd Edition), Institute of Materials, Minerals and Mining, 2013.

[104] D. J. Dingley, V. Randle, Microtexture determination by electron back-scatter diffraction, J. Mater. Sci. 27 (1992) 4545–4566.

[105] A. J. Schwartz, M. Kumar, B. L. Adams, D. Field, Electron Backscatter Diffraction in Materials Science (2nd Edition), Springer Science & Business Media, 2009.

[106] A. J. Wilkinson, T. B. Britton, Strains, planes and ebsd in materials science, Materials Today 15 (2012) 366–376.

[107] H.-R. Wenk, P. Van Houtte, Texture and anisotropy, Rep. Prog. Phys. 67 (2004) 1367–1428.

[108] B. L. Adams, S. I. Wright, K. Kunze, Orientation imaging: the emergence of a new microscopy, Metall. Mater. Trans. A 24 (1993) 819–831.

[109] G. Nolze, Image distortions in sem and their influences on ebsd measurements, Ultramicroscopy 107 (2007) 172–183.

[110] TexSEM Laboratories, OIM Analysis For Windows, User Manual (2004).

[111] M. N. Alam, M. Blackman, D. W. Pashley, High angle kikuchi patterns, Proc. Royal Soc. London A 221 (1954) 224–242.

[112] D. Dingley, Progressive steps in the development of electron backscatter diffraction and orientation imaging microscopy, J. Microsc. 213 (2004) 214–224.

[113] V. Randle, Recent developments in electron backscatter diffraction, Advances in Imaging and Electron Physics 151 (2008) 363–416.

[114] N. Gao, S. C. Wang, H. S. Ubhi, M. J. Starink, A comparison of grain size determination by light microscopy and ebsd analysis, Journal of Materials Science Letters 40 (2005) 4971–4974.

[115] K. P. Mingard, B. Roebuck, E. G. Bennett, M. G. Gee, H. Nordenstrom, G. Sweetman, P. Chan, Comparison of ebsd and conventional methods of grain size measurement of hardmetals, Int. J. Refract. Met. Hard Mater. 27 (2009) 213–223.

[116] A. L. Pilchak, A. R. Shiveley, J. S. Tiley, D. L. Ballard, Anystitch: a tool for combining electron backscatter diffraction data sets, Journal of Microscopy 244 (2011) 38–44.

[117] B. L. Henrie, T. A. Mason, J. F. Bingert, Automated twin identification technique for use with electron backscatter diffraction, Materials Science Forum 495-497 (2005) 191–196.

[118] A. Brahme, M. H. Alvi, D. Saylor, J. Fridy, A. D. Rollett, 3d reconstruction of microstructure in a commercial purity aluminum, Scr. Mater. 55 (2006) 75–80.

[119] F. Bachmann, R. Hielscher, H. Schaeben, Grain detedtion from 2d and 3d ebsd data-specification of the mtex algorithm, Ultramicroscopy 111 (2011) 1720–1733.

[120] F. J. Humphreys, Characterisation of fine-scale microstructures by electron backscatter diffraction (ebsd), Scr. Mater. 51 (2004) 771–776.

[121] A. J. Wilkinson, G. Meaden, D. J. Dingley, High resolution mapping of strains and rotations using electron backscatter diffraction, Material Science and Technology 22 (2006) 1271–1278.

[122] S.-B. Lee, A. D. Rollett, G. S. Rohrer, Three-dimensional microstructure reconstruction using fib-oim, Materials Science Forum 558-559 (2007) 915–920.

[123] S. Zaefferer, S. I. Wright, D. Raabe, Three-dimensional orientation microscopy in a focused ion beam–scanning electron microscope: A new dimension of microstructure characterization, Metallurgical and Materials Transactions A 39 (2008) 374–389.

[124] F. J. Humphreys, Review. grain and subgrain characterisation by electron backscatter diffraction, J. Mater. Sci. 36 (2001) 3833–3854.

[125] J. Tarasiuk, P. Gerber, B. Bacroix, Estimation of recrystallized volume fraction from ebsd data, Acta Mater. 50 (2002) 1467–1477.

[126] P. H. Gerber, J. Tarasiuk, R. Chiron, B. Bacroix, Estimation of recrystallized volume fraction from local misorientation calculations, Archives of Metallurgy and Materials 50 (2005) 747–755.

[127] S. Dziaszyk, E. J. Payton, F. Friedel, V. Marx, G. Eggeler, On the characterization of recrystallized fraction using electron backscatter diffraction: A direct comparison to local hardness in an if steel using nanoindentation, Mater. Sci. Eng., A 527 (2010) 7854–7864.

[128] G. Wu, D. J. Jensen, Automatic determination of recrystallization parameters based on ebsd mapping, Mater. Charact. 59 (2008) 794–800.

[129] N. Bozzolo, S. Jacomet, R. E. Logé, Fast in-situ annealing stage coupled with ebsd: A suitable tool to observe quick recrystallization mechanisms, Mater. Charact. 70 (2012) 28–32.

[130] D.-I. Kim, J. S. Kim, J. H. Kim, S.-H. Choi, A study on the annealing behavior of cu-added bake-hardenable steel using an in situ ebsd technique, Acta Mater. 68 (2014) 9–18.

[131] D. Chen, J.-C. Kuo, W.-T. Wu, Effect of microscopic parameters on ebsd spatial resolution, Ultramicroscopy 111 (2011) 1488–1494.

[132] V. Randle, Electron backscatter diffraction: Strategies for reliable data acquisition and processing, Mater. Charact. 60 (2009) 913–922.

[133] G. Petzow, Metallographic Etching: Techniques for Metallography, Ceramography, Plastography (2nd Edition), ASM International, Materials Park, Ohio, USA, 2001.

[134] M. M. Nowell, R. A. Witt, B. W. True, Ebsd sample preparation: Techniques, tips, and tricks, Microscopy Today 13 (2005) 44–48.

[135] G. L. Wynick, C. J. Boehlert, Use of electropolishing for enhanced metallic specimen preparation for electron backscatter diffraction analysis, materials characterization, Materials Characterization 55 (2005) 190–202.

[136] S. Matthies, G. W. Vinel, On the reproduction of the orientation distribution function of texturized samples from reduced pole figures using the conception of a conditional ghost correction, Phys. Status Solidi B 112 (1982) K111–120.

[137] H. J. Bunge, Texture analysis in materials science: mathematical methods, London : Butterworths, 1982.

[138] D. Ruer, A. Vadon, Quantitative Texture Analysis, DGM e.V., Société Francaise de Metallurgie, 1982, Ch. The vector method.

[139] K. Pawlik, Determination of the orientation distribution function from pole figures in arbitrarily defined cells, Phys. Status Solidi B 134 (1986) 477–483.

[140] K. Pawlik, P. Ozga, LaboTex: The Texture Analysis Software",'Göttinger Arbeiten zur Geologie und Paläontologie (1999).

[141] N. Bozzolo, F. Gerspach, G. Sawina, F. Wagner, Accuracy of orientation distribution function determination based on ebsd data - a case study of a recrystallized low alloyed zr sheet, Journal of Microscopy 227 (2007) 275–283.

[142] M. Jedrychowski, J. Tarasiuk, S. Wronski, B. Bacroix, Statistical relevance of ebsd microtexture data in the case of commercially pure hcp titanium, in: Proceedings of ICOTOM 17, 2015.

[143] N. Rajmohan, Y. Hayakawa, J. A. Szpunar, J. H. Root, Neutron diffraction method for stored energy measurement in interstitial free steel, Acta Mater. 45 (1997) 2485–2494.

[144] P. Gerber, J. Tarasiuk, T. Chauveau, B. Bacroix, A quantitative analysis of the evolution of texture and stored energy during annealing of cold rolled copper, Acta Mater. 51 (2003) 6359–6371.

[145] N. Rajmohan, J. A. Szpunar, Stored energy in can body aluminium alloy after cold rolling and stress relieving, Mater. Sci. Technol. 15 (1999) 1259–1265.

[146] F. Cruz-Gandarilla, A. M. Salcedo-Garrido, T. Baudin, H. Mendoza-León, R. Penelle, Generalized pole figures and stored energy distribution function obtained by x-ray diffraction, Materials Science Forum 702-703 (2012) 519–522.

[147] J. Tarasiuk, P. Gerber, B. Bacroix, K. Piekos, Modeling of recrystallization using monte carlo method based on ebsd data, Materials Science Forum 412 (2002) 395–400.

[148] S.-H. Choi, J. Y-S, Evaluation of stored energy in cold-rolled steels from ebsd data, Mater. Sci. Eng., A 371 (2004) 149–159.

[149] J. Tarasiuk, P. H. Gerber, B. Bacroix, Monte carlo modelling of recrystallization in metals, Journal de Physique IV 120 (2004) 217–223.

[150] B. S. El-Dasher, B. L. Adams, A. D. Rollett, Viewpoint: experimental recovery of geometrically necessary dislocation density in polycrystals, Scripta Materialia 48 (2003) 141–146.

[151] Y. Takayama, J. A. Szpunar, Stored energy and taylor factor relation in an al-mg-mn alloy sheet worked by continuous cyclic bending, Mater. Trans. 45 (2004) 2316–2325.

[152] D. P. Field, P. B. Trivedi, S. I. Wright, M. Kumar, Analysis of local orientation gradients in deformed single crystals, Ultramicroscopy 103 (2005) 33–39.

[153] W. Pantleon, Resolving the geometrically necessary dislocation content by conventional electron backscattering diffraction, Scripta Materialia 58 (2008) 994–997.

[154] M. Calcagnotto, D. Ponge, E. Demir, D. Raabe, Orientation gradients and geometrically necessary dislocations in ultrafine grained dual-phase steels studied by 2d and 3d ebsd, Mater. Sci. Eng., A 527 (2010) 2738–2746.

[155] M. Kamaya, Measurement of local plastic strain distribution of stainless steel by electron backscatter diffraction, Mater. Charact. 60 (2009) 125–132.

[156] M. Kamaya, Assessment of local deformation using ebsd: Quantification of local damage at grain boundaries, Mater. Charact. 66 (2012) 56–67.

[157] S.-H. Choi, J. H. Cho, Primary recrystallization modelling for interstitial free steels, Materials Science and Engineering: A 405 (2005) 86–101.

[158] C. Fang, C. I. Garcia, C. S. H, A. J. DeArdo, Assessment of the stored energy evolution during batch annealing process of cold rolled hsla steels, Materials Science Forum 715-716 (2012) 557–562.

[159] G. E. Moore, Cramming more components onto integrated circuits, PROCEEDINGS OF THE IEEE 86 (1998) 82–85.

[160] F. J. Humphreys, Modelling mechanisms and microstructures of recrystallisation, Mater. Sci. Technol. 8 (1992) 135–144.

[161] H. J. Frost, C. V. Thompson, Computer simulation of grain growth, Current Opinion in Solid State and Materials Science 3 (1996) 361–368.

[162] A. D. Rollet, Overview of modeling and simulation of recrystallization, Prog. Mater. Sc. 42 (1997) 72–99.

[163] M. A. Miodownik, A review of microstructural computer models used to simulate grain growth and recrystallisation in aluminium alloys, Journal of Light Metals 2 (2002) 125–135.

[164] K. G. F. Janssens, D. Raabe, E. Kozeschnik, M. A. Miodownik, B. Nestler, Computational Materials Engineering, Elsevier, London, 2007.

[165] H. Hallberg, Approaches to modeling of recrystallization, Metals 1 (2011) 16–48.

[166] A. D. Rollet, D. Raabe, A hybrid model for mesoscopic simulation of recrystallization, Computational Materials Science 21 (2001) 69–78.

[167] L. Sieradzki, L. Madej, A perceptive comparison of the cellular automata and monte carlo techniques in application to static recrystallization modeling in polycrystalline materials, Computational Materials Science 67 (2013) 156–173.

[168] E. A. Lazar, J. K. Mason, R. D. MacPherson, D. J. Srolovitz, A more accurate three-dimensional grain growth algorithm, Acta Mater. 59 (2011) 6837–6847.

[169] K. Brakke, The surface evolver, Experimental Mathematics 1 (1992) 141–165.

[170] F. Wakai, N. Enomoto, H. Ogawa, Three-dimensional microstructural evolution in ideal grain growth–general statistics, Acta Mater. 48 (2000) 1297–1311.

[171] K. Piekos, J. Tarasiuk, K. Wierzbanowski, B. Bacroix, Development of two-dimensional vertex type model, Materials Science Forum 467-470 (2004) 653–658.

[172] M. P. Anderson, D. J. Srolovitz, G. S. Grest, P. S. Sahni, Computer simulation of grain growth–i. kinetics, Acta Metallurgica 32 (1984) 783–791.

[173] D. J. Srolovitz, M. P. Anderson, P. S. Sahni, G. S. Grest, Computer simulation of grain growt–ii. grain size distribution, topology, and local dynamics, Acta Metallurgica 32 (1984) 793–802.

[174] D. J. Srolovitz, G. S. Grest, M. P. Anderson, Computer simulation of recrystallizatio–i. homogeneous nucleation and growth, Acta Metallurgica 34 (1986) 1833–1845.

[175] M. P. Anderson, G. S. Grest, D. J. Srolovitz, Computer simulation of normal grain growth in three dimensions, Philos. Mag. B 59 (1989) 293–329.

[176] E. A. Holm, J. A. Glazier, D. J. Srolovitz, G. S. Grest, The effect of lattice anisotropy and temperature on grain growth in the two-dimensional potts model, Physical Review A 43 (1991) 2662–2668.

[177] G. S. Grest, J. A. Glazier, M. P. Anderson, E. A. Holm, J. Srolovitz, Coarsening in two-dimensional soap froths and large-q potts model, Mater. Res. Soc. Symp. Proc. 237 (1992) 101–111.

[178] E. A. Holm, G. N. Hassold, M. A. Miodownik, On misorientation distribution evolution during anisotropic grain growth, Acta Mater. 49 (2001) 2981–2991.

[179] D. Zöllner, A new point of view to determine the simulation temperature for the potts model simulation of grain growth, Computational Materials Science 86 (2014) 99–107.

[180] D. Solas, P. Gerber, T. Baudin, R. Penelle, Monte carlo method for simulating grain growth in 3d, influence of lattice site arrangements, Materials Science Forum 467-470 (2004) 1117–1122.

[181] Y. J. Kim, S. K. Hwang, M. H. Kim, S. I. Kwun, S. W. Chae, Three-dimensional monte-carlo simulation of grain growth using triangular lattice, Mater. Sci. Eng., A 408 (2005) 110–120.

[182] B. Radhakrishnan, T. Zacharia, Simulation of curvature-driven grain growth by using a modified monte carlo algorithm, Metall. Mater. Trans. A 26 (1995) 167–180.

[183] Q. Yu, S. K. Esche, A monte carlo algorithm for single phase normal grain growth with improved accuracy and efficiency, Computational Materials Science 27 (2003) 259–270.

[184] C. M. Huang, C. L. Joanne, B. S. V. Patnaik, R. Jayaganthan, Monte carlo simulation of grain growth in polycrystalline materials, Appl. Surf. Sci. 252 (2006) 3997–4002.

[185] S. Xiaoyan, L. Guoquan, A simple and efficient three-dimensional monte carlo simulation of grain growth, Scripta Materialia 38 (1998) 1691–1696.

[186] S. A. Wright, S. J. Plimpton, T. P. Swiler, R. M. Fye, M. F. Young, E. A. Holm, Potts-model grain growth simulations: Parallel algorithms and applications, Tech. rep., Sandia National Laboratories (1997).

[187] M. A. Miodownik, E. A. Holm, G. N. Hassold, Highly parallel computer simulations of particle pinning: Zener vindicated, Scr. Mater. 42 (2000) 1173–1177.

[188] W. Read, W. Shockley, Dislocation models of crystal grain boundaries, Phys. Rev. 78 (1950) 275–289.

[189] P. Tavernier, J. A. Szpunar, Modelling of recrystallization textures, Acta Metallurgica 39 (1991) 549–556.

[190] O. M. Ivasishin, N. L. Vasiliev, S. V. Shevchenko, S. L. Semiatin, A 3-d monte-carlo (potts) model for recrystallization and grain growth in polycrystalline materials, Mater. Sci. Eng., A 433 (2006) 216–232.

[191] L. Zhang, A. D. Rollett, T. Bartel, D. Wu, M. T. Lusk, A calibrated monte carlo approach to quantify the impacts of misorientation and different driving forces on texture development, Acta Mater. 60 (2012) 1201–1210.

[192] Q. Yu, S. K. Esche, Modeling of grain growth kinetics with read - shockley grain boundary energy by a modified monte carlo algorithm, Mater. Lett. 56 (2002) 47–52.

[193] L. Hui, W. Guanghou, D. Feng, B. Xiufang, F. Pederiva, Monte carlo simulation of three-dimensional polycrystalline material, Mater. Sci. Eng., A 357 (2003) 153–158.

[194] N. Ono, K. Kimura, T. Watanabe, Monte carlo simulation of grain growth with the full spectra of grain orientation and grain boundary energy, Acta Mater. 47 (1999) 1007–1017.

[195] Q. Yu, M. Nosonovsky, S. K. Esche, Monte carlo simulation of grain growth of single-phase systems with anisotropic boundary energies, International Journal of Mechanical Sciences 51 (2009) 434–442.

[196] J. B. Allen, C. F. Cornwell, B. D. Devine, C. R. Welch, Simulations of anisotropic grain growth in single phase materials using q-state monte carlo, Computational Materials Science 71 (2013) 25–32.

[197] Y. B. Chun, S. L. Semiatin, S. K. Hwang, Monte carlo modeling of microstructure evolution during the static recrystallization of cold-rolled, commercial-purity titanium, Acta Mater. 54 (2006) 3673–3689.

[198] E. Fjeldberg, K. Marthinsen, A 3d monte carlo study of the effect of grain boundary anisotropy and particles on the size distribution of grains after recrystallisation and grain growth, Computational Materials Science 48 (2010) 267–281.

[199] F. Caleyo, T. Baudin, R. Penelle, Monte carlo simulation of recrystallization in fe-50(2002) 829–835.

[200] O. M. Ivasishin, S. V. Shevchenko, N. L. Vasiliev, S. L. Semiatin, 3d monte carlo simulation of texture-controlled grain growth, Acta Mater. 51 (2003) 1019–1034.

[201] O. M. Ivasishin, S. V. Shevchenko, S. L. Semiatin, Implementation of exact grain-boundary geometry into a 3-d monte-carlo (potts) model for microstructure evolution, Acta Mater. 57 (2009) 2834–2844.

[202] D. Zöllner, A potts model for junction limited grain growth, Computational Materials Science 50 (2011) 2712–2719.

[203] D. Zöllner, P. Streitenberger, Potts model simulation of grain boundary junction limited grain growth, Materials Science Forum 715-716 (2012) 623–628.

[204] D. Raabe, Scaling monte carlo kinetics of the potts model using rate theory, Acta Mater. 48 (2000) 1617–1628.

[205] G. Sawina, F. Gerspach, N. Bozzolo, K. Sztwiertnia, A. D. Rollett, F. Wagner, Modeling the evolution of orientation distribution functions during grain growth of some ti and zr alloys, Materials Science Forum 559 (2007) 1163–1168.

[206] Z. Yang, S. Sista, J. W. Elmer, T. Debroy, Three dimentional monte carlo simulation of grain growth during gta welding of titanium, Acta Mater. 48 (2000) 4813–4825.

[207] S. H. Yu, Y. B. Chun, S. K. Hwang, D. H. Shin, Texture development and monte-carlo simulation of microstructure evolution in pure zr grain-refined by equal channel angular pressing, Philos. Mag. 85 (2005) 345–371.

[208] Y. S. Seo, Y. B. Chun, S. K. Hwang, A 3d monte-carlo simulation study of recrystallization kinetics in zr with hypothetical stored energy gradients, Computational Materials Science 43 (2008) 512–521.

[209] M. Kazeminezhad, A. K. Taheri, A. K. Tieu, Utilization of the finite element and monte carlo model for simulating the recrystallization of inhomogeneous deformation of copper, Computational Materials Science 38 (2007) 765–773.

[210] B. Radhakrishnan, G. B. Sarma, T. Zacharia, Modeling the kinetics and microstructural evolution during static recrystallization - monte carlo simulation of recrystallization, Acta Materialia 46 (1998) 4415–4433.

[211] E. A. Holm, M. A. Miodownik, A. D. Rollet, On abnormal subgrain growth and the origin of recrystallization nuclei, Acta Mater. 51 (2003) 2701–2716.

[212] A. R. Eivani, J. Zhou, J. Duszczyk, A new approach to incorporating the effect of nano-sized dispersoids on recrystallization inhibition into monte carlo simulation, Computational Materials Science 54 (2012) 370–377.

[213] P. Gerber, J. Tarasiuk, D. E. Solas, S. Jakani, M.-H. Mathon, T. Baudin, Monte carlo modelling of recrystallization mechanisms in wire-drawn copper from ebsd data, Materials Science Forum 470 (2004) 635–640.

[214] M. Miodownik, A. W. Godfrey, E. A. Holm, D. A. Hughes, On boundary misorientation distribution functions and how to incorporate them into three-dimensional models of microstructural evolution, Acta Materialia 47 (1999) 2661–2668.

[215] D. M. Saylor, J. Fridy, B. S. El-dasher, K. Jung, A. D. Rollett, Statistically representative three-dimensional microstructures based on orthogonal observation sections, Metallurgical and Materials Transactions A 35 (2004) 1969–1979.

[216] D. E. Solas, C. N. Tome, H. R. Wenk, Deformation and recrystallization of hexagonal metals: Modeling and experimental results for zinc, Acta Materialia 49 (2001) 3791–3801.

[217] F. Roters, P. Eisenlohr, L. Hantcherli, D. D. Tjahjanto, T. R. Bieler, D. Raabe, Overview of constitutive laws, kinematics, homogenization and multiscale methods in crystal plasticity finite-element modeling: Theory, experiments, applications., Acta Materialia 58 (2010) 1152–1211.

[218] M. A. Groeber, M. A. Jackson, Dream.3d: A digital representation environment for the analysis of microstructure in 3d, Integrating Materials and Manufacturing Innovation 3:5 (2014) 1–17.

[219] T. Watanabe, An approach to gain grain boundary design for strong and ductile polycrystals, Res. Mech. 11 (1984) 47–84.

[220] M. Kumar, C. A. Schuh, Viewpoint set on grain boundary engineering, Scr. Mater. 54 (2006) 961–1070.

[221] V. Randle, Twinning-related grain boundary engineering, Acta Mater. 52 (2004) 4067–4081.

[222] G. S. Rohrer, V. Randle, Measurement of the Five-Parameter Grain Boundary Distribution from Planar Sections, Springer Science, Business Media, 2009.

[223] M. Jedrychowski, T. J, B. Bacroix, W. Wronski, Electron backscatter diffraction investigation of local misorientations and orientation gradients in connection with evolution of grain boundary structures in deformed and annealed zirconium. a new approach in grain boundary analysis, J. Appl. Cryst. 46 (2013) 483–492.

[224] M. Jedrychowski, J. Tarasiuk, B. Bacroix, W. Wronski, An alternative method of grain boundary characterization, Materials Science Forum 753 (2013) 93–96.

[225] N. Hansen, D. Juul Jensen, Development of microstructure in fcc metals during cold work, Philos. Trans. R. Soc. London Ser. A 357 (1999) 1447–1469.

[226] C. Cabus, H. Regle, B. Bacroix, Orientation relationship between austenite and bainite in a multiphased steel, Materials Characterization 58 (2007) 332–338.

[227] F. Bachmann, R. Hielscher, H. Schaeben, Texture analysis with mtex – free and open source software toolbox, Sol. St. Phen. 160 (2010) 63–68.

[228] A. Morawiec, Misorientation angle distribution of randomly oriented symmetric objects, J. Appl. Cryst. 28 (1995) 289–293.

[229] J. Pospiech, K. Sztwiertnia, F. Haessner, The misorientation distribution function, Textures and Microstructures 6 (1986) 201–215.

[230] J. Pospiech, K. Lucke, K. Sztwiertnia, Orientation distribution and orientation correlation functions for description of microstructures, Acta metallurgica 41 (1993) 305–321.

Internet resources

[www-Documentation] http://www.fis.agh.edu.pl/kfms/simulations-of-rex-and-gg

[www-GGsoft] http://www.matforge.org/cmu/wiki/pgg3d

[www-OIM] http://www.edax.com/Products/EBSD/OIM-Data-Analysis-Microstructure-Analysis.aspx

[www-OpenMP] http://www.openmp.org/wp

[www-Paraview] http://www.paraview.org